



# Properties and evolution of galaxies in galaxy clusters up to a redshift of $z \sim 1.0$

by

**Zelege Beyoro Amado**

A Dissertation Submitted to Astronomy and Astrophysics Research  
and Development Department

In partial fulfillment of the degree of Doctor of Philosophy (PhD)  
in Astronomy and Astrophysics at Entoto Observatory and  
Research Center

the Ethiopian Space Science and Technology Institute  
affiliated with Addis Ababa University

April, 2021

Addis Ababa, Ethiopia

© Copyright by Zeleke Beyoro Amado, 2021

All Rights Reserved






# Declaration of authorship

I hereby declare that the investigation presented in this dissertation titled, **Properties and evolution of galaxies in galaxy clusters up to a redshift of  $z \sim 1.0$**  and has been carried out by me independently in Astronomy and Astrophysics Research and Development Department under the supervision of **Dr. Solomon Belay Tessema, Dr. Mirjana Pović and Dr. Miguel Sánchez-Portal** at Entoto Observatory and Research Centre (EORC), Ethiopian Space Science and Technology Institute (ESSTI) affiliated with Addis Ababa University (AAU). This dissertation has not been reported either in published form in a journal or in a thesis by anyone (other than me), to the best of my knowledge. It is entirely my original work. I further declare that this dissertation has not been considered by any University or institute, for the award of a degree, diploma, associateship or fellowship.

Zelege Beyoro Amado (PhD Candidate)

Signature  Date 08/02/2021

This PhD dissertation has been submitted for examination with our approval as University supervisors

	<u>Signature</u>	<u>Date</u>
1. Dr. Solomon Belay Tessema (Supervisor):		<u>03/02/2021</u>
2. Dr. Mirjana Pović (Supervisor):		<u>03/02/2021</u>
3. Dr. Miguel Sánchez-Portal (Supervisor):		<u>03/02/2021</u>

Digitally signed by SANCHEZ PORTAL MIGUEL - 05259159W  
Date: 2021.02.07 20:57:33 +01'00'

**Place:** Ethiopian Space Science and Technology Institute

Addis Ababa, Ethiopia



This is to certify that this thesis submitted in partial fulfillment of the requirements for the degree of Doctor of Philosophy (PhD) in Astronomy and Astrophysics complies with the regulations of the University and meets the accepted standards with respect to originality.

Title: **Properties and evolution of galaxies in galaxy clusters up to a redshift of  $z \sim 1.0$**

By: **ZELEKE BEYORO AMADO**

Approved by the Examination Committee:

1. Dr. Shambel Sahlu (Chair Person)
2. Prof. Florence Durret (External Examiner)
3. Dr. Tolu Biressa (Internal Examiner)
4. Dr. Solomon Belay Tessema (Main Supervisor)
5. Dr. Mirjana Pović (Co-Supervisor)
6. Dr. Miguel Sánchez-Portal (Co-Supervisor)

Signature

*[Handwritten signature]* 31/03/2021

*[Handwritten signature]*

March 31, 2021

*[Handwritten signature]* 31/03/2021

*[Handwritten signature]*

Digitally signed by  
SANCHEZ PORTAL  
MIGUEL, DN: cn=SANCHEZ PORTAL,  
Date: 2021.04.08  
09:20:31 +02'00'

Date of the defense: **March 31, 2021**



Signature of the Head of the Institute

*[Handwritten signature]*

**Abdissa Yilma**  
**Director General**

*“One way to learn the mind of the Creator is to study His creation. We must pay God the compliment of studying His work of art and this should apply to all realms of human thought. A refusal to use our intelligence honestly is an act of contempt for Him who gave us that intelligence.”*

Ernest Walton, the 1951 Nobel Prize winner in Physics

*This work is dedicated to my late father Beyoro Amado  
who was so dedicated and paid a lot to educate me  
eventhough he didn't get a chance to pursue modern  
education.*

# Abstract

Clusters of galaxies are some of the large known gravitationally bound structures in the Universe. Therefore, studying the properties of galaxies inside the galaxy clusters represents one of the main steps to understand the formation and evolution of the Universe at large. We studied the properties and evolution of galaxies in clusters at redshifts up to  $z \sim 1.0$ , focussing on morphology, star forming (SF) and AGN activities, and metallicity variations in relation to other cluster properties. Three galaxy clusters (ZwCl0024+1652 at  $z \sim 0.4$ , RXJ1257+4738 at  $z \sim 0.866$ , and Virgo at  $z \sim 0.0038$ ) up to a redshift of  $z \sim 1.0$  have been selected. The GLACE TF and public data were used in this thesis. We fully performed a TF data reduction of the [OIII] and  $H\beta$  observations for ZwCl0024+1652 and partially did the reduction of  $H\beta$  images of RXJ1257+4738 cluster using a TF package called TFRed.

Detailed morphological classification of the ZwCl0024+1652 cluster member galaxies has been performed using galSVM, obtaining up to date the most detailed morphological catalogue of member galaxies up to a clustercentric distance of 1 Mpc. In line with many of previous studies, we found that ET proportion decreases with redshift while the LT proportion increases with redshift. At all redshifts, ETs dominate the LTs at cluster core and decreases with clustercentric distance. BPT-NII diagram was used to separate AGNs and SF galaxies in ZwCl0024+1652. For this cluster, it has been determined that the fraction of SF galaxies and AGNs remain roughly constant across the low- and medium- density environments, dropping sharply towards high-density environments. SFRs have been computed for the galaxies in all three clusters, and relationships have been established parameters such as stellar mass and local density.

Finally, metallicities have been studied for member galaxies of the two lower redshift clusters (ZwCl0024+1652 and Virgo), but not RXJ1257+4738 due to the lack of appropriate data. We computed the gas-phase metallicities and analysed them in relation to SFR,  $\Sigma_5$ , sSFR and  $M_*$ . The mean gas metallicity of ZwCl0024+1652 cluster galaxies ( $\bar{Z} = 8.63$ ) is greater than that of Virgo ( $\bar{Z} = 8.52$ ), but we report a strong influence of sample selection on this result. We report correlation for  $Z$  vs.  $\log(M_*/M_\odot)$ , and  $Z$  vs.  $\log(\text{SFR})$ , whereas anticorrelation for  $Z$  vs.  $\log(\text{sSFR})$  relations for both cluster galaxies, becoming more tight for higher redshift cluster.

# Acknowledgements

I am highly indebted to thank the pioneers in establishing Entoto Observatory and Research Center (EORC), especially the first director of the research center, Dr Solomon Belay Tessema and other founding staff members. This is because I got this great opportunity to carry out my research in Extragalactic Astronomy while pursuing my PhD study, where EORC has availed important facilities including working compound, internet access and support personnel to conduct my research. My gratitude also extends to the current Ethiopian Space Science and Technology Institute (ESSTI) in which EORC is structurally located under, for the continual and uninterrupted support for my study. ESSTI has provided me with financial support for my two times visit to Granada, Spain for carrying out part of my research. I would also like to thank the Astronomy and Astrophysics Research and Development Department of ESSTI-EORC for managing all the supports during this study.

Next to this, I would like to extend heartfelt thanks to my PhD thesis supervisors; Dr. Solomon Belay Tessema, Dr. Mirjana Pović and Dr. Miguel Sánchez-Portal, for all of the encouragements, support, continual devotion of their energy and time, and appropriately leading me in the correct path of my research that ultimately resulted with this PhD dissertation. I extend especial thanks to Dr. Mirjana for her extraordinary commitment and immediate support while I was at conditions where I couldn't proceed (when I became stuck), even while she had a serious family problem. Apart from his supervisory role, I would like to thank Dr. Miguel for his commitment for helping me in searching for financial support for durations abroad, especially for my three weeks stay at Santiago, Chile and my second visit to Granada, Spain.

Thirdly, I have to give great thanks to ESO-ALMA at Santiago, Chile and IRAM at Granada, Spain for their financial support and providing me with working space during my visit to respective institutes. My thanks are also extended to IAA Granada for availing working office during my first visit to Spain. Without them, it would be impossible to complete my research. I am very grateful also to Kotebe Metropolitan University (KMU) that sponsored me for my study.

My heartfelt thanks and appreciations goes to my family, especially to my wife Genet Yohannes for her great patience, continual encouragement, endless love and managing the family; and my brother Getachew Beyoro with his family, for their great support, encouragements and for continually taking my responsibilities in

supporting our common family at country side. My family were doing their best in helping me to focus on my study. Nothing would have been possible without them.

Finally, my thanks should be extended to all my collaborators at GLACE, whose names appeared in publications that came out of this thesis. My special thanks should be given to Ángel Bongiovanni (IRAM, Granada, Spain) for his committed and continual support during the analysis, especially related to Chapter 5 of this thesis. At this point I have to finally extend my thanks to my friends: Tilahun Getachew (PhD candidate, ESSTI-EORC), Melese Getinet (University of Granada, Spain), Dejene Zewdie (Universidad Diego Portales, Chile), and all the staff members of the ESSTI-EORC for their unlimited support and friendly encouragements. Their support was crucial for my progress at different stages during this study.

Sincerely,

Zelege Beyoro Amado

Ethiopian Space Science and Technology Institute (ESSTI)

Enoto Observatory and Research Center (EORC)

Astronomy and Astrophysics Research and Development Department

Addis Ababa, Ethiopia

# List of Publications

1. **Beyoro-Amado, Z.**, Pović, M., Sánchez-Portal, M., Tessema, S, B., et al., A morphological study of galaxies in ZwCl0024 + 1652, a galaxy cluster at redshift  $z \sim 0.4$ , MNRAS, 485, 1528 - 1545, doi:10.1093/mnras/stz427, 2019.
2. **Beyoro-Amado, Z.**, Sánchez-Portal, M., Bongiovanni, Á., Pović, M., Tessema, S, B., et al., GLACE survey: galaxy activity in ZwCl0024+1652 cluster from strong optical emission lines, MNRAS, 501, 2430 - 2450, doi:10.1093/mnras/staa3812, 2021.
3. **Beyoro-Amado, Z.**, Pović, M., Sánchez-Portal, M., & Tessema, S, B., Galaxy evolution studies in clusters: the case of Cl0024+1652 cluster galaxies at  $z \sim 0.4$ , Proceedings of the International Astronomical Union, 15(S356), 163-168, 2019, doi:10.1017/S174392132000280X, 2019.
4. Bilata-Woldeyes. B., Pović, M., **Beyoro-Amado, Z.**, Getachew-Woreta, T. and Shimeles T., Multiwavelength morphological study of active galaxies, Proceedings of the International Astronomical Union, 15(S356), 295-298. doi:10.1017/S1743921320003154, 2019.
5. Getachew-Woreta, T., Pović, M., Masegosa, J., Perea, J., **Beyoro-Amado, Z.** and Márquez Perez, I. , Study of AGN contribution on morphological parameters of their host galaxies, Proceedings of the International Astronomical Union, 15(S356), 158-162, doi:10.1017/S1743921320002793, 2019.

# Contents

<b>Declaration</b>	<b>iii</b>
<b>Abstract</b>	<b>vii</b>
<b>Acknowledgements</b>	<b>viii</b>
<b>List of Publications</b>	<b>x</b>
<b>Table of Contents</b>	<b>xi</b>
<b>List of Figures</b>	<b>xv</b>
<b>List of Tables</b>	<b>xviii</b>
<b>List of abbreviations</b>	<b>xx</b>
<b>Astronomical constants</b>	<b>xxiii</b>
<b>1 General introduction</b>	<b>1</b>
1.1 Galaxy clusters: general overview . . . . .	1
1.2 Physical mechanisms within galaxy clusters . . . . .	3
1.3 The SF and AGN in galaxy clusters . . . . .	5
1.4 Analysed parameters for evolution of galaxy populations in galaxy clusters . . . . .	7
1.4.1 Morphological properties . . . . .	7
1.4.2 Star formation rates (SFR) . . . . .	9
1.4.3 AGN fractions in clusters . . . . .	10
1.4.4 Metallicity distributions . . . . .	11
1.4.5 Colour-magnitude diagrams . . . . .	14
1.5 ZwCl0024+1652 galaxy cluster . . . . .	15
1.6 RXJ1257+4738 galaxy cluster . . . . .	16
1.7 The Virgo cluster . . . . .	17
1.8 GaLaxy Cluster Evolution (GLACE) survey . . . . .	18
1.9 Rational of the study . . . . .	22



1.10	Objectives of the thesis . . . . .	23
1.10.1	General objective . . . . .	23
1.10.2	Specific objectives . . . . .	23
1.11	General methodology . . . . .	24
1.12	Significance of the study . . . . .	26
1.13	Scope of the study . . . . .	27
1.14	Limitations of the study . . . . .	27
1.15	Outline of the thesis . . . . .	28
<b>2</b>	<b>The Observational data</b>	<b>29</b>
2.1	The GLACE Tunable Filter (TF) data . . . . .	29
2.1.1	The Gran Telescopio CANARIAS (GTC) . . . . .	30
2.1.2	OSIRIS and tunable filters . . . . .	30
2.2	The data used for ZwCl0024+1652 cluster . . . . .	36
2.2.1	The [OIII] and $H\beta$ imaging GLACE TF data . . . . .	36
2.2.1.1	[OIII] imaging data . . . . .	36
2.2.1.2	$H\beta$ imaging data . . . . .	37
2.2.2	Other GLACE TF data . . . . .	37
2.2.3	Non-GLACE public data . . . . .	38
2.2.3.1	The HST/ACS data . . . . .	38
2.2.3.2	WFP2 catalogue data . . . . .	39
2.2.3.3	Galaxy data for cluster-field comparison . . . . .	41
2.3	RXJ1257+4738 data . . . . .	41
2.3.1	The GLACE raw TF imaging: $H\beta$ . . . . .	41
2.3.2	The [OII] TF imaging data . . . . .	43
2.3.3	Public GLACE data . . . . .	44
2.4	Data used for Virgo cluster . . . . .	44
<b>3</b>	<b>Tunable filter (TF) data reduction</b>	<b>46</b>
3.1	The basic raw image reduction . . . . .	46
3.1.1	ZwCl0024+1652 cluster data . . . . .	46
3.1.1.1	Bias and flat-field correction . . . . .	47
3.1.1.2	Removal of cosmic rays . . . . .	47
3.1.1.3	Subtraction of sky rings . . . . .	48
3.1.1.4	Aligning the images . . . . .	48
3.1.1.5	Image combination and creation of a deep image . . . . .	49
3.1.1.6	Astrometry . . . . .	52
3.1.1.7	Degradation of images . . . . .	53
3.1.2	RXJ1257+4738 cluster data . . . . .	53
3.2	Generating the catalogues of sources . . . . .	54
3.3	Wavelength and flux calibration . . . . .	58
<b>4</b>	<b>Morphology of galaxies in galaxy clusters</b>	<b>60</b>
4.1	Introduction . . . . .	60

4.2	Morphological properties of galaxies in ZwCl0024+1652 cluster at $z \sim 0.4$	63
4.2.1	Morphological classification	63
4.2.1.1	Methodology	63
4.2.1.2	Training sample of local galaxies	64
4.2.1.3	The measured morphological parameters	64
4.2.1.4	galSVM applied to ZwCl0024+1652	67
4.2.1.5	Final classification	69
4.2.2	Morphological analysis	70
4.2.2.1	Comparisons with visual morphological classification	70
4.2.2.2	Morphological parameters	73
4.2.2.3	Morphological diagnostic diagrams	73
4.2.2.4	Colour-colour and colour-magnitude relations	75
4.2.2.5	Morphology vs. clustercentric distance	76
4.2.3	Results and discussion	80
4.2.3.1	Morphological classes	80
4.2.3.2	Morphology vs. ELGs	81
4.2.3.3	Morphological fractions	82
4.2.3.4	Morphology-density relation	83
4.2.3.5	Relevance of morphological parameters	84
4.2.3.6	Morphological parameters vs. clustercentric distance	85
4.3	Morphological properties of galaxies in the RXJ1257+4738 cluster at $z \sim 0.866$	87
4.3.1	The morphological classes	87
4.3.2	Morphological fractions and density relations	87
4.4	Morphological properties of galaxies in the Virgo cluster at $z \sim 0.0038$	91
4.4.1	The morphological classes	91
4.4.2	Morphological fractions	92
4.4.3	Morphology vs. density relation	97
4.5	Discussion: comparison among the three clusters	97
4.6	Conclusions	100
<b>5</b>	<b>The star formation and AGN properties of galaxy clusters</b>	<b>104</b>
5.1	Introduction	104
5.2	ZwCl0024+1652 galaxy cluster ( $z \sim 0.4$ )	106
5.2.1	The [OIII] and $H\beta$ line emitters	106
5.2.1.1	Identifying the emission line candidates through $H\alpha$ priors	106
5.2.1.2	Computation of the [OIII] line fluxes	107
5.2.1.3	Derivation of $H\beta$ fluxes and the extinction correction from Balmer decrement	108
5.2.1.4	Analysis of individual objects and selection of the final sample of [OIII] and $H\beta$ emitters	111
5.2.2	Analysis and results	115

5.2.2.1	Redshift measurements . . . . .	115
5.2.2.2	Flux and luminosity distributions in [OIII] and H $\beta$ . . . . .	116
5.2.2.3	Morphologies of the [OIII] and H $\beta$ emitters . . . . .	118
5.2.2.4	AGN versus SF classes: BPT diagrams . . . . .	119
5.2.2.5	Extinction-corrected star formation rate . . . . .	122
5.2.3	Discussions with ZwCl0024+1652 results . . . . .	125
5.2.3.1	Morphological and spectral classes of the cluster members with [OIII] and H $\beta$ emission . . . . .	125
5.2.3.2	Colour and stellar masses . . . . .	127
5.2.3.3	The phase-space relation and the local density effects . . . . .	132
5.2.3.4	Cluster-field comparison at $z \sim 0.4$ . . . . .	138
5.3	RXJ1257+4738 cluster at $z \sim 0.866$ . . . . .	141
5.4	Virgo local cluster at $z \sim 0.0038$ . . . . .	144
5.5	Comparisons across the three clusters . . . . .	148
5.6	Conclusions . . . . .	151
<b>6</b>	<b>Metallicity study of galaxies in galaxy clusters</b>	<b>155</b>
6.1	Introduction . . . . .	155
6.2	Metallicity computation . . . . .	158
6.3	Gas metallicity of ZwCl0024+1652 cluster galaxies . . . . .	160
6.4	Gas metallicity of galaxies in the Virgo cluster . . . . .	164
6.5	Discussion . . . . .	169
6.6	Conclusions . . . . .	175
<b>7</b>	<b>Summary and conclusions</b>	<b>177</b>
7.1	General summary . . . . .	177
7.2	Conclusions . . . . .	181
7.3	Future work . . . . .	182
	<b>Bibliography</b>	<b>184</b>
<b>A</b>	<b>Morphological catalogue of galaxies in ZwCl0024+1652 galaxy cluster</b>	<b>205</b>
<b>B</b>	<b>Catalogue of [OIII] and H<math>\beta</math> emitters in ZwCl0024+1652 galaxy cluster</b>	<b>211</b>

# List of Figures

1.1	Summary of the cluster regions with the major physical mechanisms operating	4
1.2	Ground-based image of the galaxy cluster ZwCl0024+1652	16
1.3	The Virgo cluster of galaxies as imaged with the Palomar Observatory	19
1.4	Spectra of the night sky showing the OH emission-lines and windows relatively free of atmospheric OH emissions	20
2.1	3D image of OSIRIS with the main parts, taken from OSIRIS User's manual 3.1.	31
2.2	Fabry-Pérot interferometer scheme, formed of two glass parallel plates with a gap $L$ between them	32
2.3	Difference between Fabry-Pérot interferometer and TF	33
2.4	TF transmission profiles for different plate spacing values	34
2.5	Spectral response of a TF with respect to a Gaussian	34
2.6	The description of the observing techniques with TF	36
2.7	The ACS/WFC image of ZwCl0024+1652 galaxy cluster	39
2.8	Redshift distribution of ZwCl0024+1652 member galaxies from HST/ACS data	40
3.1	Sample $H\beta$ image of ZwCl0024+1652 cluster before, and after sky ring subtraction	49
3.2	The deep image from the OIII observations of ZwCl0024+1652	51
3.3	The deep image from the $H\beta$ observations of ZwCl0024+1652	51
3.4	Sample RXJ1257+4837 image of the result obtained for removing the sky rings with TFRed	54
4.1	Magnitude and redshift distributions of local sample; morphology	64
4.2	Magnitude and redshift distributions of real sample	68
4.3	Final error-corrected probability distributions of morphologically classified galaxies in different magnitude ranges	71
4.4	Final error-corrected probability distributions of morphologically classified galaxies	72
4.5	The I band magnitude comparison between our sample and Moran et al. (2007) visually classified sample	72
4.6	Distribution of morphological parameters for morphologically classified galaxies	74

4.7	Standard morphological diagnostic diagrams showing parameter relations . . . . .	76
4.8	Rest-frame C–C and C–M diagrams . . . . .	77
4.9	ET and LT distributions across the clustercentric distance . . . . .	78
4.10	Surface brightness vs. clustercentric distance and magnitude vs. clustercentric distance . . . . .	79
4.11	Morphological fractions with amplitude and clustercentric distance . . . . .	80
4.12	Diagrams of morphological parameters vs. clustercentric distance; ZwCl0024+1652 . . . . .	86
4.13	Distribution of r-band magnitude of galaxies: RXJ1257+4738 . . . . .	88
4.14	Diagram of morphological fractions with magnitude: RXJ1257+4738 . . . . .	89
4.15	Morphological fractions vs. local density and clustercentric distance: RXJ1257+4738 . . . . .	90
4.16	Distribution of the r-band magnitude against morphological types: Virgo . . . . .	93
4.17	Morphological fractions vs. r-band magnitude: Virgo . . . . .	94
4.18	Morphological fractions vs. clustercentric distance: Virgo cluster . . . . .	96
4.19	Histo of morphological classes out to 6 Mpc: Virgo cluster . . . . .	98
5.1	Distribution of $H\beta$ absorption line equivalent widths . . . . .	110
5.2	Sample HST/ACS thumbnails with $H\alpha$ , $H\beta$ and OIII pseudo-spectra . . . . .	112
5.3	Sample HST/ACS thumbnails with $H\alpha$ and OIII pseudo-spectra . . . . .	113
5.4	Sample HST/ACS thumbnails with $H\alpha$ and $H\beta$ pseudo-spectra . . . . .	114
5.5	Redshift distribution of OIII and $H\beta$ ELGs . . . . .	116
5.6	Linear correlation between our TF derived redshifts with $H\alpha$ redshifts . . . . .	116
5.7	The projected phase–space diagrams for $H\beta$ and OIII ELGs . . . . .	117
5.8	Comparison of the flux and luminosity of emitters of different lines . . . . .	119
5.9	Morphologies of the sources with emission lines . . . . .	120
5.10	BPT-NII diagram for cluster and field galaxies at $z \sim 0.4$ . . . . .	122
5.11	RGB mosaic of the OSIRIS/GTC deep images of ZwCl0024+1652 cluster . . . . .	123
5.12	Distribution of extinctions derived from the Balmer decrement . . . . .	124
5.13	Distribution of the logarithm of corrected and uncorrected SFR. . . . .	124
5.14	Relation between extinction corrected and uncorrected SFR for ZwCl0024+1652 . . . . .	125
5.15	The projected phase–space diagram for $H\beta$ and OIII ELGs with morphological classifications . . . . .	127
5.16	Local density versus clustercentric distance for our ELGs . . . . .	128
5.17	B–R rest-frame colour versus absolute magnitude $M_B$ relation . . . . .	129
5.18	Histogram representing the distribution of stellar masses . . . . .	130
5.19	Dependence of the SFR and sSFR on the stellar mass ( $M_*/M_\odot$ ) for cluster and field galaxies at $z \sim 0.4$ . . . . .	131
5.20	The stellar mass distribution for our $H\beta$ and/or OIII emitters . . . . .	132
5.21	The clustercentric distance distribution for the OIII and $H\beta$ emitters . . . . .	134

5.22	The SFR and sSFR versus local density ( $\Sigma_5$ ) relations for cluster and field galaxies at $z \sim 0.4$ . . . . .	134
5.23	Variation of the fraction of SF galaxies versus local density and stellar mass for cluster and field galaxies at $z \sim 0.4$ . . . . .	136
5.24	Variation of the fraction of AGN galaxies versus local density and stellar mass for cluster and field galaxies at $z \sim 0.4$ . . . . .	138
5.25	The distribution of SFR for SF galaxies in ZwCl0024+1652 cluster and field galaxies at $z \sim 0.4$ . . . . .	139
5.26	Histograms of the $\log(\text{SFR})$ , $\log(\text{sSFR})$ and $\log(M)$ for RXJ1257+4738 cluster . . . . .	142
5.27	Variation of SFR and sSFR on local density for RXJ1257+4738 cluster . . . . .	143
5.28	Variation of SFR and sSFR on stellar mass for RXJ1257+4738 cluster	143
5.29	A plot of $\log(\Sigma_5)$ vs. clustercentric distance for RXJ1257+4738 cluster . . . . .	144
5.30	BPT-NII diagram of galaxies in Virgo cluster, separating the SF, composite and AGN galaxies. . . . .	146
5.31	Histograms of the $\log(\text{SFR})$ , $\log(\text{sSFR})$ and $\log(M)$ for Virgo cluster	147
5.32	Variation of SFR and sSFR on local density for Virgo cluster . . . .	147
5.33	Variation of SFR and sSFR on stellar mass for Virgo cluster . . . .	148
5.34	A diagram describing dependence of $\log(\Sigma_5)$ on clustercentric distance for galaxies in Virgo cluster. . . . .	149
5.35	Histograms for comparison of properties (logarithmic values) of the SF galaxies in clusters at different redshifts . . . . .	150
5.36	2D plots describing the variation of different SF related properties of clusters at different redshifts . . . . .	152
6.1	Distribution of properties of ZwCl0024+1652 galaxies . . . . .	161
6.2	The histogram distribution of N2 metallicity of galaxies in ZwCl0024+1652 galaxy cluster. . . . .	163
6.3	2D plots describing the variation of Z of galaxies in ZwCl0024+1652 with other parameters . . . . .	164
6.4	Variation of Z of galaxies in ZwCl0024+1652 on Stellar mass against local density . . . . .	165
6.5	Distribution of properties of Virgo galaxies . . . . .	166
6.6	The histogram distribution of the N2-determined metallicity of galaxies in Virgo galaxy cluster. . . . .	167
6.7	Two dimensional plots showing variation of Z with other galaxy parameters in Virgo cluster . . . . .	168
6.8	Variation of Z of galaxies in Virgo on Stellar mass against local density . . . . .	169
6.9	Comparison of star-forming properties and stellar masses among cluster galaxies . . . . .	170
6.10	Comparison of metallicity among the galaxies in both clusters . . .	172
6.11	Z versus SFR scatter plots for both clusters . . . . .	174

# List of Tables

1.1	The nine GLACE sample galaxy clusters with coordinates and corresponding redshifts . . . . .	22
2.1	ZwCl0024+1652 imaging data targeting [OIII] lines. . . . .	37
2.2	ZwCl0024+1652 imaging data targeting $H\beta$ lines. . . . .	38
2.3	RXJ1257+4738 imaging data targeting the $H\beta$ lines . . . . .	42
3.1	Description of parameters used in <b>SExtractor</b> configuration . . . . .	56
3.2	<b>SExtractor</b> derived parameters for <b>tespect</b> task . . . . .	56
3.3	Spectrophotometric standard stars . . . . .	58
4.1	The final measured probability values in the three magnitude ranges	69
4.2	The final measured probability errors in the three magnitude ranges	69
4.3	Final classification of the ZwCl0024+1652 cluster members . . . . .	70
4.4	I band magnitude comparison between our sample and Moran+07 visually classified sample . . . . .	73
4.5	Statistics of the measured morphological parameters of classified galaxies of ZwCl0024+1652 . . . . .	75
4.6	Statistics of the morphological class distribution with respect to clustercentric distance and brightness . . . . .	78
4.7	Statistics of r-band magnitude of galaxies in RXJ1257+4738 cluster, $R \leq 2.5$ Mpc . . . . .	88
4.8	Statistics of r-band magnitude of galaxies in RXJ1257+4738 cluster, $R \leq 1$ Mpc . . . . .	88
4.9	Morphological distribution of galaxies of Virgo cluster from EVCC .	92
4.10	Morphological distribution of galaxies of Virgo cluster within 1 Mpc	92
4.11	Comparison of the morphological classification of galaxies in the three target clusters within 1 Mpc. . . . .	99
5.1	The number of preliminary candidates for OIII and/or $H\beta$ emission	111
5.2	The statistical distribution of fluxes of OIII and $H\beta$ emitters . . . . .	118
5.3	The statistical distribution of logarithmic luminosities . . . . .	118
5.4	Spectral classes of the ELGs with BPT-NII diagnostic diagram . . .	121
5.5	Statistical description of stellar masses of $H\alpha$ versus $H\beta$ and OIII emissions . . . . .	130
5.6	Summary of the placement of our sample SF galaxies into active or quenching phase. . . . .	131

5.7	Statistical description of the SFR of galaxies in RXJ1257+4738 . . .	141
5.8	Statistical distribution of the SFR of galaxies in Virgo . . . . .	146
5.9	Comparison of $\log(M_*)$ of SF galaxies among the three clusters . . .	149
5.10	Comparison of $\log(\text{SFR})$ of galaxies among the three clusters . . . .	149
5.11	Comparison of $\log(\text{sSFR})$ of galaxies among the three clusters . . .	149
5.12	Comparison of $\log(\Sigma_5)$ of galaxies among the three clusters . . . . .	150
6.1	Statistics of SFR of galaxies in ZwCl0024+1652 . . . . .	162
6.2	Statistics of sSFR of galaxies in ZwCl0024+1652 . . . . .	162
6.3	Statistics of $M_*$ of galaxies in ZwCl0024+1652 . . . . .	162
6.4	Statistics of $\Sigma_5$ of galaxies in ZwCl0024+1652 . . . . .	162
6.5	KS2 statistical test results among galaxies in ZwCl0024+1652 . . .	162
6.6	Statistical description of metallicity of galaxies in ZwCl0024+1652 .	163
6.7	Statistics of SFR of galaxies in Virgo . . . . .	166
6.8	Statistics of sSFR of galaxies in Virgo . . . . .	166
6.9	Statistics of $M_*$ of galaxies in Virgo . . . . .	167
6.10	Statistics of $\Sigma_5$ of galaxies in Virgo . . . . .	167
6.11	KS2 statistical test results among galaxies in Virgo . . . . .	167
6.12	Statistical description of metallicity of galaxies in Virgo . . . . .	167
6.13	Comparison of $\log(M_*)$ of galaxies among both clusters . . . . .	170
6.14	Comparison of $\log(\text{SFR})$ of galaxies among both clusters . . . . .	171
6.15	Comparison of $\log(\text{sSFR})$ of galaxies among both clusters . . . . .	171
6.16	Comparison of $Z$ ( $\equiv 12 + \log(\text{O}/\text{H})$ ) of galaxies among both clusters	171
A.1	A complete morphological catalogue of ZwCl0024+1652 cluster (Beyoro-Amado et al., 2019). . . . .	205
B.1	The [OIII] and $\text{H}\beta$ catalogue of ZwCl0024+1652 cluster (Beyoro-Amado et al., 2021). . . . .	211



# List of abbreviations

<b>Acronym:</b>	What it stands for:
<b>ACS:</b>	Advanced Camera for Surveys
<b>ADU:</b>	Analog to Digital Unit
<b>AGN:</b>	Active Galactic Nucleus
<b>ASYM:</b>	Asymmetry index
<b>bET:</b>	Blue early-type galaxy
<b>BH:</b>	Black hole
<b>BLAGN:</b>	Broad-Line AGN
<b>BPT:</b>	Baldwin-Phillips-Terlevich diagram
<b>BO effect:</b>	Butcher-Oemler effect
<b>CABR:</b>	Abraham concentration index
<b>CCD:</b>	Charge-Coupled Device
<b>CCON:</b>	Bershad-Concelice concentration index
<b>CFHT:</b>	Canada-France-Hawaii Telescope
<b>CLASH:</b>	Cluster Lensing and Supernova Survey with Hubble
<b>CMR:</b>	Colour-magnitude relation
<b>CSP:</b>	Composite Stellar Population
<b>ELG:</b>	Emission line galaxies
<b>ELLIP:</b>	Ellipticity
<b>ESA:</b>	European Space Agency
<b>ESAC:</b>	European Space Astronomy Centre
<b>ESO:</b>	European Southern Observatory
<b>ET:</b>	Early-type galaxy
<b>EVCC:</b>	Extended Virgo Cluster Catalogue

---

<b>EW:</b>	Equivalent width
<b>FIR:</b>	Far infra-red
<b>FMR:</b>	Fundamental metallicity relation
<b>FWHM:</b>	Full width half maximum
<b>GAIA:</b>	Global Astrometric Interferometer for Astrophysics
<b>galSVM:</b>	galaxy Support Vector Machine
<b>GAMA:</b>	GAlexy and Mass Assembly
<b>GINI:</b>	GINI coefficient
<b>GLACE:</b>	GaLAXy Cluster Evolution
<b>GTC:</b>	Gran Telescopio CANARIAS
<b>HeViCS:</b>	Herschel Virgo Cluster Survey
<b>HRS:</b>	Herschel Reference Survey
<b>HST:</b>	Hubble Space Telescope
<b>IR:</b>	Infra-red
<b>ICM:</b>	Inter-cluster medium
<b>IMF:</b>	Initial mass function
<b>IRAF:</b>	Image Reduction and Analysis Facility
<b>LINER:</b>	Low-Ionization Nuclear Emission-line Region
<b>LIRG:</b>	Luminous Infra-red galaxies
<b>LT:</b>	Late-type galaxy
<b>M20:</b>	Moment of Light at 20%
<b>MIR:</b>	Mid infra-red
<b>MS:</b>	Main sequence
<b>MUMEAN:</b>	Surface brightness
<b>MZR:</b>	Mass-metallicity relation
<b>NASA:</b>	National Aeronautics and Space Administration
<b>NIR:</b>	Near infra-red
<b>NLAGN:</b>	Narrow-line AGN
<b>OB:</b>	Observation block
<b>OSIRIS:</b>	Optical System for Imaging and low-intermediate-Resolution Integrated Spectroscopy

---

<b>OTELO:</b>	OSIRIS Tunable filter Emission - Line Object
<b>ROSAT:</b>	Röntgen Satellite
<b>SDSS:</b>	Sloan Digital Sky Survey
<b>SED:</b>	Spectral Energy Distribution
<b>SF:</b>	Star formation
<b>SFR:</b>	Star Formation Rate
<b>SMBH:</b>	Super Massive Black Hole
<b>SMOOTH:</b>	Smoothness or Clumpiness
<b>sSFR:</b>	specific Star Formation Rate
<b>SSP:</b>	Single Stellar Population
<b>STScI:</b>	Space Telescope Science Institute
<b>SVM:</b>	Support Vector Machine
<b>TF:</b>	Tunable filter
<b>TFRed:</b>	Tunable Filter data Reduction
<b>TOPCAT:</b>	Tool for OPERations on Catalogues And Tables
<b>UD:</b>	Undecided morphology
<b>VCC:</b>	Virgo Cluster Catalogue
<b>VIMOS:</b>	Visible Multi-Object Spectrograph
<b>VLT:</b>	Very large telescope
<b>VVDS:</b>	VIMOS-VLT Deep Survey
<b>WFC:</b>	Wide Field Camera
<b>WFP2:</b>	Wide Field and Planetary camera 2

# Astronomical constants

Constant Name Symbol = Constant Value (with units)

Astronomical unit AU =  $1.496 \times 10^{11}$  m

Light year ly =  $9.463 \times 10^{15}$  m

Parsec Pc =  $3.086 \times 10^{16}$  m

Solar luminosity  $L_{\odot}$  =  $3.85 \times 10^{26}$  Js<sup>-1</sup>

Solar mass  $M_{\odot}$  =  $1.989 \times 10^{30}$  kg

Solar radius  $R_{\odot}$  =  $6.96 \times 10^8$  m

Gravitational constant  $G$  =  $6.674 \times 10^{-11}$  Nm<sup>2</sup>kg<sup>-2</sup>

year yr =  $3.156 \times 10^7$  s

Speed of light  $c$  =  $2.9979 \times 10^8$  ms<sup>-1</sup>

# Chapter 1

## General introduction

### 1.1 Galaxy clusters: general overview

Galaxy clusters are some of the large known gravitationally bound structures in the Universe with masses ranging from about  $10^{14} - 10^{15} M_{\odot}$  consisting of hundreds to thousands of galaxies (e.g., [Press and Schechter, 1974](#); [Trenti et al., 2012](#); [Falco et al., 2014](#); [Brodwin et al., 2015](#)). Until the discovery of superclusters in 1980s, people were believing that clusters were the largest structures known in the Universe. Galaxy clusters differ from star clusters (open or globular) in such a way that open star clusters are star structures within galaxies and, the globular clusters reside in the halo as well as in the bulge and orbit around galaxies. If small number of galaxies (up to 50) exist in aggregate it is said to be group. Aggregation of a number of galaxy groups form clusters. One can take Virgo cluster and Coma cluster as examples of galaxy clusters in a relatively local Universe. A further clustering of galaxy clusters form larger structures called superclusters. Recently with observations of radio emissions like radio halos, massive galaxy clusters in the early Universe are found to be appropriate areas for the studies of particle acceleration (e.g., [Stuardi et al., 2019](#); [Bonafede et al., 2020](#)). Galaxy clusters are some of the fundamental structures in studying the Universe and therefore an area of active research in astronomy and cosmology (e.g., [High et al., 2010](#); [Brodwin et al., 2010](#); [Falco et al., 2014](#); [Bîrzan et al., 2019](#); [Zhang et al., 2020](#)). Galaxy clusters contain 100s to 1000s of galaxies, X-ray emitting hot intergalactic gas and a plenty of dark matter. They span across 2 to 10 Mpc diameter with velocity dispersion of the member galaxies of about 100 to 1400 km/s ([Lang, 2013](#)).

The beginning of studying the aggregation of galaxies in sky dates back to late 1770s to early 1780s, when Pierre Méchain and Charles Messier discovered and described the Virgo cluster. Virgo Cluster is the closest galaxy cluster to the Milky Way, with about 2000 known member galaxies, and spanning an area on the sky of about  $5 \times 3 \text{ deg}^2$ . The systematic surveys of large structures by Zwicky and Abell, about 200 years later, could be taken as a good starting point for organized research in galaxy clusters (Abell, 1958; Zwicky et al., 1961, 1963, 1966). Investigating the way galaxies form and evolve in both field and clusters gives a very important information for the concern of modern cosmology. Moreover, to understand how galaxies transform inside the clusters presents one of the main steps in disentangling the picture of galaxy formation and evolution, and the formation and evolution of the Universe at large.

Some of previous works observed differences between the properties of galaxies in the field and those in clusters (e.g., Dressler et al., 1985; Balogh et al., 1997; Koopmann and Kenney, 1998; Cucciati et al., 2010; Chung et al., 2011; Hwang et al., 2012; Delaye et al., 2014; Cantale et al., 2016; Allen et al., 2016; Maier et al., 2016; Saracco et al., 2017; Matharu et al., 2020; Old et al., 2020; Pérez-Martínez et al., 2020; Tiley et al., 2020), although the difference seems to be more significant for star-forming than for quiescent galaxies (e.g., Allen et al., 2016; Saracco et al., 2017; Old et al., 2020; Tiley et al., 2020). Specifically, the star formation activity seems to be anti-correlated with the local density (Haines et al., 2013; Kovač et al., 2014). Considering the effect of global environment, it is observed that the fraction of blue galaxies is higher in field than in clusters up to redshift of  $\sim 1.2$  (Muzzin et al., 2012). Concerning the variations with local density, the fractions of SF and blue galaxies seem to decline as the local density increases, in low- to intermediate-redshift clusters (e.g., Kodama et al., 2004; Baldry et al., 2006; Cooper et al., 2008; Cucciati et al., 2017). On the other hand, there are studies showing correlation of the rate of quenching and the fraction of quiescent galaxies in relation to the stellar mass and local environment (e.g., Baldry et al., 2006; Vulcani et al., 2010; Kovač et al., 2014; Darvish et al., 2017; Nantais et al., 2017). Moreover, a well established relation called morphology–density relation is in place (Dressler, 1980), showing that the fraction of early-type (ET) galaxies increases with local density while the fraction of late-type (LT) galaxies decreases.

Studying morphological evolution of galaxies in clusters then became important,

and it was confirmed that red passively evolving elliptical galaxies reside dominantly at cluster cores (e.g., Balogh et al., 1999; Pimbblet et al., 2001; Dressler et al., 1997), while according to Butcher and Oemler 1984 (the so called Butcher-Oemler effect), blue galaxies increase in fraction with clustercentric distance. Moreover, they are found to be characterized by less virialization as a result of larger velocity dispersions they have than their red companions associated with shorter permanence within the cluster potential (Biviano and Katgert, 2004). Another point that can be highlighted is that the increase in the fraction of spirals at  $z \sim 1$ , the star formation (SF) activity and the fraction of luminous infra-red galaxies (LIRG) was also recorded (Metcalf et al., 2005). On the other hand, the fraction of blue galaxies was also observed to increase with redshift. Different authors found that the obscured SF has increased and the number of active galactic nuclei (AGNs) were detected in infra-red at a relatively large distances (e.g., Coia et al., 2005; Martini et al., 2009; Altieri et al., 2010; Martini et al., 2013). Haines et al. (2013) used a model for fraction of star-forming galaxies expressed by the equation  $f_{SF} \propto (1+z)^n$  where  $n = 7.6 \pm 1.1$ . With this, an accelerated increase in LIRGs is observed with star formation rate (SFR)  $< 3M_{\odot}/year$  in virialized zone. Haines et al. (2013) also pointed out a decrease in the mean specific SFR (sSFR) by factor of 3 and a number density decrease by 1.5 times. The steady cosmic decline in sSFR of field galaxies accreted into the clusters contributes for the two thirds of this decrease, whereas the action of the cluster on the infalling objects shares the remaining one third contribution for the usual decrement (Haines et al., 2009, 2013, 2015).

## 1.2 Physical mechanisms within galaxy clusters

Regarding galaxy transformation in clusters, many aspects such as its nature, corresponding timescales, and the responsible physical processes are still some of the open questions. Understanding the role of environmental factors in the evolution of galaxies in clusters is crucial in the context of a hierarchical cosmological scenario. As described in Treu et al. (2003), the possible mechanisms usually proposed for explaining the effect of environment on galaxy evolution are broadly categorized in the following three groups, summarized also in Figure 1.1:

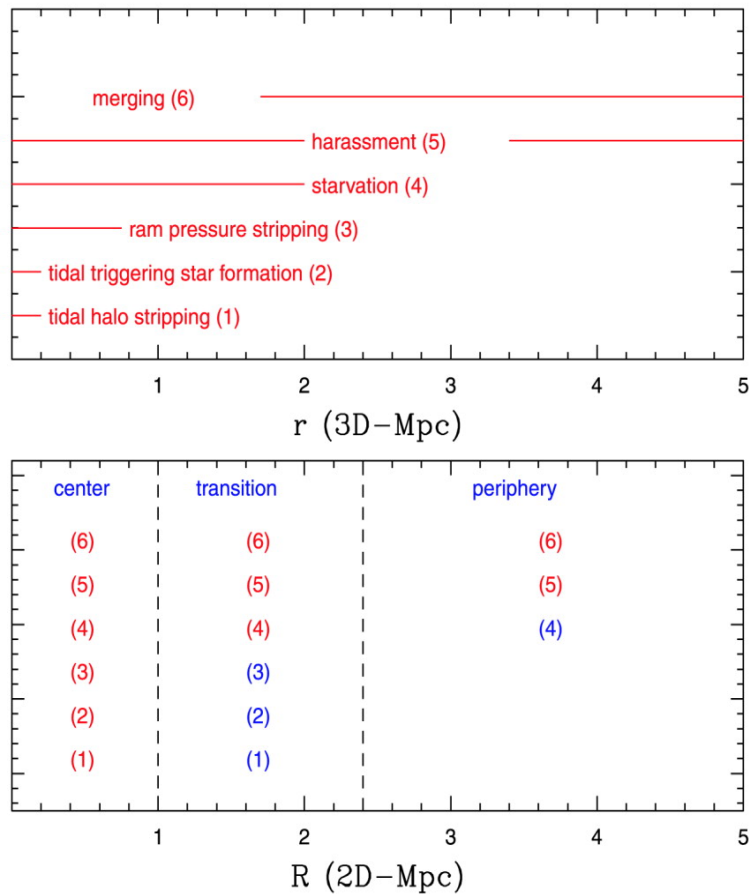


**Figure 1.1:** Summary of the cluster regions where the major physical mechanisms are likely to operate. Top: Horizontal lines indicate the radial region where the mechanisms are most effective. Bottom: For each projected annulus, we can identify the mechanisms that could have affected the galaxy in the region (red). The blue numbers indicate processes that are marginally functioning. The virial radius taken for reference is  $r_{vir} \sim 1.7$  Mpc. Credit: [Treu et al. \(2003\)](#)

1. **Galaxy-galaxy interaction within cluster.** The effect of galaxy-galaxy interaction varies with the impact parameter and the relative velocities of the galaxies. For low relative velocities, this interaction results with accretion for different masses, but with merger for similar masses case. Moreover, the effects of galaxy-galaxy interaction for low relative velocities could be responsible for increased SF, AGN activity, and disturbed morphologies, while for higher relative velocities interactions may result in harassment and removal of dust and gas (e.g., [Moore et al., 1996](#); [Jáchym et al., 2007](#); [Park and Hwang, 2009](#)).
2. **Galaxy-ICM interaction.** This interaction results with the possible depletion of the gas contents of the galaxy through different processes. One



of the processes would be thermal evaporation of the interstellar medium by the hot intra-cluster plasma and with viscous stripping (e.g., [Nipoti, 2009](#)). The other process would be the ram pressure stripping of the gas and dust reservoirs of the galaxies by the ICM (e.g., [Lee et al., 2016](#)). The SF would be stopped by the removal of the matter supply as a result of these two stripping mechanisms. Moreover, the ICM also compresses the intergalactic medium, and triggers SF (e.g., [Bekki and Couch, 2003](#); [Gregg and West, 2017](#); [Okabe et al., 2019](#)).

3. **Galaxy-cluster gravitational interaction.** This mechanism manipulates the morphological transformation of the galaxies by truncating the outer regions like halos and arms. Hence, the SF will be quenched by removal of gas as a result of the truncation. The SF can also increase because of the intergalactic medium compressed by the potential well (e.g., [Park and Hwang, 2009](#)).

### 1.3 The SF and AGN in galaxy clusters

Generally discussing, the SF can be completely quenched or slowly decreased (the so called starvation) based on the proportion of gas removed in the described physical processes (e.g., [Haines et al., 2013](#)). Both the SF and the starburst activity within the galaxies may occur as a result of the amount of gas compressed by the physical mechanisms stated in Section 1.2 (e.g., [Vollmer et al., 2012](#); [Vulcani et al., 2018](#)). The interactions are summarized in Figure 1.1. Accordingly, the galaxy-galaxy interactions dominate the outskirts of clusters, where the potential well and the effect of the ICM remain weak. Even though, they are less familiar in specific objects undergoing successive encounters, these interactions extend across the full cluster structure ([Mihos, 2003](#)). The ICM effects, namely the ram pressure gas stripping and pressure enhanced SF, significantly dominate the intermediate region. On the other hand, the gravitational well effects namely tidal halo stripping and triggering of the SF dominate in the most inner regions (e.g., [Treu et al., 2003](#); [Rowlands et al., 2018](#); [Owers et al., 2019](#)).

It is determined that there are disparities between the populations of local clusters as compared to clusters at intermediate redshifts ( $z \sim 0.5$ ) in such a way that larger fractions of typically luminous SF spiral galaxies exist at higher distances.

As pointed out by previous studies, this indicates that during the transformation a significant addition of new stars have been made (e.g., Poggianti et al., 1999; Kodama and Smail, 2001; George et al., 2013; Nishizawa et al., 2018). However, such activities are not detected in surveys that use  $H\alpha$  as SF indicator (Sánchez-Portal et al., 2015), but the missing SFRs could be compensated by the heavily obscured infra-red (IR) derived SF. It is still an open question that the observed SFR could be because of the large scale structure or the effect of dense environment (e.g., Popesso et al., 2007).

Different results have been reported regarding AGN activity in clusters. However, the way how the AGN fraction varies with environment, and the role of AGN in galaxy transformations and evolution in galaxy clusters is still not clear. Some studies suggest that AGN activity increases with redshift as revealed using X-ray data (e.g., Martini et al., 2002; Eastman et al., 2007; Sivakoff et al., 2008; Martini et al., 2013). There are studies that suggest that AGN fraction does not depend on the local density at all (e.g., Miller et al., 2003; von der Linden et al., 2010; Pimbblet et al., 2013; Pintos-Castro et al., 2016; Marziani et al., 2017), whereas others argue that high density regions and luminous AGNs look disjoint (e.g., Kauffmann et al., 2004; Alonso et al., 2007; Argudo-Fernández et al., 2018; Bornancini and García Lambas, 2020).

It is also clear that any process that disturbs the contents and distribution of cold gas affects the population of AGN in the cluster because AGNs are mainly fuelled by cold gases (e.g., Alberts et al., 2016; Mishra and Dai, 2020). In the other hand, there are results showing an effect of increasing density making the AGN fraction to decline (e.g., Kauffmann et al., 2004). Moreover, a weak galaxy-galaxy interaction, has been confirmed from the findings that large amounts of AGN reside in cluster outskirts (e.g., Ruderman and Ebeling, 2005; Caglar and Hudaverdi, 2017; Koulouridis and Bartalucci, 2019)). There are also studies (e.g., Miller et al., 2003; Porqueres et al., 2018), showing that AGN counts are not affected by environmental factors. Moreover, Pimbblet et al. (2013) have shown a fast vanishing of the merging signs and an increase of AGN population as clustercentric distance increases within the virial radius.

Generally speaking, especially based on the results of optical data from central parts ( $r_c \leq 0.5$  Mpc) of the local clusters, observations confirm that galaxy clusters are dominated by red passive ellipticals (e.g., Cooper et al., 2012; Woo et al.,

2013). However, we need further inclusive studies considering the wider wavelength ranges as well as wider areas or clustercentric distances. Hence, to contribute significantly to the area of galaxy evolution through the transformation from typical field characteristics to the cluster behaviour, it needs comprehensive study of populations encompassing a larger redshift ranges as well as wider clustercentric distances.

## 1.4 Analysed parameters for evolution of galaxy populations in galaxy clusters

### 1.4.1 Morphological properties

A consolidated observational fact is the outstanding difference in the properties of galaxies located in the cores (or regions of high local galaxy density) and in the external parts (or low density ones) of low- and intermediate- redshift clusters. The former regions are dominated by red, massive and passive ET galaxies, comprising of elliptical and S0, while a substantial increase of the fraction of LT galaxies, consisting of spiral and irregular objects, is observed in the latter. This was early identified by Zwicky (1942), and quantified by Dressler (1980) in the so-called morphology-density relation linking the increasing fraction of ET galaxies with local galaxy density. Similarly, a decrease of the fraction of star forming (SF) galaxies is observed with increasing local galaxy density (the SF-density relation, see for instance Pintos-Castro et al., 2013, and references therein). The morphology-density relation is defined to be a correlation between different Hubble types, and the local density of galaxies or simply defined as the projected number of galaxies within the area enclosed by the number of the nearest neighbours, usually 5 - 10 nearest sources. The relation was observed to be valid in the environments of galaxy groups and galaxy clusters up to  $z \sim 1$  (e.g., Postman et al., 2005; Houghton, 2015). Moreover, these relations evolve with cosmic time, as was realized by Butcher and Oemler (1978), who found that cluster galaxy populations evolve as redshift changes in such a way that rich clusters at higher redshift ( $z > 0.2$ ) are populated with a higher fraction of blue galaxies than low redshift clusters. This is the so-called Butcher-Oemler (BO) effect. Likewise, an increase of the cluster

SF and active galactic nuclei (AGN) activity is observed (see for instance, [Haines et al., 2009](#); [Martini et al., 2013](#)).

The morphology-density relation seems to hold from nearby clusters up to redshifts as high as  $z \sim 1.5$  (e.g., [Dressler et al., 1997](#); [Postman et al., 2005](#); [Holden et al., 2007](#); [Mei et al., 2012](#); [Nantais et al., 2013](#)). Likewise, star formation takes place in low density regions where LTs dominate, while high density regions are dominated by quiescent ET galaxies since  $z \sim 1.5$  to the local Universe (e.g., [Postman and Geller, 1984](#); [Kauffmann et al., 2004](#); [Cooper et al., 2012](#); [Wetzell et al., 2012](#); [Woo et al., 2013](#)). At higher redshift, there is some controversial evidence of the existence of a reversal of the SF-density relation: some authors, as [Tran et al. \(2010\)](#) find an (even dramatic) increase of the fraction of SF galaxies from low- to high-density regions in clusters at  $z \sim 1.6$ , while other authors (e.g., [Ziparo et al., 2014](#)) do not find a clear evidence of such type of reversal when studying clusters at the same redshift. [Quadri et al. \(2012\)](#), using mass-selected samples from the UKIDSS Ultra-Deep Survey, conclude that galaxies with quenched SF tend to reside in dense environments out to at least  $z \sim 1.8$ .

Between the redshift range of  $z=0.2$  to  $z=0.5$ , a significant increase of spiral galaxies has been found even though the number of ellipticals remain constant while the number of the lenticular (S0) galaxies decreases ([Dressler et al., 1997](#); [Houghton, 2015](#)). This is also related with the evolution of the morphology-density relation. However, at higher redshifts, e.g.,  $z \sim 1$ , the existence of the morphology-density relation was verified by [Postman et al. \(2005\)](#), with a slow increase in the E + S0 (ET) fraction with density. It is known that up to a redshift of  $z \sim 1.3$ , there is no evolution of the elliptical galaxies' fraction as a function of the density of local galaxy (e.g., [Saracco et al., 2017](#)). Hence, as seen at intermediate redshifts, the variation in the morphology-density relation at higher redshifts, e.g.,  $z \sim 1$ , is mainly due to the deficiency of S0 galaxies, and surplus of spirals and irregular galaxy populations as compared to the local galaxies. Based on this, we can say that there is no evolution of the ET fraction with density, but as redshift increases, the ET fraction changes as a consequence of galaxy transformation from LTs to ETs because of the environmental influence (e.g., [Holden et al., 2007](#); [Vulcani et al., 2015](#)). Here the S0 are taken to be in the intermediate stage in terms of morphology. Moreover, the existence of a large number of S0 galaxies in rich clusters at  $z \sim 1$  assumes that a significant amount of S0 could have formed at high redshifts namely  $z > 1.3$  (e.g., [Vulcani et al., 2015](#)). According to [Park et al.](#)

(2008), as a result of a high rate of galaxy-galaxy interactions, transforming the LT galaxies into ETs through cosmic time, the evolution of the fraction of ET galaxies in high density environments is much faster (e.g., [Perez et al., 2009](#); [Alonso et al., 2012](#)).

The morphological taxonomy of galaxies can be backdated to [Reynolds \(1920\)](#). Visual inspection is the traditional method, and even now a very common way to perform morphological classification of galaxies (e.g., [Lintott et al., 2008](#); [Nair and Abraham, 2010](#); [Fasano et al., 2012](#); [Kocevski et al., 2012](#); [Kartaltepe et al., 2012, 2015](#); [Buitrago et al., 2013](#); [Kuminski and Shamir, 2016](#); [Willett et al., 2013](#); [Simmons et al., 2017](#); [Willett et al., 2017](#); [Mahoro et al., 2019](#)). One of the drawbacks of the visual classification method is the subjectivity, that can be alleviated by performing multiple instances of the classification of each object carried out by different persons, where an outstanding example is Galaxy Zoo project ([Lintott et al., 2008, 2011](#)). In the framework of this “citizen science” initiative, nearly one million of galaxies from the Sloan Digital Sky Survey (SDSS) were classified by  $\sim 10^5$  participants who performed more than  $4 \times 10^7$  classifications. Needless to say, when dealing with large number of sources, the visual classification method can be really time-consuming. It works well for closer and well resolved objects for accurate estimation. For such objects it agrees with the results of modern classification methods (for more details see Chapter 4).

### 1.4.2 Star formation rates (SFR)

Optical photometric studies can be taken as pioneers in detecting a very large number of blue galaxies in high-redshift clusters, described as the BO effect ([Butcher and Oemler, 1984](#)), giving the first evidence of the larger number of star-forming galaxies in high-redshift clusters as compared to local ones. Studies with optical and near infra-red (NIR) data indicate that luminosity function in cluster galaxies is in line with a model of short energetic star bursts at high redshifts ( $z \gtrsim 2$ ), followed by passive evolution (e.g., [Stanford et al., 1998](#); [Eisenhardt et al., 2008](#)). Looking for optical emission-lines such as  $H\alpha$ , is a direct way for identifying galaxies with ongoing SF activity.  $H\alpha$  is one of the most known and cleanest (except when there is AGN) signatures of SF and is within the coverage of optical spectroscopy near the intermediate redshift clusters (e.g., [Kodama et al., 2004](#); [Koyama et al., 2010](#); [Sánchez-Portal et al., 2015](#); [Beyoro-Amado et al., 2021](#)). However,  $H\alpha$

is located in the NIR when dealing with high-redshift sources, making impossible its detection in optical. Therefore, at higher redshifts, [OII] is often used for detecting the SF (e.g., [Pintos-Castro et al., 2016](#)). It has been verified by many studies that the fraction of emission-line galaxies (ELGs) is higher in distant clusters as compared to that in nearby clusters (e.g., [Couch et al., 2001](#); [Kodama et al., 2004](#); [Finn et al., 2005](#); [Guo et al., 2019](#)). Comparing the cluster and field galaxies, the fraction of ELGs in clusters is lower than in fields at similar redshifts ([Cucciati et al., 2017](#); [Beyoro-Amado et al., 2021](#)).

SFR can also be determined from UV and FIR measurements (e.g., [Hirashita et al., 2003](#); [Elbaz et al., 2018](#); [Mahajan et al., 2019](#); [Martis et al., 2019](#)). We use a UV continuum luminosity to trace SFRs of galaxies in high redshifts (e.g.,  $z \sim 1-2$ ), where all the strong emission lines are located out of the optical range (e.g., [Madau et al., 1998](#); [Kennicutt, 1998](#)). FIR luminosity can be taken as a good indicator for a total UV/optical emissivity of a galaxy (e.g., [Mas-Hesse and Kunth, 1991](#)). Thermal emission in FIR possibly results after the absorption of the UV/optical flux fraction by dust. Then SFR is computed from FIR luminosity and the UV/optical flux fraction ([Kennicutt, 1998](#)).

### 1.4.3 AGN fractions in clusters

Star formation activity in galaxies evolves together with the super-massive black hole (SMBH) indicating co-evolution between the two events, SF and AGN activity (e.g., [McAlpine et al., 2015](#); [Florez et al., 2020](#)). As discussed earlier, cold gas is the primary fuel source of the central black hole. The way the AGNs are distributed in clusters in comparison to fields gives more constraints on the processes of fuelling. As pointed out by many studies, the luminous X-ray AGN fraction in clusters is reasonably lower than their fraction in fields at the same redshift (e.g., [Kauffmann et al., 2004](#); [Haggard et al., 2010](#); [Ehlert et al., 2014](#); [Mo et al., 2018](#)). While probing lower luminosity AGNs, several studies have reported similar AGN fractions in galaxy clusters and field for redshifts up to  $z \sim 1.05$  (e.g., [Pimblet et al., 2013](#); [Koulouridis et al., 2014](#)). However, for local Universe, larger AGN fraction has been observed in fields than in the groups/clusters (e.g., [Martini et al., 2013](#); [Li et al., 2017](#)). According to studies on proto-clusters at higher redshifts (e.g., [Lehmer et al., 2009](#); [Digby-North et al., 2010](#); [Umehata et al., 2015](#); [Krishnan et al., 2017](#)), denser environments are favourable for AGN activity. Moreover,

AGN fraction in clusters evolves with redshift as  $f_{AGN} \sim (1+z)^{5.3}$  (Martini et al., 2009). This is almost similar to the evolution of the fraction of star-forming galaxies in clusters given by  $f_{SF} \sim (1+z)^{5.7}$  (Haines et al., 2009).

#### 1.4.4 Metallicity distributions

Metallicity is defined in astronomy as the abundance of chemical elements heavier than both hydrogen and helium in a given astronomical object like star, galaxy, etc. Metals are defined in astronomy not in the same or similar way as in chemistry. A term “metal” in astronomy is used to represent all elements except hydrogen and helium for convenience, since most of the content of the Universe comprises of hydrogen and helium. That is, if a given astronomical object is characterized by a relatively higher abundances of elements like carbon, nitrogen, oxygen, and iron as compared to hydrogen and helium proportion, then the object can be called metal-rich. We can briefly define a stellar composition of a given astronomical object as in Equation 1.1 with parameters X, Y and Z that represent mass fractions, such that X stands for hydrogen mass fraction, Y for the mass fraction of helium, and Z for the collective mass fraction of all the remaining chemical elements. Accordingly, the fractions have a mathematical relation given by:

$$X + Y + Z = 1, \quad (1.1)$$

where  $X = m_H/M$  and  $Y = m_{He}/M$ , with  $m_H$  being a fractional mass of hydrogen,  $m_{He}$  denotes the mass of helium and M stands for the total mass of the object. For the remaining chemical elements (collectively called metals) we compute the metallicity (denoted by Z) that is the fractional mass of the elements other than hydrogen and helium is given by Equation 1.2 as:

$$\sum_{i \neq H, He} \frac{m_i}{M} = 1 - X - Y. \quad (1.2)$$

As stated in Ciocan et al. (2020), among the tools to study the evolution of galaxies, chemical abundance of galaxies is an important parameter. Chemical abundance in general manifest the connection between the SF, a wind and/or supernovae driven outflow of gases, and the inflows of the galactic gas. As described by Lian et al. (2018), metallicity in galaxies is related to two components,



a gas-phase and stellar metallicity components. The gas component is a metallicity obtained by measuring emission lines in star-forming regions of the galaxy. On the other hand, the stellar metallicity component is derived using stellar continuum and absorption line analysis. It is a metallicity computed for non star-forming regions with no emission lines. Moreover, the metal content in the gas at the time of observation is revealed by gas-phase metallicity, whereas the metal content in stars during their formation is given by stellar metallicity (Leethochawalit et al., 2018). The stellar mass ( $M_*$ ) and gas-phase metallicity ( $Z$ ) are important properties of galaxies and tracers of galaxy formation and evolution (e.g., Tremonti et al., 2004; Erb et al., 2006; Ellison et al., 2009; Kacprzak et al., 2015; Saracco et al., 2019). On the one hand, the stellar mass provide information about the amount of gas locked up into stars (e.g., Tremonti et al., 2004; Lian et al., 2018; Zu, 2020). On the other side, the gas-phase metallicity traces the history of star formation and exchange of the gas between object and its environment (e.g., Yates et al., 2012; Leethochawalit et al., 2018; Ciocan et al., 2020; Nadolny et al., 2020). Hereafter, we deal with metallicity component derived using different emission lines hence wherever it appears “metallicity” or “ $Z$ ” it refers to gas-phase metallicity.

Metals are produced in general as a result of SF in galaxies. Different studies have found a strong relationship between  $Z$  and the stellar mass ( $M_*$ ) of galaxies in clusters (e.g., Tremonti et al., 2004; Maiolino et al., 2008; Ellison et al., 2009; Maier et al., 2015; Leethochawalit et al., 2018). According to previous studies, higher metallicities characterize the massive galaxies, whereas lower mass galaxies are characterized by lower metallicities. This was suggested to be related to the environment in such a way that the local processes dominate the relation by being metallicity insensitive to the environment. On the other hand, as described by Finlator and Davé (2008), the SF triggering may result in a seasonal change in metallicity of galaxy, i.e., the enrichment rate owing to SF, but the dilution rate owing to accretion of gas, before getting back to an equilibrium metallicity. The evolution of metallicity in galaxy clusters has been detected to extend out to at least  $z \sim 3$  indicating more flatness at cluster outskirts (e.g., McDonald et al., 2016; Mantz et al., 2017).

Studying the distribution of cluster galaxies’ metallicities with cluster-centric distance and local density is a powerful way to investigate evolution within clusters. As galaxies fall into clusters and travel towards the cluster centre along their radial



orbits, they interact with the intra-cluster medium (ICM) and other cluster galaxies, thus getting progressively stripped of their gas reservoir. This process is expected to influence the SFR, metal abundances and possibly generate a metallicity gradient across a cluster (e.g., [De Grandi and Molendi, 2001](#); [Molendi et al., 2016](#); [Mernier et al., 2017](#)). To further point out, luminosity function depends on environment such that the densest parts of the Universe (cores of clusters and groups) are characterized by having the most luminous galaxies ([Zandivarez and Martínez, 2011](#)). Moreover, it has been verified that a decrease in fraction of red galaxies in going radially outwards from the cluster centre is observed (e.g., [Martínez et al., 2008](#)). This implies that SFR increases with clustercentric distance. [Maier et al. \(2016\)](#) have reported that the accreted region of galaxy clusters are composed of more fraction of metal rich galaxies than those in the infalling region (outskirts). In addition, [Gupta et al. \(2016\)](#) analysing clusters in the CLASH survey at  $z = 0.35$  out to clustercentric distances of 2.5 Mpc, determined that metallicity varies inversely with clustercentric distance. By analysing properties of galaxies in A779 cluster at  $z = 0.023$ , [Sreedhar et al. \(2012\)](#) have shown that the correlation between metallicity and clustercentric distance is poor. [Sreedhar et al. \(2012\)](#) further described that the metallicity distribution for old ET galaxies looks random with radial distance, but for young LT galaxies a slight trend is observed with 6 Gyr being observed at a radial distance of  $\sim 0.1$  Mpc to  $\sim 0.7$  Gyr at  $\sim 0.4$  Mpc. It could result with a conclusion that the variation of metallicity and age follow similar trend with clustercentric distance (e.g., [Worthey, 1994](#)).

Considering redshift dependence, cluster galaxies at  $z \sim 2$  have lower metallicities compared to the local ones ([Erb et al., 2006](#)). A strong metallicity is recorded at redshift of  $z \sim 3.5$  by [Maiolino et al. \(2008\)](#), suggesting this redshift to be one where the SF activity mainly occurs. There are many studies confirming that the environmental effect on the M-Z relationships would be vital. It has been found that close paired galaxies with the same luminosity are more poor with metals by about  $\sim 0.1$  dex as compared to galaxies not in pair (e.g., [Ellison et al., 2008](#); [Cortijo-Ferrero et al., 2017](#); [Thorp et al., 2018](#); [Bustamante et al., 2020](#)). It has been suggested that cluster galaxies have higher metallicities by about  $\sim 0.04$  dex as compared to field galaxies of the same stellar mass, rest-frame g-r colours and redshift ([Ellison et al., 2009](#)). It was also indicated that metallicity enhancements are related in general with high local densities. Even though there are few studies describing the variation of metallicity of cluster galaxies to other galaxy parameters, the results are not in agreement with each other mainly due to the small

sample used (e.g., Skillman et al., 1996; Mouhcine et al., 2006). Hence, they remain insufficient to clearly put the trends, so that more studies with increased sample involving many interrelated parameters versus metallicity are needed to fully understand the picture.

### 1.4.5 Colour-magnitude diagrams

A clear bi-modality exists in distribution of galaxies when comparing their colour and absolute magnitude, the so called colour-magnitude relation (CMR) (e.g., Tully et al., 1982; Bower et al., 1992; Chilingarian and Zolotukhin, 2012; Pović et al., 2013; Schawinski et al., 2014). Accordingly, the first population is a red sequence showing a tight correlation, with a loosely bound blue cloud population (Tully et al., 1982; Bower et al., 1992). Bell et al. (2004) determined the colour bi-modality that is visible in field galaxies up to  $z \sim 1$ , while the phenomenon is observed both in field as well as cluster galaxies. Even though this is visible, the blue cloud population is scattered in cluster galaxies while the red sequence becoming narrower as going towards the denser cluster environments (e.g., Milone et al., 2017). The star-forming galaxies reside in a blue cloud, but once it completes the formation of stars it moves to the red sequence. Even though this happens, the migration depends highly on the galaxy morphology (Schawinski et al., 2014). For the ET galaxies the rapid destruction of the galaxy gas reservoir triggers the quenching of SF and the transition of a galaxy from the blue cloud to the red sequence is very fast of the order of  $\sim 1$  Gyr. However, for the LT galaxies a complete cut-off of the galaxy gas reservoir from the cosmic supply of fresh gas initiates the quenching of the SF. Because of the decreasing SF, the stellar mass remain increasing to make the galaxy slow in moving out of the blue cloud. Hence, by this time the galaxies quenched at high redshifts may have probably reached the red sequence, increasing the population of the red spiral population. In galaxy clusters, CMR is a relation put on place by the red passive-evolving galaxies in the cluster and becomes a very important relation in cluster studies, continued being used in detecting and classifying new galaxy clusters. Because it is detected not only in local cluster but even up to  $z \sim 2$ , the CMR is very helpful in studying the properties of a specific galaxy population in clusters within a vast range of redshifts (Strazzullo et al., 2013). The trend that CMR primarily manifests the influence of various stellar metallicities is supported by the absence of the strong evolution in the slope parameter since  $z = 1.5$  (Kodama and Arimoto,

1997; Lidman et al., 2008). The age variations of galaxies is majority thought to yield the scatter where the amount of scatter indicates the redshift of formation of elliptical galaxies. According to Menci et al. (2008) using simulations based only with hierarchical model, the slope of CMR evolves with redshift flattening at  $z \sim 0.7-1.0$ , while turning towards positive for higher redshifts. Therefore, mathematical models involving more physical processes are required to alleviate the knowledge in the area.

## 1.5 ZwCl0024+1652 galaxy cluster

The galaxy cluster ZwCl0024+1652 is a cluster of galaxies located in Pisces constellation at about 4 billion light years away ( $z \sim 0.395$ ). It is a rich cluster of galaxies that was first described by Humason and Sandage (1957). Oemler (1974) used this cluster as one of the four for studying the colours of galaxies in clusters. In previous works (Sánchez-Portal et al., 2015), it has been estimated using caustic profile analysis that the mass of this cluster at virial radius of  $r_{200} = 1.7 \pm 0.1 h_{70}^{-1}$  is  $M_{200} = 5.9 \pm 0.3 \times 10^{14} h_{70}^{-1} M_{\odot}$ . The values reported for the mass distribution agree fully with previous results of Kneib et al. (2003) where  $M_{200} = 5.7_{-1.0}^{+1.1} \times 10^{14} h_{70}^{-1} M_{\odot}$  out to  $r_{200} = 1.7 h_{70}^{-1}$  Mpc, derived using weak lensing analysis. On the other hand, X-ray studies (e.g., Zhang et al., 2005) result with a total cluster mass of  $M_{200} = 2.3 \pm 0.1 \times 10^{14} h_{70}^{-1} M_{\odot}$ , that is much lower than that determined with weak lensing studies. Czoske et al. (2001) explained this difference that it may be due to a possible complex structure in the projected centre of the cluster. This is further characterized by bi-modality in the radial velocity distribution that is consistent with an infalling group towards the line of sight. Even though the cluster and its member galaxies have been analysed thoroughly by different authors (e.g., Kneib et al., 2003; Treu et al., 2003; Moran et al., 2007; Geach et al., 2009; Natarajan et al., 2009; Sánchez-Portal et al., 2015; Beyoro-Amado et al., 2019), it still lacks a comprehensive study of morphology, metallicity, SF and AGN properties of its member galaxies. This galaxy cluster was included as part of the GLACE sample clusters (see sec Section 1.8) since the lines [OIII],  $H\alpha$ , and  $H\beta$  fall within atmospheric windows relatively free of sky lines at a redshift of the cluster  $z = 0.4$  and since public data are also available. The ground based image for ZwCl0024+1652 galaxy cluster is shown in Figure 1.2.



**Figure 1.2:** Ground-based image of the galaxy cluster ZwCl0024+1652 at  $z \sim 0.4$ . This is a colour image measuring  $21 \times 21$  arcminutes obtained with the CFHT12k camera at the Canada France Hawaii Telescope on Mauna Kea (Hawaii). **Credit:** European Space Agency, NASA, Jean-Paul Kneib (Observatoire Midi-Pyrénées, France/Caltech, USA) and the Canada France Hawaii Telescope

## 1.6 RXJ1257+4738 galaxy cluster

The sign of the cluster RXJ1257+4738 was first detected with X-ray observations as indicated in the Röntgen Satellite (ROSAT) data archive, and latter confirmed spectroscopically at  $z \sim 0.866$  with optical and NIR observations (Ulmer et al., 2009). This was done on the basis of an extensive observational study including Chandra, XMM-Newton, Spitzer, Gemini, Subaru and observations of the Astrophysics Research Consortium (ARC) telescope. In both, Chandra and XMM-Newton observations, the authors identified the diffuse emission of the cluster and modelled the detected emission with an ellipse centred at  $\text{RA}(J2000) = 12^h 57^m 12.2^s$  and  $\text{Dec}(J2000) = +47^d 38^m 06.5^s$ . The X-ray luminosity of RXJ1257+4738 cluster is determined to be about  $2 \times 10^{44} \text{erg s}^{-1}$  and its temperature is about 3.6 keV. The X-ray mass of  $(1 - 5) \times 10^{14} M_{\odot}$  was inferred by Ulmer et al. (2009) and they obtained an independent mass estimate

of  $6.1 \times 10^{14} M_{\odot}$  using a velocity dispersion of 600 km/s derived with the method of [Serna and Gerbal \(1996\)](#). The measured mass confirms that RXJ1257+4738 cluster is a massive one. [Ulmer et al. \(2009\)](#) also derived the virial radius of the cluster to be  $r_v = 1.05$  Mpc. Limited number of studies exist for this cluster and its member galaxies (e.g., [Ulmer et al., 2009](#); [Pintos-Castro et al., 2013](#); [Pintos-Castro, 2014](#); [Pintos-Castro et al., 2016](#)), and therefore it still lacks a comprehensive study of morphology, metallicity, SF and AGN properties of its member galaxies. This galaxy cluster was also included in GLACE sample since the lines [OII], [OIII], and  $H\beta$  fall within atmospheric windows relatively free of sky lines at a redshift of the cluster  $z = 0.866$ .

## 1.7 The Virgo cluster

As recorded after the inclusion of M91 in Messier’s catalog in 1784, Pierre Méchain and Charles Messier discovered the cluster of galaxies called Virgo cluster as an accumulation of nebulae during the late 1770s and early 1780s. In fact the Virgo cluster members were not recognized as galaxies until the 1920s when the discovery of Cepheid variables in spiral nebulae and established the distance to classical Cepheid variables in the Andromeda Galaxy ([Hubble, 1925](#)) has been reported. Cepheid variables are stars used to determine distances. The Virgo cluster, named as such since observed in the direction of the Virgo constellation, is both the largest and closest (at a distance of about  $\sim 16.5$  Mpc, or  $\sim 53.8$  Mly) galaxy cluster to the Local Group. It spans an area of the sky about  $5 \times 3$  deg<sup>2</sup> in size ([Mei et al., 2007](#)). Virgo cluster is identified with coordinates  $RA(J2000) = 12^h 26^m 32.1^s$  and  $DEC(J2000) = +12^d 43^m 24^s$  at a redshift of  $\sim 0.0038$  ([Wu et al., 1998](#); [Mahdavi and Geller, 2001](#)).

Virgo cluster has an estimated mass of  $\sim 1.2 \times 10^{15} M_{\odot}$  ([Fouqué et al., 2001](#)) and contains of order of 2,000 galaxies ([Mei et al., 2007](#)), with higher concentration of spiral galaxies than typically acceptable proportion for cluster of similar size. Because of a very large mass of the Virgo cluster, the motions of most of galaxies in its neighbourhood are highly influenced by it and attracted towards it (the ‘Virgo-centric flow’). Therefore, Virgo cluster has a significant gravitational effect that slows down the recession of the Local Group. Because of this, the galaxies in the Local Group may fall eventually into the Virgo Cluster.

According to [Binggeli et al. \(1987\)](#) Virgo cluster shows a clearly identifiable double structure, where the main concentration is cluster A and the other is cluster B. Cluster A which is mainly made up of ET galaxies is centred at M87 (supergiant elliptical galaxy), and characterized by a large velocity dispersion of  $\sim 750$  km/s. On the other side, cluster B, showing the smaller and looser concentration, is made mainly of LT galaxies and is centred around M49 (the brightest known member), and characterized by smaller velocity dispersion of  $\sim 400$  km/s. This cluster has an average diameter of  $\sim 15 \times 10^6$  ly (slightly larger than that of the Local Group), but comprises of about  $\sim 50$  times higher number of members than the Local Group. As can be verified from results of [Binggeli et al. \(1985\)](#) and [Kim et al. \(2014\)](#), most of the Virgo cluster members are dwarf galaxies, but the most prominent ones are ellipticals and spirals. At most 10% of the cluster member stars are intergalactic stars, most likely kicked out of their host galaxies as a result of galaxy-galaxy interactions. As shown by [Karachentsev and Nasonova Kashibadze \(2010\)](#), the cluster members accelerate to remarkably high velocities relative to the cluster centre because of the mass of the cluster. This could be a reason for some of the cluster members to exhibit the highest known blue-shifts while moving fast to the cluster centre from the opposite side than our location. Many studies have been recently carried out with different properties of galaxies in Virgo cluster (e.g., [Gavazzi et al., 2018a,b](#); [Graham et al., 2019](#); [Mohamad Nizam et al., 2019](#); [Su et al., 2019](#); [Grossi et al., 2020](#); [Lee et al., 2020](#); [Mayes et al., 2020](#), etc). However, to fully understand the cluster, comprehensive studies focusing on SF, AGN, morphology and metallicity properties of the member galaxies are still needed. The ground based image for the Virgo cluster of galaxies is given in [Figure 1.3](#).

## 1.8 GaLaxy Cluster Evolution (GLACE) survey

As inferred from different studies for star-forming galaxies, the narrow-band imaging and IR surveys could be powerful tools for studying galaxy evolution in clusters. For instance, [Koyama et al. \(2010\)](#) performed a MOIRCS<sup>1</sup> narrow band H $\alpha$  and Akari mid infra-red (MIR) survey of the cluster RXJ1716.4+6708 at  $z = 0.81$ , finding that both H $\alpha$  and MIR emitters avoid the central regions of the cluster. A red star-forming galaxy population involve both H $\alpha$  and MIR emitters. Therefore

---

<sup>1</sup>multi-object infra-red camera and spectrograph





**Figure 1.3:** The Virgo cluster of galaxies as imaged with the Palomar Observatory 48-inch Schmidt telescope as part of the Digitized Sky Survey. Credit: NASA, ESA, and the Digitized Sky Survey

this population resides in a medium-density environments like cluster peripheries, groups or filaments (Koyama et al., 2010). This gives clues that dusty SF is triggered in the infall regions of clusters, suggesting a probable link between galaxy transition and dusty SF. However, these surveys suffer from various limitations that they could not clearly identify the right fluxes of detected sources. Hence, they couldn't be able to provide either accurate cluster membership information as well as the dynamical information. Using the power of narrow-band surveys in trying to tackle the limitations, the GLACE survey has been designed as an innovative survey of ELGs in a well-studied and well-defined sample of clusters (Sánchez-Portal et al., 2015). GLACE is designed to exploit the outstanding capabilities of tunable filters (TFs) (see Section 2.1 for technical details) to map a set of important optical emission-lines (ELGs). The GLACE programme is developed to undertake a panoramic census of the SF and AGN activity within a sample of clusters at three redshift bins. These redshifts were defined to map a set of important lines ( $H\alpha$ ,  $[NII]$ ,  $H\beta$ ,  $[OII]$ , and  $[OIII]$ ) within the windows relatively free of strong atmospheric OH emission-lines (see Figure 1.4):  $z \sim 0.40$ ,  $0.63$  and  $0.86$ .

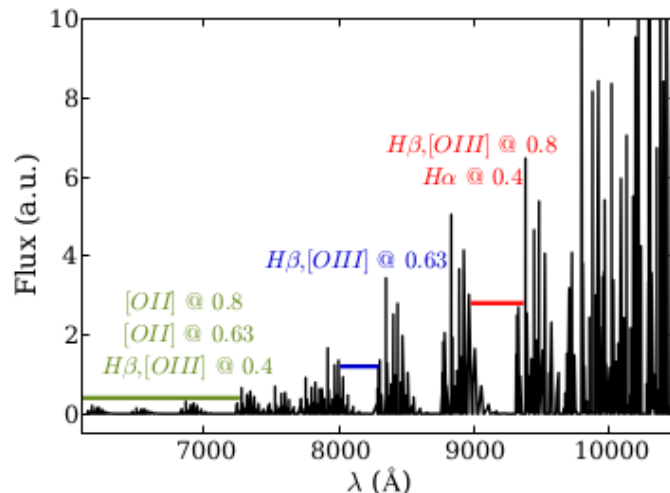


**Figure 1.4:** Spectra of the night sky showing the OH emission-lines (Rousselot et al., 2000) and windows relatively free of atmospheric OH emissions marked with green, blue and red horizontal lines. At each window, GLACE is observing the lines at the corresponding redshift indicated with the same colour (adapted from Sánchez-Portal et al., 2015).

Maps of ELGs are compared with other galaxy and global cluster properties to address several crucial issues, such as:

1. **Star formation.** Here, we determine the way the SF properties of galaxies are related to their position in the large scale structure like the host cluster. This gives a very important diagnostics for comparisons among different models related to the environmental effect on the evolution of galaxy. As described in Figure 1.1 by Treu et al. (2003) the effectiveness of each physical mechanism is different in different environments mainly depending on the clustercentric distance, leaving a footprint in the data. In GLACE, the extinction-corrected SF through  $H\alpha$  and [OII] lines are mapped (Pintos-Castro, 2014; Sánchez-Portal et al., 2015; Beyoro-Amado et al., 2021). GLACE survey is designed to reach SFR of  $\sim 2 M_{\odot}/\text{yr}$ , lower than that of the Milky Way by about 1 mag of extinction at  $H\alpha$ . This survey also addresses the class of galaxies with type or mass, that are forming stars within clusters. For this, the study of the morphology of confirmed ELGs helps in describing the relation between morphological transformation of infalling galaxies and the SF truncation (e.g., Poggianti et al., 1999; Poggianti, 2003; Kelkar et al., 2019). Finally, the SF histories of the cluster galaxies



is constructed by finding the total integrated SFRs, as determined for field galaxies (e.g., [Madau et al., 1998](#); [Cucciati et al., 2012](#); [Oemler et al., 2013](#)).

2. **The AGN role.** It is very important to determine the number and distribution of AGNs in clusters since it gives an outstanding information about the growth of the SMBH at the cluster centre, the nature of the fuelling of AGN, and the impacts of AGN on the ICM over cosmic time (e.g., [Klesman and Sarajedini, 2014](#); [Mo et al., 2018](#)). The physics behind the onset of the AGN activity in galaxies is constrained by addressing whether the AGN fraction is environment-dependent or not. Therefore, a complete survey of the AGN population in clusters at different redshifts, and in cluster regions with different mean densities and velocity dispersions becomes significantly important (e.g., [Bufanda et al., 2017](#); [Bilton et al., 2020](#)). GLACE survey is mainly sensitive to the AGN population within the sample clusters, achieved by disentangling the AGN from pure SF by using standard diagnostics such as BPT diagrams ([Baldwin et al., 1981](#); [Kewley et al., 2006a, 2013a](#)).
3. **The metallicity distribution.** Another important means to investigate the evolution of galaxies within clusters is studying the distribution of metallicity of galaxies with clustercentric distance (e.g., [Tiwari et al., 2020](#)). As galaxies fall into clusters and travel toward the centre of the cluster along their radial orbits, they interact with the ICM and other cluster galaxies. Hence they continue to get stripped progressively of their gas reservoir, affecting the metal abundances resulting with metallicity gradients across the cluster (e.g., [Hayashi et al., 2017](#); [Maier et al., 2019a](#)). The existing knowledge about the metallicities of ELGs in clusters and how it varies with clustercentric distances is very limited (e.g., [De Grandi and Molendi, 2001](#); [Molendi et al., 2016](#); [Mernier et al., 2017](#)). The GLACE allows for deriving the extinction corrected metallicities using N2 ([Denicoló et al., 2002](#)), R23 ([Pagel et al., 1979](#)), and O3N2 ([Alloin et al., 1979](#)) methods, where R23 degeneracy is to be broken by N2 and O3N2. The N2 and O3N2 are also used to evaluate the possible differences between the abundances versus metallicity of N and O.

The GLACE survey can also address many other interesting topics in extragalactic astronomy. For instance by studying the ELGs census at different clustercentric distances, the accretion history of the cluster can be traced. Moreover, it gives an

**Table 1.1:** The nine GLACE sample galaxy clusters with coordinates and corresponding redshifts (Sánchez-Portal et al., 2015)

NAME	RA(J2000)	DEC(J2000)	z
ZwCl0024.0+1652	00:26:36.0	+17:08:36	0.395
Abell 851	09:42:56.6	+46:59:22	0.407
RXJ1416.4+4446	14:16:28.7	+44:46:41	0.40
XMMLSS-XLSSC 001	02:24:57.1	-03:48:58	0.613
MACSJ0744.8+3927	07:44:51.8	+39:27:33	0.68
ClJ1227.9-1138	12:27:58.9	-11:35:13	0.636
XLSSC03	02 27 38.2	-03:17:57.0	0.839
RXJ1257.2+4738	12:57:12.2	+47:38:07	0.866
Cl1604+4304	16:04:23.7	+43:04:51.9	0.89

accurate check up of the cluster membership without requiring the spectroscopic analysis. The outstanding characteristics of the tunable filters and the tomography technique (see Sect. 2.1) are used for the GLACE survey. For tracing the relation between SF and environment in a wide range of local densities, the survey has required to cover 2 virial radii (some 4 Mpc) within the targeted clusters. The proposed GLACE sample includes nine clusters indicated in Table 1.1, three at each redshift bin (Sánchez-Portal et al., 2015). The observation of two of the clusters (ZwCl0024.0+1652 and RXJ1257.2+4738) has been completed yet using OSIRIS/GTC with Sánchez-Portal being a principal investigator.

## 1.9 Rational of the study

Our knowledge about galaxy clusters has been significantly improved in the last few decades with plenty of research results. However, there are still a lot of open questions such as: the way SF/AGN is changing with environment and their role in evolution of galaxy clusters, variations of metallicities of ELGs in galaxy clusters with other parameters, morphological classifications of cluster members and their variation with respect to other parameters, like clustercentric distance are not fully described yet.

The study of morphology, SF/AGN population, and distribution of metallicities within galaxy clusters present a powerful mean to investigate evolution of galaxies in clusters. This is because different galaxy properties such as colours, SF activity, morphology, nuclear activity, etc., are observed to vary with environment as well as redshift (e.g., Geach et al., 2006; Haines et al., 2009; Altieri et al., 2010; Koyama

et al., 2011; Pintos-Castro et al., 2013; Sánchez-Portal et al., 2015; Stroe et al., 2015; Alberts et al., 2016; Pintos-Castro et al., 2016; Beyoro-Amado et al., 2019). However, a clear picture of morphological transformation, SF/AGN activity, as well as metallicity distribution of ELGs in clusters still remains unknown, and therefore more studies are required. This PhD thesis aims in contributing to some of the mentioned open questions.

## 1.10 Objectives of the thesis

### 1.10.1 General objective

The general objective of this thesis is to study the properties of galaxies in galaxy clusters and understand better their evolution up to a redshift of  $z \sim 1.0$ .

### 1.10.2 Specific objectives

The specific objectives of this thesis are:

1. To study a detailed morphological classification of cluster member galaxies.
2. To study the properties related to SF/AGN in galaxy clusters. Here the SF and AGN contribution will be disentangled using appropriate diagnostic diagrams.
3. To study the variation of metallicity within galaxy clusters. Since it can be a powerful means to investigate evolution within galaxy clusters, metallicities will be derived through different methods depending on the redshift of the galaxy cluster.
4. To better understand the galaxy transformation and evolution within clusters at different cosmic times by analysing morphology, SF/AGN role, and metallicity in relation to other properties of galaxy clusters.

## 1.11 General methodology

For studying the properties and the evolution of galaxies in galaxy clusters up to  $z \sim 1.0$ , we initially planned to use Entoto observatory 1 m telescope for observing the local Virgo cluster (at  $z \sim 0.0038$ ) and GLACE TF data as a main data for studying the properties of higher redshift clusters (ZwCl0024+1652 at  $z \sim 0.4$  and RXJ1257+4837 at  $z \sim 0.87$ ). Because of technical problems, we couldn't get data from Entoto telescopes, while the GLACE tunable filters (TF) observations ( $H\alpha$ , [NII], [OIII],  $H\beta$  and [OII]) are already available for the two higher redshift clusters to be used for this thesis. For Virgo cluster galaxies, we used instead the Virgo Cluster Catalogue (VCC, [Binggeli et al., 1985](#)) and Extended Virgo Cluster Catalogue (EVCC, [Kim et al., 2014](#)) as a base for members detections and photometric comparisons. For all three clusters we use other existing public catalogues for further analysis and comparison; gathered from different databases (e.g., NED, VizieR, or Simbad). In addition, public multiwavelength data are also available and used where needed: e.g., optical HST data, X-ray data from Chandra and XMM, Spitzer and Herschel IR data, optical broad-band photometry data from GTC and Gemini, etc are used. Then using the available data, we use different methods for achieving our research objectives.

To achieve our first specific objective of performing a detailed morphological study of the cluster members we implement different methods. For galaxies in Virgo cluster we use visual classification results from EVCC. For the ZwCl0024+1652 cluster, morphology is determined visually using the data from HST ([Moran et al., 2005](#)). We further perform detailed morphological study of this cluster by measuring the morphological parameters with galSVM code (non-parametric method), and compare the obtained non-parametric classification with the available visual one. For the cluster at  $z \sim 0.87$ , we use the study results of morphological classification described in ([Pintos-Castro et al., 2016](#)). Different statistical parameters are computed and comparison is performed among the three clusters. We published our work related to morphology in [Beyoro-Amado et al. \(2019\)](#) and described in Chapter 4 of this thesis.

Secondly, to study the role of SF/AGN in galaxy clusters we can use the appropriate diagnostic diagram to discriminate the AGN from pure star-forming galaxies. For our purpose, we will use the standard BPT-NII diagnostic diagram ([Baldwin et al., 1981](#); [Kewley et al., 2006a](#)). The parameters used in BPT-NII diagram are

emission-line ratios:  $[OIII]/H\beta$  and  $[NII]/H\alpha$ . The combination of these line-ratios showed to be useful in disentangling different mechanisms of ionization and to separate between the HII (SF) regions, Seyfert 2, LINER, and composite galaxies (Kewley et al., 2006a, 2013a). The diagnostic lines use the classification criteria for AGNs, composites and pure SFs devised by Kauffmann et al. (2003), Kewley et al. (2006a) and Schawinski et al. (2007). While using the BPT diagnostic diagrams for this thesis we adapt the demarcations from (Kewley et al., 2006a) as follows.

The star-forming galaxies (HII regions) are identified by a condition:

$$\log([OIII]/H\beta) < 0.61/(\log_{10}([NII]/H\alpha) - 0.05) + 1.30, \quad (1.3)$$

and

$$\log([NII]/H\alpha) < 0.0. \quad (1.4)$$

From remaining sources in the sample, a region with composite galaxies satisfies the conditions:

$$\log([OIII]/H\beta) < 0.61/(\log([NII]/H\alpha) - 0.47) + 1.19, \quad (1.5)$$

and

$$\log([NII]/H\alpha) < 0.3. \quad (1.6)$$

Finally the remaining sources would be AGNs (Seyfert-2 or LINERs), where for Seyferts-2:

$$\log([OIII]/H\beta) > 1.05 \times \log([NII]/H\alpha) + 0.45, \quad (1.7)$$

While for LINERs:

$$\log([OIII]/H\beta) < 1.05 \times \log([NII]/H\alpha) + 0.45. \quad (1.8)$$

For ZwCl0024+1652 cluster at  $z \sim 0.4$ , the  $H\alpha$ ,  $[NII]$ ,  $H\beta$  and  $[OIII]$  lines are available. Therefore, we apply the BPT-NII diagram. We also compute the extinction corrected SFRs star-forming galaxies. For RXJ1257+4837 cluster ( $z \sim 0.866$ ),  $[OII]$ ,  $H\beta$  and  $[OIII]$  lines are available (Pintos-Castro, 2014). For Virgo cluster we use public data of emission lines (Gavazzi et al., 2004). Analysis against different cluster properties is performed for all the clusters and comparison (evolution

studies) is performed with redshift mainly using statistical analysis. We published our work related to this objective in [Beyoro-Amado et al. \(2021\)](#) and described in Chapter 5 of this thesis.

To contribute to the general objective by attaining the third specific objective, metallicities can be derived through different methods depending on the redshift of the galaxy cluster in our sample. Metallicity is derived by using N2 abundance indicator,  $12 + \log(O/H) = 8.90 + 0.57N2$ , ([Pettini and Pagel, 2004](#)) for ZwCl0024+1652 and Virgo clusters. We look for public data to compute the metallicity of RXJ1257+4837 cluster galaxies. Then metallicity is statistically analysed against different cluster parameters and across different redshifts. We implement these analysis in Chapter 6.

Finally, the galaxy transformation and evolution within clusters at different cosmic times is studied by consolidating the results obtained for three different clusters. Using the results we analyse their relationship with other properties such as: cluster radii, local density, stellar populations, SFR and environment. This is done throughout Chapters 4, 5 and 6. We use different software packages (`IRAF`, `SExtractor`, `galSVM`, `TOPCAT`, `GIMP` and `Le Phare`), and programming languages (`FORTRAN`, `Python` and `IDL`) for the thesis.

## 1.12 Significance of the study

Some of the main contributions that we expect to achieve with this thesis are:

- First, our study contributes to the advancement of extragalactic astronomy and helps Entoto Observatory to be visible and known among the international scientific community.
- Second, since we are going to analyse the AGN activity, and metallicity variations in relation to other cluster properties like cluster radii, local density, stellar populations, SFR, and environment, and compare between the low- and high-redshift clusters, this will provide interesting clues about the galaxy transformation and evolution within clusters at different cosmic times.
- Third, there are limited number of studies about galaxy metallicity variation with environments. Moreover, the existing results are contrasting due to

a small number of galaxies involved in the study sample to exhaustively handle the relationships between all the parameters (Skillman et al., 1996; Mouhcine et al., 2006). Therefore, this thesis is hopefully to contribute with additional results clarifying some of the existing results. It plays a significant role in advancing science and popularizing our observatory for the scientific community through our publications containing new results.

- Finally, our results provide key diagnostics to test between different ideas of galaxy transformation within the clusters. We also test the environmental influence on galaxy evolution, so that it contributes to the area of galaxy transformation and evolution in galaxy clusters.

### 1.13 Scope of the study

In this thesis, we study the properties and evolution of galaxies in clusters to  $z \sim 1.0$ . Hence, the scope of our study is limited to redshift range from 0 to 1.0. More specifically, we have selected three galaxy clusters at representative redshifts in the range: ZwCl0024+1652 at  $z \sim 0.4$ , Virgo at  $z \sim 0.0038$  and RXJ1257+4837 at  $z \sim 0.87$ . Our main focus is to study properties like SF/AGN activity, metallicity and morphology of galaxies in galaxy clusters apart from using other available parameters for analysis. Therefore, it will not end up with complete parameter analysis.

### 1.14 Limitations of the study

This study has suffered from the following limitations.

- Our initial idea was to include photometric observations from Entoto observatory 1 m telescope for studying Virgo cluster. The aim of that was to use and test local facilities, to give more visibility to Entoto Observatory, and that PhD candidate can get experience in astronomical observations and broad-band data reduction. However, due to different technical challenges at Entoto Observatory, planned observations were not carried out and only public data have been used in case of Virgo.

- Due to time limitations and a time consuming nature of TF data reduction, we were not able to finalise the reduction of RXJ1257+4738 TF data. Data reduction has been initiated and finalised until fringing correction. However, since special experience and dedicated time was needed for fringing reduction of TF data, this part of work will be carried out after thesis defence. Therefore, during the thesis only public data (both from GLACE and other sources) have been used.
- This study is limited to different sample sizes and properties of galaxies in three analysed clusters. Therefore, we were not able to fully compare all three clusters and to analyse in details the possible evolutionary trend since  $z \sim 1$ , especially in relation to metallicity. We are however planing to continue with work in the near future.

## 1.15 Outline of the thesis

This thesis comprises of seven chapters including general introduction. The contents of each chapter are briefly described here under. Chapter 1 is the general introduction to this thesis, where the basic concepts and terminologies, motivation, and objectives of this work are presented. Chapter 2 gives description of the data used in this work. Chapter 3 describes the used tunable filter (TF) data reduction process. The remaining three chapters present analysis, results and discussions, where chapter 4 discusses morphological studies, Chapter 5 deals with SF and AGN properties of galaxies in galaxy clusters and in Chapter 6, the metallicity properties are studied. Finally in Chapter 7, we present the overall summary and conclusions.

The following cosmological parameters are assumed throughout this thesis:  $\Omega_M = 0.3$ ,  $\Omega_\Lambda = 0.7$ ,  $\Omega_k = 0$  and  $H_0 = 70 \text{ km s}^{-1} \text{ Mpc}^{-1}$ . All magnitudes are given in AB system as described by Oke and Gunn (1983), unless otherwise stated.



# Chapter 2

## The Observational data

In this chapter, we briefly describe the data used in the thesis. Since most of our work is based on the GLACE data, we first describe the basics of the GLACE observations. Then, we describe the data that we used for each of the three galaxy clusters one by one. To this end we first review the data used for ZwCl0024+1652, then for RXJ1257+4738 and finally for Virgo cluster.

This chapter is organized into four major sections. Section 2.1 discusses the basics of GLACE observation, briefly describing the Gran Telescopio CANARIAS (GTC) and the tunable filters (TF). Then the data used for ZwCl0024+1652 cluster is presented in Section 2.2, where the GLACE and non-GLACE data are included. Section 2.3 describes the data, both GLACE and non-GLACE, used for RXJ1257+4738 cluster. Finally, in Section 2.4, the data used for Virgo throughout this thesis are presented briefly.

### 2.1 The GLACE Tunable Filter (TF) data

Here we describe the basics of the GLACE observations. First, we deal with the features of the Gran Telescopio CANARIAS (GTC), the OSIRIS and tunable filters with their operating principles.

### 2.1.1 The Gran Telescopio CANARIAS (GTC)

GRANTECAN<sup>1</sup> is a public society founded in 1994 for the purpose of designing and constructing the 10.4 m GTC, located at the Roque de los Muchachos Observatory at the Island of La Palma. The telescope started its scientific operation in 2009. Then the society took responsibility to serve the scientific community through operating the telescope. It is actively supported by the Spanish Government and the Regional Government of the Canary Islands through the European Funds for Regional Development provided by the European Union. The Mexican Instituto de Astronomía de la Universidad Nacional Autónoma de México (IA-UNAM) and the Instituto Nacional de Astrofísica, Óptica y Electrónica, and the University of Florida from USA are also collaborators of the project. Facilitating a world class science observations is the ultimate goal of GTC.

Currently, GTC is among the largest and the most advanced optical and IR telescopes in the world. The primary mirror of the telescope consists of 36 individual hexagonal segments acting as a single mirror (see for instance [Cepa et al., 2005](#), and references therein). The surface area of its light collecting mirror is equivalent to that of a telescope with single monolithic mirror of 10.4 m diameter. It is also largest in terms of its large light collecting surface of 75.7 m<sup>2</sup> (73 m<sup>2</sup> effective area). The telescope has secondary and tertiary mirrors in addition to the primary one to produce the telescope's focal plane in the focal station of own choice ([Cepa et al., 2005](#)). The scientific instruments placed at focal station detect light, then by analysing the light they store the final data (adapted from OSIRIS User's manual 3.1). The telescope is also characterized by an excellent image quality and hence the good sky quality can be exploited to its maximum. Thanks to the features mentioned above, the telescope puts a great influence on the study of key questions in astrophysics such as the nature of black holes, the SF history and early universe galaxies, the physics of distant planets, and the nature of dark matter and dark energy in the universe (adapted from OSIRIS User's manual 3.1).

### 2.1.2 OSIRIS and tunable filters

The Optical System for Imaging and low-intermediate-Resolution Integrated Spectroscopy (OSIRIS) is both an imager and spectrograph for the optical wavelength

---

<sup>1</sup><http://www.gtc.iac.es/gtc/grantecan.php>

range, located in the Nasmyth-B focus of the GTC (Cepa, 1998; Cepa et al., 2005). In addition to the standard broad-band imaging and long-slit spectroscopy, OSIRIS provides capabilities such as the narrow-band tunable filters imaging and multi-object spectroscopy. Moreover, the modes can benefit from the charge-shuffling capabilities of the detector. It provides standard broad-band imaging with SDSS filters and spectroscopic data, both with a single long-slit and multi-object mode. Moreover, the major instrumental characteristic that is unique to OSIRIS is the use of TF for the imaging in narrow-band. The detector consists of a mosaic of two Charge-Coupled Devices (CCDs) of  $2048 \times 4096$  pixels with a 72 pixel gap between them. It covers a total field of view (FoV) of  $8' \times 8'$ <sup>2</sup>. The CCDs are labelled in such a way that the one placed on the left side is CCD1 while that on the right side is labelled CCD2. In the standard mode of  $2 \times 2$  binning operation, the pixel scale is  $0.25''$ . The 3 dimensional image of OSIRIS is given in Figure 2.1 showing the main subsystems (adapted from OSIRIS User's manual 3.1)<sup>3</sup>.

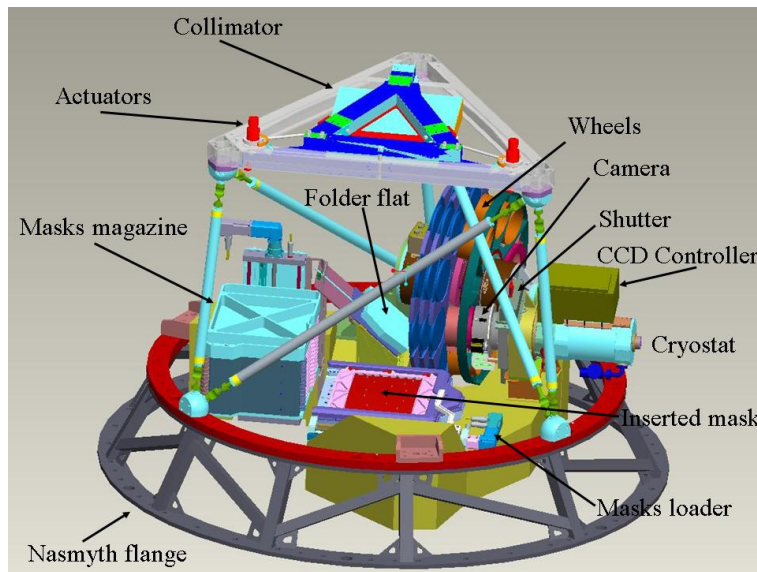


**Figure 2.1:** 3D image of OSIRIS with the main parts, taken from OSIRIS User's manual 3.1.

OSIRIS is an imaging as well as spectrograph system covering the 365-1000 nm spectral range. The use of two tunable filters (TFs)<sup>4</sup> is a key feature of OSIRIS. The interferometers are formed by two plane transparent plates that are parallel

<sup>2</sup>precisely  $7.8' \times 7.8'$  of effective unvignetted field, while  $7.5' \times 6'$  in the case of multi-object spectroscopy

<sup>3</sup>[http://www.gtc.iac.es/instruments/osiris/media/OSIRIS-USER-MANUAL\\_v3-1.pdf](http://www.gtc.iac.es/instruments/osiris/media/OSIRIS-USER-MANUAL_v3-1.pdf)

<sup>4</sup>A pair of tunable narrow-band interference filters (FabryPerot etalons) covering 450-671 nm (blue 'arm') and 651-935 nm (red 'arm'), adapted from OSIRIS User's manual 3.1.

to each other and coated for optimal performance over a wavelength range of 370-960 nm. The standard optical scheme of an etalon is depicted in Fig 2.2 (adapted from [Pintos-Castro, 2014](#)).

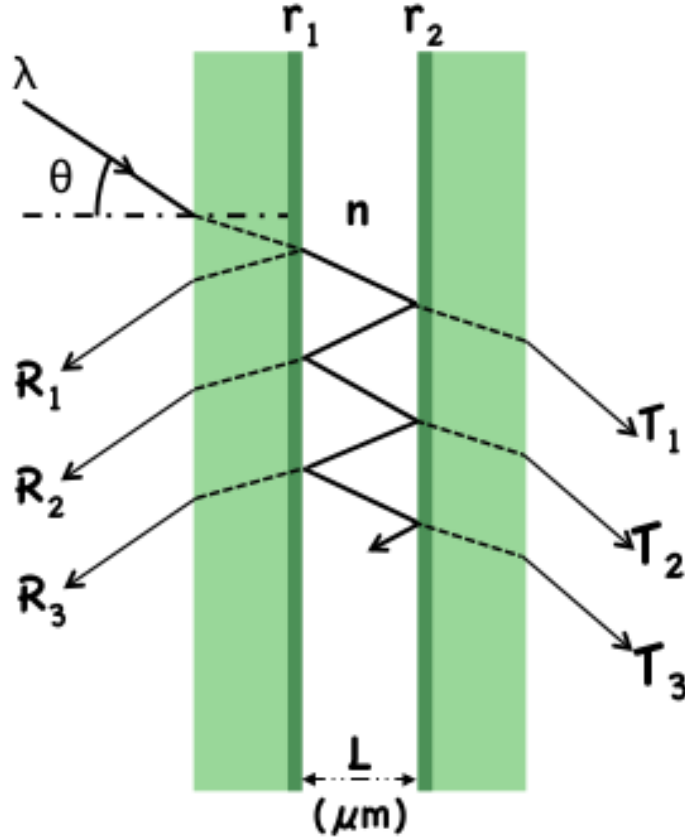


**Figure 2.2:** Fabry-Pérot interferometer scheme (adapted from [Pintos-Castro, 2014](#)), formed of two glass parallel plates with a gap  $L$  between them. The inner surfaces are coated with high reflectivities  $r_1$  and  $r_2$ ,  $\theta$  stands for the angle of incidence and  $n$  for the refractive index of the medium within the gap (typically the air).

The separation between the plates sets to wavelength resonance subject to constructive interference resulting from the internal reflections in the etalon. This interference builds up a broad image in which there is an area (called the Jacquinot spot) where change in wavelength is utmost  $\sqrt{2}$  times the FWHM ([Sánchez-Portal et al., 2015](#)). It is possible to vary the plate spacing over a large range with high accuracy being controlled by means of a stack of piezoelectric transducers. A wide spectral region, with a moderate spectral resolution between 12 and 20 Å of FWHM for red TF, with moderate resolution and with a tuning accuracy of 1 Å in the central wavelength of the filter is hence accessible ([Sánchez-Portal et al., 2015](#)).

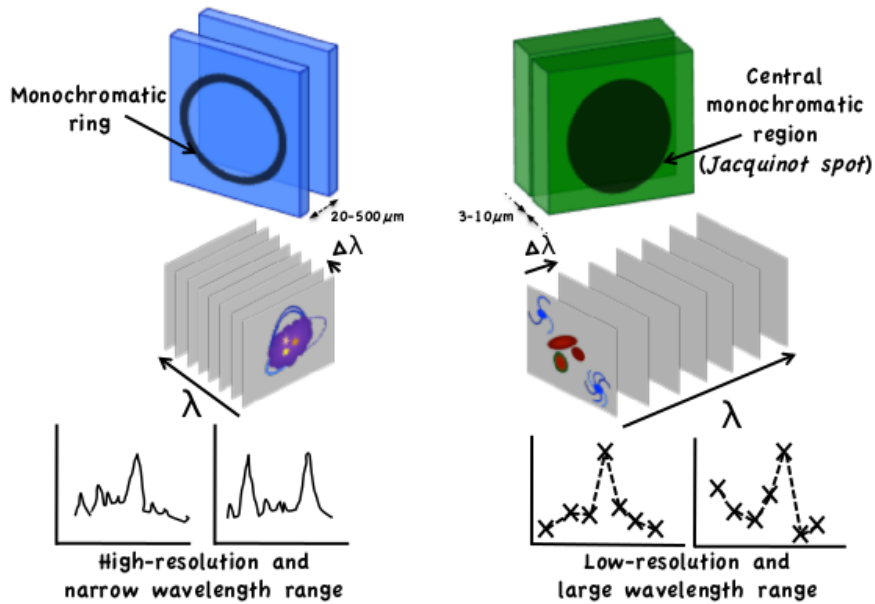


**Figure 2.3:** The way Fabry-Pérot interferometer (**left**) differs from TF (**right**) (adapted from [Pintos-Castro, 2014](#)).

Exploiting the advantage of TFs over the conventional Fabry-Pérot interferometers, TFs are characterized by the plates operating at much smaller spacings that widens the central interference region. Moreover, TFs can access a much wider range of plate spacings leading to a wider range of wavelengths. The difference between Fabry-Pérot interferometers and TF is given diagrammatically in Figure 2.3 (adapted from [Pintos-Castro, 2014](#)). While using OSIRIS TFs, the spectral range for the blue TF is 3650-6710 Å whereas 6510-9345 Å for red TF. Because of all the features described above, low resolution spectral observations are possible for all the targets within a wide field of view as well as having a large collecting area.

The TF transmission profile (the so called Airy function) is periodic as a function of the incident light wavelength ([Pintos-Castro, 2014](#); [Sánchez-Portal et al., 2015](#)) as shown in Figure 2.4. The spectral response of the TF can be taken as Gaussian with good approximation above the value of FWHM (see Figure 2.5).

If the angle of incidence of the beam entering the TF is  $\theta$ , the condition for peak transmission is given (as described in, [Pintos-Castro, 2014](#); [Sánchez-Portal et al., 2015](#)) by the Equation 2.1.

$$m \lambda = 2 \mu L \cos \theta, \quad (2.1)$$

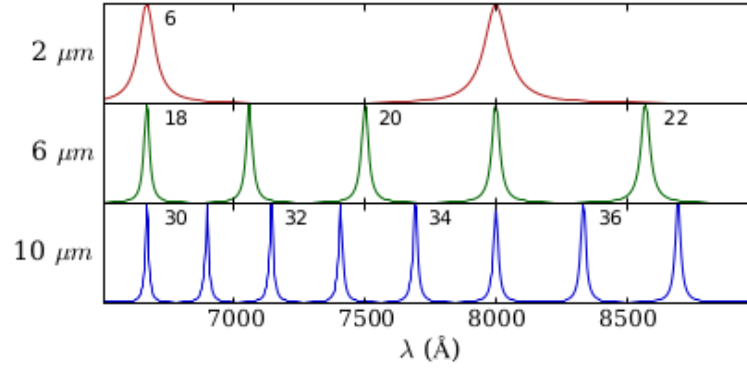


**Figure 2.4:** Transmission profile for different plate spacing values in TF with numbers indicating even interference orders (adapted from [Pintos-Castro, 2014](#)).

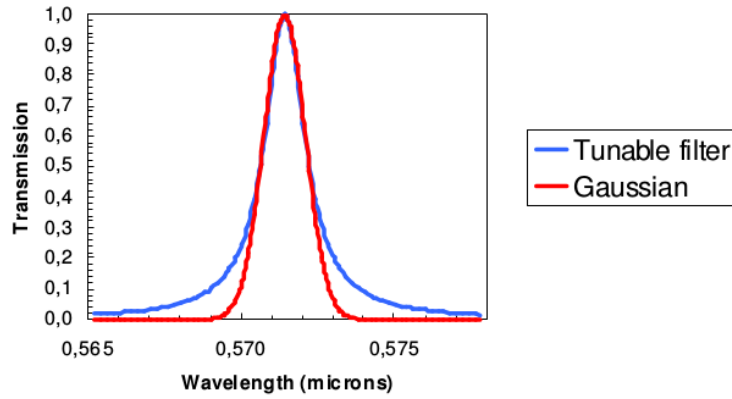


**Figure 2.5:** Spectral response of a TF with respect to a Gaussian (taken from OSIRIS User's manual 3.1).

where  $m$  is the integer order of interference,  $\mu$  is the refractive index of the medium in the space between the plates ( $\mu = 1$ , usually for air) and  $L$  is the separation (gap) between the plates. The details of observing with TF are presented in [Pintos-Castro \(2014\)](#) and [Sánchez-Portal et al. \(2015\)](#). The peak transmission wavelength varies with the radial distance  $r$  (in arcmin) of the source from the optical center according to the Equation 2.2 (as described in [González et al., 2014](#); [Sánchez-Portal et al., 2015](#)).

$$\lambda = \lambda_0 - 5.04r^2 + a_3(\lambda)r^3, \quad (2.2)$$

where  $\lambda_0$  is the central wavelength tune in Å, and  $a_3(\lambda)$  being a parameter describing the wavelength dependency of the coatings (González et al., 2014; Sánchez-Portal et al., 2015) given by the Equation 2.3.

$$a_3(\lambda) = 6.0396 - 1.5698 \times 10^{-3}\lambda + 1.0024 \times 10^{-7}\lambda^2, \quad (2.3)$$

As described in Sánchez-Portal et al. (2015), TF transmission profile  $T(\lambda)$  can be approximated by Equation 2.4.

$$T(\lambda) \simeq \left( 1 + \left( \frac{2(\lambda - \lambda_0)}{\Delta_{FWHM}} \right)^2 \right)^{-1}, \quad (2.4)$$

where  $\Delta_{FWHM}$  stands for the bandwidth of TF FWHM.

As defined by Pintos-Castro (2014), images are taken with TF at individual basis (slice) at the same nominal position and central wavelength, with or without dithering. We produce a scan (series of slices) by taking images of the same pointings at consecutive wavelengths. Consecutive slices are separated with a scan step measured in wavelength or FWHM of the TF. The integrated flux of the object in each and every slice results in a data array called pseudo-spectrum, resulting from the convolution of spectra of the object and the TF response for each slice combination.

As described by Pintos-Castro (2014) and depicted in Figure 2.6, there are three possible observing strategies with TFs. The first method called *on/off band*, implements the on-line, and off-line imaging of only continuum to be subtracted from the on-line image to get the emission line. The second strategy is executed by superposing set of images of the same pointing at different consecutive wavelengths to create a wider synthetic filter. This strategy is said to be the *band synthesis*. *Tunable tomography* is a third strategy in which the set of images of the same pointings at different consecutive wavelengths are separately analysed. In this case, aperture photometry should be performed for the sources in each individual image (slice) to create the pseudo-spectra.

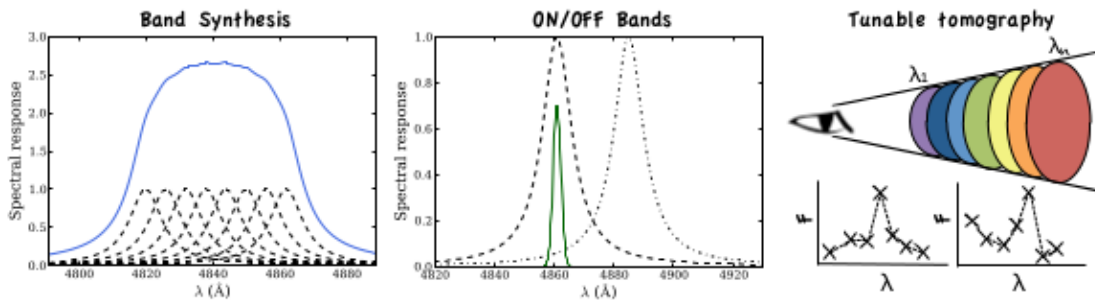


**Figure 2.6:** The description of the observing techniques with the TF (Credit: Pintos-Castro, 2014)

## 2.2 The data used for ZwCl0024+1652 cluster

### 2.2.1 The [OIII] and $H\beta$ imaging GLACE TF data

The [OIII] and  $H\beta$  imaging in ZwCl0024+1652, two pointings have been carried out with OSIRIS/GTC using the red TF. The first pointing (termed as "centre position" or "position A") was executed in GTC observing runs GTC63-09B, GTC08-10AGOS and GTC75-13B (semesters 09B, 10A and 13B), targeting the [OIII] and  $H\beta$  lines (Sánchez-Portal et al., 2015). In the centre position observations the core of the cluster was centred within CCD1. The second pointing termed as "offset position" or "position B" was performed in GTC semesters 75-13B and 47-10B targeted to the same emission lines. Position B was adjusted offset with right ascension (RA) and declination (Dec) by  $\Delta RA = -2.3'$ ,  $\Delta Dec = +2.5'$  that is about  $3.4'$  in the NW direction.

#### 2.2.1.1 [OIII] imaging data

For [OIII] line observations of ZwCl0024+1652 cluster, the spectral range was 6894.8-7154.8 Å (Sánchez-Portal et al., 2015) and the target in this case was covered by 27 evenly spaced scan steps of  $\Delta\lambda = 10 \text{ \AA}$ . Hence, there are 27 individual image slices for each position (centre and offset) corresponding to each wavelength. In GTC semesters 8-10A and 47-10B, three individual exposures have been recorded for each TF tune with dithering pattern (0,0), (0,10") and (10",10") hereafter referred as 00, 01 and 11, respectively and an amplitude (chosen similarly as the gap between the detectors) of 10" was implemented to easily identify the



diammetric ghosts (Sánchez-Portal et al., 2015). In GTC semester 13B, two individual exposures for each TF tune only with two dithers (00 and 11) have been mapped for the same wavelengths as in other semesters. The observational data of [OIII] imaging for ZwCl0024+1652 are summarized in Table 2.1.

**Table 2.1:** ZwCl0024+1652 imaging data targeting [OIII] lines.

**Centre position:** [RA = 00<sup>h</sup> 26<sup>m</sup> 35.70<sup>s</sup>, DEC = 17<sup>d</sup> 09<sup>m</sup> 45.0<sup>s</sup>]

$\lambda_{0,i}$ (Å)	OS filter	Date	Seeing (")	N Steps	N Exp.	Exp-time (sec.)
6894.8	f680/43	28 July 2010	0.9-1.3	4	3	45
6934.8	f694/44	28 July 2010	1.0-1.3	14	3	45
7074.8	f709/45	28 July 2010	0.9-1.3	9	3	45
6894.8	f680/43	09 October 2013	<1.0	4	2	53
6934.8	f694/44	09 October 2013	<1.0	14	2	53
7074.8	f709/45	09 October 2013	<1.0	9	2	53

**Offset position:** [RA = 00<sup>h</sup> 26<sup>m</sup> 26.5<sup>s</sup>, DEC = 17<sup>d</sup> 12<sup>m</sup> 15.0<sup>s</sup>]

$\lambda_{0,i}$ (Å)	OS filter	Date	Seeing (")	N Steps	N Exp.	Exp-time (sec.)
6894.8	f680/43	20 September 2010	0.9-1.3	4	3	45
6934.8	f694/44	20 September 2010	1.0-1.3	14	3	45
7074.8	f709/45	20 September 2010	0.9-1.3	9	3	45
6894.8	f680/43	09 October 2013	<1.0	4	2	53
6934.8	f694/44	09 October 2013	<1.0	14	2	53
7074.8	f709/45	09 October 2013	<1.0	9	2	53

### 2.2.1.2 H $\beta$ imaging data

The spectral range for H $\beta$  observations (Sánchez-Portal et al., 2015) was 6701.1-6911.1 Å. For this line, the target was covered by 22 evenly spaced scan steps for center position while for offset position two scan steps at 6901.1 and 6911.1 were omitted accidentally, hence we only have 20 image slices for position B. The same mechanism was used for both [OIII] and H $\beta$  observations. The observational data of H $\beta$  imaging for ZwCl0024+1652 are summarized in Table 2.2.

### 2.2.2 Other GLACE TF data

We used a catalogue consisting of an H $\alpha$  emitting ELGs that was generated based on the two OSIRIS/GTC pointings with the red TF executed towards

**Table 2.2:** ZwCl0024+1652 imaging data targeting H $\beta$  lines.**Centre position:** [RA = 00<sup>h</sup> 26<sup>m</sup> 35.70<sup>s</sup>, DEC = 17<sup>d</sup> 09<sup>m</sup> 45.0<sup>s</sup>]

$\lambda_{0,i}$ (Å)	OS filter	Date	Seeing (")	N Steps	N Exp.	Exp-time (sec.)
6701.1	f666/36	24 November 2009	0.8-1.0	5	3	124
6751.1	f666/36	25 November 2009	1.1-1.2	3	3	124
6781.1	f680/43	25 November 2009	0.8-1.0	2	3	124
6801.1	f680/43	17 August 2010	1.0	3	3	130
6831.1	f680/43	24 November 2009	0.9-1.1	5	3	124
6881.1	f680/43	24 November 2009	0.8-1.0	4	3	124

**Offset position:** [RA = 00<sup>h</sup> 26<sup>m</sup> 26.5<sup>s</sup>, DEC = 17<sup>d</sup> 12<sup>m</sup> 15.0<sup>s</sup>]

$\lambda_{0,i}$ (Å)	OS filter	Date	Seeing (")	N Steps	N Exp.	Exp-time (sec.)
6701.1	f666/36	09 October 2013	<1.0	5	3	138
6751.1	f666/36	09 October 2013	<1.0	3	3	138
6781.1	f680/43	09 October 2013	<1.0	2	3	138
6801.1	f680/43	09 October 2013	<1.0	5	3	138
6851.1	f680/43	09 October 2013	<1.0	5	3	138

ZwCl0024+1652 galaxy cluster under the framework of GLACE (Sánchez-Portal et al., 2015). The first pointing carried out in GTC semesters 09B, 10A, and 13B, targeted on the observation of H $\alpha$ /[NII], H $\beta$  and [OIII] lines gave results for centre position. While the second pointing was carried out in semesters 10B and 13B, and targeted on the same emission lines, but focused on investigating the offset position. The results of observations were published by GLACE members in Sánchez-Portal et al. (2015) as a catalogue of unique ELGs in ZwCl0024.0+1652 containing a total of 174 ELGs (with 16 columns of measurements) mainly with H $\alpha$  and [NII] results. We used the catalogue<sup>5</sup> for comparison and for analysis of different properties like AGN and metallicity properties.

## 2.2.3 Non-GLACE public data

### 2.2.3.1 The HST/ACS data

We used the public Hubble Space Telescope (HST) reduced scientific image of ZwCl0024+1652, and obtained from the Hubble Legacy Archive, which is a collaboration between the Space Telescope Science Institute (STScI/NASA), the

<sup>5</sup>The catalogue can be accessed at: <http://cdsarc.u-strasbg.fr/viz-bin/cat/J/A+A/578/A30>.

Space Telescope European Coordinating Facility (ST-ECF/ESA) and the Canadian Astronomy Data centre (CADC/NRC/CSA) and from the observation carried out on 16 November 2004 with the ACS Wide Field Camera (WFC) using the F775W filter. The ACS/WFC has a pixel scale of 0.05 arcsec/pixel and field of view of  $202 \times 202$  arcsec<sup>2</sup>. The cluster is centred at RA = 6.64433 deg and DEC = 17.16211 deg, and the used image covers the central part of cluster of  $\sim 1$  Mpc. The image data is given in Figure 2.7 with all the sources labelled.

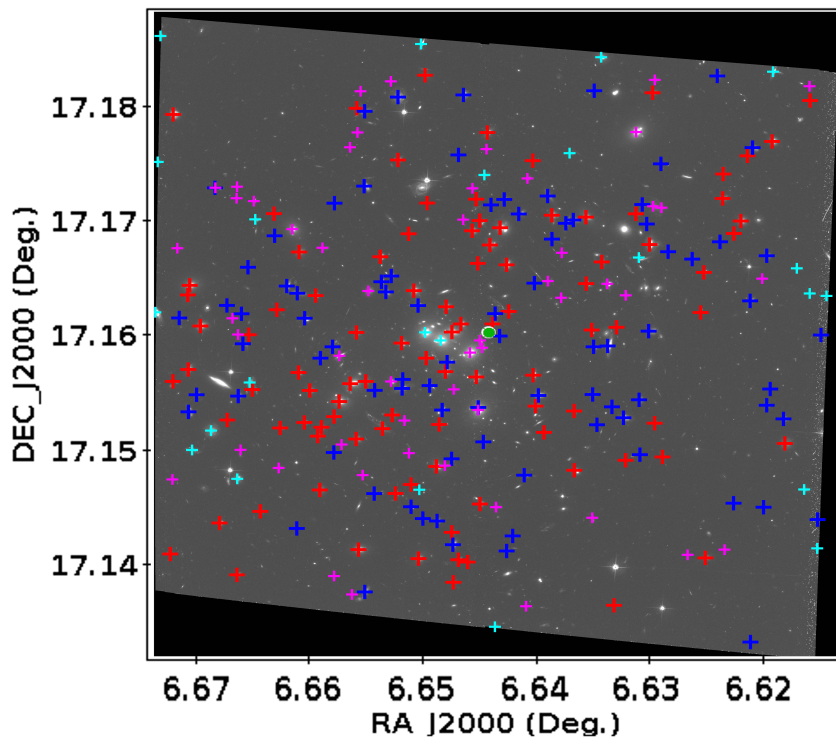


**Figure 2.7:** The ACS/WFC image of ZwCl0024+1652 galaxy cluster used in this work, where East is to the left and North at the top. The centre of the cluster is indicated by a large green dot. The larger red and blue crosses indicate galaxies classified as ET and LT, respectively. While the smaller cyan crosses show those galaxies for which the probabilities are not measured and the magenta crosses show galaxies with measured probabilities but undecided morphologies (see Section 4.2.1).

### 2.2.3.2 WFP2 catalogue data

To extract redshift information and to identify cluster members, we used the public ZwCl0024+1652 master catalogue<sup>6</sup> described in Treu et al. (2003) and Moran et al.

<sup>6</sup>Accessed at: <http://www.astro.caltech.edu/~smm/clusters/>

(2005). The catalogue consists of 73,318 sources, with photometric and/or spectroscopically confirmed redshifts available, and covering the area of  $0.5 \times 0.5 \text{ deg}^2$  up to the clustercentric distance of about 5 Mpc. All observations were carried out with CFHT<sup>7</sup> and its CFH12K wide field camera, and/or the HST WFP2<sup>8</sup>, as described in Treu et al. (2003). Beside redshifts, this catalogue includes the visual morphological classification of sources brighter than  $I = 22.5$  (Moran et al., 2005). We cross-matched this catalogue with our SExtractor catalogue (3515 sources) using a maximum radius of 2 arcsec. This radius was selected after testing different ones from 1 to 5 arcsec and finding it to be the best compromise between losing the counterparts and having multiple matches. We obtained a total of 255 counterparts (hereafter cluster sample) with available redshifts. In total, 126 and 129 sources have spectroscopic and photometric redshift measurements, respectively. The redshift distribution of the members is given in Figure 2.8, including spectroscopic and photometric measurements.

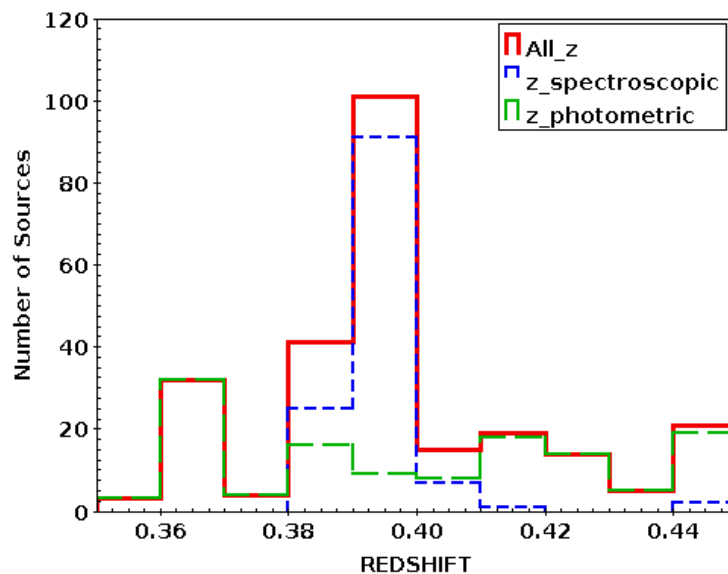


**Figure 2.8:** Redshift distribution of our real ZwCl0024+1652 sample from HST/ACS data where the red solid lines stand for the total sample, the blue dashed lines for spectroscopic redshifts and the dashed green lines for photometric redshifts.

<sup>7</sup>Canada-France-Hawaii Telescope

<sup>8</sup>Wide Field and Planetary Camera 2

### 2.2.3.3 Galaxy data for cluster-field comparison

In order to compare selected properties of field galaxies with the cluster parameters described in this work, we explored different observed spectroscopic data sets which match the flux depth and redshift domains explored by GLACE survey, in particular the surveyed one of ZwCl0024+1652 at  $z = 0.395$ . We found that the VIMOS-VLT Deep Survey (VVDS-Deep; [Le Fèvre et al., 2013](#)) data sample in the field 0226-04 ( $0.61 \text{ deg}^2$ ) meets this purpose. This publicly available database<sup>9</sup> contains reduced fluxes and equivalent widths (EW) of strong lines in the optical, as well as SFR and  $M_*$  estimations of 11 486 sources limited to  $17.5 \leq I_{AB} \leq 24$ . A detailed description of these measurements can be found in [Lamareille et al. \(2009\)](#). According to these authors, the VVDS-Deep data have a mass-to-light completeness of 50% at  $z \sim 0.4$  and  $\log(M_*/M_\odot) \geq 8.5$ . With this mass constraint, we prepared a representative field galaxy sample by selecting from VVDS-Deep data all sources within a redshift range ( $0.37 \leq z \leq 0.42$ ) with a continuum magnitude  $R_{AB} < 23$ , according to the cluster galaxy distributions given by [Sánchez-Portal et al. \(2015\)](#). A total of 177 galaxies satisfy these criteria, increasing the final completeness of the sample to about 90%.

## 2.3 RXJ1257+4738 data

### 2.3.1 The GLACE raw TF imaging: $H\beta$

We reduced a subset of the raw observational data for this cluster. The observations of this cluster were made as part of the GTC2012-11ESO large program carried out in 43 observational blocks. The observations were made between central wavelength  $\lambda_0$  range of 8980.6 - 9280.6 Å. The scan step used was 12 Å resulting with a total of 51 scans. Due to the presence of a very bright star in the middle of the field (that was conveniently placed in the gap between CCDs, dithering was not implemented. Moreover, we used the results obtained earlier by GLACE team members (Section 2.3.3) for comparison and further computation purpose. We have the following data sets (in Table 2.3) generated on the same framework.

---

<sup>9</sup>Accessed at: <http://cesam.lam.fr/vvds>

**Table 2.3:** RXJ1257 imaging data targeting the H $\beta$  lines: RA = 12<sup>h</sup>57<sup>m</sup>12.2<sup>s</sup>, DEC = +47°38'6.5"

$\lambda_{0,i}$ (Å)	OS filter	Date	N Steps	Exp-time (sec.)
8980.6	f893/50	05 April 2013	2	800
8992.6	f893/50	06 April 2013	2	800
9004.6	f893/50	01 May 2013	2	800
9016.6	f893/50	02 May 2013	2	800
9028.6	f893/50	02 May 2013	1	800
9040.6	f893/50	03 May 2013	1	800
9052.6	f893/50	03 May 2013	1	800
9064.6	f893/50	11 May 2013	1	650
9070.6	f893/50	11 May 2013	1	600
9076.6	f893/50	11 May 2013	1	550
9082.6	f902/40	29 May 2013	1	600
9088.6	f902/40	31 May 2013	1	750
9094.6	f902/40	06 May 2013	2	800
9106.6	f902/40	09 June 2013	1	800
9112.6	f902/40	09 June 2013	1	550
9118.6	f902/40	09 June 2013	1	700
9124.6	f902/40	11 June 2013	1	550
9130.6	f902/40	11 June 2013	1	650
9136.6	f902/40	11 June 2013	1	700
9142.6	f902/40	11 June 2013	1	550
9148.6	f910/40	11 June 2013	1	650
9154.6	f910/40	11 June 2013	1	800
9160.6	f910/40	12 June 2013	1	750
9166.6	f910/40	12 June 2013	1	650
9172.6	f910/40	12 June 2013	1	650
9178.6	f910/40	13 June 2013	1	500
9184.6	f910/40	13 June 2013	1	550
9190.6	f910/40	13 June 2013	1	450

continued on next page

$\lambda_{0,i}$ (Å)	OS filter	Date	N Steps	Exp-time (sec.)
9196.6	f910/40	13 June 2013	1	500
9202.6	f910/40	13 June 2013	1	500
9208.6	f910/40	13 June 2013	1	600
9214.6	f910/40	02 July 2013	1	650
9220.6	f910/40	02 July 2013	1	800
9226.9	f910/40	04 July 2013	1	800
9232.6	f919/41	04 July 2013	1	650
9244.6	f919/41	04 July 2013	3	600
9262.6	f919/41	02 July 2013	1	600
9268.6	f919/41	02 July 2013	1	650
9274.6	f919/41	03 July 2013	1	650
9280.6	f919/41	03 July 2013	1	800

### 2.3.2 The [OII] TF imaging data

We have made use of results from the study of [OII] TF imaging data on the RXJ1257+4738 cluster carried out by I. Pintos and collaborators in the framework of the GLACE survey (Pintos-Castro, 2014; Pintos-Castro et al., 2016, Pintos-Castro et al., in prep.). The [OII] $\lambda$ 3727 TF imaging with OSIRIS were executed in semesters 11A, 12A, and 13A, as a large ESO/GTC program (PI: Miguel Sanchez-Portal). The observations, covering 24 scans in the spectral range 6884-7114 Å with steps of 10 Å, were carried out in photometric and non-photometric nights. It lasted for a total exposure time of 18 h. Dithering was not applied, but three individual exposures of 900 s were taken at each TF tuning, to get rid of saturation and wavelength shift problems. For flux calibration, a long-slit spectroscopy was obtained with OSIRIS instrument for two stars in the cluster field. The [OII] data was reduced and calibrated, and a total of 271 ELGs were identified after visual inspection of the pseudo-spectra. The data we used finally consist of 87 [OII] line emitters within a complete line-of-sight velocity over the entire OSIRIS FOV. More detailed description of the [OII] data is found in Pintos-Castro (2014) and Pintos-Castro et al. (2016), and for details of the [OII] data reduction and calibration, see Sánchez-Portal et al. (2015).

### 2.3.3 Public GLACE data

For this high redshift cluster, we used different data sets that are already published by the GLACE team. To this end we used a data table of properties of the FIR emitting cluster members published by [Pintos-Castro et al. \(2013\)](#). The data consist of 38 member galaxies with FIR emission characterised by SFR in the range  $0.5 - 45 M_{\odot}/yr$ . Several measured parameters are included for these galaxies such as: age, mass, IR luminosity, SFR and sSFR.

The other data set used was the catalogue of morphological properties of galaxies in RXJ1257+4738 presented by [Pintos-Castro et al. \(2016\)](#). The dataset was based on optical broadband observations obtained in the framework of the GLACE project. There are 90 cluster galaxies that are morphologically classified and different morphological properties are presented. The morphological classification was done for these 90 sources between ET, LT, and, based on their colour, blue ET using non-parametric methods of morphological classification implemented with galSVM code ([Pintos-Castro et al., 2016](#)).

## 2.4 Data used for Virgo cluster

In this thesis, we used different public data sets for all the analysis, since the Virgo cluster was not observed within GLACE. The data are described briefly as follows.

The first comprehensive data set that we used is the Virgo Cluster Catalogue (VCC) ([Binggeli et al., 1985](#)). This catalogue consists of 2096 galaxies in total covering an area of  $140 \text{ deg}^2$  centred at Virgo cluster. This data set contains a complete list of all possible and certain members of the cluster (1277 cluster members, 574 possible members and 245 sources being a background Zwicky galaxies). This catalogue identifies the cluster membership, galaxy coordinates, morphologies and the total apparent blue magnitude.

Another data set that we used is a catalogue with spectrophotometry of Virgo cluster galaxies published by [Gavazzi et al. \(2004\)](#). The data comprise long-slit spectra of 333 galaxies, recorded in an approximately 50 nights within six years (1998 - 2003) with the 1.93 m telescope of the Observatoire de Haute Provence (OHP), the ESO 3.6 m telescope, the Loiano 1.52 m telescope and the San Pedro Martir (SPM) 2.1 m telescope observed in the "drift-scan" mode. In this data



set, different parameters are given for 124 galaxies, emission line properties for 165 galaxies, Balmer absorption lines for 42 galaxies and absorption indices for 33 galaxies.

In addition to the above mentioned data, we also used the ACS Virgo cluster survey results (Peng et al., 2008). These data result from a large program of imaging 100 ET galaxies in the Virgo cluster with HST/ACS. This catalogue comprises the absolute V and z magnitudes, projected distances from the centre, stellar luminosity in the z band and stellar mass values for 100 galaxies.

As fourth data set we used a catalogue containing the abundances of oxygen and related properties of Virgo member galaxies published by Hughes et al. (2013). In this catalogue there are 272 galaxies with oxygen abundances computed from a total of 478 observations. Moreover, additional physical parameters are included for 169 galaxies from Herschel Reference Survey (HRS). The data here are used for investigating the stellar mass, gas metallicity and gas content estimates as well as the interrelations.

The final and the most extensive data set we used for the analysis of the Virgo cluster galaxies is the Extended Virgo Cluster Catalogue (EVCC) published by Kim et al. (2014). This is a catalogue consisting of member galaxies in the Virgo cluster based on SDSS data release 7 (Abazajian et al., 2009), covering an area of  $725 \text{ deg}^2$  ( $60.1 \text{ Mpc}^2$ ). The area coverage is about 5.2 times greater than the footprint of the Virgo Cluster Catalogue (VCC) and extends out to about 3.5 times the virial radius of the Virgo cluster. There are 1589 galaxies in the catalogue with sky coordinates, morphologies and magnitudes available in different bands. Out of the 1589 galaxies included in EVCC, 676 are not included in the VCC catalogue.

# Chapter 3

## Tunable filter (TF) data reduction

In our work, we have used the GTC/OSIRIS/TF data of the two galaxy clusters, ZwCl0024+1652 and RXJ1257+4738, as mentioned in Chapter 2. Here we describe the major steps of TF data reduction. The TF data reduction process in our case can be divided into three parts: basic reduction of the raw images, wavelength and flux calibration, and flux measurements and selection of emission lines.

This chapter is organised as follows. Section 3.1 is dedicated to the basic data reduction of the raw TF data, applied for both ZwCl0024+1652 and RXJ1257+4738 clusters. In Section 3.2 we analyse the reduced images and generate the catalogues of sources. Finally, in Section 3.3, the flux and wavelength calibration are presented.

### 3.1 The basic raw image reduction

#### 3.1.1 ZwCl0024+1652 cluster data

We carried out the basic data reduction using the TF data Reduction (TFReD) package developed by Jones et al. (2002) and modified by GLACE team members to fit OSIRIS data (Sánchez-Portal et al., 2015; Ramón-Pérez et al., 2019a,b; Bongiovanni et al., 2019, 2020). In addition, the IDL and Python scripts tailored

for our specific data sets, and IRAF<sup>1</sup> (Image Analysis and Analysis facility) have been used. In the following we describe the major tasks performed while doing the basic data reduction carried out using standard and specific IRAF procedures.

### 3.1.1.1 Bias and flat-field correction

We used the standard IRAF tasks (Tody, 1986, 1993) here. The first step to be carried out in the data reduction is to correct the instrumental (i.e. intrinsic) defects of the electronic device used for imaging. In this aspect, there are two types of intrinsic effects: the additive effect that is a consequence of spurious signals added to the normal one, and the multiplicative effect due to variations in sensitivity from pixel to pixel. All the Observation Blocks (OBs) have respective set of bias images. In order to read the zero level of each pixel the bias images are taken without exposing the detector. Apart from this, there are few columns that can not get light (shadowed) in each CCD image and are known as overscans. Overscans provide the possible deviations of the zero level along the direction of reading. In this we used a `zerocombine` task of IRAF for creating a bias image for each OB. `Zerocombine` task gives the average of the zero level for each pixel. Then using the `ccdproc` task of IRAF we made the first correction. This task is accomplished using two steps: first, subtracting from each line the corresponding mean value of the overscan region, and second, subtracting the average bias image that contains the spatial structure. Set of flat images are also included in each OB. These images are images generated with uniform illumination so that the same intensity reaches each pixel. For our data, each OB includes five dome flats for each tuned wavelength. These flats have been obtained inside the closed dome using the artificial light. During our basic data reduction process we used a median scaled `flatcombine` task for creating an average flat image. Then we performed dividing the science images by the normalized average flat image by using a `ccdproc` task.

### 3.1.1.2 Removal of cosmic rays

Cosmic rays are random traces on the CCDs caused by very energetic particles. The cosmic rays removal can be performed in different ways. For our data of ZwCl0024+1652 cluster, we simply included the cosmic ray rejection option

---

<sup>1</sup><http://ast.noao.edu/data/software>

`crreject` inside the `combine` function in IRAF. This operation is performed when combining the individual images for each wavelength.

### 3.1.1.3 Subtraction of sky rings

We now go to the tunable filter specific data reduction step. This is a step of removing the diffuse, optical-axis centred sky rings. The rings are the result of atmospheric OH emission lines as a consequence of the radially changing wavelength shift described mathematically (e.g., González et al., 2014; Sánchez-Portal et al., 2015) by as in equations 2.2 and 2.3. To perform rings subtraction, the TFRed task `tringSub2` was used during the basic reduction process. The main activity of this task is to correct each individual exposure by using a background map created by determining the median of several dithered copies of the image in case of ZwCl0024+1652 cluster. Here the maximum shift permitted for the copies was 15 pixels. It is important to mask the sources with `objmask` task before making the map to minimize their contribution to the sampling of the sky. An increase of the background flux by about 30% is possible, even up to 70% in brightest cases if represented by the average amplitude of the sky rings. Except for slight improvements at the edge, subtraction of rings did not affect the standard deviation of the flux. Since the sky ring correction couldn't impose noise, we could better be able to detect the image sources. An example of the output as a result of the sky rings subtraction with this procedure is given in Figure 3.1 for a sample ZwCl0024+1652 images. It is common to also remove fringes<sup>2</sup> for images taken at higher wavelengths (as in case of H $\alpha$  data). However, here we focused on [OIII] and H $\beta$  observations around a wavelength of  $\sim 7000\text{\AA}$ , and have negligible effect of fringing.

### 3.1.1.4 Aligning the images

We have to register all existing frames to a common spatial reference image. Therefore, we selected a respective reference image for each of the [OIII] and H $\beta$  data of ZwCl0024+1652 cluster (both central and offset positions). To perform this, we measured the pixel position of a set of six stars in both positions (centre and offset) for each CCD. Then we created a text file with four columns with entries:

---

<sup>2</sup>Fringes are some of the possible sources of peculiar variations in the background caused by thin-film interference effects in the CCDs.

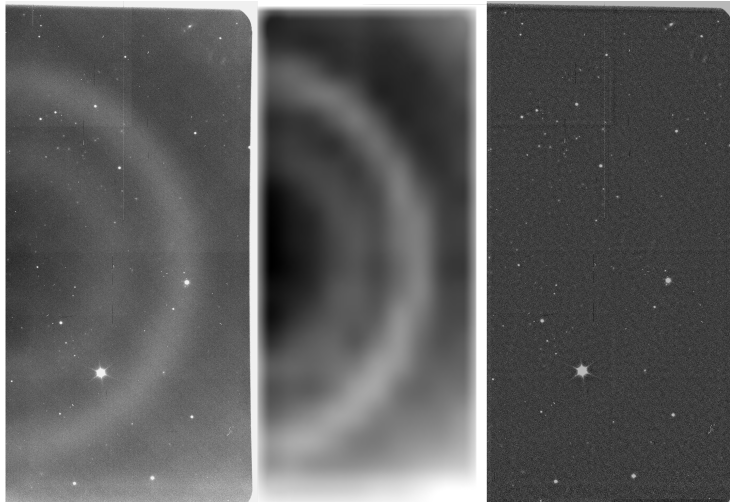


**Figure 3.1:** One sample of the result obtained for removing the sky rings using TFRred package. This is CCD2 obtained with the TF tuned at  $6881.1 \text{ \AA}$  before subtraction of the sky rings (*left*), the background sky map created by the tringSub2 task (*centre*), and the same image after the subtraction of the sky rings (*right*). This is the image of ZwCl0024+1652 cluster during  $H\beta$  imaging.

$x_{ref}$ ,  $y_{ref}$ ,  $x_i$ , and  $y_i$  by measuring the same set of six stars in all individual frames. We used this text file as an input for the IRAF `geomap` task, which calculates the transformation from coordinates system of the reference image to the rest and stores the coefficients. Finally with IRAF task `geotran` (a complementary task to `geomap`), the images were transformed so that the image alignment is done.

### 3.1.1.5 Image combination and creation of a deep image

Tomography technique, a method used in GLACE project, consists of acquiring series of images, known as scans, at consecutive tuned central wavelengths, called slices. The scans are carried out either with the same pointing or with dithering and the scan step. It is typically given by half of the full width half maximum (FWHM) of the tunable filter (TF) response as described by [Lara-López et al. \(2010a\)](#). In ZwCl0024+1652, [OIII] observations were carried out following two dither positions for each slice in the range from  $6895 - 7155 \text{ \AA}$  in GTC75-13B program, while the cluster was observed with three dither positions for each slice in the same wavelength range (as in GTC75) in other programs (GTC47-10B and GTC8-10AGOS). On the other hand,  $H\beta$  observations were carried out with three dither positions for each slice in the wavelength range from  $6701 - 6911 \text{ \AA}$ . Because of the dithering applied the pixels see different wavelength for individual exposures

for the same central tuned wavelength. Combination of images for creating a deep image involves the tasks described below:

- ⊙ **Mosaics.** All reduction procedures until now have been carried out with CCD1 and CCD2 separately. However, our cluster covers the full field, so it is needed to generate a unique image. We proceed to do that by joining the images in the two CCDs. Knowing the optical centre position (essential to compute the wavelength at each pixel), we performed the combination of images by first creating empty images with an IRAF tasks `mkimage` and `imcopy` (for copying each individual image into its respective half), and then reproducing the correct CCD positions in the instrument. This has been done both for [OIII] and  $H\beta$  data.
- ⊙ **Scaling.** It has been seen previously for [OIII] observations that in GTC75-13B program, cl0024 was observed with two ditherings and the exposure time was longer as compared to other programs. Hence before performing the combination to create deep image we scaled down all the images of this program by using a scale factor equal to 0.7. We did this with an IRAF task `imarith`, by multiplying all the images of GTC75 with 0.7 to scale them down and synchronize them to images in other programs that we can use with similar efficiencies.
- ⊙ **Deep image.** For all data ([OIII] and  $H\beta$ ) in both positions (central and offset) we obtained a deep image of the field by combining all individual exposures of every slice of a scan using an IRAF task `imcombine`. For [OIII] data, the combination was first done separately for GTC75 and other programs by applying a median filter. Then the resulting two images for each position were combined by applying an average filter. In case of  $H\beta$  data, the combination was done with median filter for each position because all observations were carried out with three dithers. The deep images created are given in Figures 3.2 and 3.3, for [OIII] and  $H\beta$ , respectively. The final deep image in each case is given as an input to the SExtractor package 2.5.0 (Bertin and Arnouts, 1996) to extract the sources.

Employing a median filter for combining the images is a best method to remove spurious features as ghosts even though this could potentially result with loss of some line emitters with very low-continuum level. Our deep image is better than test image that could be created by adding up all the

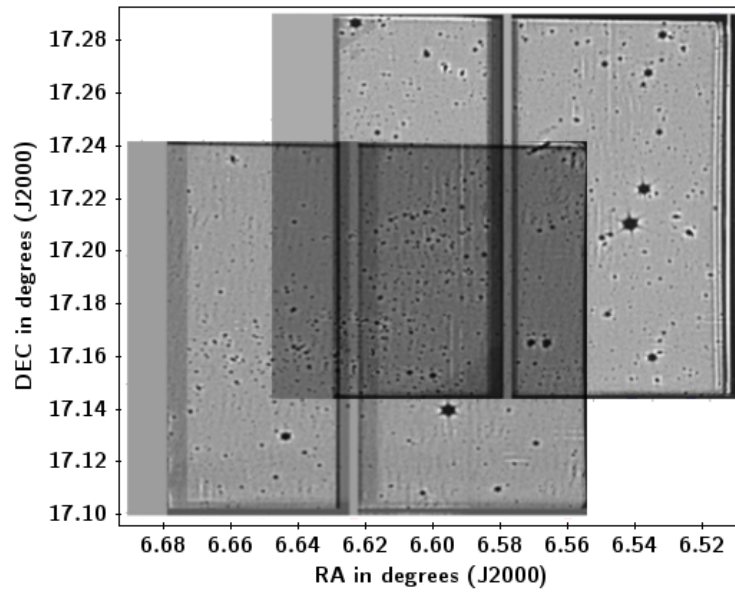


**Figure 3.2:** The deep image created from the [OIII] observations of ZwCl0024+1652 galaxy cluster involving the two GTC/OSIRIS pointings of: centre position (position A, left bottom) and offset position (position B, right top). The plot is put at standard orientation, north at the top and east to the left.

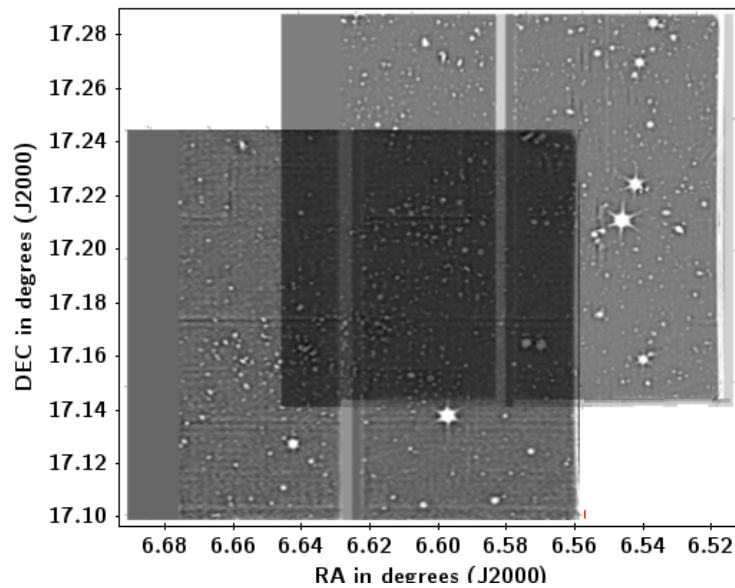


**Figure 3.3:** The deep image created from the  $H\beta$  observations of ZwCl0024+1652 galaxy cluster involving the two GTC/OSIRIS pointings of: centre position (position A, left bottom) and offset position (position B, right top). The plot is put at standard orientation, north at the top and east to the left.



scans applying a simple minimum-maximum rejection filter. Comparing the two, at most one line emitter per CCD gets lost but more than one-hundred spurious features are effectively removed in our deep image.

- ⊙ **Combinations.** Let us consider two images having the same central wavelength in two different positions of the dithering pattern, the wavelength difference for a particular source can then be estimated by using the equation 2.2 as:

$$\Delta\lambda = \lambda_1 - \lambda_2 = 5.04(r_2^2 - r_1^2) + a_3(\lambda)(r_1^3 - r_2^3), \quad (3.1)$$

where  $r_1$  and  $r_2$  are the respective distances of the source to the optical centre in image1 and image2, measured in arcsec.

For not losing emission lines due of the combination of different wavelengths, we re-ordered the usual steps by first applying SExtractor on the deep image to have the sources detected before combining the individual exposures. Therefore, for the tuned wavelength and each source detected the best possible combination of slices is determined, that is the best combination of the dither position and the TF tuning at the location of the detected source. Both for [OIII] and H $\beta$  observations of ZwCl0024+1652 cluster, we define the best combination as the sum of the images for which the TF wavelength at the position of the source lies within a range of 10 Å ( $\pm 5$  Å, corresponding to half of the scan step of TF, at intersection of the consecutive TF response. We derived the transmission profile, since this method does not introduce error in wavelength as well as in FWHM (Sánchez-Portal et al., 2015). As a result of H $\beta$  data we obtained 325/298 different combinations, that form 20/20 slices of each detected source in the order given by central/offset results, respectively. For [OIII] data we obtained 1301/1162 different combinations, that form the 27/27 slices for each detected source in similar order as for H $\beta$  case.

### 3.1.1.6 Astrometry

To map a cluster it is essential to have the sky position of the sources extracted by SExtractor. Therefore we performed the astrometry in the resulting deep image for each of the four cases: H $\beta$  center position, H $\beta$  offset position, [OIII] center position, and [OIII] offset position, using standard IRAF tasks as follows:



1. We built a catalogue of digital positions of several objects within the field, using a standard IRAF task `daofind`.
2. Selecting a catalogue that covers the entire field with sky positions (with minimum error) of reference objects is an important task. In this regard we selected GAIA catalogue that consists of 266 sources covering the entire field.
3. Using a standard IRAF task `ccxymatch`, we performed matching between the catalogue built with `daofind` and GAIA sources catalogue. This task uses a reference object, its logical and sky positions as an input.
4. Finally, using IRAF task `ccmap` and above matched catalogue, we determined the astrometric solution. Here we used the interactive mode for fitting by rejecting the most dispersed values (outliers). We performed the astrometry only on the deep image, because we are going to use this reference image for extracting the sources with dual mode of SExtractor (Bertin and Arnouts, 1996) on the combined images.

### 3.1.1.7 Degradation of images

Since observations took long time being done at different nights, there are variations in atmospheric conditions. This results in variation of source profile from one exposure to the other. Because of these, it is advisable to create another version of images consisting of the images degraded to the worst seeing. To do this, we used the `tfwhm` task of (TFRed) to measure the FWHM in each slice. We calculated the average seeing and the worst seeing over the scan, and we used another TFRed task `tgauss` for degrading each slice by convolving each with a Gaussian function whose FWHM is  $\sqrt{\langle W_W \rangle^2 - \langle W_0 \rangle^2}$ , where  $\langle W_0 \rangle$  stands for the average seeing in each image and  $\langle W_W \rangle$  denotes the average worst seeing of the scan. Then we used this set of degraded images to measure the flux at each slice and position of the source.

### 3.1.2 RXJ1257+4738 cluster data

For this cluster at  $z \sim 0.866$ , we carried out the basic data reduction using TFRed package version developed by Jones et al. 2002 as for the Zwcl0024+1652 cluster.

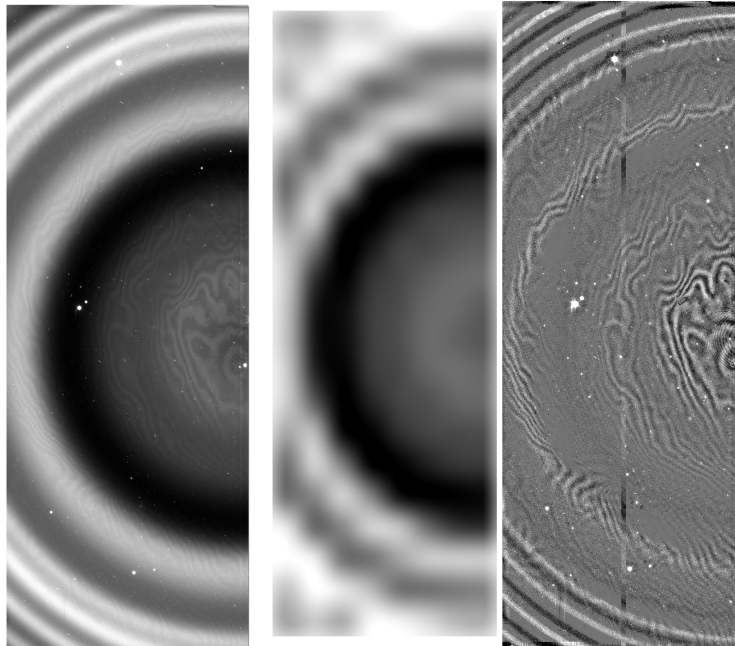


**Figure 3.4:** One sample of the result obtained for removing the sky rings using TFRed package. This is CCD1 image of H $\beta$  of RXJ1257+4738 cluster obtained with the TF tuned at 8980.5 Å before subtraction of the sky rings (*left*), the background sky map created by the tringSub2 task (*centre*), and the same image after the subtraction of the sky rings (*right*).

In this case, only the first three steps, corrections for bias and flat fielding with usual procedures, cosmic rays removal by including the `crreject` option in the combine task, and the sky rings subtraction have been performed. The result of the sky ring subtraction for this cluster is given in Figure 3.4. Images of this cluster are significantly affected by fringing patterns and therefore fringing reduction has to be performed before proceeding to the following steps. However, fringing reduction of TF data is very time consuming, and due to the time constraints during this PhD work we were not able to go through it. We are however planning to continue with it in near future, after thesis defence.

## 3.2 Generating the catalogues of sources

In this section, we produce catalogues of preliminary sources first by initial detection followed by the photometry of the sources and then by extracting the pseudo-spectra. A pseudo-spectrum is a file consisting of tuples with wavelength ( $\lambda$ ) at source position and flux value. It differs from a standard spectrum produced

by dispersive medium in that it's flux at each point results from integrating within a passband of the filter centred at the point's wavelength as depicted in [Sánchez-Portal et al. \(2015\)](#). We generate the catalogues of candidate sources, by using two routines in TFRed: namely `tsex` and `tespect`. We first generate the raw sources catalogue by running `SExtractor` on the deep images and performing photometry on the degraded images obtained in Section 3.1.1.7. Here the catalogues of the combined images from Section 3.1.1.5 are used (325/298 for H $\beta$ ; 1301/1162 for [OIII] in centre/offset positions respectively) as an input. For this procedure, the `SExtractor` configuration file, the parameters list file and an average seeing list file are also required, and are described as follows:

1. **SExtractor configuration file.** This file contains the majority of the parameters that `SExtractor` is going to use as an input. These parameters may be default, or they may depend on the property of the images, the configuration of the CCD or the output intended. Configuration parameter values used in this work are given in Table 3.1.
2. **Parameters list file.** This file contains column names or parameters to be measured with `SExtractor` and contained in the output catalogue. Eight parameters have been measured in this case to form an input catalogue for `tespect` task. They are given in Table 3.2. We used four aperture diameters for photometry starting with 7.8 with steps of 3.9 pixels.
3. **Average seeing list file.** This is a single file containing a list of average seeing measured in each image by running the TFRed task `tfwhm`.

Correctly performing this step results in a raw catalogue of parameters plus the slice number for all the objects detected in every scan slice. This raw catalogue is then used as an input to a `tespect` task. The `tespect` task prepares a FORTRAN program and operates by executing. Its operation starts with recording the observation in memory, then inspecting the lines looking for matches with the stored position, and writes the contents of the memory to the files when found in all the slices. During this, `tespect` omits the objects with negative fluxes. Finally, the task cleans the memory and repeats the procedure. A correct final operation of `tespect` task results with 14 text catalogue files: eight for star-like and six for non-star-like sources, where we used only two of the catalogue files (flux and flux\_error of the non-star-like sources). The 14 resulting table files are described as follows:

**Table 3.1:** Description of the parameters used in **SExtractor** configuration file.

Parameter	Value	Description
CATALOG_TYPE	ASCII_HEAD	# Name of the output catalogue
DETECT_TYPE	CCD	# Type of device that produced the image
DETECT_MINAREA	7	# minimum number of pixels above threshold
DETECT_THRESH	3.0	# Relative detection threshold with respect to the background rms
ANALYSIS_THRESH	3.0	# Threshold value at which FWHM functions in $mag.arcsec^{-2}$
DEBLEND_NTHRESH	64	# Number of de-blending sub-thresholds
DEBLEND_MINCONT	0.0002	# Minimum contrast parameter for de-blending
CLEAN_PARAM	1.0	# Cleaning efficiency of spurious detections
PHOT_APERTURES	7.8,11.7, 15.6,19.5	# Aperture diameter(s) in pixels for the photometry
SATUR_LEVEL	55000.0	# Saturation level (in ADUs)
SATUR_KEY	SATURATE	# keyword for saturation level (in ADUs)
GAIN	0.95	# Detector gain in $e^-/ADU$
GAIN_KEY	GAIN	# keyword for detector gain in $e^-/ADU$
PIXEL_SCALE	0.254	# size of pixel in arcsec
SEEING_FWHM	1.15	# Average stellar FWHM of the images in arcsec

**Table 3.2:** Parameters measured by **SExtractor** to be used as an input for **tespect** task

Parameter	Description
NUMBER	Ordered Id number
X_IMAGE	X coordinate (in pixels)
Y_IMAGE	Y coordinate (in pixels)
FLUX_APER(4)	Flux within the four fixed apertures (in ADUs)
FLUXERR_APER(4)	The aperture flux RMS error (in ADUs)
ELLIPTICITY	Ellipticity $(1 - \frac{b}{a})^1$ of the profile
FWHM_IMAGE	Full width at half maximum of the profile (in pixels)
CLASS_STAR	Star/Galaxy classifier output
FLAGS	Indicator for detection or photometry problems

<sup>1</sup> 'a' is the length of the major axis, while 'b' is the minor axis length.

1. **Tables of parameters.** This consists of `SExtractor` measured parameters of every source in each slice.
2. **Tables of the mean values of the parameters.** Each of this tables contains the appropriate flux aperture, the wavelength correction, the number of observations, and averaged value of each `SExtractor` measured parameter.
3. **Flux tables.** Consist of two files each containing the fluxes extracted for each source in each slice.
4. **Flux error (noise) tables.** This comprises of two files each containing the flux error for each source in each slice.
5. **Signal to noise ratio files.** These are files each containing the ratio of flux to the corresponding error of each source.
6. **Position files:** Two separate files only consisting of the position and number of observation of each source.  
  
Note that the number of tables in each of the above outputs are two: one for star-like-sources and the other is for non-star-like sources.
7. **Flux to reference flux ratio.** This is a single table only for star-like sources that contains the flux of each source in a slice to the flux of the same source in the reference slice.
8. **Flux error to reference flux error ratio.** A single table for star-like sources that contains the error in flux of each source in a slice to the flux error of the same source in the reference slice.

Each line of the two catalogues used (`flux` and `flux_error` files of non-star-like sources) contain the pseudo-spectra that is not calibrated and the corresponding error in flux respectively for each source. For `[OIII]` centre position, out of the total of 758 sources extracted, we have 724 non-star-like sources with measured flux and the `flux_error` files, 34 sources being star-like sources. Similarly, for `[OIII]` offset position, 1168 sources remain non-star-like out of 1355 detected sources, and 187 are star-like.

The same task applied on  $H\beta$  centre position data resulted in 945 non-star-like sources out of 966 extracted ones while 21 are star-like. In  $H\beta$  offset position, 1277 sources are identified as non-star-like sources with fluxes and `flux_error` values, with

64 sources being star-like. For each of the four cases, by cross matching the flux catalogue (non-star-like sources) with the corresponding astrometric catalogue we determined the sky coordinates. With these performed, we had catalogues of sources with measured fluxes and flux\_errors (with sky coordinates) to be used in the calibration process.

### 3.3 Wavelength and flux calibration

In performing the calibration of the results of our data reduction the first thing is to accurately determine the wavelength of observation of each source at each slice by performing the wavelength calibration. To do this, the position of the optical centre has been first determined in all images. Then we compute the effective wavelength using Equations 2.2 and 2.3, after having the source position, the coordinates of the optical centre, and the central wavelength ( $\lambda_0$ ) at which the TF was tuned in each image. We considered that solution converges for consecutive wavelength difference lower than  $1 \text{ \AA}$ , since the TF tuning precision is  $\sim 1 \text{ \AA}$  (Sánchez-Portal et al., 2015).

We went through two steps in performing the flux calibration of each TF tune. First we derived the total efficiency  $\epsilon(\lambda)$  (Sánchez-Portal et al., 2015) of the system (telescope, optics and detector). The total efficiency  $\epsilon(\lambda)$  then is determined by Equation 3.2 as:

$$\epsilon(\lambda) = F_m(\lambda)/F_p(\lambda), \quad (3.2)$$

where  $F_m(\lambda)$  is a measured flux while  $F_p(\lambda)$  is a published flux at a given wavelength for set of the spectrophotometric standard stars. The exposures are taken within compatible tunes (ideally at the same tunes) to that of the cluster observations. The spectrophotometric standard stars used in our observations are given in Table 3.3.

**Table 3.3:** Spectrophotometric standard stars

Name	Mag ( $\lambda$ , $\text{\AA}$ )	Reference	Position
G158-100	14.87 (5400)	Filippenko and Greenstein (1984)	centre
L1363-3	13.28 (5560)	Oke (1974)	centre
Feige 110	11.82 (5556)	Massey and Gronwall (1990)	centre
G191-B2B	11.72 (5460)	Oke (1990)	offset
G157-34	15.35 (5400)	Filippenko and Greenstein (1984)	offset

For the standard stars, the fluxes ( $F_m(\lambda)$ ) are determined by aperture photometry by using Equations 2.2 and 2.3 to derive their actual position. At corresponding wavelengths, the published fluxes ( $F_p(\lambda)$ ) are determined using fitting a polynomial to the magnitudes in Table 3.3.

The final step in flux calibration is to convert the flux that we extracted directly from the image to physical units since the flux measured is in Analog to Digital Unit (ADU) (Sánchez-Portal et al., 2015). The flux is then converted from ADU to physical unit of  $ergs^{-1} cm^{-2} \text{Å}^{-1}$  using the following:

$$F_m(\lambda) = F_{ADU}(\lambda) \frac{g K(\lambda) E_\gamma(\lambda)}{t A_{tel} \delta\lambda_e}, \quad (3.3)$$

where  $g$  denotes the CCD gain in  $e^{-1} ADU^{-1}$ ,  $E_\gamma(\lambda)$  stands for the energy of a photon in  $ergs$ ,  $t$  is the exposure time in seconds,  $A_{tel}$  is the area of the primary mirror of the telescope in  $cm^2$ ,  $\delta\lambda_e$  is the effective passband width given by Equation 3.4 measured in  $\text{Å}$ , and  $K(\lambda)$  is the correction for atmospheric extinction given by an Equation 3.5:

$$\delta\lambda_e = \frac{\pi}{2} FWHM_{TF}, \quad (3.4)$$

$$K(\lambda) = 10^{0.4k(\lambda)\langle\chi\rangle}. \quad (3.5)$$

We can see that  $K(\lambda)$  depends on the extinction coefficient  $k(\lambda)$  and the average airmass of the observations given by  $\langle\chi\rangle$ . For our work,  $k(\lambda)$  can be estimated by the extinction curve fitting of La Palma in the concerned wavelength range. For each source at each single  $i^{th}$  exposure, having the total efficiency  $\epsilon(\lambda)$  already estimated, we can convert the measured flux  $f_{ADU}(\lambda)_i$  in ADUs to actual flux in  $ergs^{-1} cm^{-2} \text{Å}^{-1}$  as (see Sánchez-Portal et al., 2015):

$$f_m(\lambda)_i = f_{ADU}(\lambda)_i \frac{g K(\lambda) E_\gamma(\lambda)}{\epsilon(\lambda) t A_{tel} \delta\lambda_e}. \quad (3.6)$$

The errors in flux measurement are computed by propagation given by:

$$\Delta f = (A_{pix} \sigma^2 + f/g)^{\frac{1}{2}}, \quad (3.7)$$

where  $A_{pix}$  stands for the measurement aperture area in pixels,  $\sigma$  is the standard deviation of the background noise, and  $g$  is the gain in  $e^{-1} ADU^{-1}$ .

# Chapter 4

## Morphology of galaxies in galaxy clusters

1

### 4.1 Introduction

The structural and morphological properties of a galaxy are important tracers of its evolutionary stage. Thus, the correlation of the morphology (and/or SF activity) of the clusters' galaxies with the local density provides valuable information on the stage of in-fall at which galaxies experience the bulk of their transformations. To explore these relations, it is important to perform wide-area surveys (to study the density-dependent effects) in clusters that span a range of redshifts (to assess the evolution with cosmic time).

With a currently overgrowing amount of observational astronomical data, the visual inspection method (Section 1.4.1) is not the most appropriate or even not feasible for morphologically classifying high-redshift galaxies. Modern classification techniques include galaxy fitting algorithms, which can give reliable results for a large number of galaxies in a relatively shorter period and with minimal human resources. To deal with the vast and growing amount of astronomical data currently available, machine learning techniques employing Convolutional Neural Networks (CNN) are widely under use for morphological classification of galaxies

---

<sup>1</sup>The results presented in this chapter have been published in [Beyoro-Amado et al. \(2019\)](#)



(e.g., Banerji et al., 2010; Kuminski et al., 2014; Dieleman et al., 2015; Huertas-Company et al., 2015; Aniyani and Thorat, 2017; Domínguez Sánchez et al., 2018; Lukic et al., 2018).

Modern galaxy classification methods can either be *parametric* or *non-parametric*. *Parametric methods* use some parameters of the galaxies to classify them by fitting (one or two dimensional) mathematical models to their images assuming some predefined parametric model. In this approach the Sérsic profile (Sérsic, 1963) and a two-component profile (bulge + disk decomposition) are the commonly used models. The classification is obtained by fitting a one- or two- component profile as described in detail by Simard et al. (2002) and Peng et al. (2002). Simard et al. (2011) have performed a classification of 1.12 million galaxies using a bulge + disk decomposition approach with SDSS data release seven (Abazajian et al., 2009). In addition to this, a structural and morphological catalogue of 45 million sources has been presented by Tarsitano et al. (2018) with the Dark Energy Survey (Dark Energy Survey Collaboration et al., 2016) data of the first year observation employing both a single Sérsic parametric fits and non-parametric methods. The parametric method is generally useful since it gives a complete set of parameters describing the quantitative morphology. Since a large number of parameters need to be fitted, the results may be degenerated as shown in Huertas-Company et al. (2007). Degeneracy occurs as a result of correlation between parameters, the results of the local minima in the parameter space of the chi-square minimization, or by numerical divergence in the process of fitting (Peng et al., 2002; Peng et al., 2010a). The peculiar characteristic of the parametric method is the assumption that a galaxy is described well by a simple analytic model although this does not always work for well resolved as well as irregular and merging/interacting galaxies.

On the other hand, the *non-parametric* approach does not assume any specific analytic model and is performed on the basis of measuring a set of well-chosen observables. The effects of seeing, being one of the major challenges in galaxy fitting, are not included in non-parametric measurements unlike the parametric ones where the assumed mathematical model is convolved with the PSF. The non-parametric method was introduced for the first time by Abraham et al. (1994, 1996) with the definition of two observables: the Abraham concentration index and asymmetry. A third quantity, namely smoothness, was introduced by Conselice et al. (2000, 2003). The classification has been further enhanced with additional

observables: the GINI coefficient (Abraham et al., 2003), M20 moment of light (Lotz et al., 2004), and Conselice-Bershady concentration index (Conselice et al. 2000; Bershady et al. 2000). These six parameters, together with ellipticity are described in more details in subsection 4.2.1.3. *Non-parametric* methods are in advantage when classifying large sample of galaxies at higher redshifts, even for low resolution data (e.g., Scarlata et al., 2007; Tasca et al., 2009; Pović et al., 2009, 2013, 2015; Pintos-Castro et al., 2016; Beyoro-Amado et al., 2019). Furthermore, no analytic predefined profile is required in this approach.

In this work, we apply a *non-parametric* classification method to ZwCl0024+1652 as described in Section 4.2.1.4. This cluster has been extensively studied by several groups (e.g., Morrison et al., 1997; Broadhurst et al., 2000; Kneib et al., 2003; Treu et al., 2003; Moran et al., 2007; Geach et al., 2009; Natarajan et al., 2009; Sánchez-Portal et al., 2015). Although this cluster has been deeply studied in some aspects, a visual morphological classifications has been performed for a limited number (214) of member galaxies within a clustercentric distance extending to 5 Mpc (Moran et al., 2007). Only 66 galaxies have been classified within 1 Mpc radius ( $\simeq 31\%$  of the total sample). While for RXJ1257+4738 and the Virgo cluster we use GLACE data (Pintos-Castro et al., 2016) and public data (Kim et al., 2014), respectively.

In our present work for morphological classification, we use a *non-parametric* method called *galSVM* introduced by Huertas-Company et al. (2008). *galSVM* fits a number of parameters simultaneously and assigns probabilities for each galaxy to be classified. Then based on the probabilities, the galaxies are classified into two broad morphological classes, namely ET and LT. For more details about this classification, we refer the reader to Section 4.2.1.5.

This chapter is organized into three general and three specific sections, where Section 4.2, Section 4.3 and Section 4.4 are sections specific to each redshift cluster; while Section 4.1, Section 4.5 and Section 4.6 are general sections discussing across all the the three clusters. Section 4.2 focuses on the detailed morphological analysis of ZwCl0024+1652 galaxy cluster at  $z \sim 0.4$ . In section 4.3 the analysis of the morphology of galaxies in RXJ1257+4738 cluster is presented. Then in section 4.4, the analysis of the galaxy properties related to morphologies of galaxies in the Virgo cluster is performed. The comparison of the galaxy properties in relation to morphology is done across the three clusters in section 4.5. Finally, the overall concluding remarks for this chapter are presented in section 4.6.

## 4.2 Morphological properties of galaxies in ZwCl0024+1652

### 4.2.1 Morphological classification

In this section we describe in details the morphological classification of selected ZwCl0024+1652 cluster members. We first go briefly through the methodology used, obtained results, and final classification.

#### 4.2.1.1 Methodology

In this work we used the `galSVM`<sup>2</sup> code (Huertas-Company et al., 2008) for classifying morphologically galaxies in the ZwCl0024+1652 cluster. `galSVM` is a public code that uses the free library `libSVM` (Chang and Lin, 2011) and works in IDL environment. It has been successfully tested previously, at different redshifts, and on both field and cluster galaxies (e.g., Huertas-Company et al., 2009, 2010, 2011; Pović et al., 2012, 2013, 2015; Pintos-Castro et al., 2016).

Briefly, `galSVM` uses a training sample of local galaxies with known visually classified morphology (see Section 4.2.1.2), for classifying the real sample (in this case the ZwCl0024+1652 cluster members). It consists of several steps. First, it simulates local galaxies, by placing them to the redshift and magnitude distributions characteristic of the real sample. Secondly, it drops simulated local galaxies into the background that corresponds to the real sample image. Third, it measures different morphological parameters (see Section 4.2.1.3), first of the simulated local sample, and then of the real sample of galaxies that we want to classify. Finally, it compares morphological parameters of the training simulated local galaxies with their known visual classification, and determines conditions inside the multiple-parameters space that are then applied to the real sample to be classified. The final classification is based on a number of Montecarlo simulations, where each simulation gives a probability that the galaxy is ET. The average probability ( $P_{avg}$ ) and measured error give the final classification that the galaxy is ET. The probability that galaxy is LT will be then  $1 - P_{avg}$ . For all details regarding `galSVM` see Huertas-Company et al. (2008).

---

<sup>2</sup>galaxy Support Vector Machine

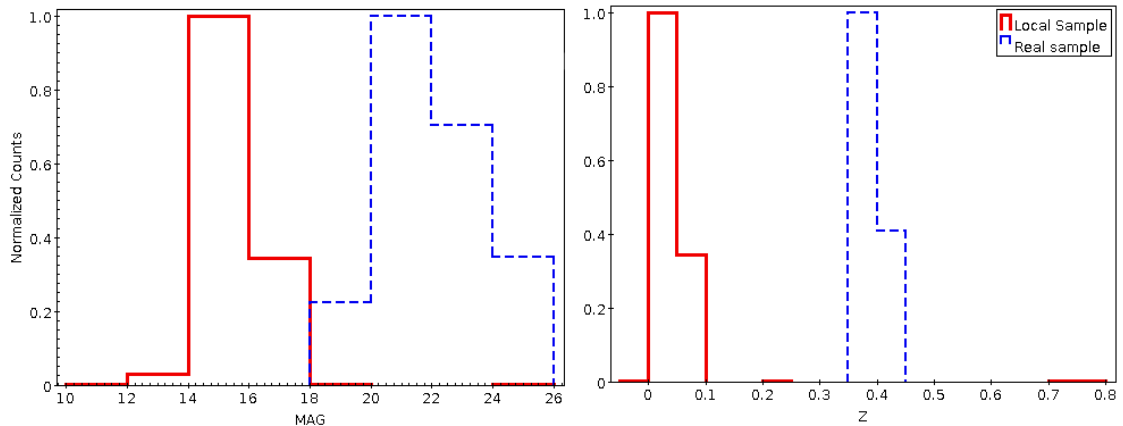


**Figure 4.1:** Magnitude (**left plot**) and redshift (**right plot**) distributions of the local training sample with known morphology (red solid lines) and the real ZwCl0024+1652 sample that should be classified (blue dashed lines).

#### 4.2.1.2 Training sample of local galaxies

We used a catalogue of 3000 visually classified local galaxies, with known redshifts and magnitudes. The sample was selected randomly from the [Nair and Abraham \(2010\)](#) catalogue of visual morphology consisting of about 14000 galaxies taken from the Sloan Digital Sky Survey DR4 data. The redshift distribution of our local sample is in the range 0.01-0.1, and most of the galaxies are bright with r band magnitude between 13 and 17. The magnitude and redshift distributions of the used local training sample vs. that of the real data are shown in the two plots of [Figure 4.1](#), while the detailed description of the training local sample can be found in [Pović et al. \(2013\)](#). The training sample of 3000 local galaxies was selected as a good compromise between the computing time and accuracy in classification (both being highly sensitive to the training sample size). In addition, equal number of ET and LT galaxies were taken into account to obtain more precise morphology, and the selected sample can be considered as representative of the whole data with respect to general galaxy properties, as shown in [Pović et al. \(2013\)](#).

#### 4.2.1.3 The measured morphological parameters

For classifying the cluster galaxies, we have measured seven morphological parameters: one parameter comes from **SExtractor**, and the remaining six parameters by using **galSVM**. The parameters measured are used simultaneously to train the SVM for classifying the galaxies. These parameters are usually used in non-parametric

methods for the galaxy morphological classification. A brief description of each of the parameters measured in our process is given below.

- **Ellipticity (ELLIP)**. This is one of the parameters used in classifying galaxies into different morphological classes. Ellipticity is defined as:

$$ELLIP = 1 - \frac{b}{a}, \quad (4.1)$$

where  $b$  stands for the length of the minor axis, and  $a$  denotes the length of the major axis. ELLIP is the parameter that is measured by running SExtractor on the real data (while creating the input catalogue to be used).

- **Asymmetry (ASYM)**. This is a morphological parameter measuring the degree of rotational symmetry of the light of a particular galaxy (see Abraham et al. (1996, 1994) and Conselice et al. (2003)). It is mathematically computed by subtracting a 180° rotated image of a galaxy from the original image of the galaxy before rotation:

$$ASYM = \frac{1}{2} \left( \frac{\sum (|I(i, j) - I_{180}(i, j)|)}{\sum I(i, j)} - \frac{\sum (|B(i, j) - B_{180}(i, j)|)}{\sum I(i, j)} \right), \quad (4.2)$$

where  $I(i, j)$  stands for the flux of the original image while  $I_{180}(i, j)$  denotes the flux of the rotated image by 180°. On the other hand,  $B(i, j)$  stands for the flux of the background image while  $B_{180}(i, j)$  denotes the flux of the rotated background image by 180°. The index  $(i, j)$  is for pixel position to vary.

- **Abraham Concentration (CABR)**. This parameter was defined by Abraham et al. (1996, 1994) as the ratio of fluxes of the inner isophote to that of the outer isophote. For our computation of CABR we take the outer isophote with 90% of the total flux and the inner isophote with 30% of the total flux. It can be written mathematically as:

$$CABR = \frac{\sum \sum_{i,j \in (0.3)} I(i, j)}{\sum \sum_{i,j \in (0.9)} I(i, j)}, \quad (4.3)$$

where  $I(i, j)$  stands for the pixel index of the original image.

- **GINI Coefficient (GINI)**. The GINI coefficient is a statistical term derived from the Lorentz curve (Abraham et al., 2003; Lotz et al., 2004). It

specifies the overall distribution function of the pixel values  $i$  of the galaxy. Taking  $N$  to be the total number of pixels of the galaxy,  $X_i$  being the value of the pixel flux, and with  $|\bar{X}|$  being the mean throughout the whole pixel values, the GINI coefficient is computed as:

$$GINI = \frac{1}{|\bar{X}|N(N-1)} \sum_i^N (2i - N - 1) |X_i|. \quad (4.4)$$

- **Smoothness or clumpiness (SMOOTH).** As described by [Conselice et al. \(2003, 2000\)](#), this parameter quantifies the galaxy's small scale structure. In this case we make the image to be smooth using a box having a width of one quarter of the Petrosian radius ( $r_p$ ), and then the smoothed image is subtracted from the original image. The value of smoothness is calculated as:

$$SMOOTH = \frac{1}{2} \left( \frac{\sum (|I(i, j) - I_S(i, j)|)}{\sum I(i, j)} - \frac{\sum (|B(i, j) - B_S(i, j)|)}{\sum I(i, j)} \right), \quad (4.5)$$

where  $I$  and  $B$  are defined in Equation 4.2 while the subscript  $S$  stands for the smoothed image.

- **$M_{20}$  moment of light (M20).** As described in [Abraham et al. \(2003\)](#) and [Lotz et al. \(2004\)](#),  $M_{20}$  stands for the second order moment of the 20% brightest pixels of the galaxy that is normalised and is given by:

$$M_{20} = \log \frac{\sum_i^n M_i}{M_{total}}, \quad (4.6)$$

where  $n = \sum f_i < 0.2f_{total}$ , and  $f_i$  being the flux at  $i$  pixel. If  $(x_i, y_i)$  stands for the each pixel coordinate and  $(x_c, y_c)$  be the coordinate of the centre of the galaxy, then the total second order moment over all the existing pixels is given by:

$$M_{total} = \sum_i^N f_i \left[ (x_i - x_c)^2 + (y_i - y_c)^2 \right]. \quad (4.7)$$

Using the value of  $M_{20}$ , one can get a clue about the spatial distribution of any bright core, any bar, or arm and off-centre star cluster.

- **Bershady-Concelice concentration index (CCON).** As defined in [Bershady et al. \(2000\)](#), this parameter is defined as the ratio of the circular radius ( $r_{20}$ ) containing 20% of the total flux to the radius ( $r_{80}$ ) containing 80% of

the total flux of the galaxy. More specifically, CCON is defined as:

$$CCON = 5 \log \frac{r_{80}}{r_{20}}. \quad (4.8)$$

Note that for all our parameters, the total flux is defined as the amount of flux contained within 1.5 times the Petrosian radius ( $r_p$ ). It can be referred from [Huertas-Company et al. \(2008\)](#) that Petrosian radius is measured by running `SExtractor` on the image. Moreover, one can determine the centre of the galaxy by minimizing the ASYM index.

The above morphological parameters have been measured for our galaxies of the low redshift local training sample as well as the intermediate redshift cluster galaxies intended to be classified using the `galSVM` technique.

#### 4.2.1.4 `galSVM` applied to ZwCl0024+1652

To measure the morphologies of the ZwCl0024+1652 cluster members, we run `galSVM` on the HST/ACS F775W image described in Section 2.2.3.1 and used the `SExtractor` catalogue of 255 sources with all needed input parameters and redshifts available (see Chapter 2). We went through all `galSVM` steps described in Section 4.2.1.1, using the 3000 SDSS local galaxies as a training sample (see Section 4.2.1.2). We measured all parameters described in Section 4.2.1.3 of both training and real samples. For the final classification we run 15 Montecarlo simulations, where in each simulation we used 2000 different randomly selected local galaxies (out of 3000) with the same number of ETs and LTs.

Taking into account previous results obtained in [Pović et al. \(2013\)](#), dividing a sample into different magnitude ranges can increase the accuracy of the morphological classification by optimizing the `galSVM` code for fainter galaxies to be classified. Therefore, in this work to classify ZwCl0024+1652 cluster members we run `galSVM` three times, using the following ranges of `SExtractor` MAG\_AUTO magnitude in F775W band:

1.  $F775W \leq 22.0$  (137 galaxies),
2.  $F775W \leq 24.0$  (216 galaxies), and
3.  $F775W \leq 26.0$  (255 galaxies).

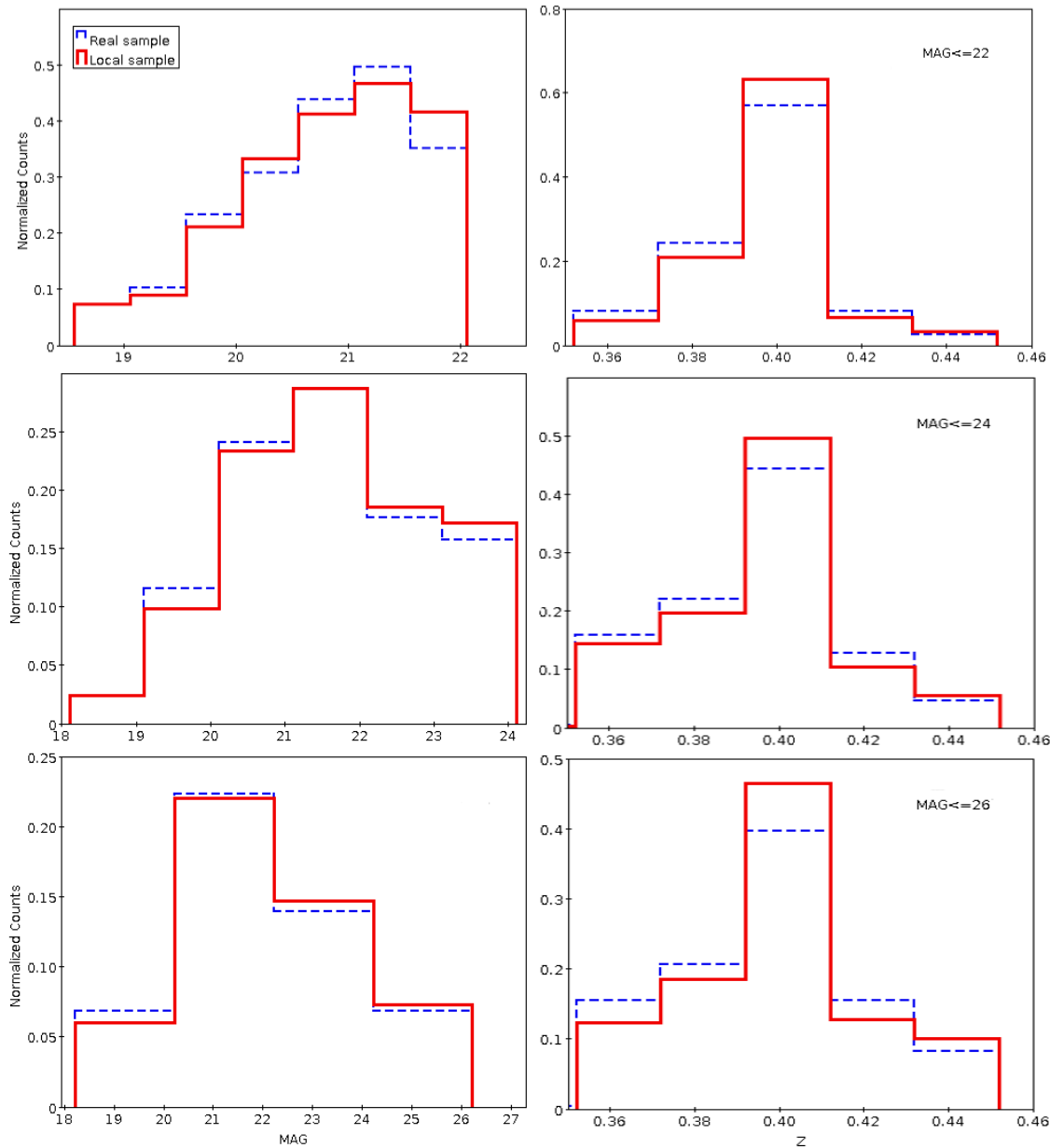


**Figure 4.2:** Magnitude (left plots) and redshift (right plots) distributions of our real data (blue dashed lines) and the simulated local sample (red solid lines). The distributions are plotted for  $F775W \leq 22.0$  (top plots),  $F775W \leq 24.0$  (middle plots), and  $F775W \leq 26.0$  (bottom plots).

For each range we provided the corresponding magnitude and redshift distributions of cluster members for moving the local training sample to the same once during the classification process. These distributions are shown in Figure 4.2 for both training sample after being simulated and the real sample to be classified. As can be see in all plots, after being simulated, local galaxies are following distributions of the higher-redshift cluster sample. As in Pović et al. (2013), in the



**Table 4.1:** The final measured probability (PROBA\_FINAL) values, for the galaxy to be an ET, in the three magnitude ranges

	Median	[Q1 - Q3]
$F775W \leq 22.0$	0.745	0.263 - 0.877
$22.0 < F775W \leq 24.0$	0.474	0.170 - 0.727
$24.0 < F775W \leq 26.0$	0.478	0.271 - 0.569

**Table 4.2:** The final measured probability errors (PROBA\_ERROR), for the galaxy to be an ET, in the three magnitude ranges

	Median	[Q1 - Q3]
$F775W \leq 22.0$	0.044	0.030 - 0.067
$22.0 < F775W \leq 24.0$	0.045	0.032 - 0.059
$24.0 < F775W \leq 26.0$	0.069	0.054 - 0.122

final classification we considered the results from the first magnitude bin, then from the second, but only for those sources not present in the first one (i.e., with  $22.0 < \text{MAG\_AUTO} \leq 24.0$ ), and finally from the third bin, but only for those sources not present in the previous two ( $24.0 < \text{MAG\_AUTO} \leq 26.0$ ). In all three bins the final averaged probabilities and their errors for a galaxy to be ET were measured through 15 Montecarlo simulations.

#### 4.2.1.5 Final classification

Finally, we obtained PROBA\_AVG with the corresponding uncertainty values for 231 galaxies (111 with spectroscopic and 120 with photometric redshifts), out of 255. For the remaining 24 galaxies, PROBA\_AVG was not measured either because one or more parameters have values out of the allowed range, or they simply were not measured by `galSVM`. Taking into account previous experiences with `galSVM`, and current image inspections, most of these sources are either located close to the image border or have close companions. Tables 4.1 and 4.2 give the median values and Q1-Q3 ranges<sup>3</sup> of average probability and its error in three magnitude bins. It can be seen that most of the brightest galaxies ( $F775W \leq 22.0$ ) are characterized by larger probability values (closer to 1), characteristic of ETs, while for fainter galaxies final probabilities are more centred around 0.5. Moreover, the probability error values are larger for the faintest galaxies than the most brightest ones, as can be seen in Table 4.2.

<sup>3</sup>Q1 and Q3 stand for first and third quartile, respectively.

**Table 4.3:** Final classification of the ZwCl0024+1652 cluster members

	<b>ET</b>	<b>LT</b>	<b>UD</b>	<b>Total</b>
$F775W \leq 22.0$	68 (55%)	39 (32%)	16 (13%)	123
$22.0 < F775W \leq 24.0$	23 (32%)	29 (40%)	20 (28%)	72
$24.0 < F775W \leq 26.0$	6 (17%)	15 (42%)	15 (41%)	36
<b>Total</b>	<b>97</b>	<b>83</b>	<b>51</b>	<b>231</b>

For the final classification we took into account the measured errors and considered a galaxy to be ET if  $\text{PROBA\_FINAL} \equiv \text{PROBA\_AVG} \pm \text{PROBA\_ERR} > 0.6$  (or 0.7 in the last magnitude bin), and to be LT if  $\text{PROBA\_FINAL} < 0.4$  (or 0.35 in the last magnitude bin). For those galaxies with  $0.4 < \text{PROBA\_FINAL} < 0.6$  (or between 0.35 and 0.7 in the last magnitude bin) we are not able to classify them morphologically, and remain inside the 'undecided class' (UD). For placing the classification boundaries, we used previous works of [Pović et al. \(2012, 2013\)](#) and [Pintos-Castro et al. \(2016\)](#). Figure 4.3 shows the  $\text{PROBA\_FINAL}$  distributions in the three magnitude ranges, while the final classification is summarised in Table 4.3. As can be seen, out of a total of 231 galaxies with measured final probabilities, we have 97 (42%), 83 (36%), and 51 (22%) galaxies classified as ET, LT, and UD, respectively. Figure 4.4 shows the  $\text{PROBA\_FINAL}$  of the whole classified sample.

## 4.2.2 Morphological analysis

### 4.2.2.1 Comparisons with visual morphological classification

The visual morphological classification of 214 galaxies with spectroscopically confirmed redshifts in ZwCl0024+1652 was carried out previously by [Moran et al. \(2007\)](#), covering the clustercentric distance of 5 Mpc. In this section we compared our non-parametric classification of 231 galaxies, within the clustercentric distance of 1 Mpc (see Section 2.2.3.1), with the visual one. Within the region of our data ( $\sim 1 \text{ Mpc}$  radius) there are 111 sources with spectroscopically confirmed redshifts having visual morphology from [Moran et al. \(2007\)](#). We cross-matched the two catalogues using the radius of 2 arcsec, and found in total 63 counterparts. The reason of a small number of counterparts is related with the covered clustercentric distances in the two classifications, and the fact that [Moran et al. \(2007\)](#) visual classification only considers the best resolved galaxies. The I-band magnitude

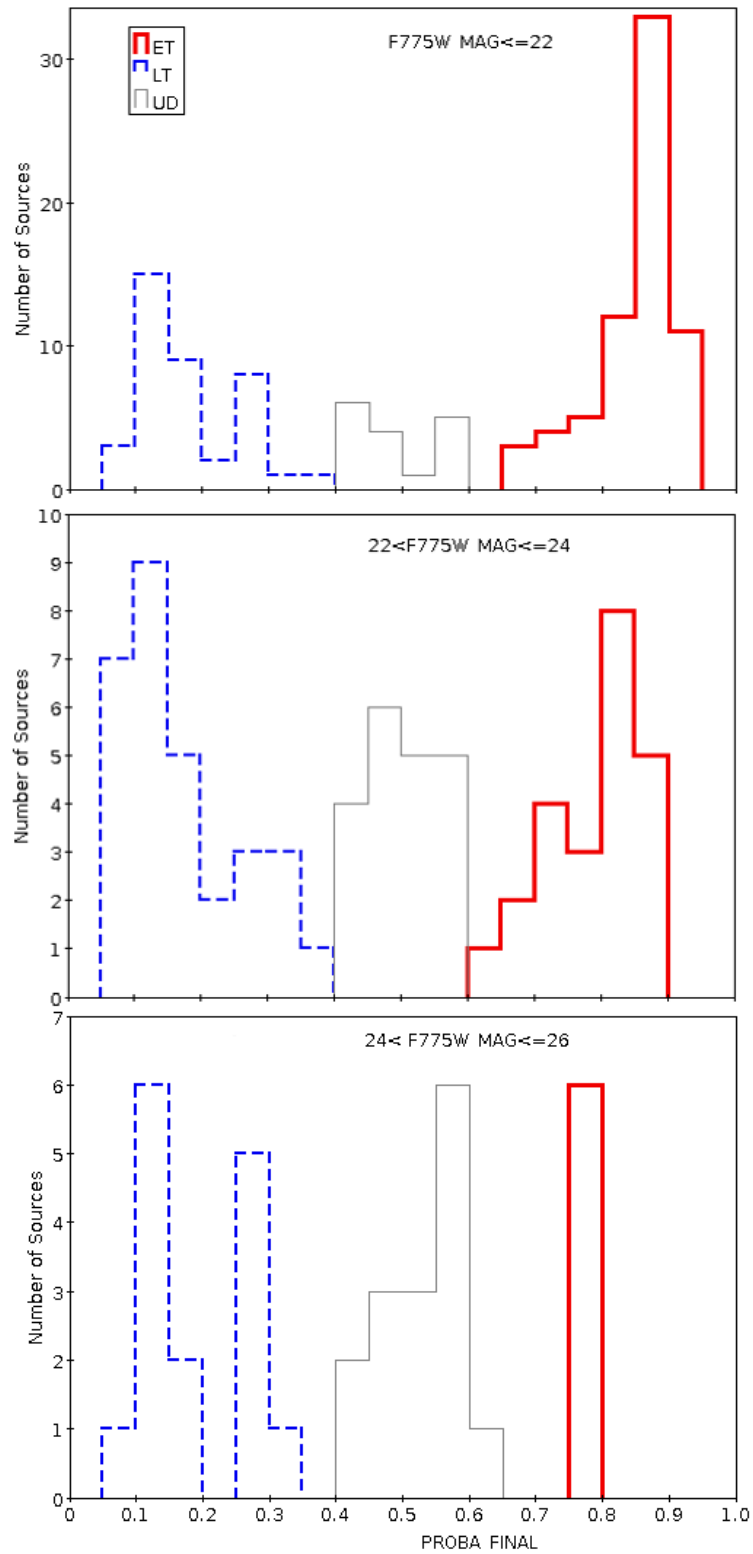


**Figure 4.3:** Final error-corrected probability distributions of all galaxies classified as ET (red thick solid lines), LT (dashed blue lines), and UD (grey thin solid lines) in the three magnitude ranges.

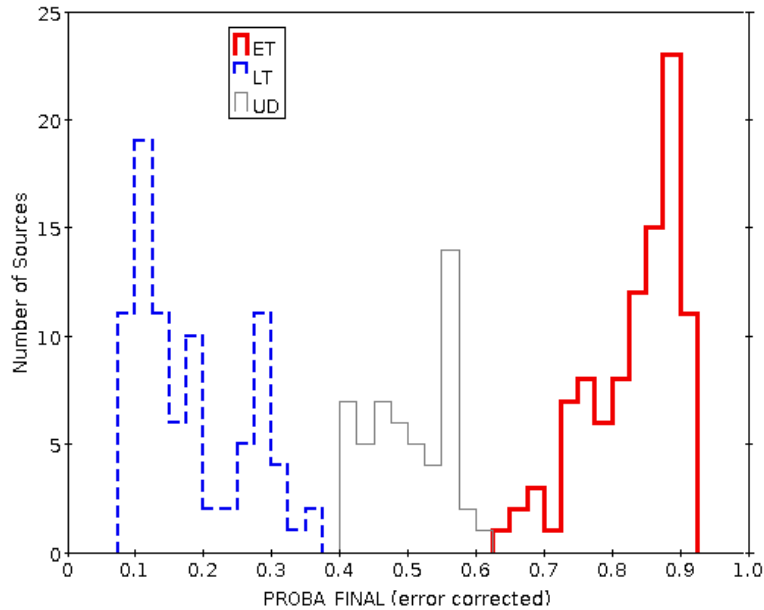


**Figure 4.4:** Final error-corrected probability distributions of all ET (red thick solid lines), LT (dashed blue lines), and UD (grey thin solid lines)

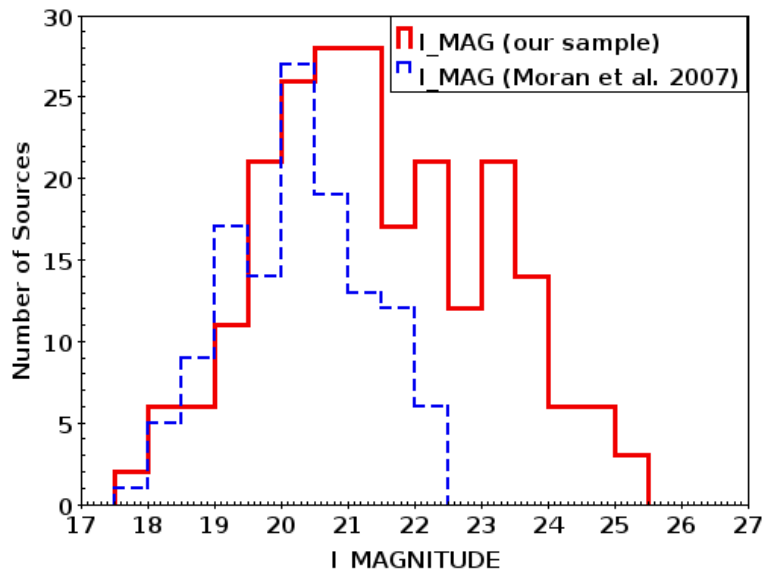


**Figure 4.5:** Comparison between the I band magnitude (red solid line) of our sample galaxies classified in this work using ga1SVM and the I band magnitude of Moran et al. (2007) visually classified cluster members (blue dashed line).

limit of galaxies in Moran et al. (2007) is 22.3, with 201 (95%) of galaxies being brighter than  $I = 22$ , whereas our classification using the F775W\_MAG goes up to 26 in magnitude. The I\_magnitude distribution comparison of both works is given in Figure 4.5 and the statistical comparison is shown in Table 4.4.

Out of 63 counterparts, 47 and 16 galaxies were classified visually by Moran et al. (2007) as ET and LT, respectively. When compared with our results, 52 galaxies,

**Table 4.4:** The I band magnitude comparison between our sample and [Moran et al. \(2007\)](#) visually classified sample within similar region (about  $\sim 1$  Mpc radius) giving the median and the [Q1 - Q3] range

Sample data	Median	[Q1 - Q3]
I_MAG (Ours)	21.21	20.27 - 21.81
I_Mag (Moran07)	20.20	19.40 - 21.00

or 82.54%, match the visual classification, of these 40 being classified as ET, and 12 as LT. Of the remaining 11 galaxies, 5 have visual classification available, but were classified as UD in our work, while for the other 6 galaxies the ET/LT classification is in disagreement between the two works.

Finally, after these comparisons we can conclude that 82.54% of our classification is in a good agreement with the visual classification. Moreover, in this work we provide a reliable classification of additional 117 galaxies within 1 Mpc of cluster-centric distance, being classified for the first time.

#### 4.2.2.2 Morphological parameters

The distributions of different measured morphological parameters of 180 ET and LT classified cluster members are given in Figure 4.6. In addition to the histograms, Table 4.5 summarizes the median values of each parameter and Q1–Q3 range characteristic of cluster members classified as ET or LT. As can be seen from both Figure 4.6 and Table 4.5, all parameters follow the expected trends of ET and LT galaxies, with concentration indices such as CABR, CCON and GINI being characterised with higher values in case of ETs, while ASYM, M20, and ELLIP are showing higher values for LTs. If we compare our results with those obtained by [Pović et al. \(2013\)](#), using the same methodology and data of the ALHAMBRA survey ([Moles et al., 2008](#)) in F613W band, ZwCl0024+1652 galaxies classified as ET seem to be slightly more concentrated (in terms of all concentration indices), and characterised with lower asymmetries in the case of both ET and LT.

#### 4.2.2.3 Morphological diagnostic diagrams

In this section, we tested some of the commonly used morphological diagnostic diagrams by comparing the measured morphological parameters. Figure 4.7 shows six different diagrams and relations between CABR and ASYM, GINI, and CCON

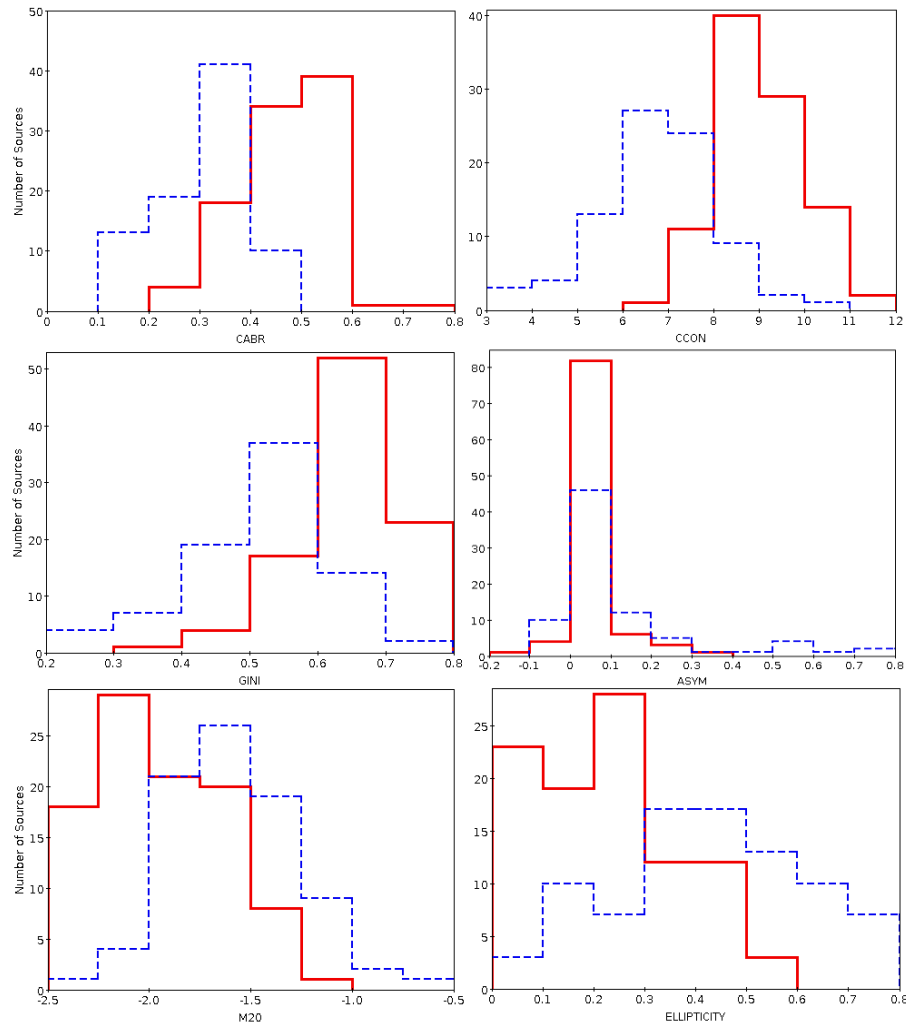


**Figure 4.6: From top left to bottom right:** Distributions of CABR, CCON, GINI, ASYM, M20 moment of light, and ellipticity parameters of ET (red solid lines) and LT (blue dashed lines) galaxies. The plots show that more LTs have lower values of concentration parameters (CABR, CCON, GINI) than ETs. However, larger values of M20 and Ellipticity characterize more LTs than ETs and vice versa.

(left plots, from top to bottom, respectively), and M20 and CCON, GINI, and CABR (right plots, from top to bottom, respectively). These relations have been used in many previous works, showing a separation between ET and LT galaxies (e.g., Abraham et al., 1994, 1996; Conselice et al., 2000; Abraham et al., 2003; Conselice et al., 2003; Lotz et al., 2004; Cassata et al., 2007; Scarlata et al., 2007; Tasca et al., 2009; Pović et al., 2009, 2013; Pintos-Castro et al., 2016).

It can be seen in all plots that ZwCl0024+1652 cluster members classified as ET and LT are occupying different areas on diagrams, as expected. ETs are located

**Table 4.5:** Median and Q1 - Q3 range of measured morphological parameters of galaxies classified as ET or LT.

Parameter	Measure	ET	LT
CABR	median	0.493	0.322
	[Q1 - Q3]	0.430 - 0.532	0.268 - 0.374
CCON	median	8.894	6.865
	[Q1 - Q3]	8.265 - 9.548	6.020 - 7.470
GINI	median	0.650	0.534
	[Q1 - Q3]	0.614 - 0.694	0.452 - 0.587
ASYM	median	0.040	0.062
	[Q1 - Q3]	0.025 - 0.059	0.021 - 0.158
M20	median	-1.996	-1.597
	[Q1 - Q3]	-2.195 - -1.726	-1.805 - -1.401
ELLIP	median	0.224	0.433
	[Q1 - Q3]	0.102 - 0.307	0.303 - 0.585

again in the regions characterised with higher concentrations (larger values of CABR, GINI, and CCON and lower of M20), in comparison to LTs. The ASYM parameter is less effective to separate sources into ET and LT, as pointed out by [Pović et al. \(2015\)](#), and as can be seen in Figure 4.7 (top left plot). However, it can be efficient in selecting interacting systems, showing larger values as can be seen in the same plot for sources with  $ASYM > 0.5$ . The relationships depicted are all in agreement with recent works (e.g., [Nilo Castellón et al., 2014](#); [Parekh et al., 2015](#); [Pintos-Castro et al., 2016](#)).

#### 4.2.2.4 Colour-colour and colour-magnitude relations

In this section we tested the colour-colour and colour-magnitude diagrams for ZwCl0024+1652 cluster members classified as ETs and LTs (see Figure 4.8). These diagrams have been tested at both lower and higher redshifts, and it is very well known that the distribution of galaxies on them is bi-modal, with ETs being mainly located in the red sequence and LTs in the blue cloud (e.g., [Bell et al., 2003](#); [Cassata et al., 2007](#); [Melbourne et al., 2007](#); [Pović et al., 2013](#); [Schawinski et al., 2014](#), etc.). We applied the k-correction to the observed magnitudes to get the rest frame B-R and R-K colours, and the absolute magnitude in B band ([Blanton and Roweis, 2007](#)). In Figure 4.8 we used the k-corrected colours to represent the relation between the R-K vs. B-R rest-frame colours (left plot), and between the B-R rest-frame colour and absolute magnitude in the B band (right plot). We also represent the histograms of all parameters used in the plots,

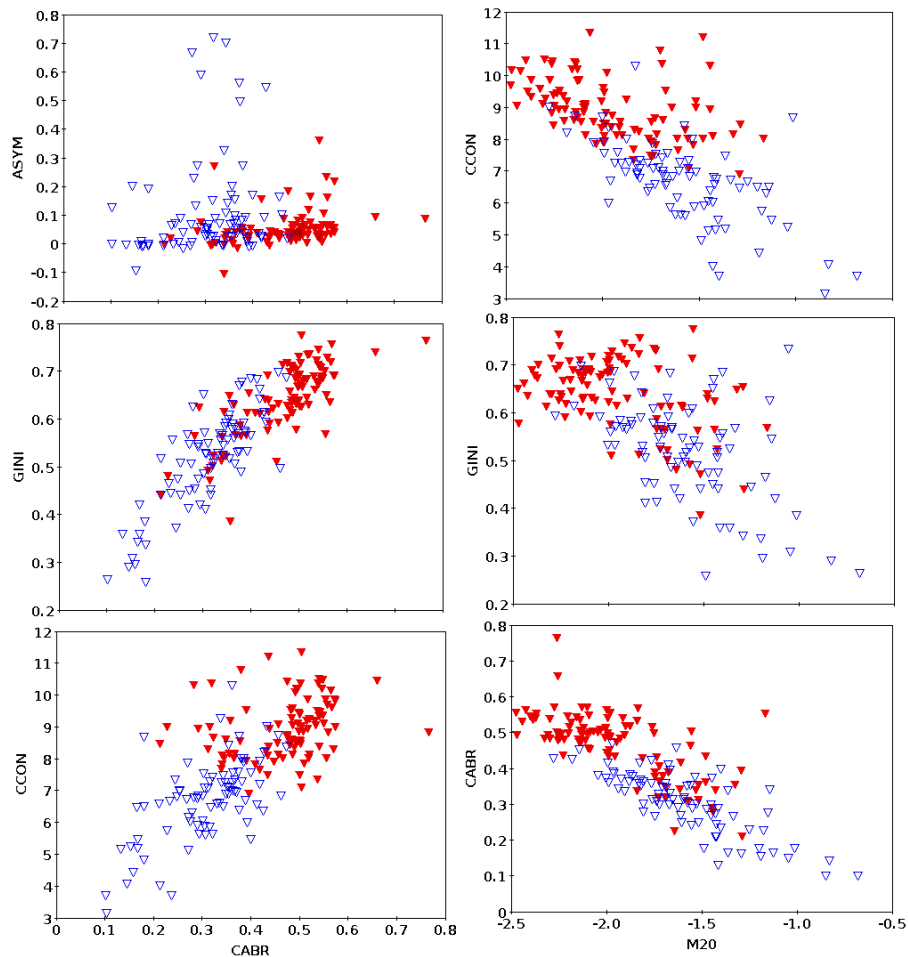


**Figure 4.7:** Standard morphological diagnostic diagrams showing the relation between CABR and ASYM, GINI, and CCON (left plots, from top to bottom, respectively), and M20 and CCON, GINI, and CABR (right plots, from top to bottom, respectively). In all the plots red solid and blue open triangles stand for ET and LT galaxies, respectively.

and their distributions for both ET and LT galaxies. In the two plots we can see the area with a higher density of ET sources, and that in general brighter and redder regions have higher fractions of ETs, as expected, while fainter and bluer parts of the diagram are populated more with LTs.

#### 4.2.2.5 Morphology vs. clustercentric distance

The distance between member galaxy and the centre of the cluster is calculated using the spherical law of cosines (e.g., [Van Brummelen, 2012](#)) as:

$$\cos(D_s) = \sin(\delta_c) \times \sin(\delta_g) + \cos(\delta_c) \times \cos(\delta_g) \times \cos(|\alpha_c - \alpha_g|), \quad (4.9)$$



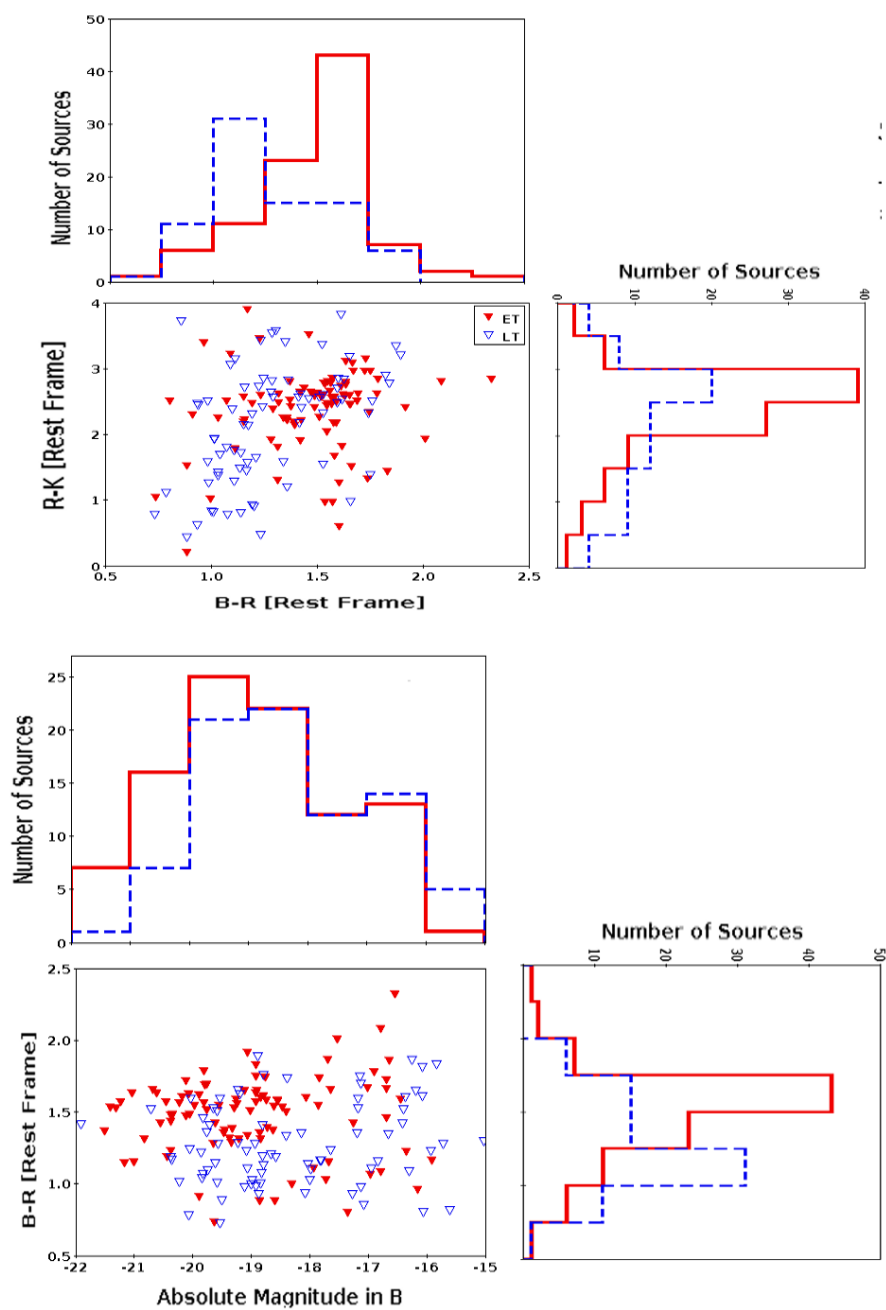


**Figure 4.8:** Rest-frame R-K vs. B-R colour-colour diagram (top plot), and B-R rest-frame colour and absolute magnitude in B diagram (bottom plot)

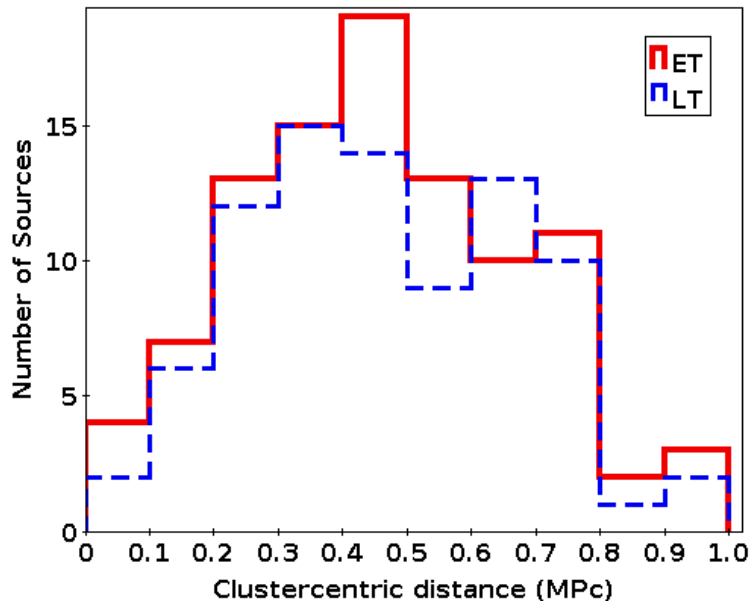


**Figure 4.9:** Distribution of the clustercentric distance of galaxies classified as ET (red solid lines) and LT (blue dashed lines).

**Table 4.6:** Statistical analysis of the morphological class distribution with respect to the clustercentric distance ( $D_{gc}$ ), the MUMEAN and the F775W\_MAG values. Here the median and the value range [ $Q1 - Q3$ ] for 50% of the sources in each class to fall is computed.

Parameter	Measure	ET	LT
$D_{gc}$	median	0.455	0.477
	[ $Q1 - Q3$ ]	0.308 - 0.623	0.324 - 0.636
MUMEAN	median	22.022	22.120
	[ $Q1 - Q3$ ]	21.925 - 22.105	22.074 - 22.143
F775W_MAG	median	21.284	22.169
	[ $Q1 - Q3$ ]	20.324 - 22.538	21.384 - 23.492

where  $(\alpha_c, \delta_c)$  are right ascension and declination of the cluster centre in radians, while  $(\alpha_g, \delta_g)$  are galaxy coordinates. To measure the clustercentric distance in Mpc, we used the following:

$$D_{gc} = D_{cl} \times \tan(D_s) \simeq D_{cl} \times D_s, \quad (4.10)$$

where  $D_{cl} = 1500 \text{ Mpc}$  and is a distance to ZwCl0024+1652. Figure 4.9 shows the distribution of clustercentric distance of 181 cluster members classified as ETs and LTs, while Table 4.6 provides the basic statistics (median and Q1–Q3 ranges) of both morphological types.

We also analysed the relation between the galaxy brightness, in terms of F775W

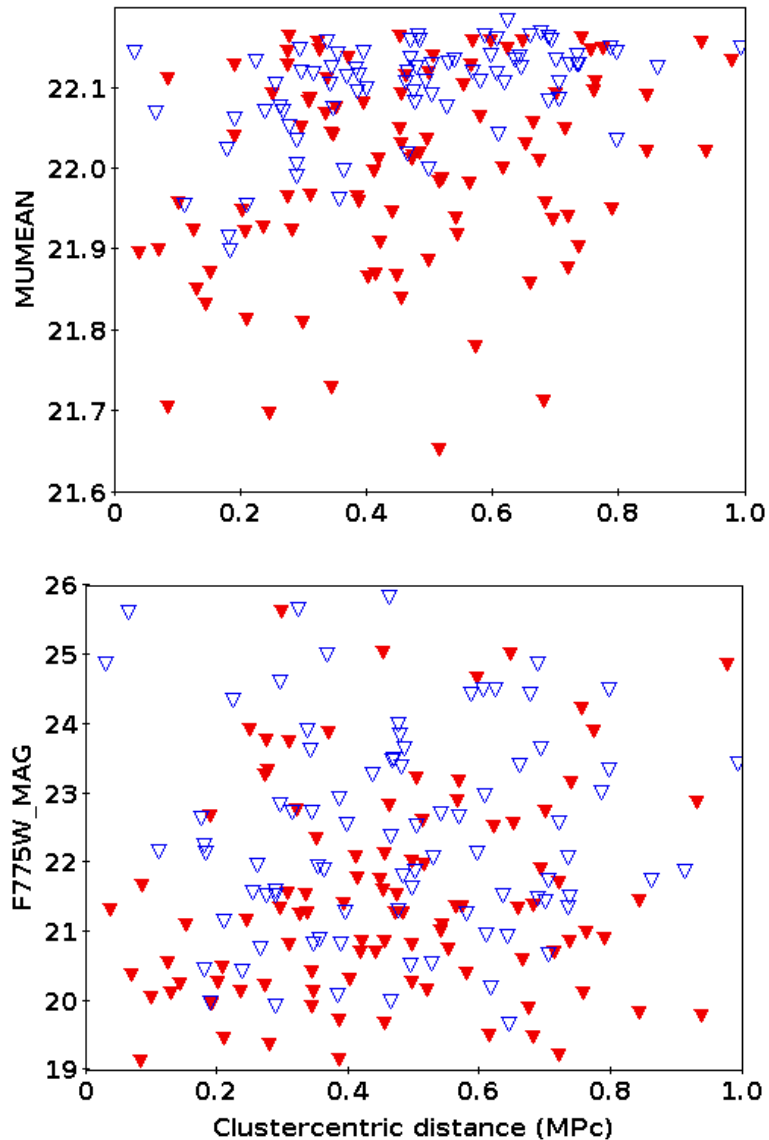


**Figure 4.10:** Relation between the surface brightness (top) and F775W magnitude (bottom) with clustercentric distance, symbols as in Figure 4.7.

magnitude and surface brightness (MUMEAN), and clustercentric distance, as shown in Figure 4.10. For the two morphological types, Table 4.6 gives again the main statistics regarding the brightness.

Finally, we analysed the relation between the clustercentric distance ( $D_{gc}$ ) and morphological parameters measured in previous section. Figure 4.12 shows how the six morphological parameters vary with respect to the clustercentric distance in the case of cluster members classified as ET and LT. We also selected those sources classified as LTs in this work, and that taking into account previous results from

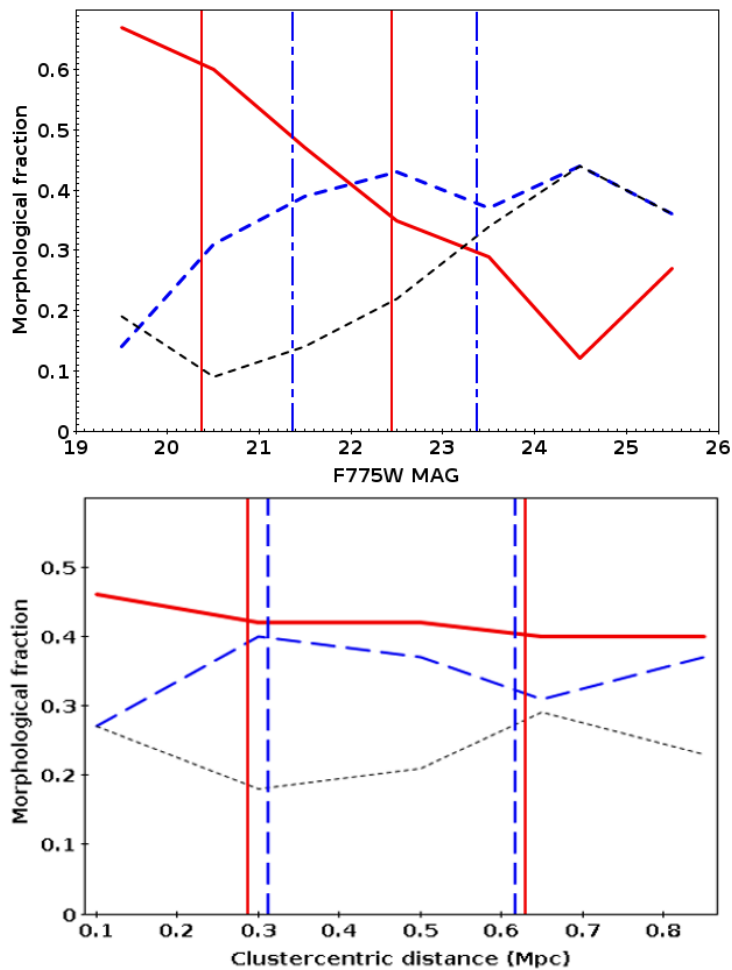


**Figure 4.11:** Morphological fractions as a function of F775W (top panel) with a binning size of 1 MAG and as a function of clustercentric distance (bottom panel) with a binning size of 0.2 Mpc along the x-axis. The thick red plot is for ET fraction, the blue dashed plot for the LT and the black thinner dashed plot for UD fraction. The thick red vertical lines indicate the Q1 and Q3 for ET fraction while the dashed blue vertical lines stand for the Q1 and Q3 of the LT fraction.

Parekh et al. (2015) and visual inspection seem to be mergers. We discussed all plots in Section 4.2.3.

## 4.2.3 Results and discussion

### 4.2.3.1 Morphological classes

It was pointed out that the evolution of the ET proportion is affected by redshift in addition to density and clustercentric distance (Smith et al., 2005; Postman

et al., 2005; Simard et al., 2009). The BO effect (Butcher and Oemler, 1984) verified with works for different redshift ranges, have been indifferently shown that LT proportion increases with redshift (e.g., Fairley et al., 2002) for  $z \sim 0.2 - 0.5$ , De Lucia et al. 2007 for  $z \sim 0.4 - 0.8$ , Barrena et al. 2012 for  $z \sim 0.2 - 0.5$  and Nilo Castellón et al. 2014 for  $z \sim 0.17 - 0.6$ ). These studies show that the proportion of LTs at  $z \sim 0.4$  accounts about  $\sim 35\% - 40\%$ . In our current work the fraction of LT galaxies is  $\sim 36\%$ , which is in agreement with previous results.

Moreover, according to Parekh et al. (2015) it was determined that galaxies are classified into most relaxed, relaxed and non-relaxed ones based on values of the GINI coefficient where the non relaxed (peculiar/most disturbed) galaxies being characterized by  $GINI < 0.4$  criterion. It is also described for the most disturbed galaxies that GINI value is small because bright pixels are not compact while equally distributed in the given aperture radius. Accordingly eight non-relaxed galaxies (peculiar) were identified from LT class closer to the cluster core leaving the spiral population near the core to be very small.

For the overall galaxy population, Moran et al. (2007) determined that for 123 matching galaxies within the 1 Mpc region, 65.6% were ET while 34.1% being LT. In the same work the morphology was determined for MS0451-0305 galaxy cluster at  $z \sim 0.5$  with 52% and 48% being ET and LT, respectively. We confirm previous results that ET population is greater than the LT population (see Postman et al., 2005; Moran et al., 2007). As shown in Section 4.2.1.5, out of the 231 galaxies we have 42% and 36% galaxies classified as ET and LT, respectively.

#### 4.2.3.2 Morphology vs. ELGs

Using GLACE survey data, Sánchez-Portal et al. (2015) has presented a catalogue of 174  $H\alpha$  emission line galaxies (ELGs) in our cluster within 4 Mpc clustercentric distance. Approximately  $\sim 37\%$  of the ELGs (64 galaxies) were shown to be AGN (broad line AGN (BLAGN) and narrow line AGN (NLAGN)) whereas  $\sim 63\%$  being star forming (SF) galaxies (110 in number). Out of the 174 ELGs, 79 galaxies (52 SFs  $\sim 66\%$  and 27 AGNs  $\sim 34\%$ ) were within the clustercentric distance of 1 Mpc (region of our concern). Matching the GLACE result with ours we found 43 ( $\sim 54.4\%$ ) counterparts. Here 26 ELGs had no match in our catalogue. Out of the matching 43 sources, 26 ( $\sim 60.5\%$ ) are SF while the remaining 17 ( $\sim 39.5\%$ ) are AGN. Morphologically comparing the matching ELGs; 11 galaxies ( $\sim 26\%$ )

correspond to ET, 28 galaxies ( $\sim 65\%$ ) belong to the LT classes and the remaining 4 galaxies ( $\sim 9\%$ ) correspond to the UD class in our results. More specifically 18 SF galaxies are in the LT class and 5 SF galaxies fall in the ET one while the remaining 3 SF galaxies belong to the UD class. Similarly, for AGN, 10 galaxies belong to the LT category, six galaxies belong to the ET class while only one AGN falls in the UD one. This confirms that ELGs (SF as well as AGN) are mostly LT galaxies rather than ET ones.

#### 4.2.3.3 Morphological fractions

In Figure 4.11 we compared the morphological fraction with both F775W magnitude and clustercentric distance. To compare it with magnitude (the top plot of Figure 4.11), the morphological fraction is computed for each 1 magnitude bin in such a way that a particular class fraction is the ratio of the number of a given class galaxies to the total number of galaxies of all classes within the same bin. Hence, for the ET fraction in a given bin:

$$MAG\_ET_{frac} = \frac{\text{number of ETs}}{\text{total number of galaxies}}, \quad (4.11)$$

where number of ETs  $\equiv$  ETs with magnitudes within the range of the bin; total number of galaxies  $\equiv$  number of all galaxies (ET+LT+UD) with magnitudes within the same magnitude bin.

Once it is computed for all the bins it is plotted against the central magnitude of the bin. It can be seen that the fraction of ET galaxies decreases as a function of increasing magnitude while that of LT galaxies increases up to F775W  $\sim 22.5$ , remaining nearly constant for fainter magnitudes. The median F775W magnitude value for ET is determined to be 21.28 and that for LT is 22.16 while that for UD galaxies is 23.20. Hence we can see that the brightest galaxies are most likely to be resolved and classified into ET/LT whereas fainter galaxies could not easily be resolved, significant number of these galaxies are unlikely to be classified then left as UD. For magnitudes F775W  $> 24.5$ , the number of sources are very small and therefore the statistics are very poor to draw a conclusion.

According to Fasano et al. (2012), the fraction of ET galaxies is high near the centre of a nearby cluster while decreasing as a function of clustercentric distance. The fraction of LT galaxies on the other hand being smaller closer to the core while

increasing as a function of clustercentric distance (see also Zwicky, 1942; Dressler, 1980; Whitmore et al., 1993; Pintos-Castro et al., 2016). Here to compare with clustercentric distance (bottom panel of Figure 4.11) we compute the morphological fraction in each 0.2 Mpc bin for 0 to 0.6 Mpc, 0.1 Mpc bin for 0.6 to 0.7 Mpc and 0.3 Mpc bin for 0.7 Mpc to 1 Mpc in the same way as in Equation 4.11. Once it is computed for all the bins it is plotted against the centre of the bin. Our results (see Figure 4.9 and the bottom plot of Figure 4.11) confirm that closer to the core, the ET population fraction is higher than the LT fraction, but the ET fraction is observed to decrease and the LT fraction to increase up to the clustercentric distance of  $\sim 0.3$  Mpc. Beyond  $\sim 0.3$  Mpc fractions of both populations continue nearly flat in parallel up to a clustercentric distance of  $R \sim 1$  Mpc. For clustercentric distances  $R > 0.7$  Mpc, the number of sources is very small and the statistics are very poor to draw a conclusion. We can see in general on Figure 4.11 throughout the entire region that the fraction of ET galaxies is consistently higher than the LT fraction and higher fraction of galaxies is classified into ET/LT near the core (lower UD fraction) than further from the centre (having higher UD fraction). Hence, our results are in a good agreement with previous results.

Moreover, out of the total number of 231 galaxies within the cluster, 111 have spectroscopically confirmed redshifts while 120 have photometric redshifts. Different trends are observed in morphological fractions throughout the clustercentric distance. It can easily be seen that for galaxy population with spectroscopic redshifts, the ET fraction is greater than the LT fraction throughout the region, while for galaxies with photometric redshifts, the LT fraction dominates throughout over the ET fraction.

#### 4.2.3.4 Morphology-density relation

An important point to be raised is the morphology-density relation (Dressler, 1980). As shown by Hoyle et al. (2012), there is a trend of an increase in the population of ET galaxies towards the cluster centre accompanied by a strong correlation between morphology and local density. Previous studies have already described high-, intermediate- and low-density regions in a cluster (see Jee et al., 2005; Demarco et al., 2010). Analysing a cluster at  $z = 0.84$ , Nantais et al. (2013) determined that the cluster outskirts (intermediate- to low-density region) are characterised with a higher LT fraction. However, a high density region (cluster

core) with dominating ET population, few peculiar galaxies and almost devoid of spirals. It has been determined near the cores of clusters that the proportion of ET galaxies is  $\sim 47\%$ , that is  $\sim 2.8$  times greater than the ET fraction in the field at the same intermediate redshift (see [Delgado-Serrano et al. 2010](#), and [Nantais et al. 2013](#)). This is a relationship that holds also for low redshift rich clusters as determined for galaxies with redshift of  $z \sim 0.1 - 0.2$  by [Fasano et al. \(2000\)](#). In our case, we classified the galaxies into broad classes (ET and LT). There is no explicit distinction of peculiar (merging) galaxies and these will be included in our classification as either LT or UD. In our work, the proportion of ET is observed decreasing as going outwards (decreasing density) from the cluster core at least up to  $\sim 0.7$  Mpc (see the right plot in [Figure 4.11](#)). As mentioned previously, after the  $R = 0.7$  Mpc the number of sources decrease significantly in all three morphological groups, which affects the measured fractions. Moreover, LT population decreases approaching to the cluster core in agreement with existing results. It must be noted that the variations in fractions are very slow, that further studies with increased sample and area coverage about the cluster center are needed for well substantiated conclusions.

#### 4.2.3.5 Relevance of morphological parameters

[Parekh et al. \(2015\)](#) classified galaxies into relaxed and dynamically disturbed system using data of clusters at different redshifts from Chandra archive, they indicated GINI, M20 and concentration<sup>4</sup> as very promising parameters for identifying mergers. The criteria set for the most relaxed system is that  $\text{GINI} > 0.65$ ,  $\text{M20} < -2.0$  and  $\text{concentration} > 1.55$ . For the most dynamically disturbed (non relaxed) systems, the criteria were  $\text{GINI} < 0.4$ ,  $\text{M20} > -1.4$  and  $\text{concentration} < 1$ . Intermediate between the two extreme conditions is the mildly disturbed situation. They identified that GINI is the most useful parameter in determining substructure because it does not depend on the exact position of the centre. Our classification was done with six morphological parameters (subsection [4.2.1.3](#)) to classify the galaxies into ET and LT. Adapting the criteria from [Parekh et al. \(2015\)](#) for our work,  $\text{GINI} < 0.4$  gave us 12 galaxies classified into ET/LT (ET=1 (8.3%), LT=11 (91.7%)). These 11 LT galaxies are checked visually to be the most perturbed (non relaxed) galaxies, where  $\text{M20} > -1.4$  for 9 galaxies out of the 11 LTs (with

---

<sup>4</sup>Concentration here is given by  $C = 5 \times \log\left(\frac{r_{80}}{r_{20}}\right)$  (as defined by [Bershady et al., 2000](#); [Conselice et al., 2003](#)).



$\sim 82\%$  agreement). On the other hand, corresponding to  $\text{GINI} > 0.65$ , 58 galaxies were classified into ET/LT (ET=49 (85%), LT=9 (15%)) and are the most relaxed ones accordingly. Hence our result is in approximately 85% agreement with previous works (amount of ETs). While, in our work,  $\text{M20} < -2.0$  is too small to be used while it is better to take  $\text{M20}$  cut off for the most relaxed galaxies to be  $\lesssim -1.8$  to establish an accuracy of at least 79%. Moreover, since concentration parameters are defined as in subsection 4.2.1.3, from our results the cut off values of  $\text{CABR} < 0.2$  and  $\text{CCON} < 7.0$  can be used for the most perturbed galaxies with  $\sim 91\%$  agreement while  $\text{CABR} > 0.45$  and  $\text{CCON} > 7.5$  can segregate about  $\sim 94\%$  of the most relaxed galaxy population. Therefore, with this cut off limits,  $\text{CCON}$  and  $\text{CABR}$  parameters could also be important parameters as  $\text{GINI}$  and  $\text{M20}$  for morphological classification of galaxies.

#### 4.2.3.6 Morphological parameters vs. clustercentric distance

In this work, we studied for the first time the properties of different morphological parameters in relation to the clustercentric distance ( $R$ ). In Figure 4.12 we showed how  $\text{GINI}$ ,  $\text{ELLIP}$ ,  $\text{M20}$ ,  $\text{CABR}$ ,  $\text{ASYM}$  and  $\text{CCON}$  change with  $R$  for ET and LT galaxies. In general, we do not find any clear trend in the case of  $\text{ASYM}$ ,  $\text{CCON}$  and  $\text{ELLIP}$  with  $R$ . In the case of  $\text{GINI}$ ,  $\text{CABR}$  and  $\text{M20}$  a slight trend is observed of decreasing  $\text{GINI}$  and  $\text{CABR}$  showing and increasing  $\text{M20}$  moment of light, suggesting that as going outwards from the cluster centre the light concentration decreases. However, much better statistics are needed to confirm this result.

As shown in the right plot of Figure 4.11 for ET class galaxies, the median and [Q1 - Q3] range of  $R$  being lower on average than LT, and this can be explained against each parameter. This is accompanied by higher values of  $\text{GINI}$ ,  $\text{CCON}$  and  $\text{CABR}$  while lower values of  $\text{ELLIP}$ ,  $\text{M20}$  and values about zero for  $\text{ASYM}$  for ET galaxies. However, for LT galaxies, the median and [Q1 - Q3] range of  $R$  are slightly higher on average than for ET galaxies. This can be seen from the plot describing morphological fraction in Figure 4.11. It can also be seen that the  $\text{GINI}$  value slightly decreases as a function of increasing  $R$  for LT galaxies. Similar trend is observed from the plot of  $\text{CABR}$  vs.  $R$  but very slow decrease for both classes in this case. For other parameters the values almost remain stagnant with  $R$ .

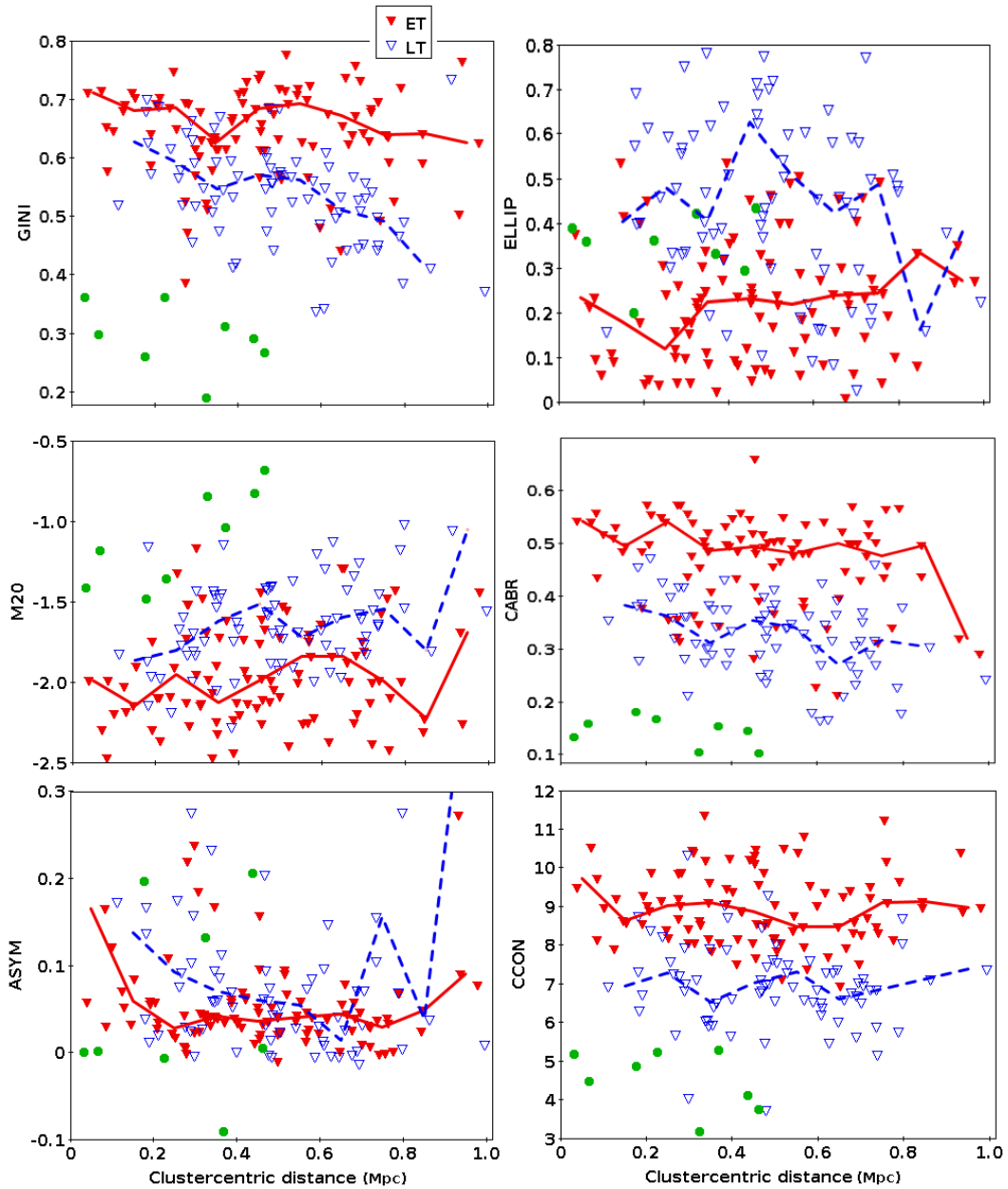


**Figure 4.12:** From top to bottom, and from left to right: Relation between the GINI, ellipticity, M20 moment of light, CABR concentration index, asymmetry, and CCON concentration index and distance from the cluster centre. In all plots red solid triangles stand for ET, and blue open triangles for LT galaxies. The disturbed (merging) galaxies selected from LT based on GINI < 0.4 criteria are indicated with green dots (solid circles). Median values of each parameter with clustercentric distance are shown with the red solid and blue dashed lines of ET and LT galaxies, respectively.

### 4.3 Morphological properties of galaxies in the RXJ1257+4738 cluster at $z \sim 0.866$

#### 4.3.1 The morphological classes

For classifying galaxies in RXJ1257+4738 galaxy cluster, the morphological classification was done by [Pintos-Castro et al. \(2016\)](#) following the same procedure by running `galSVM` code in the framework of the GLACE project, as we did for the cluster galaxies at  $z \sim 0.4$ . The morphological catalogue was published by [Pintos-Castro et al. \(2016\)](#). The morphological classification was presented for 90 member galaxies. For each galaxy, the catalogue presents the r-band magnitude, morphological parameters and the final morphological class. All galaxies were classified into LT, ET and blue early-types (bET) classified as ET, but being located in the blue cloud.

In our analysis for easier comparisons, we consider the broad morphological classification only into two classes. Therefore, we took the bETs to be grouped under ETs. This classification was made up to a clustercentric distance of about  $\sim 2.5$  Mpc. Hence the resulting sample consists of a total of 72 (80%) ETs, where 22 (24%) are ETs and 50 (56%) are bET in the original classification, while 18 (20%) LTs. There are only 40 galaxies clearly classified into ET with 22 (56%) and 18 (45%) LT classes. With aim of checking the properties of galaxies around the cluster core with respect to the clustercentric distance, we identified 35 galaxies (10 ET, 21 bET and 4 LTs) within the distance out to 1 Mpc from the centre. We produced a histogram of an r-band magnitude of each morphological type as shown in [Figure 4.13](#). The statistical distributions of the r-band magnitude of each morphological type are presented in [Table 4.7](#) (for R to 2.5 Mpc) and [Table 4.8](#) (for R within 1 Mpc).

#### 4.3.2 Morphological fractions and density relations

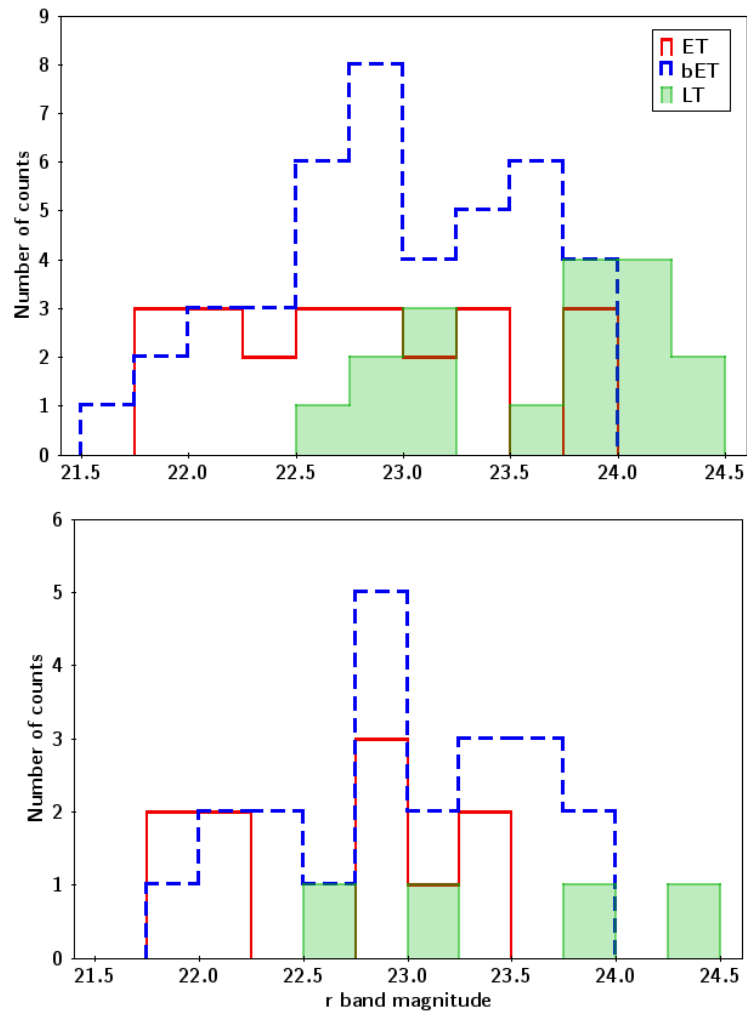
As briefly discussed in previous section, morphological classification exists only for 90 galaxies within the clustercentric distance of  $\sim 2.5$  Mpc. Out of these galaxies, only 35 are within a distance of 1 Mpc with 4 LTs, 21 bETs and 10 ETs. Therefore, taking into account the small number of sources up to  $R = 1$  Mpc, we will see the

**Table 4.7:** Statistical analysis of r-band magnitude of ET, bET and LT galaxies in RXJ1257+4738 up to the clustercentric distance  $R = 2.5$  Mpc.

Morpho_class	No of Sources	r-band MAG		
		Q1	Median	Q3
ET	22 (24.5%)	22.23	22.88	23.25
bET	50 (55.5%)	22.54	22.95	23.47
LT	18 (20%)	23.17	23.79	24.19

**Table 4.8:** Statistical analysis of r-band magnitude of ET, bET and LT galaxies in RXJ1257+4738 up to the clustercentric distance  $R = 1$  Mpc.

Morpho_class	No of Sources	r-band MAG		
		Q1	Median	Q3
ET	10 (28.6%)	22.06	22.90	23.04
bET	21 (60%)	22.63	22.95	23.37
LT	4 (11.4%)	23.17	23.82	24.26

**Figure 4.13:** The distribution of r-band magnitude of ET, bET and LT galaxies in RXJ1257+4738 cluster up to the clustercentric distance  $R = 2.5$  Mpc (**top**) and 1 Mpc (**bottom**).

trends for the whole sample up to  $R=2.5$  Mpc. In this regard we will analyse the morphological fractions in relation to r-band magnitude, local density, and clustercentric distance.

In addition to a histogram plot given in Figure 4.13, we have plotted a fraction of morphological classes as a function of r-band magnitude using the GLACE data from Pintos-Castro et al. (2016). The morphological fraction in this case is computed by making each magnitude bin to 1 following the same procedure as in Section 4.4.2. After computing the fractions for each magnitude bin we plotted them against the centre of the bin, where for r-magnitude range of 21-22 the centre of the bin is at 21.5. Morphological fraction vs. the r-band magnitude is shown in Figure 4.14 for all RXJ1257+4738 member galaxies up to a clustercentric distance of 2.5 Mpc.

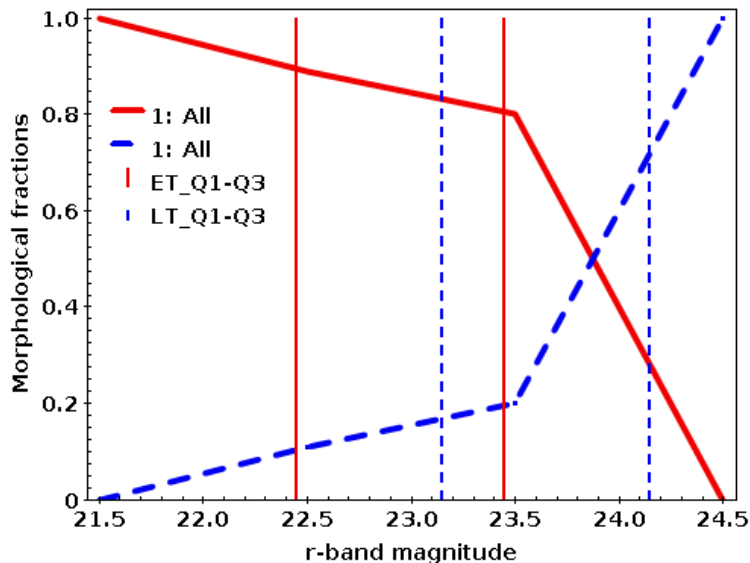


**Figure 4.14:** The fraction of ET (ET + bET), and LT galaxies vs. the r-band magnitude in the RXJ1257+4738 cluster to a clustercentric distance of 2.5 Mpc.

One can see from the plot that the fractions follow a contrasting trend. This means that ET fraction decreases as we go from brighter to fainter magnitude end, while LT fraction is increasing. The median magnitude value of the ET galaxies is computed to be 22.90 while that of LT galaxies is 23.79. The first and third quartile values indicate that 50% of ET galaxies have magnitude range of 22.46-23.43, while 50% of the LT galaxies have magnitudes of 23.17-24.19. Therefore, for RXJ1257+4738 galaxy cluster the major fraction of ET galaxies have brighter magnitudes than LTs.

The plot of morphological fractions vs. the clustercentric distance and the local density was not reproduced by our work, rather taken from [Pintos-Castro et al. \(2016\)](#). As discussed in references cited earlier in this chapter (e.g., [Hoyle et al., 2012](#); [Fasano et al., 2000](#); [Jee et al., 2005](#); [Delgado-Serrano et al., 2010](#); [Demarco et al., 2010](#); [Nantais et al., 2013](#)), high concentration of ET galaxies characterise a cluster core and cluster core is characterised by high local density in comparison to cluster outskirts. Accordingly, the outskirts are verified to be characterised by increased proportion of LT galaxies than the central part.

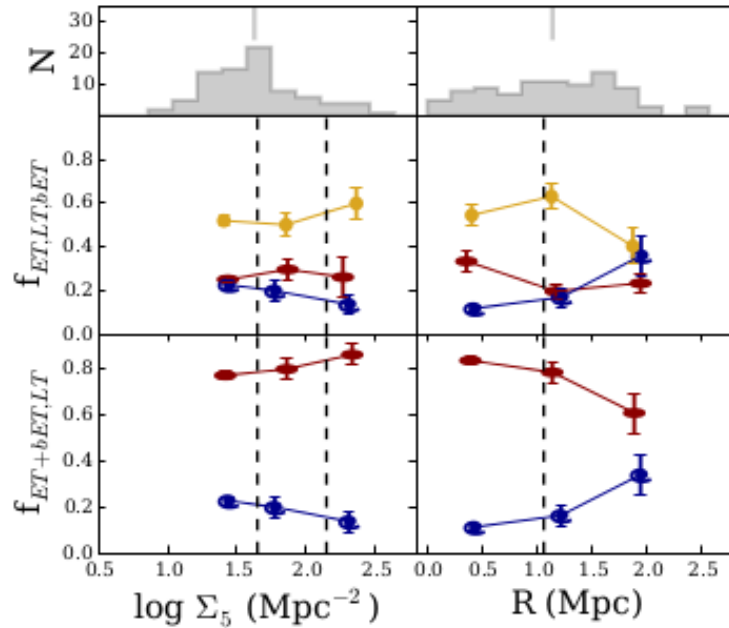


**Figure 4.15:** The fraction of the morphological types in three densities/radius: ET (red ellipses) and LT (blue spirals), and ET galaxies with blue  $g' - z'$  colours (yellow circles) vs. the local density (left plots) and clustercentric distance (right plot) of galaxies in RXJ1257+4738 cluster to a clustercentric distance of 2.5 Mpc. The dashed vertical lines stand for the original local density limit between environments defined by [Koyama et al. \(2008\)](#) (left) and the virial radius estimated by [Ulmer et al. \(2009\)](#) (right). The vertical lines stand for the mean value of each distribution. The authors estimated the error bars as the standard deviation of the fraction distribution built by bootstrap. Top panels: show the distributions of local density and clustercentric distance for the full classified sample. (adapted from [Pintos-Castro et al., 2016](#))

From the bottom left plot in Figure 4.15, we can see that the fraction of ET galaxies increases as the local density increases. On the other hand the LT fraction is decreasing with an increase of the local density throughout. Apart from this, the ET fraction is always above the LT fraction. This may be because we are in a close

proximity to the cluster centre where ETs dominate. [Pintos-Castro et al. \(2016\)](#) showed that 80% of galaxies are ET and only 20% correspond to LT morphology.

Considering the plot in the bottom right plot of [Figure 4.15](#), even though the ET fraction is above the LT fraction throughout, it can be clearly deduced that the ET fraction decreases as going outwards from the cluster centre whereas the LT fraction increases as the clustercentric distance increases. That is the fraction of ETs varies inversely with clustercentric distance whereas LT fraction varies directly with clustercentric distance.

For both the morphology-density and morphology-clustercentric distance, our work (inferred from the previous work of the GLACE team) is in line with previous results in the area.

## 4.4 Morphological properties of galaxies in the Virgo cluster at $z \sim 0.0038$

### 4.4.1 The morphological classes

The most complete catalogue that provides the morphologies of galaxies in the Virgo cluster to date is the Extended Virgo Cluster Catalogue (EVCC) that was presented by [Kim et al. \(2014\)](#). The catalogue was produced using the data from SDSS Data Release 7 ([Abazajian et al., 2009](#)). In EVCC, the galaxies of the Virgo cluster were classified into elliptical (E), lenticular galaxies (S0), spirals (Sa - Sd), ET dwarf galaxies (dE and dS0), Magellanic type spirals (Sm), barred galaxies (SB), irregulars (HSB and LSB), edge-on galaxy, or galaxies with a relatively small angular size and lack a peculiar characteristics in the process of spiral galaxy classification (S). A total of 1589 galaxies have been morphologically classified and used in the catalogue. The distribution of these morphological types is shown in [Table 4.9](#).

For our analysis here based on EVCC, we grouped the cluster galaxies into two broad morphological classes: ET, comprising all ellipticals, lenticular galaxies and ET dwarf galaxies, and LT, containing all spirals, barred galaxies, irregulars, edge on galaxies and all the S-type galaxies. This resulted in a total of 716 ( $\sim 45\%$ ) ET and 873 ( $\sim 55\%$ ) LT galaxies. This distribution includes the whole sample

**Table 4.9:** Morphological distribution of galaxies of Virgo cluster from EVCC, (Kim et al., 2014).

Morpho type	Notation	Number	% fraction
Elliptical galaxies	E	38	2.39%
Lenticular galaxies	S0	64	4.03%
dwarf elliptical	dE	494	31.09%
dwarf lenticular	dS0	120	7.55%
Spiral galaxies	S	215	13.53%
Magellanic spirals	Sm	54	3.40%
Barred galaxies	SB	130	8.18%
Irregular galaxies	Irr.	392	24.67%
Edge-on galaxies	edge-on	82	5.16%

extending up to 6 Mpc of clustercentric distance. While checking the proportions of the morphological classes about the cluster core within 1 Mpc of the clustercentric distance, we found a total of 404 classified galaxies have been morphologically classified. Out of these galaxies, 273 (68%) and 131 (32%) were classified as ET and LT, respectively.

Figure 4.16 shows the distribution of r-band magnitude of ET and LT galaxies up to the clustercentric distance of 6 Mpc (top plot) and 1 Mpc (bottom plot). It can be seen that the galaxies are classified up to  $r_{mag} \simeq 18$  for both classes. As shown in Table 4.10 within 1 Mpc clustercentric distance, at brighter magnitudes up to  $r_{mag} \simeq 13$  more LTs have been classified than ETs while at fainter magnitudes, more ETs than LTs have been classified.

**Table 4.10:** Broad morphological distribution of galaxies of Virgo cluster within 1 Mpc, separated into two groups with r-band magnitude.

Morpho type	$rmag \leq 13$	$13 < rmag \leq 18$
ET	28 (32%)	230 (73.5%)
LT	60 (68%)	83 (26.5%)

#### 4.4.2 Morphological fractions

In this section we describe the morphological fraction of galaxies in the Virgo cluster with respect to both r-band magnitude and clustercentric distance. We first computed the clustercentric distance of each classified galaxy within the Virgo cluster. For this computation we used the centre of Virgo cluster to be



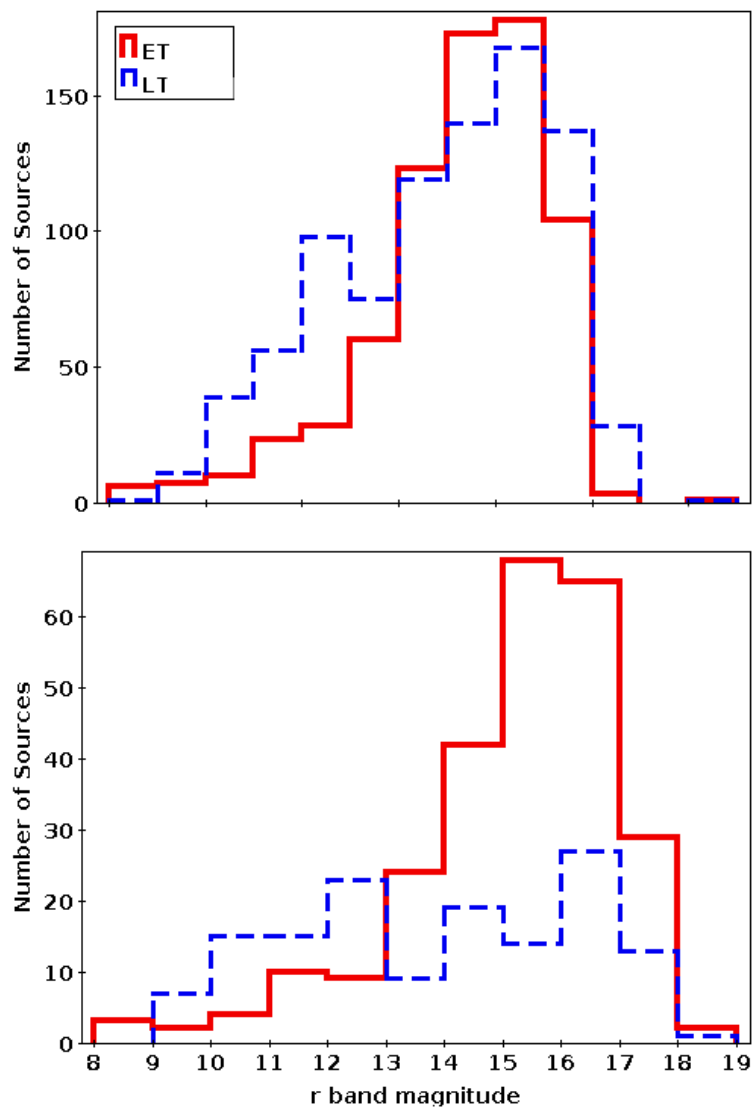


**Figure 4.16:** The distribution of r-band magnitude against the broad morphological types for galaxies in Virgo cluster, up to 6 Mpc (**top**) and 1 Mpc (**bottom**)

RA = 186.63358 degrees and DEC = 12.72330 degrees (Gavazzi et al., 2004), with the centre being located at  $\sim 16.5$  Mpc from us. The computation was then performed using Equations 4.9 and 4.10. We computed the morphological fraction with respect to r-band magnitude for each bin of two magnitudes in such a way that a particular class morphological fraction is the ratio of the number of a given class galaxies to the total number of galaxies of both classes within the same magnitude range (see Equation 4.11). The centre of the bin corresponds to average magnitude of the bin range. To discuss the relationship with r-band magnitude, we have plotted the morphological fractions in relation to the r-band magnitude up to 6 Mpc (top) and within 1 Mpc (bottom) as given in Figure 4.17. We can

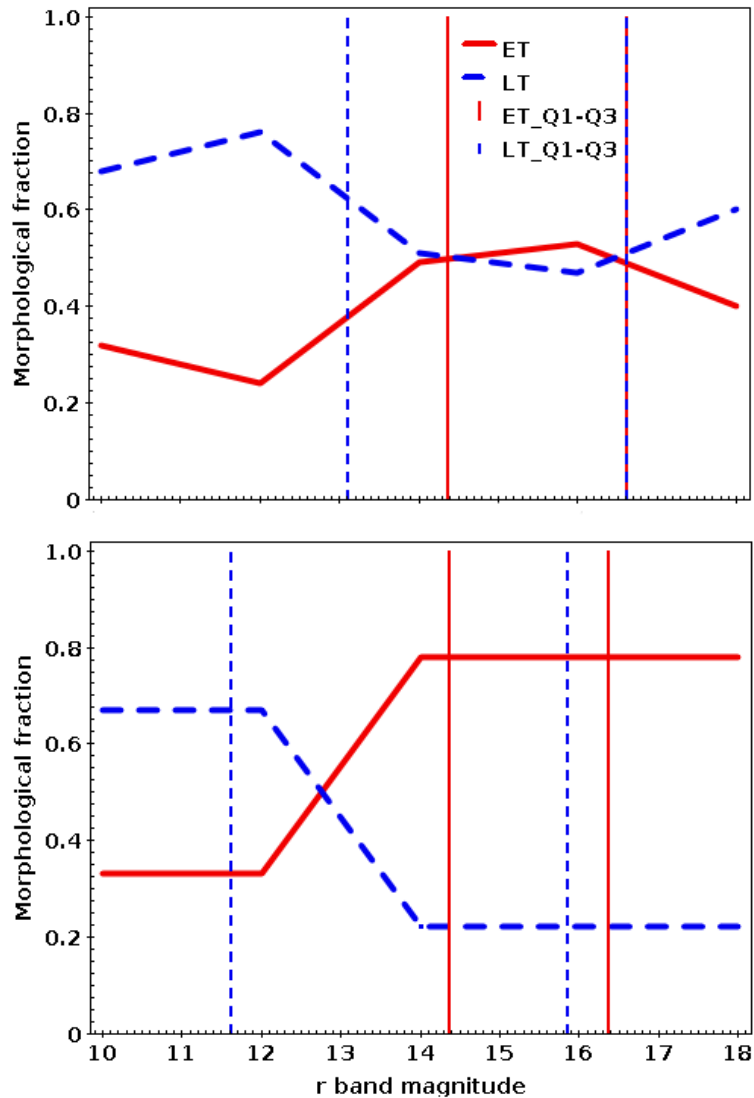


**Figure 4.17:** The fraction of broad morphological types vs. r-band magnitude for galaxies in Virgo cluster, up to 6 Mpc (**top**) and 1 Mpc (**bottom**).

see from Figure 4.17 (top plot), until the r-mag  $\sim 14$  the ET fraction on average increases while the fraction of LT galaxies decreases. Hence in this case for lower magnitudes up to r-band magnitude of  $\sim 14$ , the LT fraction is greater than the ET fraction. Beyond r-mag  $\gtrsim 14$ , ET is slightly above LT fraction. However, in mid magnitude region, r-magnitude range of  $\sim 14$ -16, the LT fraction remains consistently below the ET fraction.

From Figure 4.17 (bottom plot) for galaxies out to a clustercentric distance of 1 Mpc, a similar trend is observed for lower magnitude values up to r-band magnitude  $\sim 14$ . Both fractions being nearly constant, the LT fraction is consistently higher than ET fraction for r-band magnitude of  $\sim 12.5$ , but beyond that the LT

fraction decreases while the ET fraction increases and the LT fraction remains lower than the ET fraction throughout the magnitude ranges. The variation in fractions continue up to  $\sim 14$ , then each of the fractions remains constant for magnitudes greater than  $\sim 14$ . The median r-band magnitude of ET is 15.57 and of LT is 15.27 for galaxies up to a clustercentric distance of 6 Mpc. Note that, in our sample  $\sim 69\%$  of the ET galaxies are dwarf ellipticals (dEs). For sources within the clustercentric distance of 1 Mpc, the median value ET is 15.38 and of LT is 13.59. In addition to these, it is observed that the LT fraction has maximum value at brightest limit (lower magnitudes) while higher fractions of ETs are observed at fainter magnitudes (with majority of dEs). Statistically, 50% of LTs within  $R \sim 6$  Mpc and 1 Mpc have r-band magnitudes between Q1 - Q3 of  $\sim 13.19 - 16.69$  and  $\sim 11.70 - 15.88$ , respectively. on the other side, 50% of ETs within 6 Mpc and 1 Mpc have magnitudes Q1 - Q3 of  $\sim 14.39 - 16.70$  and  $\sim 14.29 - 16.46$ , respectively. In both cases for relatively fainter magnitude values, r-band magnitude  $\gtrsim 17$ , the statistics are poor to bring any conclusions.

We have investigated the fractions of ET and LT galaxies as a function of the clustercentric distance for ZwCl0024+1652 cluster in Section 4.2.3. Nearby clusters are characterized by a high ET fraction at small clustercentric distances (Fasano et al., 2012). On the other hand, many works (e.g., Zwicky, 1942; Dressler, 1980; Whitmore et al., 1993; Pintos-Castro et al., 2016) reveal that for such clusters the fraction of LT galaxies is lower at the centre and is increasing with clustercentric distance. To test this behaviour in the Virgo cluster, we have plotted the morphological fractions as a function of the clustercentric distance. We separately presented the plots in Figure 4.18 for galaxies in the central part of the cluster within the clustercentric distance of 1 Mpc (the bottom panel) and for the wider range up to the clustercentric distance of 6 Mpc (the top panel).

The morphological fractions have been computed for galaxies up to a clustercentric distance of 6 Mpc in bins of 1 Mpc and the fractions were plotted against the centre of the bin, as shown in Figure 4.18 (top plot). Morphological fractions were computed in the same way as in Equation 4.11. To analyse the relationship to compare with clustercentric distance for the central part up to 1 Mpc, as shown in Figure 4.18 (bottom plot), we used bins of 0.2 Mpc. Here we have five bins and the resulting values of the morphological fractions were plotted against the centre of the bin.

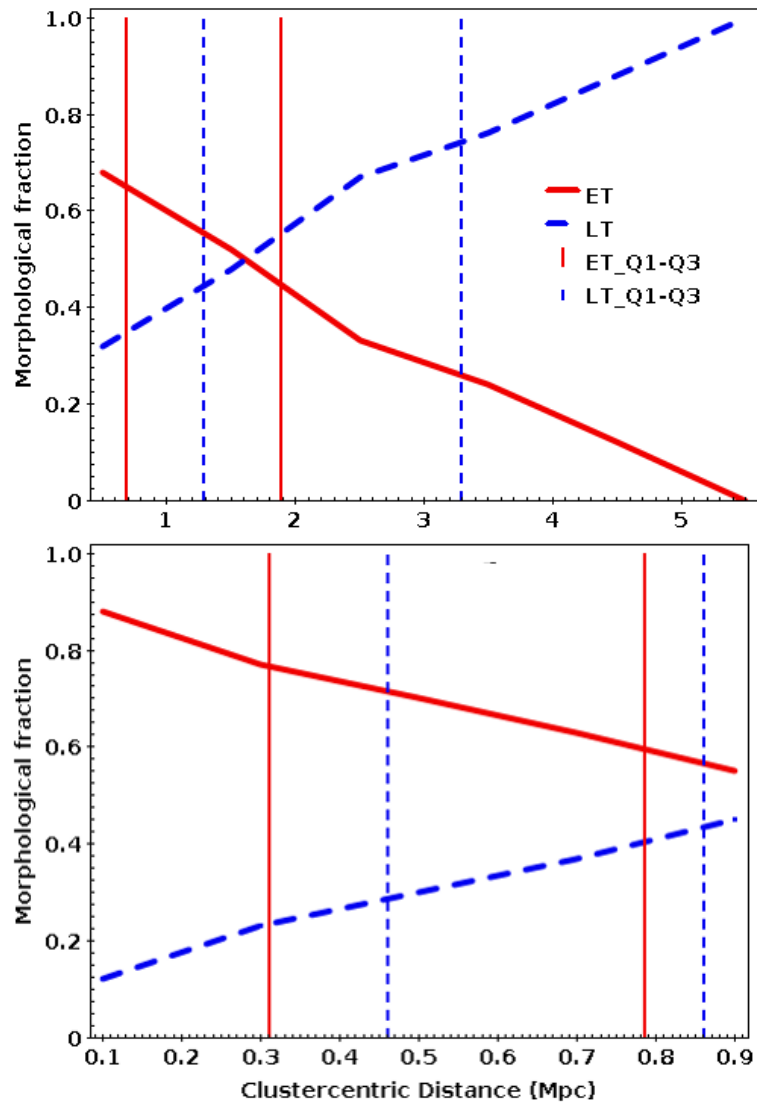


**Figure 4.18:** The fraction of the broad morphological types of galaxies in Virgo cluster vs. the clustercentric distance  $R$  up to 6 Mpc (top) and 1 Mpc (bottom).

As shown in the top plot of Figure 4.18, the ET fraction is higher than the LT one up to a clustercentric distance of  $\sim 1.5$  Mpc, but beyond this the LT population dominates. At about  $\sim 1.5$  Mpc from the center both fractions have equal values. For Virgo cluster galaxies, the central part (core) of the cluster is dominated by ET galaxies while the peripheral regions (beyond  $\sim 1.5$  Mpc) are dominated by LT galaxies. Therefore, the fraction of ET galaxies decrease while the LT fraction increases as a function of clustercentric distance. For the central part from Figure 4.18 (bottom plot), it can be clearly seen that the fraction of the ET population is higher than LT throughout, in-line with previous results (Dressler, 1980; Whitmore et al., 1993; Beyoro-Amado et al., 2019). Figure 4.18 (bottom

plot) shows that LT fraction is lowest at the core and then increases, while ET fraction is highest close to the core and decreases with clustercentric distance.

### 4.4.3 Morphology vs. density relation

The trend of a relatively higher concentration of ET galaxies about the cluster core has been revealed by previous results (e.g., [Hoyle et al., 2012](#)). A strong correlation between morphology and local density is generally observed. Different studies have been carried out in the area, describing the varying density regions (high to low), verifying that in general, cluster cores are characterized by higher densities while the cluster outskirts are characterized by lower density regions, especially for regular clusters (e.g., [Fasano et al., 2000](#); [Jee et al., 2005](#); [Delgado-Serrano et al., 2010](#); [Demarco et al., 2010](#); [Nantais et al., 2013](#)). While, for those clusters under formation like RXJ1257+4738, the monotonic correlation of local density with clustercentric distance would not be smooth (e.g., [Dressler, 1980](#); [Pintos-Castro et al., 2013](#); [Whitmore, 1994](#)). In a wide range of redshifts ( $z \sim 0.1 - 0.84$ ), there is an agreement in that the peripheral regions of the clusters (low density regions) are characterised by higher LT proportion than the ET galaxies, while the cores of clusters are characterised by higher proportion of ET (e.g., [Pintos-Castro et al., 2016](#); [Beyoro-Amado et al., 2019](#)).

We considered two cases, one for the member galaxies within 6 Mpc clustercentric distance shown in Figure 4.19 (top plot) while the other within the clustercentric distance of 1 Mpc in Figure 4.19 (bottom plot). Proportion of ET is higher than the LT proportion as going out from the cluster centre to  $\sim 1.5$  Mpc (the top plot). Moreover, the proportion of LT galaxies take a lead over the ET going out beyond  $\sim 1.5$  Mpc to outskirts of the Virgo cluster. The plots show that central region (core) of Virgo cluster has higher proportion of ET galaxies than LTs, whereas outskirts dominated by LTs over ET morphologies, conforming existing results.

## 4.5 Discussion: comparison among the three clusters

As pointed out at the beginning, we have been working on galaxy properties and evolution in galaxy clusters at redshifts ranging from the local Universe to  $z \sim 1$ . In

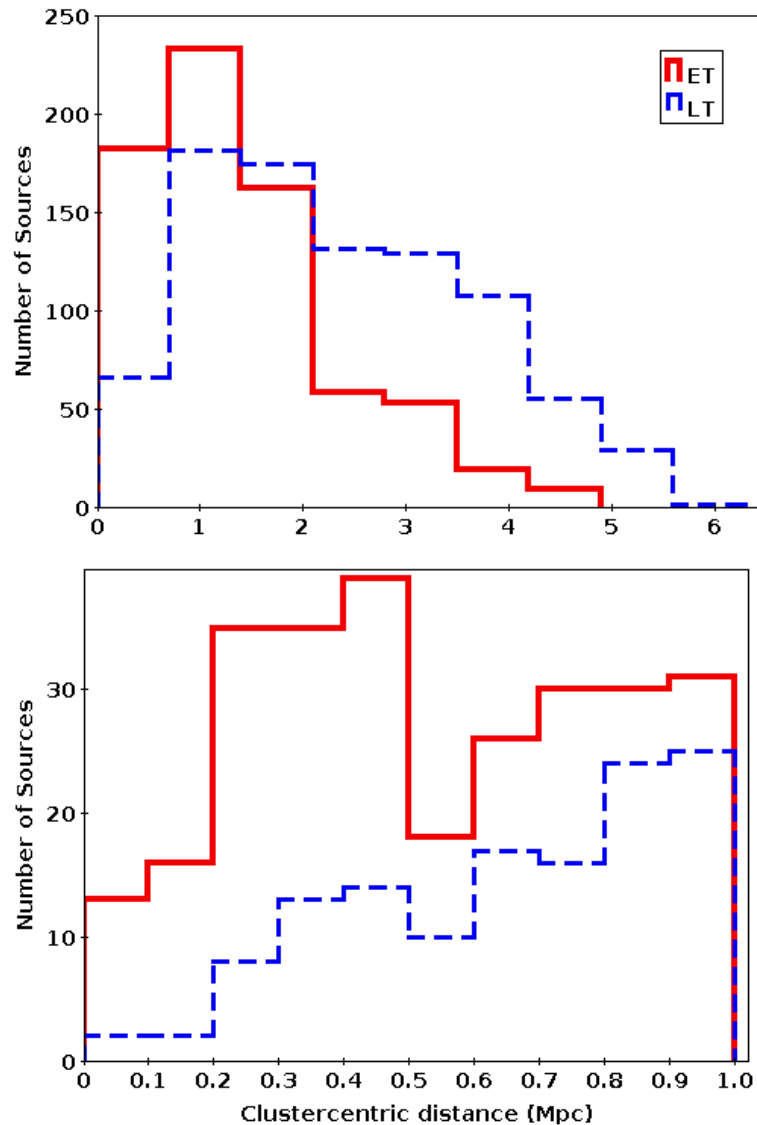


**Figure 4.19:** The histogram of the morphological classes of galaxies in Virgo cluster in relation to their location from the cluster centre R: up to 6 Mpc (**top**), and 1 Mpc (**bottom**).

this chapter, morphological properties have been analysed for galaxies in the three clusters: Virgo (local cluster at  $z \sim 0.0038$ ), ZwCl0024+1652 (intermediate redshift cluster at  $z \sim 0.395$ ) and RXJ1257+4738 (high redshift cluster at  $z \sim 0.866$ ). In terms of the morphological classification, the member galaxies have been classified into two broad classes ET and LT for ZwCl0024+1652 and Virgo clusters, while into ET, bET, and LT for RXJ1257+4738 cluster. The same method was used for the two higher redshift clusters, ZwCl0024+1652 and RXJ1257+4738, by running the `galSVM` code while morphology of galaxies in Virgo cluster has been determined visually. The morphological classification of galaxies in each of the three clusters

is summarized in Table 4.11. Note that the two clusters at lower redshifts, Virgo

**Table 4.11:** Comparison of the morphological classification of galaxies in the three target clusters within 1 Mpc.

Cluster	redshift (z)	ET	bET	LT
ZwCl0024+1652	0.395	97 (53.9%)	-	83 (46.1%)
Virgo	0.0038	273 (67.6%)	-	131 (32.4%)
RXJ1257+4738	0.866	10 (28.6%)	21 (60%)	4 (11.4%)

and ZwCl0024+1652, are well formed and virialized, whereas RXJ1257+4738 at  $z = 0.866$  is still under formation (Pintos-Castro et al., 2016). In the case of Virgo as shown in Table 4.9, all possible types of morphologies have been observed (Kim et al., 2014). In the ZwCl0024+1652 cluster, broad morphological classes (ET and LT) have been presented (Beyoro-Amado et al., 2019), but couldn't resolve into specific morphologies as in Virgo. Higher mass galaxies in the bright side of RXJ1257+4738 have been observed (Pintos-Castro et al., 2016). In the inner Mpc of RXJ1257+4738, most ET galaxies show blue colour (bETs). All of these indicate that galaxies that we observed in the three clusters are very different. We therefore were not able to make a full comparison between morphologies of galaxies in the three clusters because the samples we used are not consistent.

Comparing the magnitudes in terms of the morphological classes in the case of the ZwCl0024+1652 cluster, the ET population dominates at the brighter side, while the fraction of LT population is higher in the fainter side (Beyoro-Amado et al., 2019). Considering the classified galaxies in Virgo cluster, in the brighter magnitude side more LT galaxies are classified than the ET, while in fainter limits the LT fraction is lower than the ET fraction, in-line with other works for local clusters (e.g., Rasheed and Mohammad, 2019). For RXJ1257+4738 cluster, most of the classified galaxies are ET in a wide range of magnitudes, but most of them (21 out of 31 ETs) are bETs. In the other hand, in the fainter end of this cluster, some LT galaxies are classified even in the absence of ETs (Pintos-Castro et al., 2016). Hence, the morphological fractions tend to vary with stellar magnitude in a similar manner for the higher redshift clusters (ZwCl0024+1652 and RXJ1257+4738) in such a way that higher ET fraction has lower magnitudes than LTs and vice versa. On the other hand in Virgo, more fraction of ETs has higher magnitudes, but greater LT fraction is observed than ETs in brighter magnitudes side.

The next point of our concern is the evolution of the morphological fraction in relation to the clustercentric distance among the clusters. For ZwCl0024+1652

cluster galaxies as shown in [Beyoro-Amado et al. \(2019\)](#), morphological fraction evolves with clustercentric distance in such a way that the ET fraction is maximum closer to the cluster core and slightly decreasing until a distance of  $\sim 0.3$  Mpc from the centre. However, the LT fraction being minimum about the cluster centre increases until a clustercentric distance of  $\sim 0.3$  Mpc. Then both fractions remain slightly flat throughout until 1 Mpc of radial distance. Moreover, throughout the whole region up to 1 Mpc, the ET fraction remains greater than the LT fraction ([Beyoro-Amado et al., 2019](#)). For the Virgo cluster (shown in [Figure 4.18](#)), it is observed that the LT fraction is lowest, while the ET fraction is highest near the cluster core. The LT fraction increases while the ET fraction decreases as a function of the clustercentric distance. We can also deduce for Virgo cluster that the LT fraction dominates at the cluster outskirts unlike the core region where the ET fraction is greater. The same trends of morphology vs. clustercentric distance have been also observed in RXJ1257+4738 cluster. From the results for the three galaxy clusters at different redshifts, we can generally say that the core region of clusters is dominated by the ET galaxies, while the fraction of LTs is higher in cluster outskirts, in agreement with previous studies (e.g., [Postman and Geller, 1984](#); [Whitmore et al., 1993](#); [Goto et al., 2003](#); [Postman et al., 2005](#); [Demarco et al., 2010](#); [Nantais et al., 2013](#); [Fasano et al., 2015](#); [Campusano et al., 2018](#); [Sazonova et al., 2020](#)).

## 4.6 Conclusions

As part of a complete morphological study of the cluster ZwCl0024+1652 at an intermediate redshift  $z \sim 0.4$ , we presented a broad classification of member galaxies with available redshifts within the clustercentric distance of 1 Mpc using the HST/ACS image. We have classified galaxies up to the I - band magnitude of 26. By running the `galSVM` code on a sample of 255 galaxies, 6 morphological parameters were measured and classification was provided for 231 galaxies. Of these, 111 have spectroscopic and 120 photometric redshift measurements. In addition to this, we studied the broad morphological properties of Virgo cluster at local redshift  $z \sim 0.0038$  using the EVCC catalogue containing a total of 1589 galaxies with morphologies published by [Kim et al. \(2014\)](#) to a clustercentric distance of  $\sim 6$  Mpc. To make our work complete with our redshift range to  $z \sim 1$ , we studied the morphological properties for galaxies in RXJ1257+4738 at a redshift  $z \sim 0.866$



using the results from [Pintos-Castro et al. \(2016\)](#) by GLACE team members. From our work in this chapter, we generally concluded the following:

- In the ZwCl0024+1652 cluster, out of the sample of 231 galaxies 97 ( $\sim 42\%$ ) were classified as ET, 83 ( $\sim 36\%$ ) as LT and 51 ( $\sim 22\%$ ) stayed unclassified. If we take the well classified galaxies (180 in number), 97 ( $\sim 54\%$ ) were classified as ET and 83 ( $\sim 46\%$ ) as LT. The resulting morphological catalogue is presented as [Appendix A](#).
- For the same cluster, comparing with the visual classification of [Moran et al. \(2007\)](#) we have classified 53 galaxies matching with their morphologies, 6 galaxies classified to different classes and 121 new sources which didn't have any reported morphological classification within  $\sim 1$  Mpc radius are newly classified. Therefore, this work gives the most complete and largest morphological catalogue available up to now for this galaxy cluster.
- The comparison of our classification with the existing visual classification of [Moran et al. \(2007\)](#) is in a good agreement of 81%. Hence, applying `galSVM` for morphological classification can be taken as a reliable technique specially useful for large samples.
- We have also tested that ET and LT galaxies follow the expected distributions for different standard morphological diagrams, colour-colour and colour-magnitude diagrams.
- The ET morphological fraction is higher near the cluster core decreasing outwards while the LT fraction is lower at the cluster core, increasing outwards. Throughout the region of 1 Mpc radius, the fraction of ET galaxies is consistently greater than the LT fraction for our cluster in the region of our concern (R out to 1 Mpc). Hence, the ET/LT fraction in the cluster is in agreement with previous studies.
- Morphological fractions in our galaxy cluster at  $z \sim 0.4$  evolve with magnitude in such a way that the ET fraction dominates in the brightest magnitude limit decreasing towards the fainter end while the LT fraction increases as magnitude goes fainter.
- We compared our results with [Sánchez-Portal et al. \(2015\)](#) and found 43 ELG counterparts. From these, 11 galaxies ( $\sim 26\%$ ) correspond to ET while 28

galaxies ( $\sim 65\%$ ) were found to belong to LT. with the remaining 4 galaxies ( $\sim 9\%$ ) stayed unclassified in our work. Moreover, out of the star forming ELGs, 18 SF galaxies are LT, 5 SF galaxies fall in ET, and the remaining 3 SF galaxies belong to UD class. Similarly for AGN, 10 and 6 galaxies have been classified as LT and ET, respectively, while 1 galaxy stayed unclassified. Hence, in general we deduce that ELGs are more of LT in morphology than ET.

- We have analysed for the first time the morphological parameters as a function of clustercentric distance out to 1 Mpc. In general we do not find any clear trend, however better statistics would be valuable in future studies to revise the change of galaxy light concentration with R.
- For the RXJ1257+4738 cluster, most of the classified galaxies are ET (ET + bET) in morphology, with a small proportion of LT. Within the clustercentric distance of 1 Mpc, there are only 35 galaxies morphologically classified with 31 ETs (10 ETs + 21 bETs), and only  $\sim 11\%$  of galaxies being LTs. This is a very small number to draw any conclusions statistically. However, in the distance region to about  $\sim 3$  Mpc, there are 90 galaxies classified (72 ETs (22 ETs + 50 bETs) and the remaining 18 are LTs).
- It has been observed that the core of this cluster is also dominated by the ET population over the LTs. Going out radially from the cluster centre, the ET fraction decreases while the LT fraction increases.
- We conclude here from our measurements that, probably the brighter end of RXJ1257+4738 cluster have been observed and we have got the higher mass cluster galaxies.
- For Virgo cluster, different morphological types are available, including: ET, comprising all of the ellipticals, lenticular galaxies and the ET dwarf galaxies, and LT, containing all the spirals, barred galaxies, irregulars, edge-on galaxies and all the S-type galaxies.
- For the Virgo cluster within the clustercentric distance of 1 Mpc there are 404 galaxies classified as ET (273 or  $\sim 68\%$ ) and LT (131 or  $\sim 32\%$ ). On the other side, out to a radius of 6 Mpc, 716 ( $\sim 45\%$ ) and 873 ( $\sim 55\%$ ) are ET and LT, respectively.

- We have also verified that for this cluster the core region is dominated by the ET galaxies while the outskirts by the LT population. In other words, the LT fraction increases while the ET decreases as a function of clustercentric distance, with core characterised by higher number of ET than the LT galaxies. Here we can conclude that high local density regions are characterised by dominance of ET population over the LT population.
- Finally we conclude for all the clusters in our redshift range (up to  $z \sim 1$ ) that galaxy morphology evolves with clustercentric distance in such a way that the cluster cores are dominated by ET morphologies while the outskirts by LT morphologies.

In general, it has been known for long times that morphological proportions vary with ETs dominating the densest regions, with ETs galaxies being more than LTs in a local Universe ([Hubble and Humason, 1931](#)). This was later confirmed and analysed as morphology-density relation by different authors with evolution at different redshifts (e.g., [Dressler, 1980](#); [Postman and Geller, 1984](#); [Dressler et al., 1997](#); [Poggianti et al., 1999](#); [Postman et al., 2005](#); [Sazonova et al., 2020](#)). In addition, the LT galaxies are gas-rich, while the ETs are gas-poor ([Steyrleithner et al., 2020](#)). Galaxies passing through ICM in galaxy clusters are gradually stripped of their gases possibly due to the ram-pressure. As a result, they suffer from LTs to ET evolutions, i.e., gas-rich to gas-poor transformations (e.g., [Gunn and Gott, 1972](#); [Abadi et al., 1999](#); [Steyrleithner et al., 2020](#)). Hence, cores of the local clusters are dominated by ET galaxies in contrast to that of high-redshift clusters, so that cluster galaxies transform in passing through ICM (e.g., [Abadi et al., 1999](#)). Therefore, we conclude that our results of reporting dominant number of ETs in densest parts (cores) of clusters, are generally confirming the previous results.

# Chapter 5

## The star formation and AGN properties of galaxy clusters

1

### 5.1 Introduction

Significant evolution in the properties of galaxies in clusters has been observed as a function of redshift as well as environment (e.g., [Altieri et al., 2010](#); [Coia et al., 2005](#); [Geach et al., 2006](#); [Moran et al., 2007](#); [Haines et al., 2009](#); [Koyama et al., 2011](#); [Martini et al., 2013](#); [Pintos-Castro et al., 2013](#); [Sánchez-Portal et al., 2015](#); [Pintos-Castro et al., 2016](#); [Davidge, 2020](#); [Liu et al., 2020](#); [Longobardi et al., 2020](#); [To et al., 2020](#); [Puddu et al., 2021](#)). The study of AGN population, star formation (SF) activity, morphology, colour-magnitude relations, and distribution of galaxy metallicities with cluster properties (e.g., cluster radii and local density) present the powerful mean to investigate evolution within clusters. Concerning morphology being one of the important galaxy properties, the cores of nearby clusters are dominated by red ET galaxies, while at higher redshifts the population of blue-dominated LT galaxies increases (e.g., [Butcher and Oemler, 1984](#); [Bower et al., 1998](#); [Pintos-Castro et al., 2016](#)). In [Beyoro-Amado et al. \(2019\)](#) (discussed in Chapter 4), we performed the morphological classification of galaxies in ZwCl 0024+1652 cluster (applying the same method as in [Pović et al., 2012](#),

---

<sup>1</sup>The results presented in this chapter have been published in [Beyoro-Amado et al. \(2021\)](#)

2013, 2015; Pintos-Castro et al., 2016) using HST/ACS data confirming that the core of this cluster is dominated by ET galaxies over the LT ones. Regarding SF activity, the increase of the obscured SF was observed in mid and far infrared (IR) surveys of distant clusters (e.g., Coia et al., 2005; Geach et al., 2006; Haines et al., 2009).

Following the hierarchical model of structure formation galaxies merge into larger systems with time. This process is likely responsible for the evolution of the properties of cluster galaxies, as a function of redshift and environment (e.g., Balogh et al., 2000; Kodama and Bower, 2001). Different physical processes (discussed in Chapter 1, Section 1.2) like: mergers and harassment (both resulting from galaxy-galaxy low- and high-speed interactions, respectively), starvation (slow decrease in SF), ram-pressure stripping, thermal interstellar mass evaporation, turbulent stripping, etc, were suggested for affecting the galaxy evolution in clusters (e.g., Gunn and Gott, 1972; Larson et al., 1980; Moore et al., 1996; Cole et al., 2000; Nipoti and Binney, 2007; van den Bosch et al., 2008; Roediger, 2009; Dressler et al., 2013; Džudžar et al., 2019; Coccato et al., 2020). These processes may result from galaxy–inter-cluster medium (ICM) interactions, tidal triggering SF, or tidal halo stripping, depending on the distance from the cluster core (Treu et al., 2003). These physical processes act on the emission line galaxies (ELG) population (both SF and AGN) of the cluster (e.g., Poggianti et al., 2017). Apart from these intra-cluster physical processes, (e.g., Sobral et al., 2015) suggest that rapid and significant star formation and AGN activity could be addressed to massive cluster merging. In identifying the cluster ELGs, narrow-band imaging surveys have shown to be very efficient (Koyama et al., 2010; Sánchez-Portal et al., 2015). It has been suggested that the central regions of clusters are devoid of ELGs (SF and AGN) such as  $H\alpha$  and mid-IR emitters, and the SFRs of clusters decrease rapidly since  $z \sim 1$  (e.g., Koyama et al., 2010; Koulouridis and Bartalucci, 2019).

In this work we use the TF data in [OIII] and  $H\beta$  emission lines of ZwCl0024+1652 cluster observed under the GLACE framework by tracing the SF and AGN activities. For RXJ1257+4738 and Virgo clusters, we use the [OII] GLACE data (Pintos-Castro et al., 2016) and public data, respectively. We present the results that significantly improve the existing knowledge about the evolution of the member galaxies. This chapter is organized as follows: Section 5.2 is dedicated to the results and analysis together with the discussions for the [OIII] and the  $H\beta$  observations of ZwCl0024+1652 galaxy cluster at  $z \sim 0.4$ . In Section 5.3, evolution of

galaxies in a galaxy cluster RXJ1257+4738 cluster at  $z \sim 0.866$ , with respect to the properties discussed in Section 5.2 are discussed. Similarly, we discussed the evolution of galaxies in Virgo cluster (local) with aspects related to SF and AGN properties in Section 5.4. In Section 5.5, we compare the overall evolution of galaxies in clusters at different redshifts by analysing and discussing the effects of SF and AGN. Finally, we present a brief concluding remarks in Section 5.6.

## 5.2 ZwCl0024+1652 galaxy cluster ( $z \sim 0.4$ )

For studying the properties of galaxies in ZwCl0024+1652 with [OIII] and  $H\beta$  imaging, we used the GLACE TF data. The detailed description of the data is presented in Chapter 2, Section 2.2.1. The basic data reduction has been carried out following the procedures in Chapter 3, Section 3.1.

### 5.2.1 The [OIII] and $H\beta$ line emitters

#### 5.2.1.1 Identifying the emission line candidates through $H\alpha$ priors

As a result of our data reduction of [OIII] data described in Chapter 3 and Section 3.2, we now have two separate catalogues of sources (or [OIII] candidates). The number of candidates in each catalogue (non-star-like) that we produced are 724 for centre position and 1168 for offset position, as showed in Section 3.2. In Sánchez-Portal et al. (2015) using  $H\alpha$  line, 174 emission line galaxies have been already confirmed using TF derived redshifts that have been compared with spectroscopic ones from Moran et al. (2005). To work with confirmed ELGs ( $H\alpha$  priors), we performed a cross-matching between our sources and the  $H\alpha$  results of Sánchez-Portal et al. (2015). The cross matching was done with sky radius of 1 arcsec. Then we found 114 and 95 matches for centre and offset positions respectively with 57 duplicates. Since it is clear that both positions have some overlapping results, by cross matching the results for centre and offset positions with exact value of  $H\alpha$  ID, we identified 57 duplicates in both positions. Therefore, merging the cross match results from both positions ( $114 + 95 = 209$ ) and removing the 57 duplicates, we identified a total of 152 unique ELGs ( $H\alpha$  priors), hence we had 152 preliminary [OIII] emission line candidates.

In case of  $H\beta$  data, we followed the same procedure and generated two separate catalogues for both positions. The catalogue of sources in centre position contains 945 while the catalogue of offset position comprises of 1277 sources. We then cross-matched our results with  $H\alpha$  emitters using a sky radius of 1 arcsec. As a result, we determined 127 and 102 matches for the centre and offset positions respectively with 67 duplicates. Again by cross matching the results of the two positions with exact  $H\alpha$  ID, 67 duplicates were determined. Then merging the sources from the two positions ( $127 + 102 = 229$ ) and removing the 67 duplicates we finally identified a total of 162 ( $H\alpha$  priors) preliminary candidates for  $H\beta$  line emission. For our analysis, we take the  $H\alpha$  and [NII] fluxes for all the candidates from [Sánchez-Portal et al. \(2015\)](#). Here we compute the [OIII] and  $H\beta$  fluxes if available. Hence, cross matching both the [OIII] and  $H\beta$  results with exact  $H\alpha$  ID, we finally have identified a total of 150 ELGs identified commonly with both  $H\beta$  and [OIII] imaging. Since all of this ELGs have  $H\alpha$  and most of them have [NII] line fluxes ([Sánchez-Portal et al., 2015](#)), we look for determination of [OIII] and  $H\beta$  line fluxes if they have identified emission at the corresponding wavelengths.

### 5.2.1.2 Computation of the [OIII] line fluxes

To compute [OIII] fluxes we used the previous results of calibration obtained in Section 3.1.1.5. We used a suited python script in determining the [OIII] fluxes. With median flux value of all sources ( $\tilde{f}_{all}$ ) and standard deviation ( $\sigma_{all}$ ), we took a pseudo-continuum from the simulated pseudo-spectra as part of pseudo-spectrum points by discarding “high/low” values of the outliers: the sources with  $f > \tilde{f}_{all} + 2 \times \sigma_{all}$  (“high” outliers) or sources with  $f < \tilde{f}_{all} - 2 \times \sigma_{all}$  (“low” outliers). Hence, we defined the median as the continuum level ( $f_{cont}$ ) and its standard deviation ( $\sigma_{cont}$ ) to be the continuum noise (error). By finding the continuum subtracted flux ( $f_{cs}([OIII])$ ) belonging to the peak in a range of  $\pm 2$  scan steps ( $\pm 20 \text{ \AA}$ ) within the predicted wavelength ( $\lambda_{pred}$ ) of the [OIII] line and a TF effective transmission at the line wavelength ( $T([OIII])$ ), flux is computed as:

$$f([OIII]) = f_{cs}([OIII]) \times T([OIII]). \quad (5.1)$$

Flux error is determined with the error propagation formula as:

$$\Delta f([OIII]) = T([OIII]) \times \sqrt{(\Delta f_b([OIII]))^2 + (\sigma_{cont})^2}, \quad (5.2)$$

where  $\Delta f_b([OIII])$  is a flux error before continuum subtraction. We used equation 5.3 to compute  $\lambda_{pred}$  using the redshift ( $z$ ) derived with  $H\alpha$  results and the rest frame wavelength ( $\lambda_0 = 5007 \text{ \AA}$ ).

$$\lambda_{pred} = \lambda_0 \times (1 + z). \quad (5.3)$$

The python script was applied to all the 152 preliminary [OIII] candidates, while flux measurements have been performed for 67/50 sources in centre/offset positions respectively with 23 duplicates. At the same time we plotted the pseudo-spectra. By visually inspecting the pattern of the pseudo-spectra we plotted, we identified 51 final candidates for [OIII] emission. The total [OIII] line flux distribution peaks at about  $8.52 \times 10^{-17} \text{ erg cm}^{-2} \text{ s}^{-1} \text{ \AA}^{-1}$ .

### 5.2.1.3 Derivation of $H\beta$ fluxes and the extinction correction from Balmer decrement

#### ⊙ The uncorrected flux ( $f_{uncor}$ )

For computing the  $H\beta$  flux we used slightly different technique than in case of [OIII], since in this case absorption flux is taken into consideration. We know that each flux that we already have is the integrated flux of the galaxy in the corresponding TF slice, that is the convolution of the source's spectrum with the response of the TF. The values are converted to standard flux units ( $\text{erg s}^{-1} \text{ cm}^{-2} \text{ \AA}^{-1}$ ) by dividing them with the effective filter passband width  $\Delta\lambda_e = \frac{\pi}{2} FWHM_{TF}$ . It is known that the TF collected flux is just the sum of the continuum (absorption) and the  $H\beta$  emission line. A total  $H\beta$  emission is obtained by following a slightly similar process as for the [OIII] case, but here involving the absorption correction. We computed the total  $H\beta$  fluxes using the following steps. First defining the continuum as the subset of pseudo-spectrum points by discarding "high/low" outlier values, defined as those above  $\tilde{f}_{all} + 2\sigma_{all}$  or below the median value  $\tilde{f}_{all} - 2\sigma_{all}$ . We define the continuum level,  $f_{cont}$ , as its median and the continuum noise,  $\sigma_{cont}$ , as its standard deviation. Then we subtract the continuum level from the pseudo-spectrum to get the flux without correction for absorption defined to be  $flux - flux_{cont}$  and determining the continuum-subtracted flux,  $f_{uncor}$  that corresponds to the maximum in a range of  $\pm 2$  scan steps ( $\pm 20 \text{ \AA}$ ) about the predicted position of the  $H\beta$  emission line.



### ⊙ Flux in absorption and the total flux

The presence of Balmer series in absorption is one major signatures of young and intermediate age stars population in the optical spectra of galaxies. The emission lines are then acquired superimposed on the underlying absorption lines. The importance of this effect develops towards the higher order Balmer lines meaning that the absorption line equivalent width in  $H\alpha$  ( $EW_{H\alpha}$ ) is very small and we can safely ignore it while computing the emission line flux (Rosa-González et al., 2002). Since absorption moderately affects the  $H\beta$  line, the underlying absorption must be considered and hence  $H\beta$  is fainter than  $H\alpha$ ,  $f_{H\alpha}/f_{H\beta} = 2.85$  as for intrinsic Balmer decrement in case B recombination (Osterbrock and Ferland, 2006). Representative of the galaxy population for the sample under study has been chosen, but with a constant  $EW_{H\beta}$ . For instance, Hopkins et al. (2013) assumed a  $EW_{H\beta} = 2.5 \text{ \AA}$  for the GALaxy and Mass Assembly (GAMA) sample in the  $z$  range from 0 to 0.5 and Kennicutt (1992) used  $EW_{H\beta} = 5 \text{ \AA}$  in analysing a local ELG sample. For our data we applied a different approach deriving  $EW_{H\beta}$  for each object using the best-fitting host galaxy stellar SED template and age from Bruzual and Charlot (2003) (BC03) and Ilbert et al. (2006), as explained in Sánchez-Portal et al. (2015). Since *LePhare* code for this purpose makes use of the low-resolution Composite Stellar Populations (CSP) while for measuring the equivalent width  $EW_{H\beta}$ , we require a high-resolution SED templates. Therefore, we performed the computation using the GALAXEV<sup>2</sup> code (Bruzual and Charlot, 2003). We derive the spectral evolution of the CSPs by integrating the equation of evolution of Single Stellar Population (SSP) templates from BC03 with metallicities  $Z = 0.0001, 0.0004, 0.004, 0.008$  and  $0.02$  (models m22, m32, m42, m52 and m62, respectively) with star formation histories exponentially varying with time as  $SFR \propto e^{-t/\tau}$  where  $\tau$  ranges from 0.1 to 30.0 Gyr and taking the initial mass function (IMF) from Chabrier (2003). The output of this code includes the  $EW_{H\beta}$  at different ages as defined by Trager et al. (1998) ( $H\beta$  absorption equivalent width). Without applying the interpolation since both codes implement almost identical age steps, we have chosen the values of  $EW_{H\beta}$  at the closest ages to those given by the best fit from *LePhare*.

A histogram representing the distribution of  $EW_{H\beta}$  is given in Fig. 5.1 for the

<sup>2</sup>[//www2.iap.fr/users/charlot/bc2003/](http://www2.iap.fr/users/charlot/bc2003/)

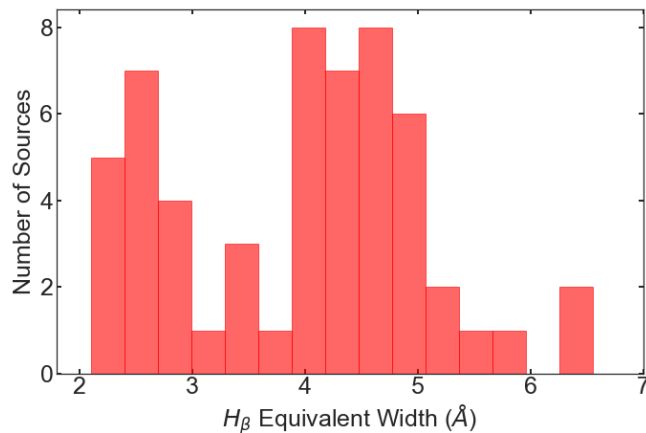


**Figure 5.1:** Distribution of  $H\beta$  absorption line equivalent widths derived from best-fitting templates and ages.

identified  $H\beta$  lines. Two maxima are precisely located about the values 2.5 and 4.8 Å. The average equivalent width is  $EW_{H\beta} \sim 4.00$  Å.

The absorption line flux was measured by multiplying the value of  $EW(H\beta)$  by the previously derived pseudo-continuum. In average, the flux ratio is

$$f_{H\beta,absorption}/f_{H\beta,emission} \simeq 0.43.$$

The next step is calculating the flux in absorption given by  $f_{abs} = EW_{H\beta} \times f_{cont}$ . The total flux ( $f_{total}$ ) is then finally computed as a sum of the continuum subtracted flux ( $f_{cs}(H\beta)$ ) and the flux in absorption as  $f_{total}(H\beta) = f_{cs}(H\beta) + f_{abs}$ , and we determined the final line flux errors using the error propagation formula (now including absorption), including error in absorption as:

$$\Delta f_{total}(H\beta) = \sqrt{(\Delta f(H\beta))^2 + (\sigma_{cont} \times EW(H\beta))^2}. \quad (5.4)$$

Performing the computation separately on the data of both positions (centre and offset), we got the flux measurements for 69 and 75 sources in centre and offset positions respectively with 28 duplicates. Then by using the visual inspection of the pattern of the pseudo-spectra, we identified 80 final candidates for  $H\beta$  line emission candidacy. The total  $H\beta$  line flux distribution peaks at about  $6.27 \times 10^{-17}$  erg s<sup>-1</sup> cm<sup>-2</sup> Å<sup>-1</sup>.

**Table 5.1:** The number of preliminary candidates for [OIII] and/or H $\beta$  emission, with final detected emission line sources.

Sources	[OIII]	H $\beta$	[OIII] and H $\beta$	[OIII] + H $\beta$ + [NII] + H $\alpha$
Pre-candidates	51	80	29	28
Final emitters	35	59	21	20

#### 5.2.1.4 Analysis of individual objects and selection of the final sample of [OIII] and H $\beta$ emitters

We obtained in total 51 [OIII] and 80 H $\beta$  emission line final candidates with 29 common candidates for both lines resulting with a total of 102 unique candidates, as described in Sections 5.2.1.2 and 5.2.1.3. For final sample selection and to make sure that fluxes are coming from single sources, we first went through the visual inspection of thumbnails from HST data described in Section 2.2.3.1. In total, we found thumbnails of 31 and 52 [OIII] and H $\beta$  candidates, respectively, with 19 sources in common. Most of the sources ( $\sim 91\%$ ) were inspected to be well isolated. Secondly, for remaining sources we inspected the H $\alpha$  pseudo-spectra (Sánchez-Portal et al., 2015), and removed those sources with line offset of  $\geq 10$  Å and/or those sources with no clearly detected peak. We finally detected all targeted emission lines ([OIII], H $\beta$ , [NII] and H $\alpha$ ) for 20 ELGs. Our final sample is summarized in Table 5.1.

A sample of five emitters (emissions detected in both H $\beta$  and [OIII], [OIII] only and H $\beta$  only, respectively) with stamps is shown in Figures 5.2, 5.3 and 5.4. In all the figures, the predicted H $\alpha$  position with spectroscopic redshifts (Moran et al., 2007) and the predicted H $\beta$  line wavelength positions derived with H $\alpha$  redshifts are represented with green vertical lines in their corresponding pseudo-spectra, while the predicted wavelength positions for [OIII] $\lambda$ 5007 and [OIII] $\lambda$ 4959 both computed with H $\alpha$  are indicated with blue and red vertical lines, respectively, when detected.

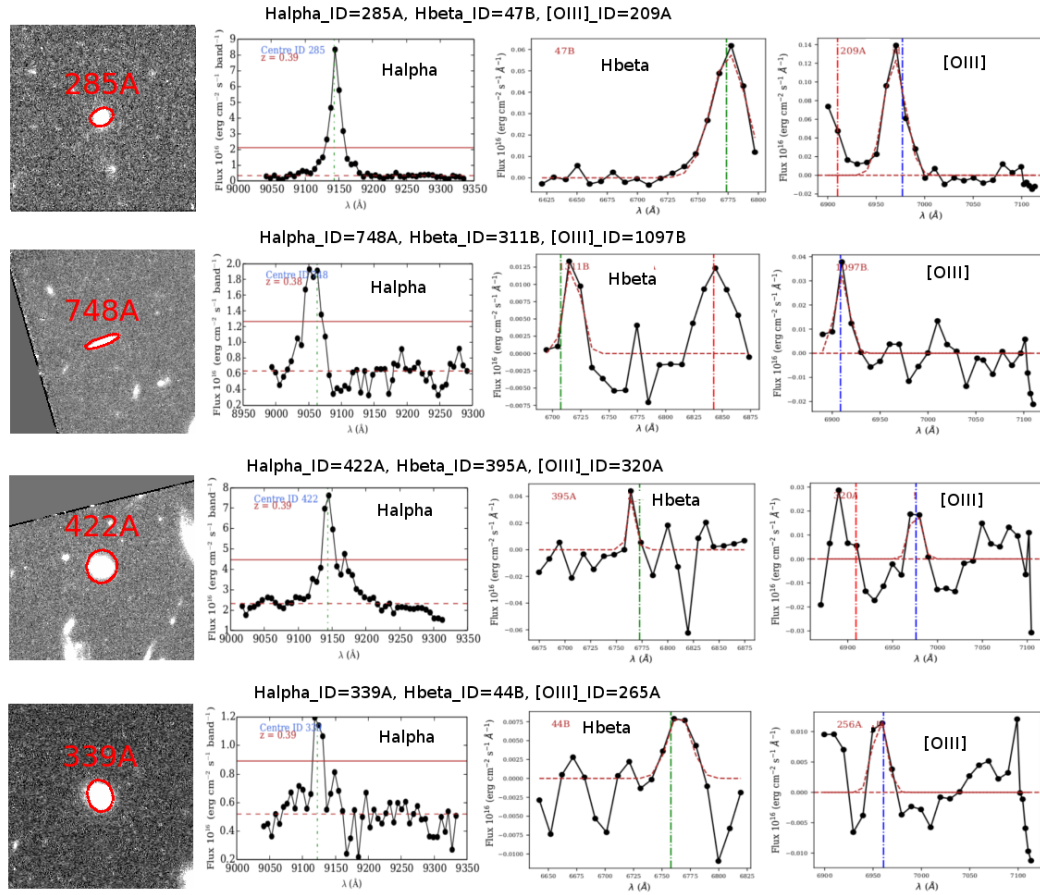


**Figure 5.2:** Example of HST/ACS thumbnails (left) and pseudo-spectra of ELGs with H $\alpha$  (second column), and [OIII] and/or H $\beta$  emissions (third and/or fourth columns, as indicated on each pseudo-spectrum). The predicted H $\alpha$  position with spectroscopic redshifts (Moran et al., 2007) and the predicted H $\beta$  line wavelength positions derived with H $\alpha$  redshifts are represented with green vertical lines in their corresponding pseudo-spectra, while the predicted wavelength positions for [OIII] and [OIII] $\lambda$ 4959 both computed with H $\alpha$  are indicated with blue and red vertical lines, respectively, when detected. The horizontal solid red line corresponds to the  $3\sigma_{cont}$  level, where  $\sigma_{cont}$  is the pseudo-continuum noise, while the dashed red horizontal line corresponds to the estimated pseudo-spectrum continuum level.

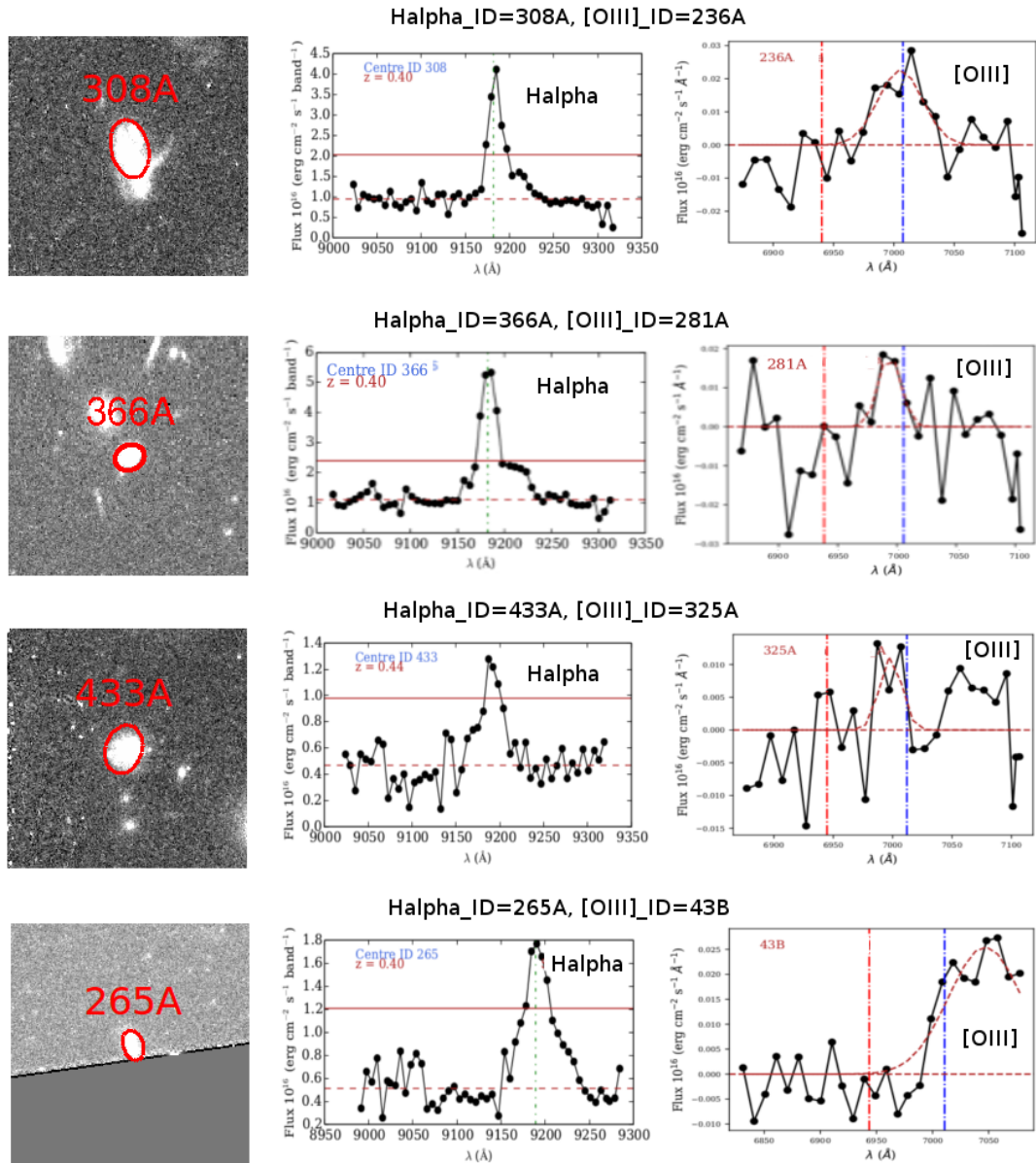


**Figure 5.3:** Example of HST/ACS thumbnails (first column) and pseudo-spectra of ELGs with H $\alpha$  (second column) and [OIII] emissions (third column). The vertical lines, the solid horizontal red line and the dashed horizontal red line are defined as in Figure 5.2. H $\beta$  emissions are not detected in this case.

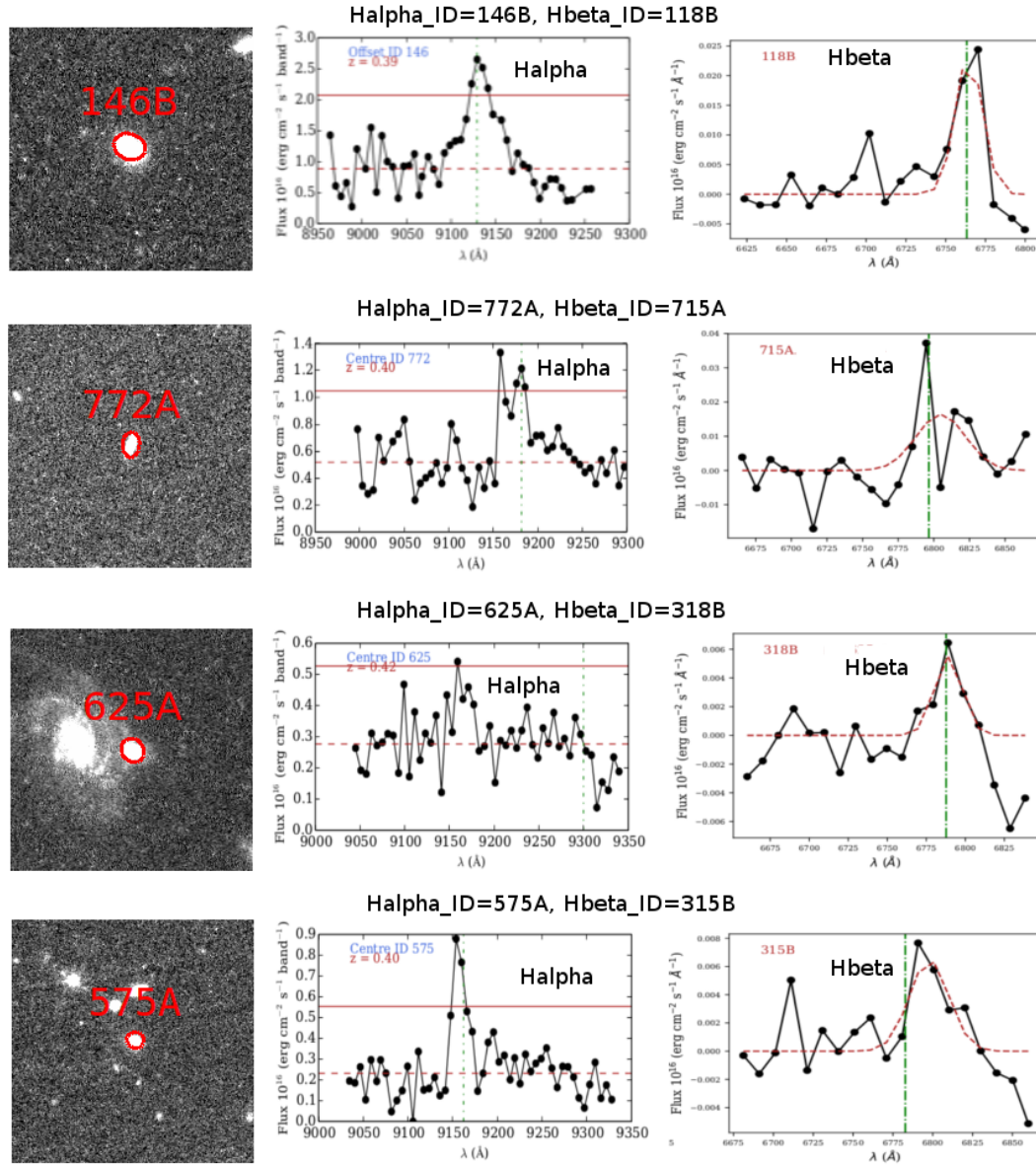


**Figure 5.4:** Example of HST/ACS thumbnails (first column) and pseudo-spectra of ELGs with H $\alpha$  (second column) and H $\beta$  emissions (third column). The vertical lines, the solid horizontal red line and the dashed horizontal red line are also defined as in Figure 5.2. [OIII] emission lines are not detected in this case.



## 5.2.2 Analysis and results

### 5.2.2.1 Redshift measurements

Redshifts of nearly spectroscopic-quality were derived in [Sánchez-Portal et al. \(2015\)](#) from the positions of the  $H\alpha$  emission lines for all our ELGs. We computed the redshifts through detected [OIII] and  $H\beta$  lines and then compared our results with  $H\alpha$  redshifts presented in [Sánchez-Portal et al. \(2015\)](#). In [Figure 5.5](#) we showed the redshift distribution and their comparison with  $H\alpha$  measurements is represented in [Figure 5.6](#). The relative redshift deviations, defined as  $|z_{\text{TF}} - z_{H\alpha}| / (1 + z_{H\alpha})$ , are  $\sim 0.002$  and  $\sim 0.001$  for [OIII] and  $H\beta$ , respectively, confirming therefore the spectroscopic quality of the TF-derived redshifts. Our redshift distributions are in line with previous results ([Czoske et al., 2002](#); [Sánchez-Portal et al., 2015](#)), with average redshifts of  $\sim 0.382$  and  $\sim 0.394$  for [OIII] and  $H\beta$  lines, respectively. Moreover, we recover two dynamical structures represented by double-peaks in the redshift distribution, where structure “A” (centred at  $z \simeq 0.395$ ) corresponds to the main cluster, while structure “B” (centred at  $z \simeq 0.380$ ) represents the infalling component ([Czoske et al., 2002](#); [Kneib et al., 2003](#); [Moran et al., 2007](#); [Sánchez-Portal et al., 2015](#)). Our redshift measurements are also in good agreement with those obtained from  $H\alpha$  data ([Sánchez-Portal et al., 2015](#)), as can be seen in [Figure 5.6](#), with linear correlation factors of 0.923 and 0.941, respectively. As determined by [Czoske et al. \(2002\)](#), the velocity distribution of structure A was determined to be regular with a dispersion of  $\sim 600 \text{ km s}^{-1}$  at projected distance  $> 3'$ , while the formal velocity dispersion within  $5'$  is  $\sigma_{\text{cent}} = 1050 \text{ km s}^{-1}$  for 193 galaxies. The environment conditions were parametrised by the local surface density computed by [Pérez-Martínez et al. \(in prep.\)](#) from the distance to the 5th-neighbour ( $\Sigma_5$ ), according to [Dressler et al. \(1985\)](#). Moreover, we computed the radial velocity of each member galaxy and derived the projected clustercentric distance separately for  $H\beta$  and [OIII] emitters to produce and discuss on the projected phase-space diagrams shown in [Figure 5.7](#).

Moreover, we also computed the radial velocity of each member galaxy and plotted the phase-space (radial velocity versus projected clustercentric distance) separately for  $H\beta$  and [OIII] emitters that clearly identifies the two structures as depicted in [Figure 5.7](#).

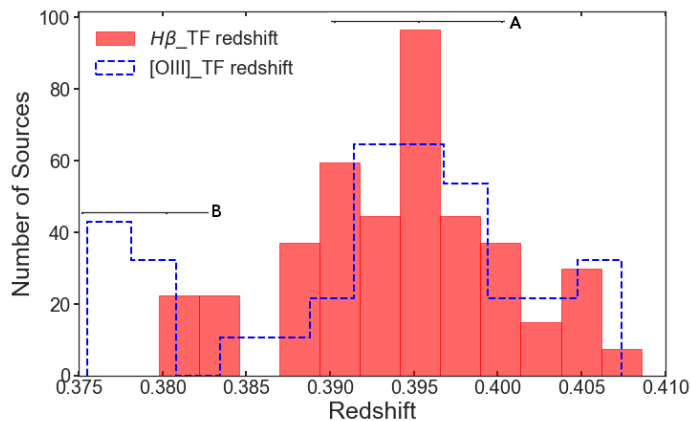


**Figure 5.5:** Redshift distribution of [OIII] and  $H\beta$  ELGs, where two dynamical structures A and B can be seen, as suggested in previous works (Czoske et al., 2002; Sánchez-Portal et al., 2015).

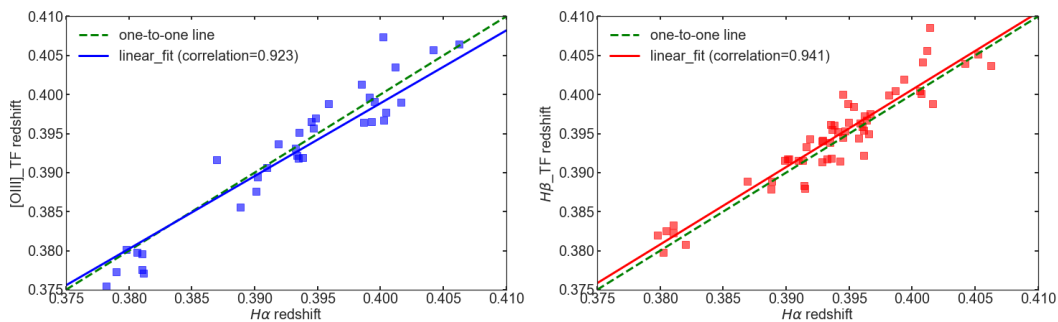


**Figure 5.6:** Linear correlation between [OIII] (left plot) and  $H\beta$  (right plot) TF derived redshifts and  $H\alpha$  redshifts.

### 5.2.2.2 Flux and luminosity distributions in [OIII] and $H\beta$

Statistically analysing, the peak value of the [OIII] flux is observed to be  $6.17 \times 10^{-16}$  with a mean value being  $9.86 \times 10^{-17}$ . Similarly the peak value for  $H\beta$  is attained to be  $3.70 \times 10^{-16}$  with mean value of  $9.74 \times 10^{-17}$  all in a flux unit given by  $\text{erg s}^{-1} \text{cm}^{-2} \text{\AA}^{-1}$ .

The statistical distribution of the [OIII] and  $H\beta$  line fluxes is given in in Table 5.2. We also derived the luminosity functions from the fluxes and computing the luminosity distance with the TF computed redshift for each case implementing the standard mechanisms. We computed the luminosity distance ( $D_L$ ) of each of the source in the catalogue using a TOPCAT function `LuminosityDistance` with the redshift from TF computation. Then the [OIII] luminosity of each of the source is



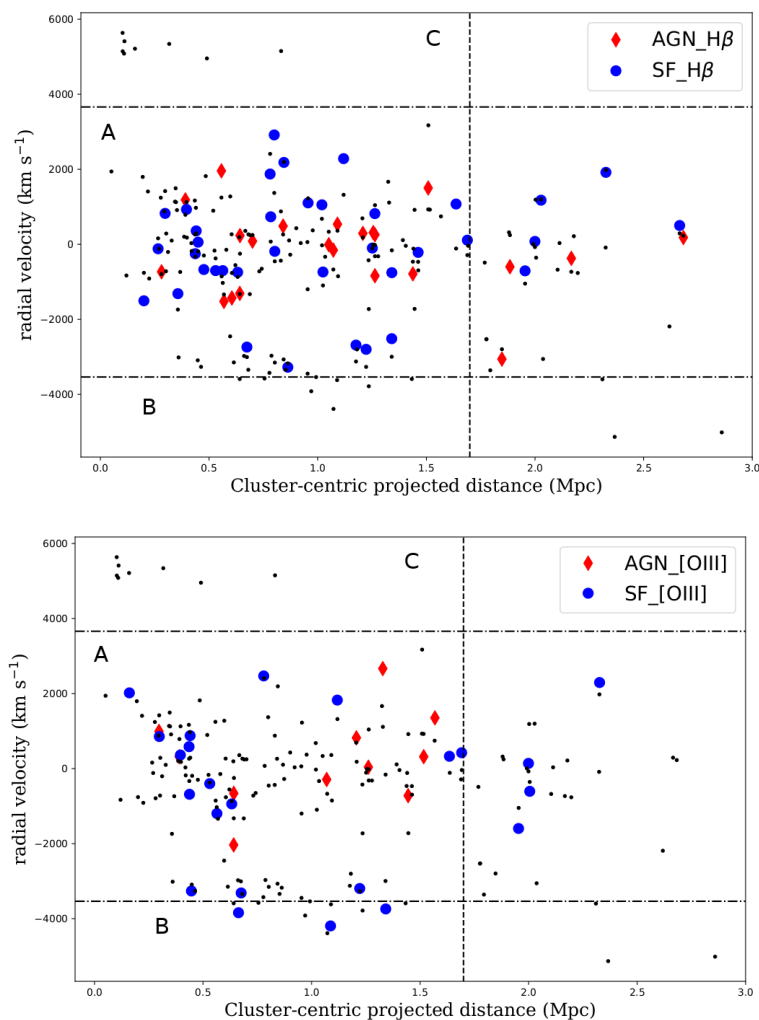


**Figure 5.7:** Radial velocity versus clustercentric distance for  $H\beta$  (top plot) and  $[OIII]$  (bottom plot) ELGs. Red diamonds represent AGNs while blue dots correspond to SF galaxies. The virial radius ( $r_{\text{vir}} = 1.7\text{Mpc}$ ) is represented by dotted vertical line (Treu et al., 2003). The dashed-dotted horizontal lines stand for the radial velocity limits fully covered within the field of view of the two OSIRIS TF pointings. The small black points correspond to ELGs from Sánchez-Portal et al. (2015) with  $H\alpha$  emission. The two reported structures of the cluster are marked with “A” and “B”, whereas the putative possible component is represented with letter “C”.

determined using the Equation 5.5 as:

$$L = 4\pi F D_L^2, \quad (5.5)$$

where  $L$  stands for  $[OIII]$  luminosity,  $F$  denotes the  $[OIII]$  flux and  $D_L$  for the luminosity distance. The statistical distribution of the  $[OIII]$  and  $H\beta$  luminosities is given in Table 5.3. Then we compared the results with each other and with  $H\alpha$  and  $[NII]$  measurements, as shown in Figure 5.8. We found that  $[OIII]$  and  $H\beta$  fluxes

**Table 5.2:** The statistical distribution of fluxes of [OIII] and H $\beta$  emitters in  $\text{erg s}^{-1} \text{cm}^{-2}$ , with Q<sub>1</sub> and Q<sub>3</sub>, and Med representing the median.

Fluxes measured	Q <sub>1</sub>	Med	Q <sub>3</sub>
[OIII]	$3.7 \times 10^{-17}$	$6.2 \times 10^{-17}$	$1.0 \times 10^{-16}$
H $\beta$	$4.1 \times 10^{-17}$	$1.3 \times 10^{-16}$	$7.4 \times 10^{-17}$

**Table 5.3:** The statistical distribution of logarithm luminosities (Q<sub>1</sub>, Med, Q<sub>3</sub>) in  $\text{erg s}^{-1}$  of [OIII] and H $\beta$  emitters.

Luminosity measured	Q <sub>1</sub>	Med	Q <sub>3</sub>
[OIII]	40.3	40.5	40.7
H $\beta$	40.3	40.6	40.9

and luminosities are on average comparable with H $\alpha$  and [NII] values, although slightly lower. H $\alpha$  and [NII] sample has median flux of  $1.9 \times 10^{-16} \text{erg s}^{-1} \text{cm}^{-2}$  and  $7.7 \times 10^{-17} \text{erg s}^{-1} \text{cm}^{-2}$ , and median luminosity ( $\log L$ ) of  $41.0 \text{erg s}^{-1}$  and  $40.6 \text{erg s}^{-1}$ , respectively.

### 5.2.2.3 Morphologies of the [OIII] and H $\beta$ emitters

In this work we used morphological classification from [Beyoro-Amado et al. \(2019\)](#), described in Chapter 4. Moreover, [Treu et al. \(2003\)](#) and [Moran et al. \(2007\)](#) have previously carried out a visual classification within 5 Mpc of the cluster centre. In all these works galaxies have been classified between ET and LT. After cross-matching our data with all the three references, we found morphological classes for 24 [OIII] emitters (8 ET and 16 LT), and 41 H $\beta$  sources (13 ET and 28 LT), leaving significant number of sources without classification. This could be because [Beyoro-Amado et al. \(2019\)](#) classification is only within 1 Mpc and others give classification only for brightest sources. This gives us similar fractions of ETs (33% for [OIII] and 32% in case of H $\beta$ ), and LTs (67% for [OIII] and 68% for H $\beta$ ).

As expected, we found a larger populations of LT galaxies, and on average their [OIII] and H $\beta$  emission lines are similar to those of ETs. Median logarithmic luminosities ( $\log L$ ) of LT and ET are  $40.59 \text{erg s}^{-1}$  and  $40.54 \text{erg s}^{-1}$  in the case of [OIII], and  $40.68 \text{erg s}^{-1}$  and  $40.62 \text{erg s}^{-1}$  in the case of H $\beta$ , respectively. The morphological distributions of the identified line emitters within the cluster is plotted against the clustercentric distance and are presented in Fig. 5.9, where the top panel stands for [OIII] line emitters while the bottom panel describes H $\beta$  line emitters.

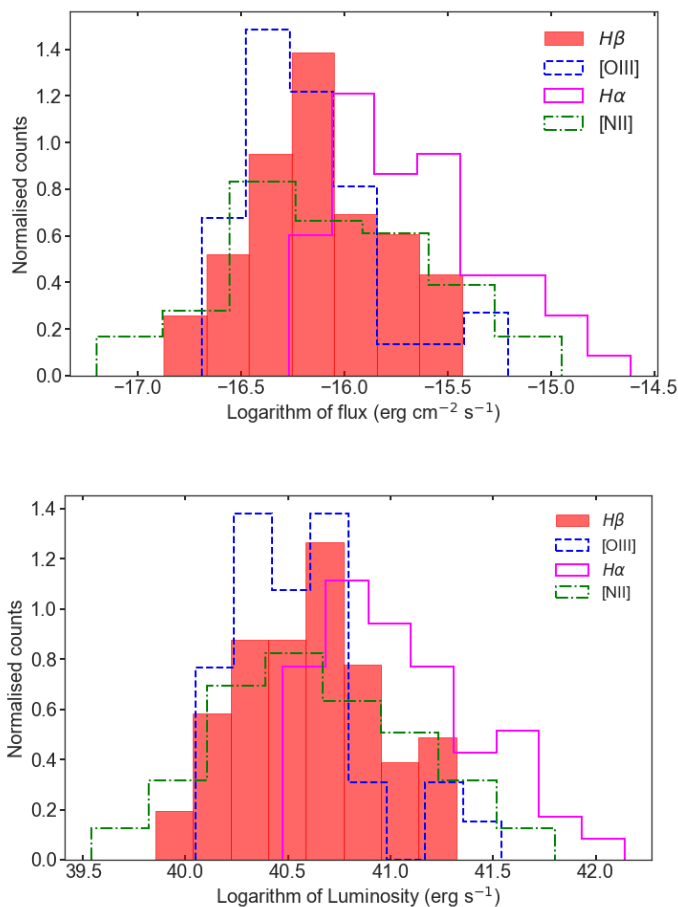


**Figure 5.8:** Comparison of the flux (top plot) and luminosity (bottom plot) of  $H\beta$  (red filled histogram),  $[OIII]$  (blue dashed line),  $H\alpha$  (violet solid line), and  $[NII]$  (green dash-dotted line) ELGs.

#### 5.2.2.4 AGN versus SF classes: BPT diagrams

Out of 174 ELGs identified in our  $H\alpha$  survey, we detected all targeted emission lines ( $[OIII]$ ,  $H\beta$ ,  $[NII]$  and  $H\alpha$ ) for 20 sources (as described in Table 5.1). For these sources we checked their spectral type using the BPT-NII diagnostic diagram (Baldwin et al., 1981; Kewley et al., 2006b), separating galaxies into star-forming (SF), composite and AGN (Seyfert-2 or LINERs), as shown in Figure 5.10. As a previous step, we segregated the 15 sources in our sample classified as broad-line AGNs (BLAGN) in Sánchez-Portal et al. (2015). We identified 9 ELGs with  $[OIII]$ ,  $[NII]$  and  $H\alpha$  detections and  $H\beta$  non detected, as well as 28 ELGs with  $H\beta$ ,  $[NII]$  and  $H\alpha$  flux measurements but without detection of the  $[OIII]$  line. In order to include these sources in the BPT-NII plot we used the flux limits shown in Table 5.2 to assign upper bounds to non-detections, which are represented with upward

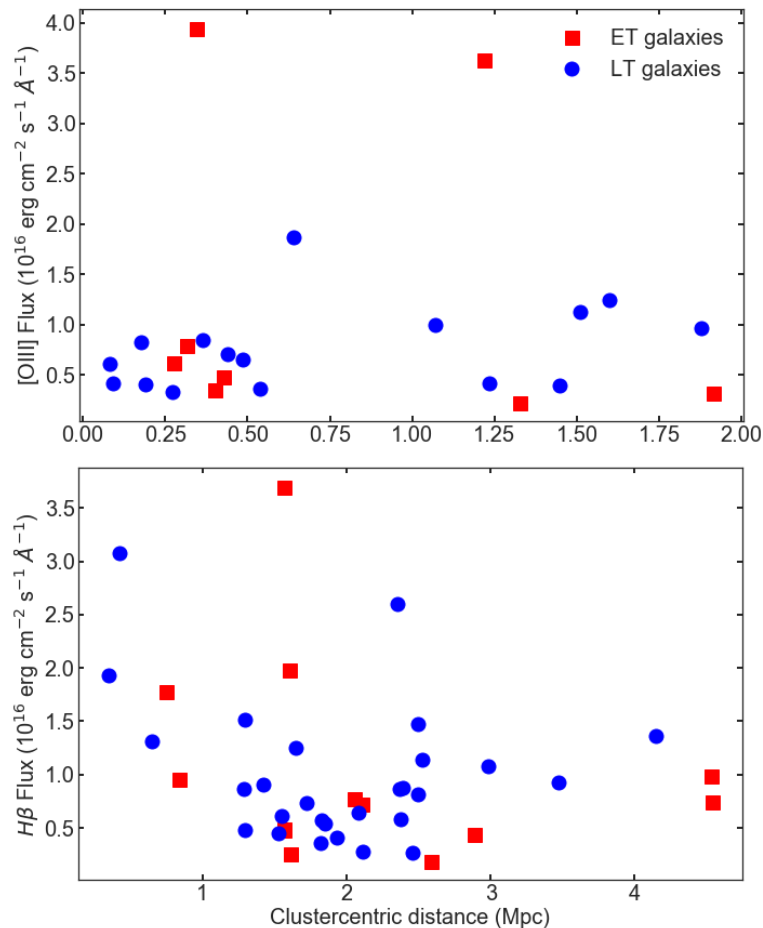


**Figure 5.9:** The existing morphologies of the sources with emission lines described only as ET or LT. The line fluxes are plotted as a function of radial distance, for [OIII] lines at top while H $\beta$  emitters in the bottom panel.

or downward arrows in this figure. The boundary between SF and composite galaxies was taken from [Kauffmann et al. \(2003\)](#), and between composite and AGNs from [Kewley et al. \(2001\)](#). To separate between LINERs and Seyfert–2 galaxies we used the prescription from [Schawinski et al. \(2007\)](#). The minimum and maximum limits (for [OIII]/H $\beta$  and [NII]/H $\alpha$ ) were adapted from [Kewley et al. \(2006b\)](#). Although all of these boundaries have been established using a sample of galaxies with redshifts  $z < 0.1$ , and although our cluster galaxies are at  $z \sim 0.4$ , we consider no significant evolution taking into account results of [Kewley et al. \(2013a\)](#) verifying that the relation remains valid up to  $z \sim 1$ .

In our cluster sample, we found a total of 29 ( $\sim 51\%$ ) SF galaxies (8 with all emission lines, 4 with no H $\beta$  detection, 17 with no [OIII] detection), 23 ( $\sim 40\%$ ) composites (11 with all emission lines, 2 with no H $\beta$  detection, 10 with no [OIII]

**Table 5.4:** Summary of our spectral classification of galaxies in ZwCl0024+1652 cluster using BPT diagram as shown in Figure 5.10.

<b>Emission</b>	<b>SF</b>	<b>Comp.</b>	<b>AGN(Sy2+LINER)</b>	<b>Total</b>
No H $\beta$ detection	4	2	3	9
No [OIII] detection	17	10	1	28
All lines detected	8	11	1	20
Total	29	23	5	57

detection), 1 ( $\sim 2\%$ ) LINER galaxy with all emission lines and 4 ( $\sim 7\%$ ) Seyfert–2 ELGs (1 with no [OIII] detection and 3 with no H $\beta$  detection). The results of our classification are summarised in Table 5.4.

Additionally, we selected all the galaxies with detected emission in the chemical species cited above from the VVDS-Deep field sample described in Section 2.2.3.3. From 177 field sources we identified 41 sources having all the four lines. We segregated 32 ( $\sim 78\%$ ) SF galaxies, 7 ( $\sim 17\%$ ) composite, and 2 ( $\sim 5\%$ ) Seyfert–2 galaxies, also represented in Figure 5.10 (open symbols). According to this, with the caveat regarding the small-number statistics, there are  $\sim 1.5$  times more SF galaxies in the field and almost one-third less AGN+composite galaxies than in cluster galaxies. These differences are about three times the mean uncertainty derived from a Poissonian statistics derived from the absolute numbers of field galaxies belonging to each spectral type.

Hereafter, and in order to overcome the limitation imposed by the need of simultaneous detection of both the [OIII] and H $\beta$  lines, we will use the simplified criterion applied by Sánchez-Portal et al. (2015) to separate SF galaxies from AGN hosts, based on the prescription of Kauffmann et al. (2003), namely the boundary defined by the flux ratio [NII]/H $\alpha$  = 0.478. With this assumption, the analysis and discussion described in the following sections is based on a segregated total of 35 SF galaxies and 22 AGN hosts. We compared our results here with statistics from Sánchez-Portal et al. (2015). Out of 174 ELGs in Sánchez-Portal et al. (2015), 60 ( $\sim 34\%$ ) were AGN hosts while 114 ( $\sim 66\%$ ) were found to be SF galaxies. Our work gave similar results with nearly comparable distribution:  $\sim 38.5\%$  AGN hosts with  $\sim 61.5\%$  SF galaxies. The sky distribution of H $\alpha$  sample including our [OIII] and H $\beta$  results is presented in Figure 5.11. The sky positions of the ELGs is described on a blended image of an inverted RGB composed of deep images determined as in Section 3.1.1.5 with H $\alpha$  image. Finally, applying the same rule to the VVDS-Deep population, we segregated a total of 39 SF field galaxies and 7

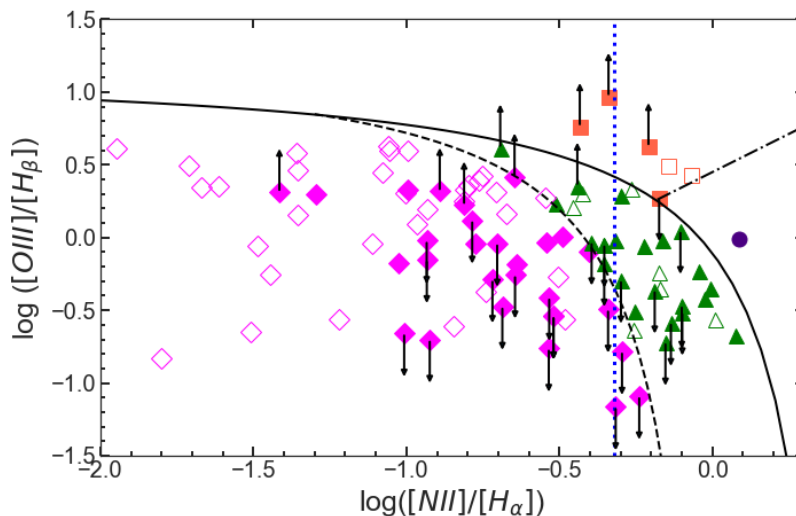


**Figure 5.10:** BPT diagram for separating SF (magenta), composite (green), Seyfert-2 (red) and AGN-LINER (indigo) ELGs. Filled symbols represent the cluster sources and the open ones the field galaxies. The arrows correspond to the cluster ELGs with either [OIII]- or  $H\beta$ -only line detection (upward for [OIII], while downward for  $H\beta$ ). Continuous, dashed, and dot-dashed lines correspond to the boundaries given by Kewley et al. (2006b), Kauffmann et al. (2003) and Schawinski et al. (2007), respectively. The vertical dotted line marks the SF-AGN separation, as suggested by Kauffmann et al. (2003). More details are given in text.

AGN hosts. A broader discussion on comparison between cluster and field galaxies is given in Section 5.2.3.4.

### 5.2.2.5 Extinction-corrected star formation rate

We used the total  $H\beta$  flux, measured as the sum of the emission and absorption components computed as explained earlier, to obtain the extinction correction from the Balmer decrement  $f_{H\alpha}/f_{H\beta}$  using Equation 5.6 below:

$$A_{H\alpha} = \frac{2.5}{k_{H\alpha}/k_{H\beta} - 1} \log \left( \frac{1}{2.85} \frac{f_{H\alpha}}{f_{H\beta}} \right), \quad (5.6)$$

where  $k_{H\alpha}/k_{H\beta} = 1.48$  for the galactic extinction law from Seaton (1979). The distribution of the computed extinction values is represented in Figure 5.12. The largest peak corresponds to unabsorbed galaxies ( $A_{H\alpha} \simeq 0$ ). This could be expected since, due to the incompleteness of the  $H\beta$  sample (the  $H\beta$  line is actually detected for 59 galaxies ( $\sim 34\%$ ) out of 174  $H\alpha$  emitters), our observations favour the

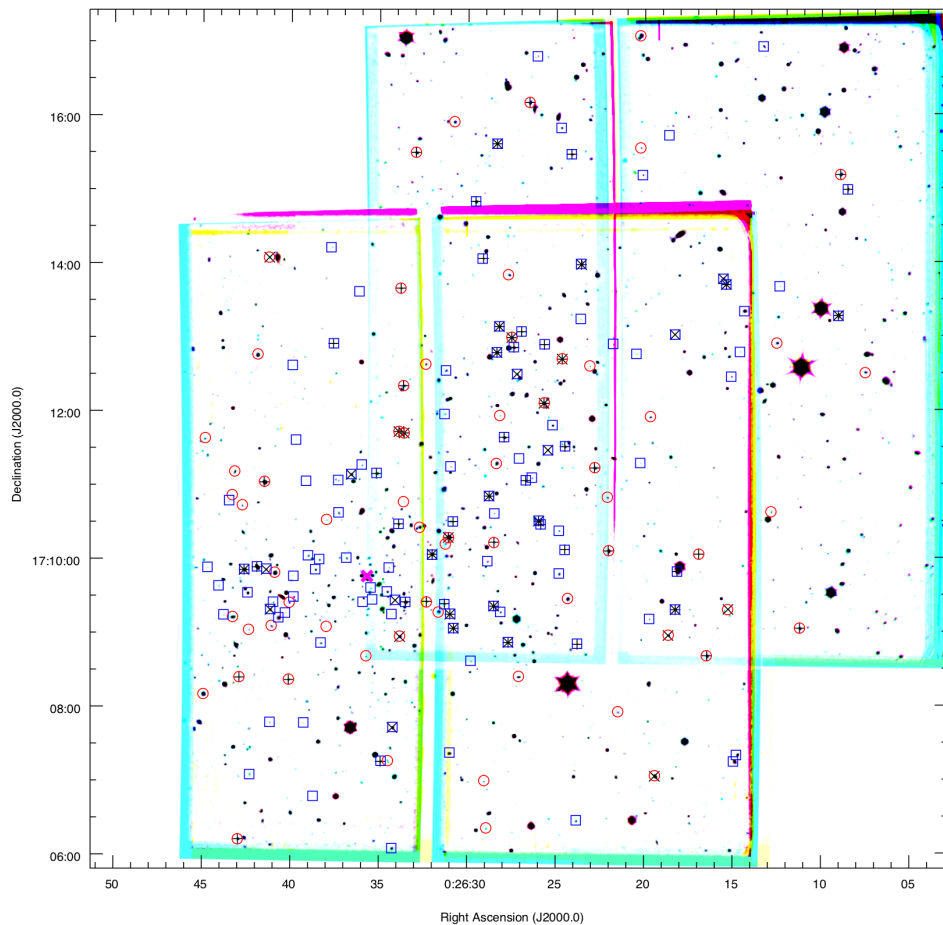


**Figure 5.11:** RGB mosaic ( $H\alpha$ ,  $[OIII]$ , and  $H\beta$ , respectively) of the OSIRIS/GTC deep images of ZwCl0024+1652. Blue squares correspond to SF galaxies and red circles represent AGN hosts, as provided by [Sánchez-Portal et al. \(2015\)](#). The “X” symbols denote  $[OIII]$  emitters while “+” signs represent  $H\beta$  ELGs from our work. The magenta cross ( $\times$ ) denotes the centre of the cluster (galaxies/BCG).

detection of strong  $H\beta$  emitters, i.e. intrinsically luminous sources or unabsorbed ones. On the other hand, a second peak close to  $A_{H\alpha} \simeq 0.75$  is observed, which is consistent with the usual assumption ( $\sim 1$  mag) after [Kennicutt \(1992\)](#).

The relative error in the Balmer decrement, as computed by error propagation, is on average 27.1/37.5% (median/mean). This translates into an uncertainty of about 0.8 mag in the extinction at the  $H\alpha$  line. More precisely, the average uncertainty obtained by error propagation from equation 5.6 is about 0.88 mag. Once we derive the extinction correction, the SFR can be computed using a suitable scaling relation, as given by [Kennicutt \(1998\)](#):

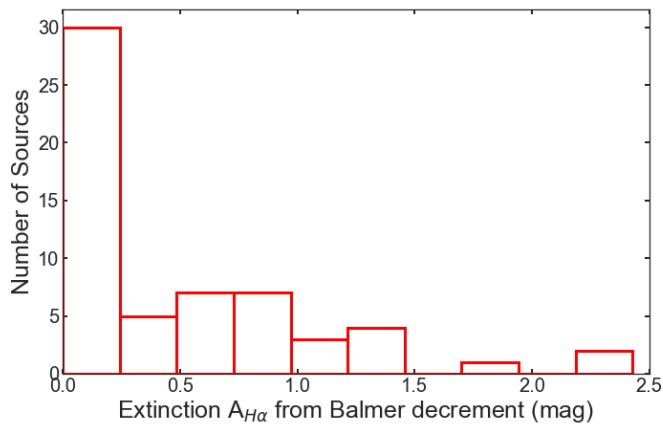


**Figure 5.12:** Distribution of extinctions derived from the Balmer decrement, assuming a galactic extinction law of [Seaton \(1979\)](#).

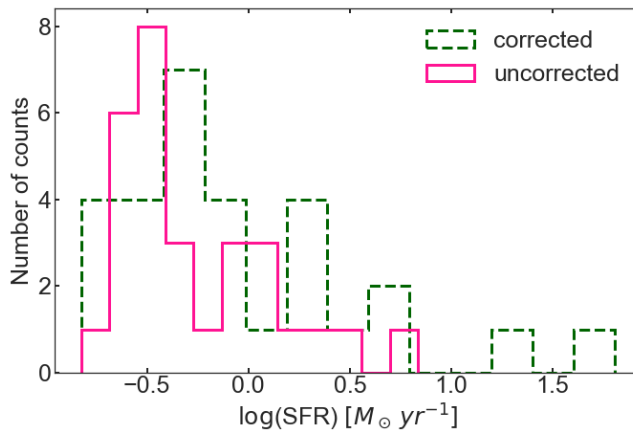


**Figure 5.13:** Distribution of the logarithm of corrected and uncorrected SFR.

$$SFR(M_{\odot}yr^{-1}) = \frac{10^{A_{H\alpha}/2.5}}{1.58} 7.94 \times 10^{-42} L(H\alpha)(ergs^{-1}), \quad (5.7)$$

where the factor 1.58 corresponds to the conversion from Salpeter to [Chabrier \(2003\)](#) initial mass function (IMF). The distribution of the uncorrected SFR and  $H\alpha$  SFR corrected using equation 5.7 are compared in Figure 5.13.

The errors in both the uncorrected and corrected SFR have been computed as usual by propagation. The average uncertainty in the uncorrected SFR is 19.5/20.9% (median/mean). However, given the large uncertainty in  $A_{H\alpha}$ , the fractional errors in the corrected SFR are much larger, 67.3/71.2% (median/mean) in our case.



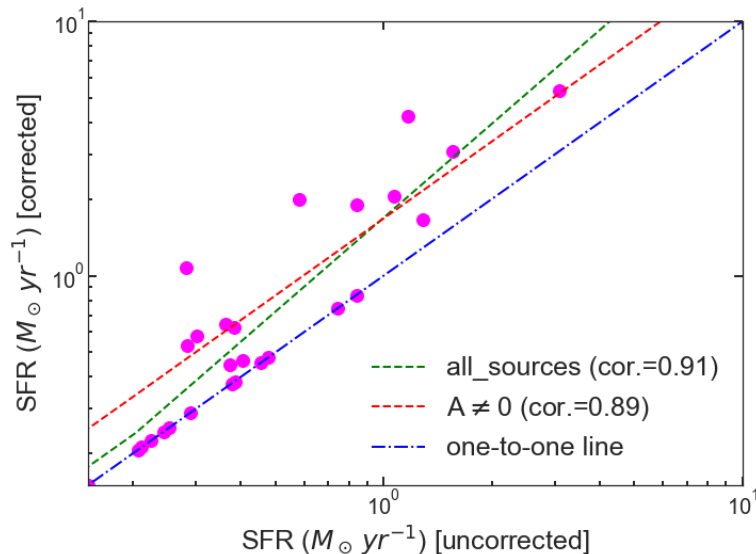


**Figure 5.14:** Relation between extinction corrected and uncorrected SFR for ZwCl0024+1652. Blue dash dotted solid and dashed green lines show one-to-one correlation and linear fit for all sources, respectively. While the dashed red line represents the linear fit by excluding those galaxies with zero extinction.

The correlation between the uncorrected and corrected SFR is depicted in Figure 5.14. Even though the results should be taken with caution, given the large uncertainties involved, a quite clear correlation is observed. Moreover, if the range is restricted to  $\text{SFR}_{\text{H}\alpha, \text{corrected}} < 12 M_{\odot} \text{ yr}^{-1}$ , thus avoiding two objects that are luminous and highly absorbed ( $A_{\text{H}\alpha} = 2.43 \text{ mag}$ ), a reasonable linear correlation equal to 0.91 with slope of 1.23 is observed considering all the sources including sources with  $A_{\text{H}\alpha} = 0$  (green dashed line in Figure 5.14), while excluding the sources with  $A_{\text{H}\alpha} = 0$ , the correlation factor is changed slightly to 0.89 with 1.00 being a new slope (red dashed line in Figure 5.14). We performed a quantitative comparison between the two (uncorrected and corrected SFR) by using Kolmogorov–Smirnov two sample (KS2) test. We computed the p-value of our data to be 0.28, showing that both are coming from the same distribution.

## 5.2.3 Discussions with ZwCl0024+1652 results

### 5.2.3.1 Morphological and spectral classes of the cluster members with [OIII] and $\text{H}\beta$ emission

In [Beyoro-Amado et al. \(2019\)](#) it was discussed in detail that the morphological fractions of ZwCl0024+1652 member galaxies vary with clustercentric distance

in such a way that ET galaxies dominate over the LTs at least up to a clustercentric distance of  $\sim 1$  Mpc. Other studies also suggested that the cores of nearby clusters have lower LT than the ET fraction, and that LT fraction increases with clustercentric distance while the ET fraction decreases (e.g., [Whitmore et al., 1993](#); [Fasano et al., 2012](#); [Fasano et al., 2015](#); [Pintos-Castro et al., 2016](#); [Kelkar et al., 2019](#)). In addition to this, [Oh et al. \(2018\)](#) showed that beside ET galaxies passive spirals can also be found in highly dense regions, such as cluster centres, suggesting that they have gone through environmental quenching. Our TF [OIII] and  $H\beta$  observations result with detection of the brightest sources. As showed in Section 5.2.2.3, despite small sample our results show that LT galaxies dominate over the ETs when dealing with ELGs, as expected. In addition to this, our results are in general in line with previous ones where LT galaxies show to be in average at larger clustercentric distances (e.g., [Nantais et al., 2013](#); [Fasano et al., 2015](#)). We found that median clustercentric distances of LT and ET ELGs are 1.82 Mpc and 1.60 Mpc when dealing with [OIII] emitters and 1.93 Mpc and 1.61 Mpc in the case of  $H\beta$  emitters, respectively. However, taking into account Figure 5.16 where local density is represented in relation to clustercentric distance it can be seen that LT ELGs are more dispersed along the clustercentric distance than ETs. We also present a phase-space relation of  $H\beta$  and [OIII] ELGs separated with morphology in Figure 5.15. Apart from small statistics, from Figure 5.15 we deduce that the inner most region of the cluster (projected clustercentric distance  $\lesssim 0.3$  Mpc) is almost devoid of ELGs with morphologies (ET as well as LT). Moreover, from Figure 5.16 taking the morphological distributions in relation to radial distance, we can be see that LT ELGs are more dispersed along the clustercentric distance than ETs. In addition to the results obtained in [Beyoro-Amado et al. \(2019\)](#) we can now see from the current work using TF [OIII] and  $H\beta$  data that ET galaxies with signs of either AGN or SF activity seem to avoid the most dense central parts of regular clusters such as ZwCl0024+1652.

Another point that we rise here is the distribution of spectral types within the cluster. Previous works showed that cores of well formed (or regular) galaxy clusters are characterised by high density while density decreases outwards with clustercentric distance (e.g., [Treu et al., 2003](#); [Weinmann et al., 2006](#); [Fasano et al., 2015](#)). Our results presented in Figure 5.16 agree with these results. When representing all ELGs that belong to the principal cluster structure, anti-correlation can be observed between  $\Sigma_5$  and clustercentric distance. This monotonic relation of local density to the clustercentric distance indicates that our cluster is

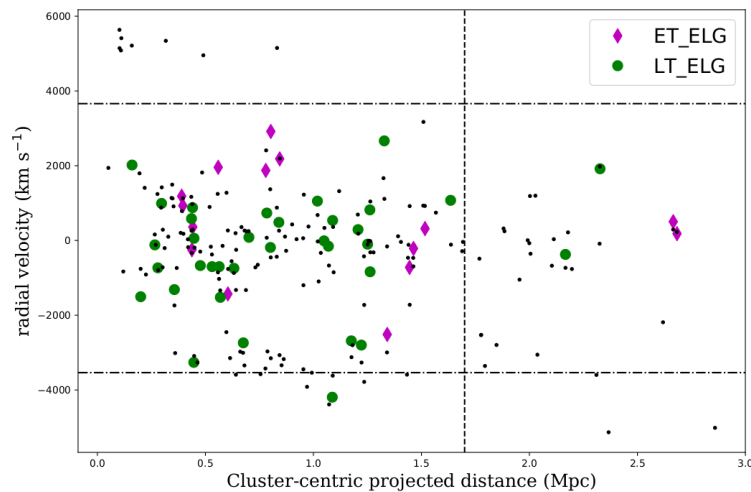


**Figure 5.15:** Radial velocity versus clustercentric distance for  $H\beta$  and  $[OIII]$  ELGs with morphological classifications. Magenta diamonds represent ETs while green dots correspond to LT galaxies. The virial radius ( $r_{\text{vir}} = 1.7\text{Mpc}$ ) (Treu et al., 2003) is represented by dotted vertical line. The dashed-dotted horizontal lines stand for the radial velocity limits fully covered within the field of view of the two OSIRIS TF pointings. The small black points correspond to ELGs with  $H\alpha$  emission from Sánchez-Portal et al. (2015).

a regular one. Taking into account Figure 5.16, and a small number of SF and AGN sources in the central part of cluster, our results are in line with previous findings which suggest that the number of SF galaxies (e.g., Gómez et al., 2003; Christlein and Zabludoff, 2005; Hansen et al., 2009; von der Linden et al., 2010) and AGN (e.g., Gavazzi et al., 2011; Davies et al., 2017; Marshall et al., 2018; Li et al., 2019; Koulouridis and Bartalucci, 2019) decreases towards the cluster centre. The majority of SF galaxies and AGN found in this work are distributed at clustercentric distances  $> 1.3\text{Mpc}$ . Moreover, the results obtained by Deshev et al. (2017) while analysing the evolution of galaxies in merging clusters with special focus on A520 at  $z=0.2$ , indicate that the core of such clusters up to a clustercentric distance of 1.5 Mpc is almost devoid of SF galaxies. Since it is well known that ZwCl0024+1652 cluster is a merging cluster (Czoske et al., 2002; Jee et al., 2007), our findings confirm the existing results.

### 5.2.3.2 Colour and stellar masses

In this section, we discuss some of the galaxy parameters such as colours and stellar masses, in relation to the SF and AGN properties. To begin with, we plotted a colour-magnitude diagram (CMD) for the cluster emitters detected in

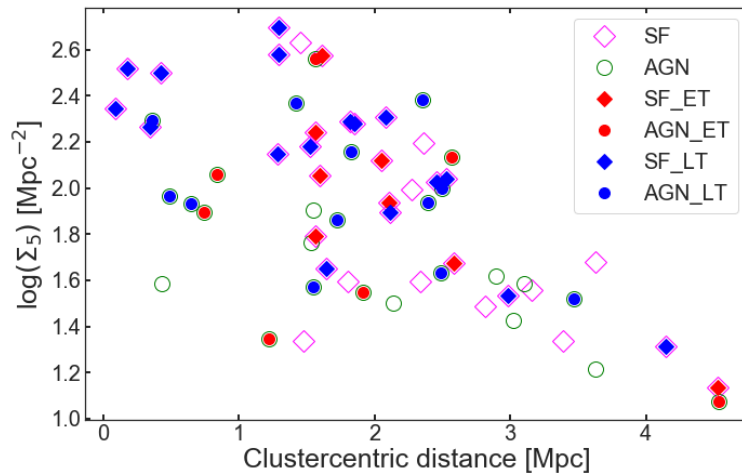


**Figure 5.16:** Dependence of the local density on the clustercentric distance of all SF galaxies (magenta open diamonds) and AGN (green open circles) that belong to the main cluster structure. Blue and red symbols stand for LT and ET galaxies, respectively.

both [OIII] and  $H\beta$ , with public photometric data gathered from [Treu et al. \(2003\)](#) and [Moran et al. \(2005\)](#). We applied the k-correction as in Section 4.2.2.4, to get the rest frame B - R colour and the absolute magnitude in B. Figure 5.17 shows the relation between these variables for all [OIII] and  $H\beta$  emitters. To separate a blue cloud (BC) and red sequence (RS) we introduced a horizontal line at  $B - R = 1.39$  as given by [Sánchez-Portal et al. \(2015\)](#). We determined that only 6 sources (9%) would belong to the RS while majority (64) of the sources (91%) remain in the BC region, as expected. The plot includes distributions of both analysed parameters. We do not find any significant difference in the distribution of  $H\beta$  and [OIII], and most of the sources in both cases (85% for [OIII] and 97% for  $H\beta$ ) are in the BC, as expected. For the galaxies identified on the CMD, 27 and 13  $H\beta$  emitters are LT and ET, respectively. In the case of [OIII] emitters 14 and 8 sources have LT and ET morphologies, respectively. A total of 69 galaxies have spectroscopic classification available, where 42 (60%) and 27 (40%) galaxies are SF and AGN, respectively.

Stellar mass is another parameter that plays an important role in determining different galaxy parameters such as SFR and sSFR. Previous studies at different redshifts (from the local universe to  $z \sim 2$ ) confirm that stellar mass plays a leading role in determining SFR (e.g., [Koyama et al., 2013](#); [Darvish et al., 2016](#); [Laganá and Ulmer, 2018](#); [Pintos-Castro et al., 2019](#)). Using a sample of SDSS galaxies

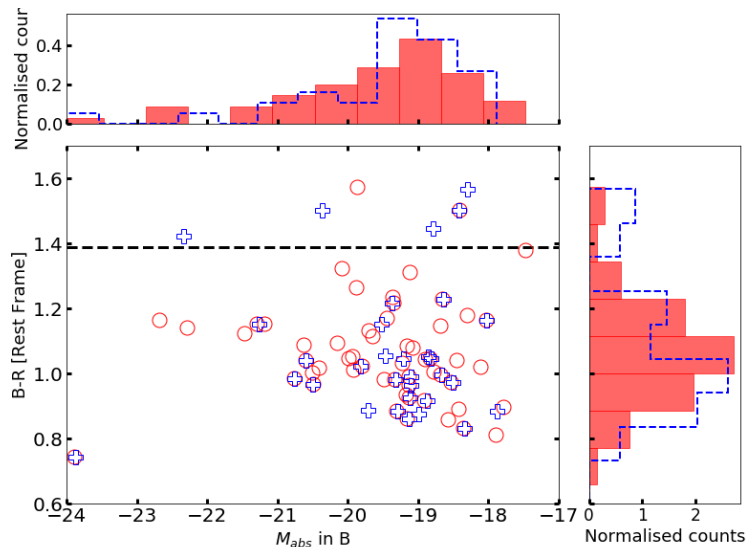


**Figure 5.17:** B-R rest-frame colour versus absolute magnitude  $M_B$ , for the case of ZwCl0024+1652. The blue crosses represent [OIII] emitters while red circles stand for  $H\beta$  emitters.

in groups, Li et al. (2019) reported higher SF fractions at all clustercentric distances for lower stellar masses, and higher stellar masses of AGN host galaxies. Moreover, at higher redshifts ( $z \sim 1-2$ ) lower masses of galaxies in clusters are accompanied by enhanced star formation (e.g., Brodwin et al., 2013; Alberts et al., 2016) with a peak value at  $M_* \simeq 10^{9.8} M_\odot$  (Patel et al., 2011). In our case, the stellar mass was computed for each cluster galaxy with LePhare code using BC03 templates, as mentioned in Section 5.2.1.3. The mass distribution of our base sample ( $H\alpha$  sample) and consecutive sub-samples ( $H\beta$  and [OIII] emitters) is presented in Figure 5.18 and statistically described in Table 5.5. From Table 5.5 the mass distributions for the base sample and consecutive ELG samples are similar, with 50% of the sample having in all cases masses in the range about 9.20–10.39, with median of  $\sim 9.9$ . From the histogram (Figure 5.18) and the statistics we can see that our consecutive samples cover a complete range of masses from the base  $H\alpha$  sample. In the following paragraphs, we discuss different galaxy properties in relation to the effects of stellar mass.

In the first place, we have investigated the behaviour of the SFR and sSFR with stellar mass, as depicted in Figure 5.19. Following Laganá and Ulmer (2018), we further discern between active star-forming galaxies and those in quenching phase, both in field and cluster environments. For this purpose, we used the redshift-dependent sSFR cut, such that  $sSFR(z) = 10^{-10} \times (1+z)^3$ , given by Koyama et al. (2013) and the result for cluster galaxies is summarised in Table 5.6. In Figure 5.19,

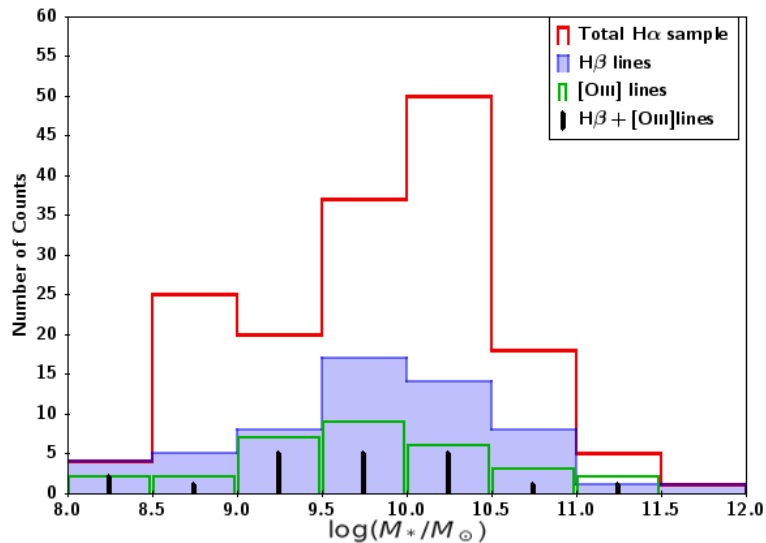


**Figure 5.18:** Distribution of the stellar masses. The base sample ( $H\alpha$  emitters) is represented with red lines,  $H\beta$  lines with blue shaded bars,  $[OIII]$  emitters with green lines and the black lines represent galaxies with both  $H\beta$  and  $[OIII]$  emission.

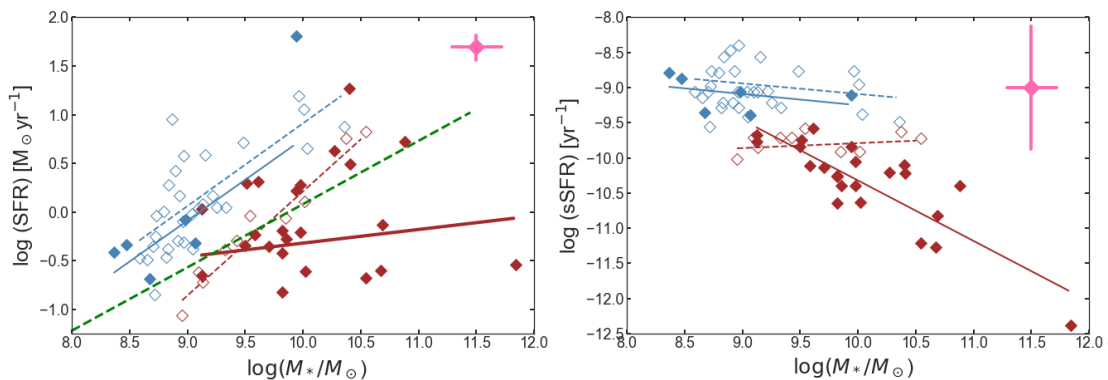
**Table 5.5:** Statistical description of stellar masses ( $\log(M_*/M_\odot)$ ) of our base  $H\alpha$  sample (Sánchez-Portal et al., 2015) with consecutive identification of  $H\beta$  and  $[OIII]$  emissions.

$\log(M_*/M_\odot)$ of	$Q_1$	Median	$Q_3$
$H\alpha$ base sample	9.16	9.97	10.39
$H\beta$ line emitters	9.22	9.82	10.39
$[OIII]$ line emitters	9.22	9.82	10.39
Both $H\beta+[OIII]$ line emitters	9.16	9.82	10.39

representative average error bars are shown in the plots with average values being 9.37, 0.587 and -10.09, for  $\log(M_*)$ ,  $\log(SFR)$  and  $\log(sSFR)$ , respectively. The upper and the lower error limits are determined for each of these parameters. As in Section 5.2.3.3, we have observed a rather different behaviour in active SF and quenched galaxies. The distribution of quenched galaxies extends to higher masses than that of active SF ones, in good agreement with previous results. On the other hand, we observed that the  $\log(M_*/M_\odot)$ – $\log(SFR)$  relation of active SF galaxies can be well fitted by a straight line roughly parallel to the main sequence of SDSS SF galaxies (and to that of field galaxies at similar redshift, see Section 5.2.3.4). However, for quenched galaxies there is a much larger dispersion of values that a linear fit is not appropriate. In addition, the behaviour of the sSFR is again remarkable such that the sSFR declines mildly with stellar mass for active SF galaxies, but for quenched galaxies this trend is really outstanding, indicating a strong reduction of the SF efficiency with stellar mass. The SFR– $M_*$

**Table 5.6:** Summary of the placement of our sample SF galaxies into active or quenching phase.

Class	Cluster	Field
Active SF	6 (21%)	30 (75%)
Quenching SF	23 (79%)	10 (25%)
Total SF	29 (100%)	40 (100%)

**Figure 5.19:** Dependence of the SFR (left) and sSFR (right) on the stellar mass ( $M_*/M_\odot$ ) for cluster galaxies (filled diamonds with solid linear fittings) and for field galaxies (open diamonds with dashed linear fittings) at  $z \sim 0.4$ . Active SF and quenching-phase SF galaxies are discriminated with blue and brown colours, respectively. A representative average error bar for cluster SF galaxies is indicated in each plot with pink colour. The dashed green line (left panel) shows the SF main sequence of SDSS galaxies.

correlation in our results, and the anti-correlation of sSFR with  $M_*/M_\odot$  conforms with existing results (e.g., Vulcani et al., 2010; Speagle et al., 2014; Vulcani et al., 2015; Guglielmo et al., 2019, and references therein). Concerning the morphologies of SF galaxies, the number of classified galaxies is very low, especially when dealing with ETs. In general, most of LT galaxies are observed to be located slightly below the SDSS main sequence of SF, while the existing small number of ETs has been found above the line.

Second, we have studied the dependence of the SF and AGN fractions on the stellar mass. The distributions of stellar masses of our sample of ELGs and that of the ancillary  $H\alpha$  cluster catalogue follow a similar, bimodal profile with two local maxima at the low- and high-mass ends. The low-mass maximum is placed around  $\log(M_*/M_\odot) = 9$  for both distributions. The high-mass local is placed at  $\log(M_*/M_\odot) \simeq 9.8$  and  $\simeq 10.5$  for our ELGs and the overall population, respectively. The mass distributions of the overall  $H\alpha$  emitting cluster sample and our ELGs are presented in Figure 5.20.

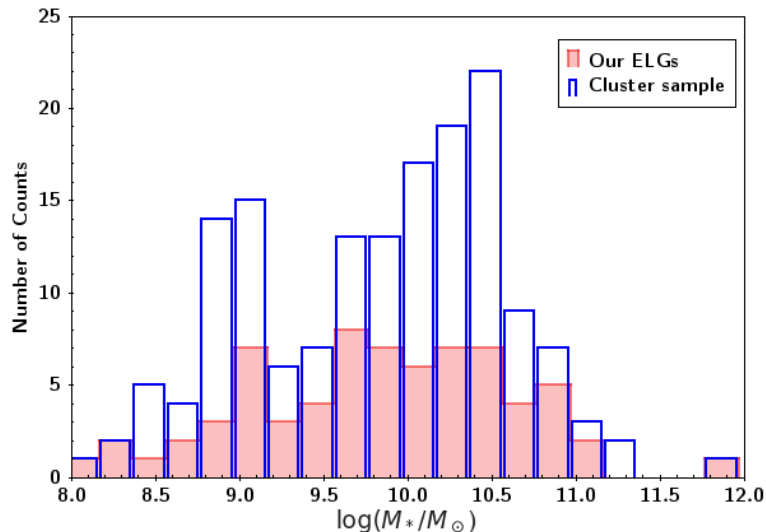


**Figure 5.20:** Distribution of the stellar masses of our H $\beta$  and/or [OIII] ELGs (red filled histograms) and H $\alpha$  cluster sample (blue open histograms).

We finally discuss the effect of stellar masses to the SF and AGN fractions. Within the footprint of the GLACE observations, we have 359 galaxies in the ancillary catalogue of cluster members with derived stellar masses. We have divided the sample into three bins, namely low- ( $\log(M_*/M_\odot) < 9.5$ ), medium- ( $9.5 \leq \log(M_*/M_\odot) < 10.5$ ) and high-mass ( $\log(M_*/M_\odot) \geq 10.5$ ) with 109, 135 and 115 galaxies, respectively. The fraction of SF galaxies as a function of the stellar mass is depicted in the right panel of Figure 5.23. There is a strong decline in the fraction of SF galaxies in the high-mass bin, confirming that SF is highly suppressed in cluster high-mass galaxies. This agrees with results of [Stasińska et al. \(2015\)](#) whose study implemented the BPT and WHAN diagrams ([Cid Fernandes et al., 2011](#)). For high mass bin, the small fraction of SF galaxies in our cluster could be because the galaxies in this bin could have formed almost all the stars at redshifts higher than  $z \sim 0.4$ . Finally, the fraction of AGN galaxies as a function of the stellar mass is depicted in the right panel of Figure 5.24. There is a slight decline of the fraction of AGNs both at the low- and high- mass bins, although not very significant.

### 5.2.3.3 The phase-space relation and the local density effects

We adopted the centre coordinates of the cluster from the results of [Diaferio et al. \(2005\)](#) given as  $RA_c = 0^h 26^m 45.9^s$  and  $DEC_c = 17^d 9^m 41.1^s$ . Taking into account the distance of the cluster of 1500 Mpc and following the procedure outlined in



Beyoro-Amado et al. (2019), we computed the clustercentric distance of each identified ELG. The radial velocity was also computed and the phase-space diagram was plotted to identify the distribution of the sources (both [OIII] and H $\beta$  emitters) as shown in Figure 5.7. We limited the sample to the main structure of the cluster ( $0.385 < z < 0.41$ ) and excluded the BLAGN galaxies as described in Section 5.2.2.4. The resulting distributions of H $\beta$  and [OIII] line emitters in clustercentric distance are given in Figure 5.21. Moreover, the phase-space diagram with two plots (for H $\beta$  and [OIII]) showing the line of site velocity versus the projected clustercentric distance is introduced in Section 5.2.2, Figure 5.7. Combining the relationships observed from both informations (clustercentric distance distribution and phase-space diagrams) one can comment on the location of member galaxies inside the cluster (e.g., Jaffé et al., 2015). From the plots in Figures 5.7 and 5.21 it can be seen that [OIII] emitters are relatively closer to the cluster centre than H $\beta$  line emitters despite all our emitters are within  $r_{\text{vir}}$  of our cluster. One of these sources has one of the highest dust extinctions ( $A_{\text{H}\alpha} = 2.43$  mag). For the remaining three [OIII]-only SF galaxies we estimated extinctions using the H $\beta$  limiting flux given in Table 5.2, obtaining  $A_{\text{H}\alpha}$  values between 1 and 2 mag. This fact could explain the lack of H $\beta$  detection for those objects. On the other hand, we verify that about half of [OIII]- and H $\beta$ -only emitters are located in intermediate clustercentric distances. The lack of [OIII]-only emitters at large clustercentric distances is intriguing, however we would need larger samples to confirm this and to understand the possible cause.

For discussion related to environment Concentrating in the main cluster structure, we found 35 SF galaxies and only 13 AGNs within the clustercentric distance range of 0-5 Mpc. Despite the small number statistics, we found that the AGN hosts belonging to the main structure of the cluster are concentrated inside  $\sim 1.5$  virial radii ( $\sim 3$  Mpc). This contrasts to the results given by Sobral et al. (2016), who do not found any strong dependence of AGN fraction on environment for the case of Cl 0939+4713 at  $z \sim 0.4$ . To support our results, we presented a phase-space relation in Figure 5.7 clearly representing the distribution of SF and AGN galaxies with [OIII] and H $\beta$  emission lines. Our findings are in line with previous results at intermediate redshifts reporting that the fraction of AGN increases with clustercentric distance, confirming the environment dependence on AGN activity (e.g., Argudo-Fernández et al., 2018; Koulouridis and Bartalucci, 2019; Mishra and Dai, 2020). On the other hand, SF galaxies are distributed across all measured

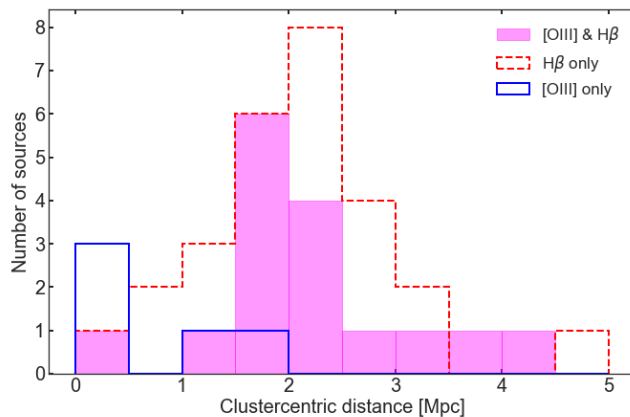


**Figure 5.21:** Distribution of [OIII] and H $\beta$  emission lines in ZwCl0024+1652 cluster with clustercentric distance, for members of the main cluster structure.

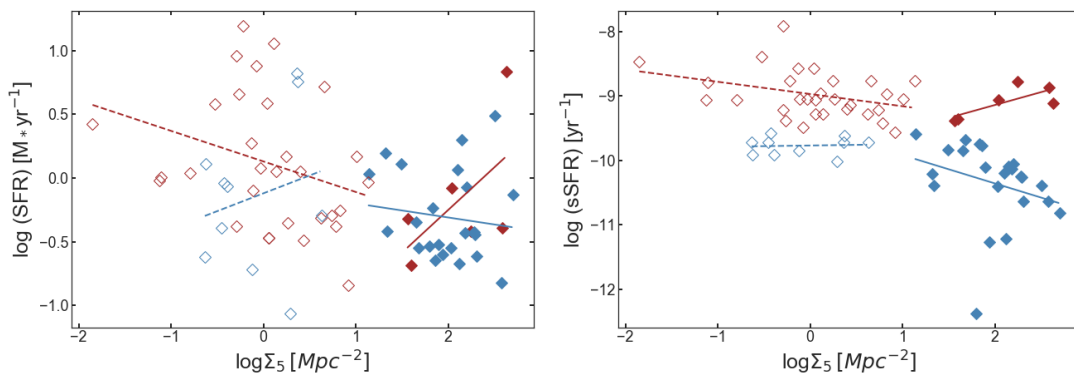


**Figure 5.22:** Dependence of the SFR (left) and sSFR (right) on the local density ( $\Sigma_5$ ) for cluster galaxies (filled diamonds with solid linear fittings) and for field galaxies (open diamonds with dashed linear fittings) at  $z \sim 0.4$ . Active SF and quenching-phase SF galaxies are discriminated with brown and blue colours, respectively.

clustercentric distances, but they are preferentially located between 0.5 and 1.5 virial radii, with the bulk of SF galaxies exhibiting the lowest extinction values.

The environment conditions were parametrised by the local surface density computed by Pérez-Martínez et al. (in prep.) from the distance to the 5<sup>th</sup>-neighbour ( $\Sigma_5$ ), using the algorithm from Dressler et al. (1985). We computed a valid local density estimation for 72 from 73 sources of the main sample. Using the same algorithm, we additionally computed the local surface density for VVDS-Deep field SF galaxies selected as described in Section 2.2.3.3. Figure 5.22 describes the relationship of SFR and sSFR to local density where it is shown separately for active as well as quenching phase SF galaxies.

Previous studies suggested that, both in the local universe and at higher redshift, regions with higher projected local density are generally characterised by smaller fractions of galaxies with ongoing star formation (e.g., [Pimblet et al., 2002](#); [Gómez et al., 2003](#); [Kauffmann et al., 2004](#)). On the other hand, different works have shown that SF could be triggered and/or quenched by the nature of environment in which the galaxy is located, as can be described through relations between different parameters (such as colour, morphology, stellar mass and SFR) and environment (e.g., [Peng et al., 2010b, 2012](#); [Tomczak et al., 2019](#), and references therein). [Poggianti et al. \(2008\)](#) used the [OII] emission line as a proxy of the SFR of galaxies in clusters in the range  $0.4 < z < 0.8$ , showing that the SFR is lower in denser environments (see also [Rudnick et al., 2017](#)). Recently, [Laganá and Ulmer \(2018\)](#) derived the SFR of cluster galaxies at  $0.4 < z < 0.9$  from broadband SED fitting, and found no clear dependence between either SFR or sSFR and local environment. [Pintos-Castro et al. \(2013\)](#) studied the dependence of the SF activity derived from IR luminosity with local environment in a young galaxy cluster at  $z \sim 0.87$ , finding that the average SFR and sSFR are roughly independent of the local environment. However, the fraction of SF galaxies varies with the local density, being enhanced in the intermediate density regions and dropping in the highest local density ones. The same behaviour is observed in both high- and low-mass galaxies. From the projected phase space diagrams in [Figures 5.7 and 5.15](#) we have determined that the most central region of the cluster ( $r \lesssim 0.3$  Mpc) is almost devoid of ELGs, leading to a conclusion that the star formation and the AGN activity could be completely quenched. We can also deduce that almost all ELGs are located in the main cluster structure (structure “A”). In a recent work, [Pintos-Castro et al. \(2019\)](#) studied the population of SF galaxies within a sample of IR-selected galaxy clusters in the range  $0.3 \leq z \leq 1.1$  by means of broadband SED fitting, finding a decrease of the fraction of SF galaxies from field towards cluster cores, strongly dependent on stellar mass and redshift.

The relations among SFR and galaxy environment have been studied by many authors in our redshift range (e.g., [Vulcani et al., 2010](#); [Stroe et al., 2015](#)). We have explored the SF activity (as given by the SFR and sSFR) for the purely SF galaxies (after removing AGN sources) as a function of the environment, as depicted in [Figure 5.22](#). No clear correlation between the SFR and local density is observed for either active SF or quenched cluster galaxies, in line with previous results. However, for the sSFR we found a remarkable behaviour: the sSFR seems to be correlated with local density for active SF galaxies, and anti-correlated for

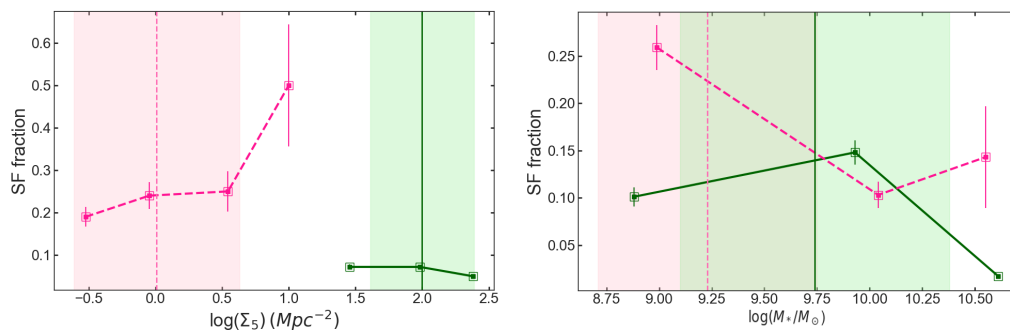


**Figure 5.23:** Variation of the fraction of SF galaxies versus local density (left panel) and stellar mass (right panel). The solid green lines show cluster galaxies and the pink dashed lines show field galaxies at  $z \sim 0.4$ . In the right panel, the sample is divided into three mass bins with low:  $\log(M_*/M_\odot) < 9.5$ , medium:  $9.5 \leq \log(M_*/M_\odot) < 10.5$  and high:  $\log(M_*/M_\odot) > 10.5$ . Error bars correspond to Poissonian statistics (see the text). Vertical lines represent the corresponding mean values with a light shaded standard deviation.

quenched ones. While the former relation is mild and could be impacted by the small size of the sub-sample (5 galaxies), the latter seems to be stronger and supported by the larger size of the set of quenched galaxies. Even though there is a mild, highly dispersed correlation between stellar mass and local density that can somehow contaminate the result, this finding suggests that star formation efficiency declines with the increase of the local density of the environment. Moreover, this trend, but with a slope about 1.4 times shallower, has been also reported by [Chung et al. \(2011\)](#) in a comprehensive study of a sample of 69 clusters at  $z < 0.1$ . Hence, this suggest a possible evolution of the quenching strength of SF galaxies, which evidently requires further studies. Moreover, morphologies of the SF galaxies have been observed against active and quenching SF phases. In active SF phase, 33% of galaxies with known morphologies are ET while 67% are LT. Similar has been found for quenching SF phase, where 37% and 63% of sources are ET and LT, respectively. Our results show that getting into quenching phase from active SF phase, the ET and LT proportions look nearly the same (with slight increase of ET fraction with a slight decrease in LT proportion), not exactly in line with previous results (e.g., [Kelkar et al., 2019](#)) that showed relatively suppressed SF in older stellar populations. That could be because of small statistics in our current work.

Finally, in order to investigate the dependence of the fraction of SF galaxies on the environment, we have determined the SF fractions as a function of the local density  $\Sigma_5$  as shown in the left panel of [Figure 5.23](#). As in [Pintos-Castro et al.](#)

(2013), we have followed the prescription of [Koyama et al. \(2008\)](#), who defined the intermediate density environment as a relative narrow range of local density where the optical colour distribution starts to change dramatically. According to their definition, the low-density environment corresponds to  $\log \Sigma_5 < 1.65$ , the medium-density range to  $1.65 \leq \log \Sigma_5 < 2.15$  and finally the high-density range to  $\log \Sigma_5 \geq 2.15$ . [Pintos-Castro et al. \(2013\)](#) demonstrated that the derived parameters are robust against small random variations of the boundaries, and therefore the selection does not condition the results of the environmental analysis. The total number of objects from the ancillary cluster catalogue within the sky area of our survey and with  $R_{AB} < 23$  are 86, 139 and 222 in the low-, medium- and high-density bins, respectively. The fractions were computed as the ratio of the number of SF galaxies in each bin to the total number of member galaxies in the same bin. The uncertainty in each fraction was computed as the ratio of the fraction in the bin to the square root of the total number of galaxies in that bin. It can be observed that the fraction of SF galaxies smoothly declines across the low- and medium-density bins, dropping towards the high-density region. Hence, we cannot support the claim of [Pintos-Castro et al. \(2013\)](#) that the intermediate density environment favours the enhancement of the SF activity, although it does not inhibit it (or quenching and triggering effects compensate). Authors of [Pintos-Castro et al. \(2013\)](#) gave results based on low ( $\log(M_*/M_\odot) < 10.5$ ) and high ( $\log(M_*/M_\odot) \geq 10.5$ ) mass bins, concluding that high density regions have scarcity of low mass SF galaxies. Moreover, they reported that high sSFR values are observed in low density regions, where high mass systems characterized by low sSFR dominate the high density environment. While examining our results in high and low mass bins as in [Pintos-Castro et al. \(2013\)](#) we observed significant number of low mass SF galaxies. In addition to this, we found that low mass SF galaxies possess high sSFR independent of environment while high mass SF galaxies in high density region have low sSFR values. Using the same bins and a similar procedure, we computed the AGN fraction, as shown in the left panel of [Figure 5.24](#), finding a similar trend as for SF galaxies, i.e. declining throughout the low- and medium-density environments and dropping sharply at higher densities. This is in line with previous results (e.g., [Li et al., 2019](#)). The mean local densities of SF galaxies and AGN are  $\log(\Sigma_5) [\text{Mpc}^{-2}] = 2.00 \pm 0.39$  and  $1.82 \pm 0.34$ , respectively.

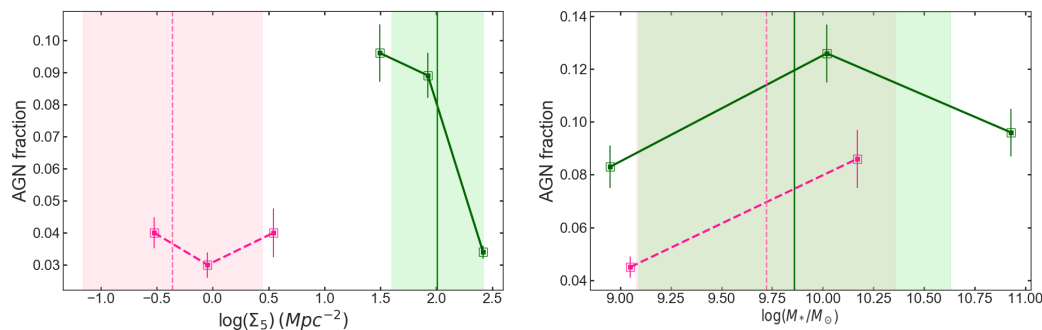


**Figure 5.24:** Variation of the fraction of AGN galaxies versus local density (left panel) and stellar mass (right panel). The solid green lines show cluster galaxies and the pink dashed lines show field galaxies at  $z \sim 0.4$ . In the right panel, the sample is divided into three mass bins with low:  $\log(M_*/M_\odot) < 9.5$ , medium:  $9.5 \leq \log(M_*/M_\odot) < 10.5$  and high:  $\log(M_*/M_\odot) > 10.5$ . Error bars correspond to Poissonian statistics (see the text). Vertical lines represent the corresponding mean values with a light shaded standard deviation.

#### 5.2.3.4 Cluster-field comparison at $z \sim 0.4$

Both the field and cluster galaxies are consistently selected in a similar approach. Figure 5.22 shows that both are quite smoothly distributed in a local density range covering about 5 decades. We are confident that GLACE data also reasonably samples the lower-density outskirts of this cluster out to  $\sim 2r_{vir} \approx 4$  Mpc (with OSIRIS TF giving a circular FOV of 4 arcmin radius), despite the angular coverage of our observations is not exhaustive. We assume that VVDS data is fairly representative of field galaxies at the cosmic epoch studied here.

Evidence from large-area surveys (e.g., Gómez et al., 2003; Bongiovanni et al., 2005) shows that the volume-averaged SFR monotonically decreases with higher environmental densities. In particular, higher average SFRs are found in the field at different redshifts from  $z \sim 1$  when compared to galaxy cluster environments (e.g., von der Linden et al., 2010; Muzzin et al., 2012; Paulino-Afonso et al., 2018; Hwang et al., 2019). At higher redshifts, SFRs of cluster galaxies showed to be greater than in the case of field galaxies (e.g., Tran et al., 2010; Alberts et al., 2014). In Figure 5.25 we show a comparison of SFRs of the ZwCl0024+1652 cluster and field galaxies from VVDS at the same cosmic epoch. A global difference of  $\sim 0.1$  dex between both sets, with higher SFRs obtained for field galaxies than cluster members, according to the results referred above.

Regarding the relation between the SFR and the local density ( $\Sigma_5$ ), it is not clear whether exists a significant change of the SFR with this parameter for both, cluster

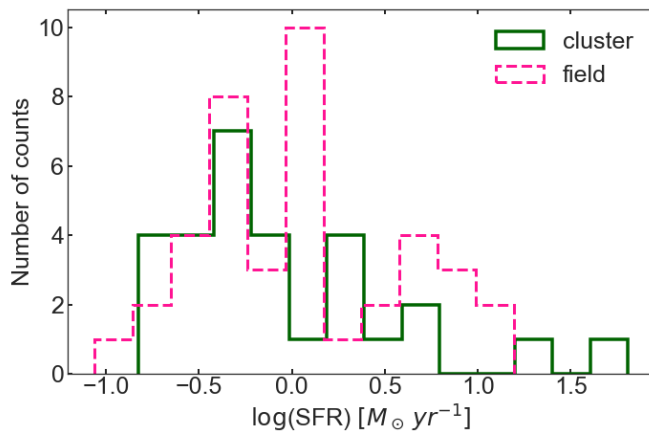


**Figure 5.25:** Histogram representing the distribution of SFR for SF galaxies in ZwCl0024+1652 (green solid) and field (dashed pink) lines. The mean value of  $\log(\text{SFR}) [M_{\odot} \text{yr}^{-1}] = -0.06 \pm 0.60$  for cluster members while the mean  $\log(\text{SFR}) [M_{\odot} \text{yr}^{-1}] = 0.05 \pm 0.054$ .

and field environments, independently from their evolutionary phase, as shown in the left panel of Figure 5.22. In contrast, the environmental dependences of the sSFR are clearer, as shown in the right panel of Figure 5.22. In fact, the ratio of field active SFGs to quenching (or transient) phase ones in the sSFR- $\Sigma_5$  relation is turned upside down with respect to that of the cluster. At redshift  $z \sim 0.4$ , we found  $\sim 21\%$  ( $\sim 79\%$ ) and  $\sim 75\%$  ( $\sim 25\%$ ) of active SFGs (quenching phase) cluster and field galaxies, respectively. Hence, while in low density environments there is a relatively low fraction of transient SF galaxies without a measurable dependence on the local density, in the case of this cluster we found a remarkable environment-dependent SF quenching, as already mentioned in Section 5.2.3.3. This finding agrees with previous studies carried out at different redshifts, e.g., with Cucciati et al. (2017), who used VIMOS Public Extragalactic Redshift Survey (VIPERS) to analyse environmental effect on the evolution of galaxies at  $0.5 \leq z \leq 0.9$ , with Baldry et al. (2006) for environment studies carried out in the local Universe, and with Cucciati et al. (2010) for intermediate redshift studies in galaxy groups. All of these studies have found in common that the ratio of active to quenching SF galaxies is smaller in higher density environments. The mean fraction of the field SFGs is comparable with that of cluster in the low-density regime, as illustrated in Figure 5.23.

About the relationships with stellar mass, there is a well-established relation between this parameter and SF phenomena, both in field and cluster (e.g., Noeske et al., 2007; Peng et al., 2010b; Lara-López et al., 2010a; Speagle et al., 2014). In



general, the SFR- $M_*$  relation has a bivariate behaviour depending on the SF activity. The active SF galaxies populate the main sequence, whereas the quenched (e.g. post-starbursts) ones tend to be grouped horizontally in this diagram.

In Figure 5.19 (left panel) we show the dependence of SFR on stellar mass both for field and cluster SFGs. Accordingly,  $\log(\text{SFR})$  and  $\log(M_*/M_\odot)$  are positively correlated with slopes 0.12/0.64, respectively for cluster/field SF galaxies. As a reference, we have represented the main sequence (MS) traced by low-redshift SFGs from SDSS (Brinchmann et al., 2004). The active SF galaxies of the cluster tends to populate a region that roughly corresponds to the MS, especially for large masses, while active SF and a few galaxies in quenching phase of the field reside above it.

From the definition given above, the sSFR traces the contribution of the star-formation processes to the mass growth of the galaxies. In general, low-mass galaxies tend to have higher sSFR than their high-mass counterparts (see Vulcani et al., 2010, and references therein). This is just one of consequences of the 'down-sizing' scenario, which favours the formation of massive galaxies in earlier epochs and shorter time-scales and the opposite situation for low-mass galaxies. From the Figure 5.19 (right panel) it can be seen that a general inverse relation is observed between the  $\log(\text{sSFR})$  and  $\log(M_*/M_\odot)$ , both field and cluster, in agreement with this scenario but at different mass scales and the same cosmic epoch. This fact suggest that the cluster environments favours a rapid transition from active SF to quenched phase compared with the field. In other words, the high-density environments at intermediate redshifts are real laboratories for testing the properties of low-redshift galaxies of high mass.

Finally, despite the relatively small statistics in the field sample, we can clearly see that irrespective of the local density values the SF fraction in the core of the cluster is around a half of that in the field environment. On the other hand, the trend of the SF fractions of field galaxies as a function of stellar mass is opposite to that of cluster galaxies. This suggests an accelerated evolution of cluster galaxies with respect to field ones. In contrast, the AGN fractions as a function of  $M_*$  have the same trend.



### 5.3 RXJ1257+4738 cluster at $z \sim 0.866$

As discussed earlier, galaxy cluster RXJ1257+4738 is a high redshift ( $z \sim 0.866$ ) cluster and is one of the targets of this study to deal with galaxy evolution in clusters to  $z \sim 1$ . Our results for this cluster are based on the observations and results of ELGs with [OII] emission lines. With GLACE based observations performing the data reduction and analysis of [OII] lines, [Pintos-Castro et al. \(2016\)](#) have presented results for various properties such as the morphological classifications of galaxies in the cluster. With results from this ELG [OII] line scanning, masses of the member galaxies were determined with Le Phare code [Ilbert et al. \(2006\)](#) using the set of SED templates from [Bruzual and Charlot \(2003\)](#) as in the case of ZwCl0024+1652. The SFRs were derived from the [OII] line emission fluxes ([Pintos-Castro et al., in prep.](#)). Furthermore, the specific star formation rate were computed as  $sSFR = SFR/M_*$ . All parameters were measured for a total of 87 sources, that is about 30% of the total (271) sample of RXJ1257+4738 members. The [OII] SFR were computed using the Equation 5.8 (see below) of [Kennicutt \(1998\)](#) and modified for our data ([Pintos-Castro, 2014](#)). Complete analysis of measured parameters will be published soon ([Pintos-Castro et al., in prep.](#)).

$$SFR (M_{\odot} yr^{-1}) = (1.4 \pm 0.4) \times 10^{-41} L_{[OII]} / 1.8 (erg s^{-1}). \quad (5.8)$$

The resulting SFR is described statistically in Table 5.7. The distributions of the

**Table 5.7:** Statistical description of the SFR of galaxies in RXJ1257+4738 galaxy cluster derived using the procedure in [Pintos-Castro \(2014\)](#).

Parameter	Minimum	Mean	Maximum	Q1	Median	Q3
$\log(SFR) [M_{\odot} yr^{-1}]$	-0.03	0.70	1.48	0.47	0.70	0.94
$\log(sSFR) [yr^{-1}]$	-11.46	-8.96	-7.27	-9.34	-8.87	-8.48
$\log(M_*) [M_{\odot}]$	8.28	9.66	11.44	9.18	9.68	10.05

SFR and the sSFR are showed in Figure 5.26. Accordingly, 50% of the sources have SFR values in a range of  $0.47 [M_{\odot} yr^{-1}] < \log(SFR) < 0.94 [M_{\odot} yr^{-1}]$ , and the sSFR values in the range of  $-9.34 [yr^{-1}] < \log(sSFR) < -8.48 [yr^{-1}]$ . We determined that the average value of  $\log(SFR)$  and  $\log(sSFR)$  of RXJ1257+4738 cluster are  $0.70 \pm 0.36 [M_{\odot} yr^{-1}]$  and  $-8.96 \pm 0.70 [yr^{-1}]$ , respectively.

We have produced a two dimensional scatter plots to describe the relationships of SFR of galaxies in this cluster to other parameters. Firstly, we used a local

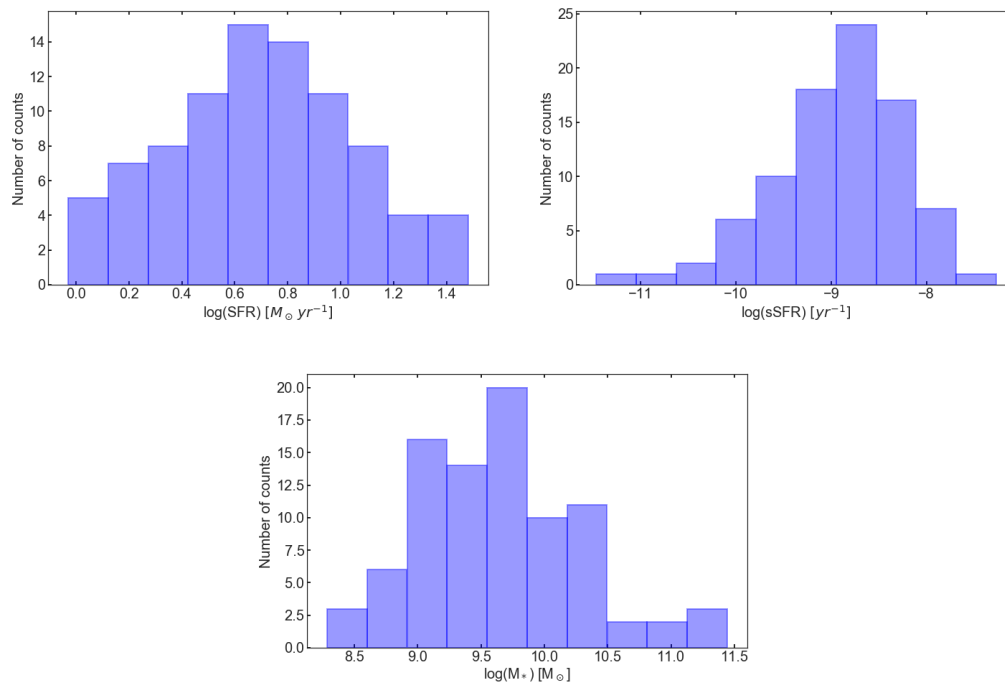


**Figure 5.26:** Distributions of  $\log(\text{SFR})$  (top left),  $\log(\text{sSFR})$  (top right) and  $\log(M)$  (bottom) of selected RXJ1257+4738 cluster members.

density ( $\Sigma_5$ ) derived in the same way as for the cluster at  $z \sim 0.4$ . The mean  $\Sigma_5$  is  $1.76 \pm 0.32 [\text{Mpc}^{-2}]$ . We observed that  $\log(\Sigma_5)$  weakly anti-correlates (correlation coefficient  $\simeq -0.10$ ) with  $\log(\text{SFR})$ , having a linear fitting slope of  $-0.10$  and an intercept of  $0.88$  (Pintos-Castro et al., in prep.). We further separated the SF member galaxies of RXJ1257+4738 into active SFs and SFs coming from quenching phase using the criteria of redshift-dependent sSFR cut given by [Koyama et al. \(2013\)](#). We obtained that 58 ( $\sim 67\%$ ) and 29 ( $\sim 33\%$ ) of member galaxies are in active and quenching SF phase, respectively. Figure 5.27 shows the relationship between SFR and  $\Sigma_5$  (left plot) and sSFR and  $\Sigma_5$  (right plot) of both types of SF galaxies. The correlation coefficients have been computed for the fits in each case: first, for the right plot getting  $-0.17$  and  $0.11$  for active and quenched phase galaxies, respectively, and for the left plot being  $-0.21$  and  $-0.08$ , respectively for active and quenched galaxies. The coefficients show that the correlations or anti-correlations observed in all the cases are very weak.

The variation of SFR with stellar mass is one of the major indicators to be studied for analysing how galaxies evolve in clusters. To this end we generated a 2D scatter plots showing the stellar mass dependence of SFR (left plot) and sSFR (right plot) showed in Figure 5.28. The linear fits to the  $\log(\text{SFR})$  versus  $\log(M_*)[M_\odot]$  plots

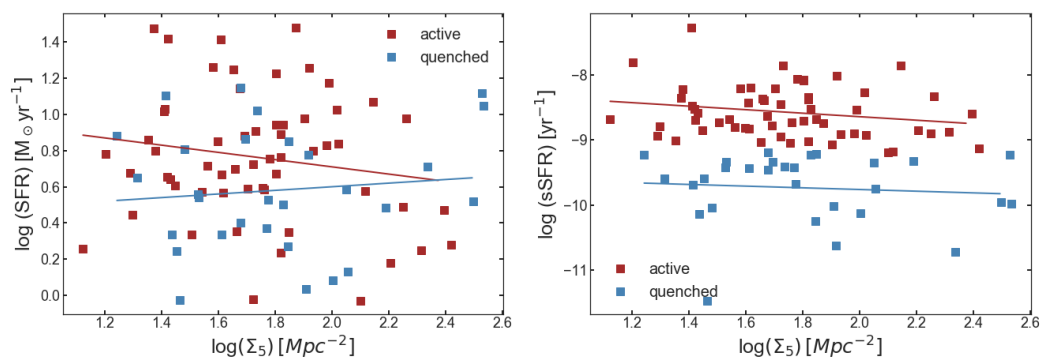


**Figure 5.27:** 2D plots describing the variation of  $\log(\text{SFR})$  (left) and  $\log(\text{sSFR})$  (right) of galaxies in RXJ1257+4738 galaxy cluster as a function of  $\log(\Sigma_5)$ , respectively. The colours used are the same as in Figure 5.22.

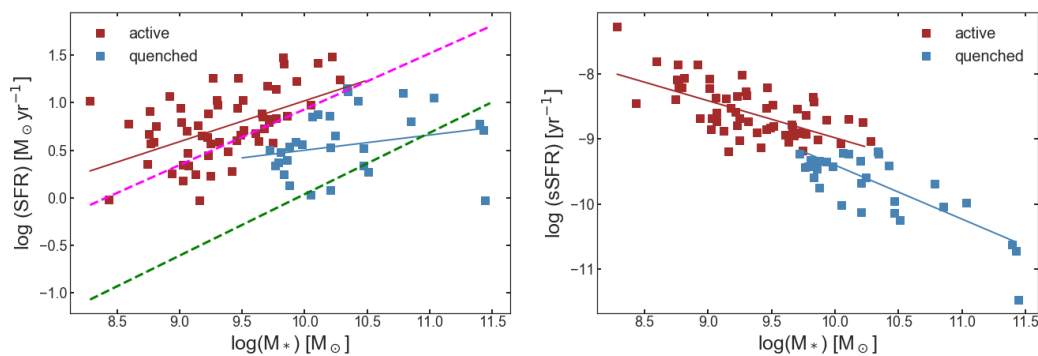


**Figure 5.28:** 2D plots describing the variation of  $\log(\text{SFR})$  (left) and  $\log(\text{sSFR})$  (right) of galaxies in RXJ1257+4738 cluster as a function of  $\log(M_*/M_\odot)$ , respectively. The colours used are the same as in Figure 5.22. Green dashed line shows the star forming main sequence from SDSS, whereas the the main sequence at higher redshift ( $z \sim 1$ ) is indicated with magenta dashed line (Whitaker et al., 2012).

have a (slope, intercept) pair of (0.07, 0.02), (0.43, -3.28), and (0.16, -1.10), for the whole, active, and quenched phase SF galaxies, respectively. To test the goodness of the fits, we measured the Pearson correlation coefficients to be 0.13, 0.53, and 0.25, respectively. Therefore, a weak positive correlation is observed for the whole and the quenched phase SF galaxies, whereas a moderate positive correlation is observed for galaxies in the active phase. We have additionally checked the correlation between the  $\log(\text{sSFR})$  versus  $\log(M_*/M_\odot)$ , finding the anticorrelation with coefficients of -0.86 (strong), -0.63 (moderate), and -0.79 (strong) for the whole, active, and quenched phase SF galaxies, respectively. We finally tried to observe the variation (distribution) of  $\log(\Sigma_5)$  with clustercentric distance as showed in

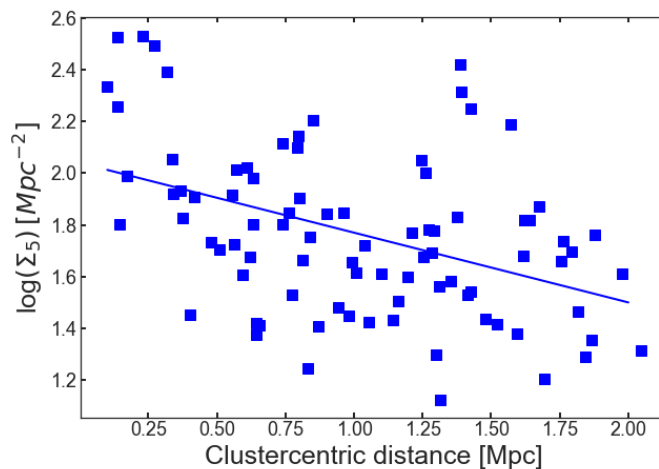


**Figure 5.29:** A diagram describing dependence of  $\log(\Sigma_5)$  on clustercentric distance for galaxies in RXJ1257+4738 cluster.

Figure 5.29. It can be seen that the local density decreases monotonically as the distance increases from the cluster centre. The linear fit has a slope of -0.27, with intercept of 2.04, and the Pearson correlation coefficient measured to be -0.43. The correlation coefficient indicates moderate anti-correlation between these two parameters for the SF galaxies in RXJ1257+4738 cluster.

## 5.4 Virgo local cluster at $z \sim 0.0038$

As mentioned previously, Virgo is the third cluster selected to be used in our work. In this section, we used the VCC (Binggeli et al., 1985) and EVCC (Kim et al., 2014) catalogues for detection of cluster members and for photometric comparisons. In addition, we used results of Grossi et al. (2015), carried out for star-forming dwarf galaxies (brighter than 18 magnitude in B band) based on observations of Herschel Virgo Cluster Survey (HeViCS). We extracted the SFRs and the stellar masses of 113 cluster members, covering only about 7% of the whole sample.

The stellar masses were computed using the method implemented by Wen et al. (2013)<sup>3</sup>, where a  $3.4 \mu\text{m}$  photometry from Wide-field Infrared Survey Explorer (WISE) all-sky catalogue (Wright et al., 2010) was employed. For deriving the

<sup>3</sup>Here the WISE All Sky Catalogue (<http://wise2.ipac.caltech.edu/docs/release/allsky/>) and the MPA-JHU SDSS catalogue (<http://www.mpa-garching.mpg.de/SDSS/DR7/>) were used for

SFR, [Grossi et al. \(2015\)](#) followed two procedures to consider both unobscured and obscured star formation. First, for those sources detected in the WISE All-Sky Survey 22  $\mu\text{m}$  band, Equation 5.9 has been used [Wen et al. \(2014\)](#).

$$SFR (M_{\odot} \text{ yr}^{-1}) = \log [L_{H\alpha} + 0.034 \nu L_{\nu}(22 \mu\text{m})] - 41.27, \quad (5.9)$$

where  $L_{H\alpha}$  and  $\nu L_{\nu}(22 \mu\text{m})$  are the  $H\alpha$  and 22  $\mu\text{m}$  luminosities, respectively, in  $\text{erg s}^{-1}$ . For galaxies without WISE 22  $\mu\text{m}$  detection, the SFR was computed using the  $H\alpha$  line, Equation 5.10 given by [Kennicutt \(1998\)](#), and [Kroupa \(2001\)](#) IMF.

from the  $H\alpha$  only, with an alternative Equation 5.10 given by [Kennicutt \(1998\)](#) with IMF from [Kroupa \(2001\)](#).

$$SFR (M_{\odot} \text{ yr}^{-1}) = 5.37 \times 10^{-42} L_{H\alpha} [\text{erg s}^{-1}], \quad (5.10)$$

after correcting the  $H\alpha$  fluxes for extinction using the Balmer decrement measured by SDSS spectra.

Moreover, emission line fluxes for member galaxies are required for our analysis involving the separation of SF from AGN galaxies, we adapted emission line fluxes from results of studying spectrophotometry of Virgo cluster galaxies by [Gavazzi et al. \(2004\)](#). Combining all these, we ended up with a purposive selection of 44 Virgo member galaxies sample (for plotting the BPT diagram), all with the four emission line fluxes ( $H\alpha$ ,  $H\beta$ ,  $[\text{OIII}]$ ,  $[\text{NII}]$ ). We plotted the BPT diagram with similar procedure as for ZwCl0024+1652 cluster galaxies using the emission lines as shown in Figure 5.30. The plot showed that almost all the galaxies in our sample with the emission lines are SF, with composite and AGN classes each containing only one galaxy. Finally, we derived the  $\text{sSFR} = \text{SFR}/M$  of all selected Virgo member galaxies. The local surface density was obtained in a consistent way as in previous two clusters, by using the distance to the 5<sup>th</sup>-neighbour ( $\Sigma_5$ ), according to [Dressler et al. \(1985\)](#), and algorithms of [Pérez-Martínez et al. \(in prep\)](#). The clustercentric distance of each member galaxy was also computed as in ZwCl0024+1652 and RXJ1257+4738 clusters.

---

matching to derive the stellar mass and the 3.4  $\mu\text{m}$  luminosity, by fitting the u, g, r, i, z photometry with model SEDs constructed from the [Bruzual and Charlot \(2003\)](#) population synthesis code assuming a [Chabrier \(2003\)](#) initial mass function (IMF) as in two higher redshift clusters ([Wen et al., 2013, 2014](#)).

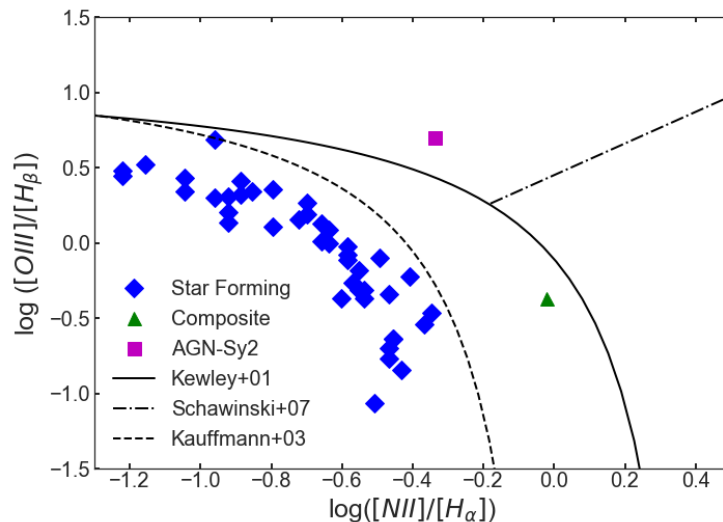


**Figure 5.30:** BPT-NII diagram of galaxies in Virgo cluster, separating the SF, composite and AGN galaxies.

Characterisation of the selected sample of galaxies in terms of SFR and stellar mass is given in Table 5.8, while the distributions of both parameters and sSFR are given in Figure 5.31. We found that 50% of the sources have,  $\log(\text{SFR})$  values in a

**Table 5.8:** Statistical distribution of the SFR of galaxies in Virgo cluster.

Parameter	Minimum	Mean	Maximum	Q1	Median	Q3
$\log(\text{SFR}) [\text{M}_{\odot} \text{yr}^{-1}]$	-2.67	-0.98	0.71	-1.45	-0.90	-0.47
$\log(\text{sSFR}) [\text{yr}^{-1}]$	-11.51	-10.24	-9.08	-10.41	-10.23	-9.96
$\log(\text{M}_{*}) [\text{M}_{\odot}]$	7.58	9.26	10.82	8.52	9.29	9.96

range of  $-1.45 [\text{M}_{\odot} \text{yr}^{-1}] < \log(\text{SFR}) < -0.47 [\text{M}_{\odot} \text{yr}^{-1}]$ ,  $\log(\text{M}_{*})$  in a range between  $8.52 [\text{M}_{\odot}]$  to  $9.96 [\text{M}_{\odot}]$ , and the sSFR in the range  $-10.41 [\text{yr}^{-1}] < \log(\text{sSFR}) < -9.96 [\text{yr}^{-1}]$ .

As in the previous two clusters, we also produced a two dimensional scatter plots for describing the relationships of SFR of galaxies in Virgo cluster to other parameters of the galaxies. The first pair of plots is that showing the variation with respect to  $\log(\Sigma_5)$  of the  $\log(\text{SFR})$  (left plot) and  $\log(\text{sSFR})$  (right plot) for our sample of Virgo member galaxies, as shown in Figure 5.32. We found for the whole sample that  $\log(\text{SFR})$  shows almost no correlation to  $\log(\Sigma_5)$  (Pearson correlation coefficient equal to -0.01) with a slope and intercept of -0.02 and -0.97, respectively. The correlation is similar for active SF galaxies (Pearson correlation coefficient equal to -0.24). We also have produced a 2D scatter plots showing

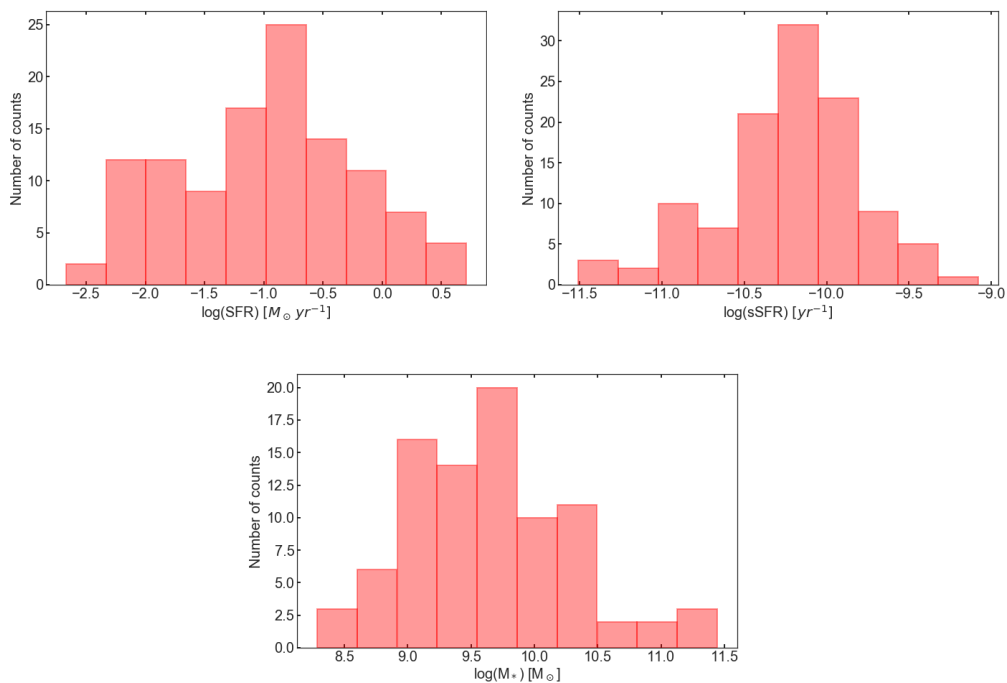


**Figure 5.31:** Distributions of  $\log(\text{SFR})$  (top left),  $\log(\text{sSFR})$  (top right) and  $\log(M)$  (bottom) of selected Virgo cluster members.

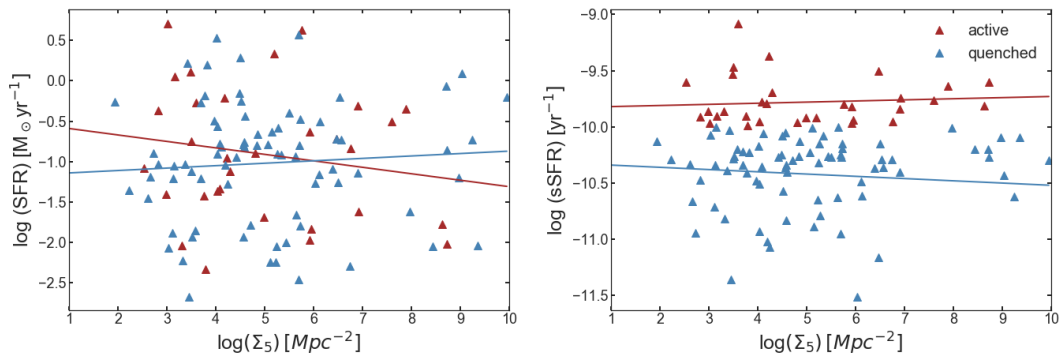


**Figure 5.32:** 2D plots describing the variation of  $\log(\text{SFR})$  (left plot) and  $\log(\text{sSFR})$  (right plot) of galaxies in Virgo galaxy cluster as a function of  $\log(\Sigma_5)$ , respectively. The colours used are the same as in Figure 5.22.

the variation of SFR (left plot) and sSFR (right plot) on  $M_*$  as shown in Figure 5.33. The plots of  $\log(\text{SFR})$  versus  $\log(M_*)[M_\odot]$  have linear fits with a (slope, intercept) pair of (0.78, -8.17), (0.96, -9.45), and (0.85, -8.99), for the whole, active, and quenched phase SF galaxies, respectively. We tested the goodness of the fits by measuring the Pearson correlation coefficients to be 0.85, 0.97, and 0.90, respectively. Therefore, a very strong positive correlation is observed for the

whole, active as well as quenched phase SF galaxies. In addition, we have checked  $\log(\text{sSFR})$  versus  $\log(M_*)[M_\odot]$  that their linear fits generally have negative correlations with coefficients of -0.43 (nearly moderate), -0.14 (very weak), and -0.34 (weak), respectively, for the whole, active and quenched phase SF galaxies.

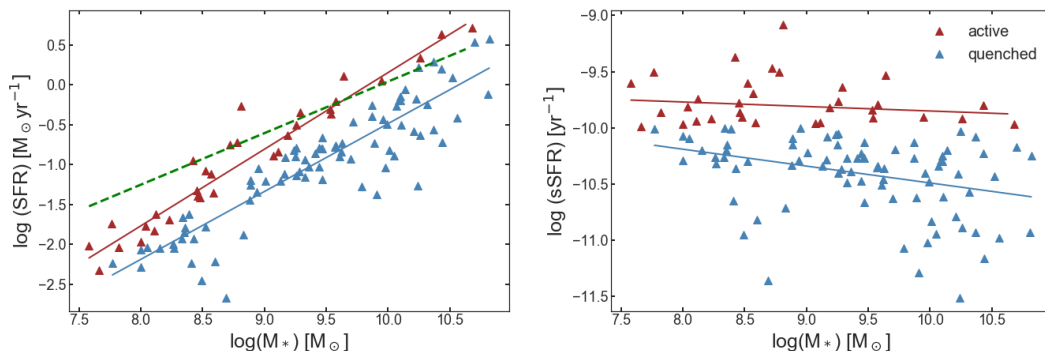


**Figure 5.33:** 2D plots describing the variation of  $\log(\text{SFR})$  (left) and  $\log(\text{sSFR})$  (right) of galaxies in Virgo cluster as a function of  $\log(M_*/M_\odot)$ , respectively. The colours used are the same as in Figure 5.22. Green dashed line shows the star forming main sequence from SDSS.

We also have investigated a variation of local density with clustercentric distance and the result is shown in Figure 5.34. The linear fit has a slope of -1.78, and intercept of 7.69, and we measured the Pearson correlation coefficient to be  $\simeq -0.50$ , confirming moderate anti-correlation between  $\Sigma_5$  and clustercentric distance.

## 5.5 Comparisons across the three clusters

In this section, we analyse the properties of three clusters in relation to SF and local density, but taking care that the three clusters are different in their properties, and that different fraction of cluster galaxies has been analysed. The comparison of three clusters in terms of their  $M_*$ , SFR, sSFR, and  $\Sigma_5$  is shown in Figure 5.35, and Tables 5.9, 5.10, 5.11, and 5.12, respectively.

According to the top left plot and Table 5.9, we can see that the stellar masses of the galaxies in three clusters are different with median values of  $\log(M_*) [M_\odot] = 9.82$  for ZwCl0024+1652,  $\log(M_*) [M_\odot] = 9.68$  for RXJ1257+4738, and  $\log(M_*) [M_\odot] = 9.29$



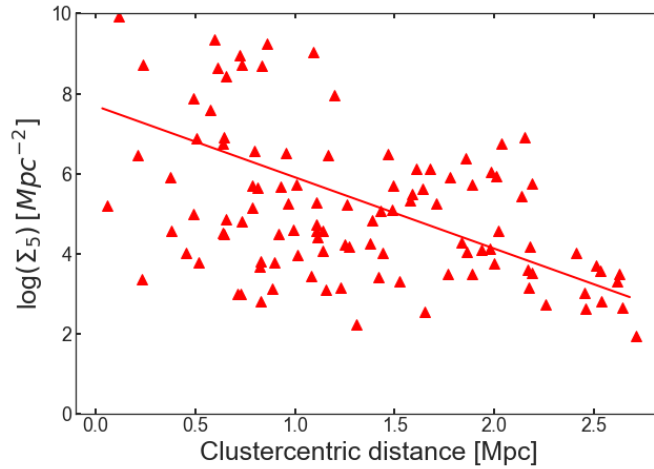


**Figure 5.34:** A diagram describing dependence of  $\log(\Sigma_5)$  on clustercentric distance for galaxies in Virgo cluster.

**Table 5.9:** Statistical comparison of  $\log(M_*)$ , in  $[M_\odot]$ , of SF galaxies among the three clusters.

Cluster	Q1	median	Q3
RXJ1257+4738 ( $z \sim 0.87$ )	9.18	9.68	10.05
ZwCl0024+1652 ( $z \sim 0.4$ )	9.50	9.82	10.27
Virgo ( $z \sim 0.0038$ )	8.52	9.29	9.96

**Table 5.10:** Statistical comparison of  $\log(\text{SFR})$  of galaxies among the three clusters. SFR values are given in  $[M_\odot \text{ yr}^{-1}]$ .

Cluster	Q1	median	Q3
RXJ1257+4738 ( $z \sim 0.87$ )	0.47	0.70	0.94
ZwCl0024+1652 ( $z \sim 0.4$ )	-0.42	-0.24	0.28
Virgo ( $z \sim 0.0038$ )	-1.45	-0.90	-0.47

**Table 5.11:** Statistical comparison of  $\log(\text{sSFR})$  of galaxies among the three clusters. The sSFR values are given in  $[\text{yr}^{-1}]$ .

Cluster	Q <sub>1</sub>	median	Q <sub>3</sub>
RXJ1257+4738 ( $z \sim 0.87$ )	-9.34	-8.87	-8.48
ZwCl0024+1652 ( $z \sim 0.4$ )	-10.40	-10.11	-9.68
Virgo ( $z \sim 0.0038$ )	-10.41	-10.23	-9.96

for Virgo galaxies. This can impose a bias to the detailed comparison of the galaxies in the three clusters at different redshifts for evolution of their properties, so that we only present our observations.

The plot at top-right and Table 5.10 shows that the  $\log(\text{SFR})$  values of galaxies

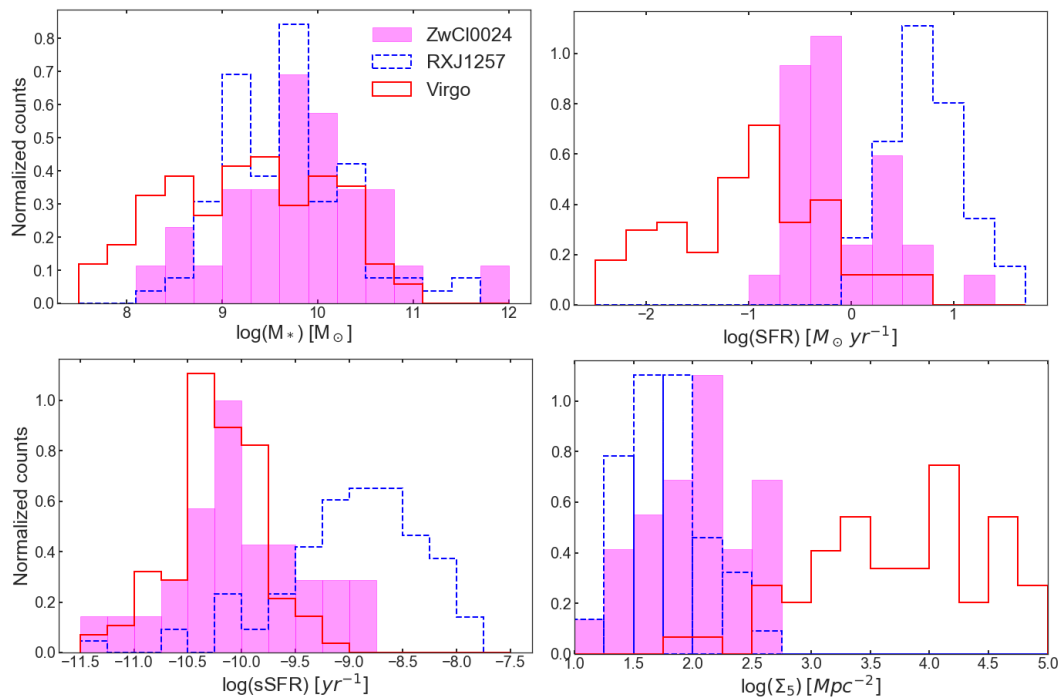


**Figure 5.35:** Histogram plots describing the comparison of properties (logarithmic values) of the SF galaxies in clusters, **top left:** stellar mass, **top right:** SFR, **bottom left:** specific SFR and **bottom right:**  $\Sigma_5$ .

**Table 5.12:** Statistical comparison of  $\log(\Sigma_5)$ , measured in  $[\text{Mpc}^{-2}]$ , of galaxies among the three clusters.

Cluster	$Q_1$	median	$Q_3$
RXJ1257+4738 ( $z \sim 0.87$ )	1.53	1.74	1.93
ZwCl0024+1652 ( $z \sim 0.4$ )	1.67	2.04	2.28
Virgo ( $z \sim 0.0038$ )	3.75	4.83	6.39

in ZwCl0024+1652 cluster (with median  $\sim -0.24 M_\odot \text{ yr}^{-1}$ ) are by far less than that of RXJ1257+4738 cluster galaxies (with median  $\sim 0.70 M_\odot \text{ yr}^{-1}$ ) but greater than the SFRs of Virgo cluster members (with median  $\log(\text{SFR}) \sim -0.8 M_\odot \text{ yr}^{-1}$ ). This roughly agrees with previous results (e.g., [Koyama et al., 2010](#); [Koulouridis and Bartalucci, 2019](#)). Considering the  $\log(\text{sSFR})$ , left bottom plot and Table 5.11, slightly similar trends are observed. While the local density ( $\Sigma_5$ ) exhibits an opposite trend (bottom right plot and Table 5.12) that galaxies in Virgo cluster are characterized by highest  $\Sigma_5$  with RXJ1257+4738 having a lowest  $\Sigma_5$ , where the ZwCl0024+1652 cluster galaxies have intermediate local densities. We observe here that galaxies in highest redshift cluster has larger SFR as well as sSFR than those galaxies in lower redshift environments. In the other hand, lower redshift cluster galaxies are characterized by higher local densities than higher redshift

cluster galaxies. Our results tend to be in-line with previous results that objects in higher density regions are characterised by lower SFR and vice versa (e.g., Cooper et al., 2008; Haines et al., 2013; Kovač et al., 2014; Cucciati et al., 2017).

Observations here lead us to a conclusion that higher redshift cluster (RXJ1257+4738 at  $z \sim 0.87$ ) is a young cluster that its member galaxies are characterized by smaller  $\Sigma_5$  resulting with higher SFR values. Virgo cluster has completed its virialization that high concentration (local density,  $\Sigma_5$ ) is exhibited resulting with suppressed SFR by its members. Two dimensional relationships among the parameters is given in Figure 5.36. We can realize from the plots that the relationship between SFR vs  $\Sigma_5$ , and sSFR vs  $\Sigma_5$  as well as  $M_*$  is inverse (anti-correlation), in agreement with existing results (e.g., Speagle et al., 2014; Vulcani et al., 2015; Guglielmo et al., 2019), while the relation evolves with redshift. At lower redshift the variation is slower than at higher redshift. In other words, the negative slope becomes steeper as we go higher in redshift. The SFR vs  $M_*$  in all cases is observed to be directly related, having fast increment (larger slopes) for galaxies in lower redshift cluster. More specifically, the slope is largest ( $m = 0.86$ ) for Virgo cluster galaxies while smallest ( $m = 0.07$ ) for RXJ1257+4738 cluster galaxies.

However, the galaxy types that we are using are different, and the methods used for measuring SFR are different as well in the three clusters. In addition, the fraction of galaxies with SFRs measured in each case is too small: 29 out of 174 (17%) for ZwCl0024+1652, 87 out of 271 (30%) for RXJ1257+4738, and 113 out of 1589 (7%) for Virgo. We also have used optical, UV and MIR data (especially in case of Virgo). These differences make difficult the comparison among the clusters, and therefore we are not able to drive any solid conclusions regarding the evolution of the galaxy clusters.

## 5.6 Conclusions

In this chapter we employed ELGs for studying a galaxy clusters at different redshifts, we presented tunable filter (TF) results under the GLACE survey related to the star formation activity. We focused on TF observations of [OIII] and  $H\beta$  emission lines for ZwCl0024+1652 cluster ( $z \sim 0.4$ ), [OII] observation results (Pintos-Castro, 2014; Pintos-Castro et al., 2016) for RXJ1257+4738 cluster ( $z \sim 0.866$ ) and public data for Virgo cluster ( $z \sim 0.0038$ ) analysis. We compared

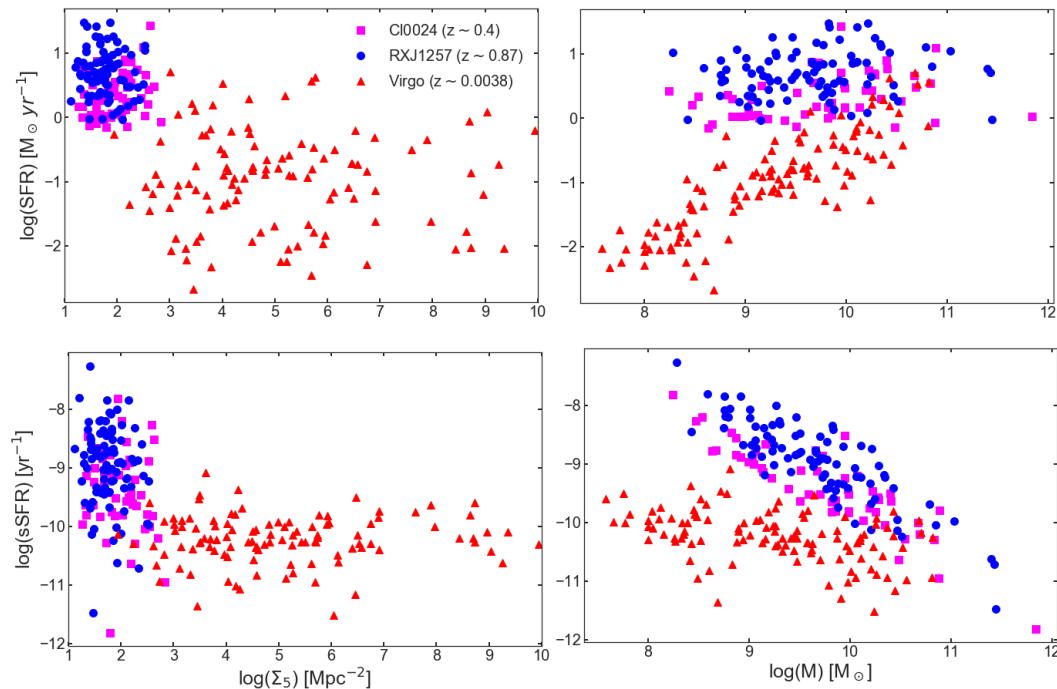


**Figure 5.36:** 2D plots describing the variation of different properties (logarithmic values). **top left:** SFR vs  $\Sigma_5$ , **top right:** SFR vs  $M_*$ , **bottom left:** sSFR vs  $\Sigma_5$  and **bottom right:** sSFR vs  $M_*$ .

the obtained fluxes and luminosities of [OIII] and  $H\beta$  lines with  $H\alpha$  and [NII] lines measured in [Sánchez-Portal et al. \(2015\)](#) for an intermediate redshift cluster. For this cluster, we studied and presented different properties of [OIII] and  $H\beta$  emitters in terms of their clustercentric distance, morphology, star formation, AGN activity, local density, and stellar mass. Finally, we compared the properties among all the three galaxy clusters. Our main conclusions are:

- In ZwCl0024+1652 cluster, out of 174 confirmed  $H\alpha$  emitters ([Sánchez-Portal et al., 2015](#)), 35 ( $\sim 20\%$ ) and 59 ( $\sim 34\%$ ) galaxies show [OIII] and  $H\beta$  emission lines, respectively, out to the  $H\alpha$  flux of  $2.43 \times 10^{-15} \text{ erg s}^{-1} \text{ cm}^{-2}$ . Our TF redshifts computed from the position of  $H\beta$  and [OIII] lines using the pseudo-spectra have been compared with previous results of [Sánchez-Portal et al. \(2015\)](#), finding a good correlation between all measurements. We have presented a catalogue of  $H\beta$  and [OIII] emitters in ZwCl0024+1652 cluster in Appendix B.
- For 20 galaxies we were able to reproduce the BPT-NII diagram finding 8 (40%) SF galaxies, 11 (55%) composites, and 1 (5%) LINER. In terms of

morphology, we found higher fraction of LT ( $\sim 67\%$ ) sources in comparison to ETs ( $\sim 33\%$ ), showing that ELG are predominantly late-types with SF and/or AGN activity going on.

- From the projected phase-space and the clustercentric distance analysis, we determined that core of this cluster is relatively free of ET galaxies with emission lines up to the clustercentric distance of  $\sim 500$  kpc.
- We found that both SF galaxies and AGN follow the local density-clustercentric distance anti-correlation, and we confirmed using TF observations that cores of regular galaxy clusters are poor with SF galaxies and AGN up to the clustercentric distance of  $\sim 1.3$  Mpc. This is in line with most of previous studies where SF and AGN activity has been detected using other than TF data.
- The sSFR seems to be anti-correlated with local density for quenched galaxies, suggesting that the star formation efficiency declines with the increase of local density of the environment.
- Considering ZwCl0024+1652 cluster, the fraction of SF galaxies and AGNs remain roughly constant across the low- and medium-density environments, dropping sharply towards high-density environments.
- The distribution of quenched galaxies extends to higher masses than that of active SF ones. The  $\log(M_*) [M_\odot]$ - $\log(\text{SFR})$  relation of active SF galaxies can be well fitted by a straight line roughly parallel to the main sequence of SF galaxies.
- The sSFR declines mildly with stellar mass for active SF galaxies, but for quenched galaxies this trend is really outstanding, indicating a strong reduction of the SF efficiency with stellar mass.
- There is a strong decline in the fraction of SF galaxies in the high stellar mass range, confirming that SF is highly suppressed in cluster high-mass galaxies. However, no remarkable trend with respect to stellar mass is observed for AGNs.
- Cluster-field comparison in terms of star formation processes suggest an accelerated evolution of galaxies in cluster with respect to field.

- Galaxies in RXJ1257+4738 are characterized on average by the highest star formation rate, while Virgo cluster galaxies with lowest SFRs in our sample. Therefore, it could be suggested that SFR decreases for cluster galaxies as the redshift of the cluster decreases. However, the sample galaxies in the three clusters have different properties, SFRs in the three clusters are measured with different methods, and the fractions of galaxies used in each cluster are very small, and therefore our observations shall be taken with precautions. Further studies with more consistent and larger samples are needed for confirming our suggestions.
- We also observed that SFR in general anti-correlates with local density for galaxies in clusters, the same as sSFR.
- A positive correlation is observed between SFR and M, being stronger for lower redshift cluster. Again, the last two points shall be taken with precautions, taking into account the possible influence of bias effects mentioned above.

# Chapter 6

## Metallicity study of galaxies in galaxy clusters

### 6.1 Introduction

We have introduced the basics of metallicity in Chapter 1, Section 1.4.4. Metallicity relates to different galaxy properties. Starting with first results by [Lequeux et al. \(1979\)](#), the mass-metallicity relation (MZR) has been studied along four decades. During this time, studies have been carried out investigating the origin and characteristics of the MZR relationship in regimes of different redshifts, environments and masses (e.g., [Kewley and Ellison, 2008](#)). These studies, focused on galaxies in the local Universe, concluded that there is a tight relationship between the stellar mass and the metallicity ( $Z$ ) of galaxies. Accordingly, the oxygen abundance ( $O/H$ ) is observed to be proportional to the stellar mass. Some studies confirm that MZR evolves with redshift (e.g., [Pérez-Montero et al., 2013](#); [Maier et al., 2015](#), etc). More recently, the stellar mass-metallicity relation (MZR) has been investigated by [Nadolny et al. \(2020\)](#) in the framework of the OSIRIS Tunable filter Emission-Line Object (OTELLO) survey with a sample of  $H\alpha$  line emitting galaxies at  $z \sim 0.4$ . They studied the possible evolution of the MZR, comparing their results comprising of the low mass end ( $M_* \sim 6.8$ ) with the local SDSS, GAMA and VVDS (deep and ultra-deep) samples. They determined the relation holding down to the low mass regime up to  $z \sim 0.4$  that the sSFR is inversely proportional to  $M_*$  and metallicity. Furthermore, massive galaxies have higher

metallicity than less massive ones. This relation holds from the local universe to high redshift (Lara-López et al., 2010a, and references therein).

Metallicity has also been studied in relation to star formation properties (SFR and sSFR). Despite small number of our sample, it is clearly observed as in Chapter 5 that an increase in redshift corresponds to higher SFR. This could be partially explained by a selection effect, since, at higher redshift, we tend to detect galaxies with higher stellar mass. Lara-López et al. (2010b) revealed that the relation between SFR and metallicity flattens with redshift while considering galaxies from SDSS DR5 at  $z=0-0.4$ . They further introduced the relations between stellar mass ( $M_*$ ), metallicity and SFR, known as fundamental plane (FP) for the star-forming field galaxies. The interrelations between these three parameters have also been reported by different authors. Metallicity and stellar mass correlate at fixed SFR. Moreover, higher metallicity galaxies are characterized by lower SFR while high SFR galaxies have lower metallicity at fixed stellar mass ( $M_*$ ) (e.g., Lara-López et al., 2010b; Mannucci et al., 2010; Andrews and Martini, 2013; Sánchez Almeida et al., 2018). Another relation has also been established that metallicity anti-correlates with sSFR where the dependence is weaker for more massive galaxies, almost vanishing below  $\log(M_*/M_\odot) \sim 10.5$  (e.g., Ellison et al., 2009; Salim et al., 2014).

To date, a limited number of studies of the metallicity of ELGs in clusters and its relationship with environment have been performed. Moreover, these studies arrived to controversial results: while some authors conclude that environment does not play a role in the metallicity of galaxies, others claim for either an enhancement/lowering of metallicity, as compared to field (e.g., Skillman et al., 1996; Mouhcine et al., 2007; Ellison et al., 2009). Ellison et al. (2009) particularly investigated the impact of cluster membership and local density on the mass – metallicity relation (MZR) for a large sample of 1318 galaxies in low-redshift clusters ( $\langle z \rangle = 0.07$ ) from SDSS-DR4. Their results show that galaxies in clusters are, on average, slightly more metal-rich than field ones, being this effect driven by local over-density rather than by simple cluster membership. Moreover, Cooper et al. (2008) had also reported results indicating a tight relationship between metallicity and environment based on SDSS data, suggesting that regions of higher density are populated with galaxies of higher metallicities. On the other hand, Mouhcine et al. (2006) analysed spectroscopic data for a small sample of 17



massive ELGs at  $\langle z \rangle = 0.42$ , finding no evidence of differences between the abundances observed in cluster and field galaxies. However, this might happen either because no such difference exists, or because the star-forming (SF) galaxies have arrived recently from the field. In contrast, [Maier et al. \(2016\)](#) performed a detailed VIMOS/VLT investigation of a sample of 76 galaxies of the cluster MACS J0416.1-2403 at  $z = 0.397$ , deriving metallicities and finding that, for intermediate and low stellar mass galaxies, the metallicity of objects falling into the cluster for the first time is found to be in agreement with the predictions of the fundamental metallicity relation (FMR). However, for already accreted SF galaxies of similar masses, metallicities are higher than those predicted by models.

At higher redshift, the situation is even more controversial. [Kacprzak et al. \(2015\)](#) compared the MZR for 43 cluster galaxies in a Virgo-like progenitor at  $z = 2$  and 74 galaxies at similar redshift, finding no detectable differences to within 0.02 dex, concluding that environmental effects are small and secondary to the ongoing inflow-outflow processes governed by halo mass.

Furthermore, [Kulas et al. \(2013\)](#) studied the metallicity of 23 proto-cluster and 20 field galaxies at  $z = 2.3$ , finding that low-mass proto-cluster galaxies show an enhancement in metallicity as compared to field. The authors explain this in the context of a shorter recycling time-scale of galaxy wind material in denser environments. In clear contrast, [Valentino et al. \(2015\)](#) investigated the metallicity of 6 galaxies in a distant X-ray cluster at  $z = 1.99$  and 31 field objects, finding that cluster SF galaxies have lower metallicity (0.25 dex) than field ones, suggesting that this could be explained by the accretion of pristine gas from cluster-scale reservoirs. Moreover, [Maier et al. \(2016\)](#) and [Maier et al. \(2019b\)](#) while studying CLASH and LoCuSS cluster member galaxies (at  $z < 0.5$ ) reported results confirming that lower mass cluster galaxies in denser regions are also observed to have enhanced metallicity as compared to the field counterparts. In addition, [Ciocan et al. \(2020\)](#) using a CLASH-VLT survey data for an intermediate redshift cluster galaxies observed that the MZR remains similar as for the local SDSS galaxies with offset of low mass galaxies ( $8.3 < \log(M_*/M_\odot) < 9.2$ ) characterized by more metallicities than the local ones. The same study shows that cluster galaxies having higher masses, ( $9.2 < \log(M_*/M_\odot) < 10.2$ ), are characterized by higher metallicities than their field counterparts.

This chapter is organized into six sections including this introductory part describing metallicity and related studies in galaxy clusters. In Section 6.2, we reviewed

different methods of estimating metallicity. In Section 6.3, we presented the results related to metallicity of galaxies in ZwCl0024+1652 cluster ( $z = 0.4$ ). Then Section 6.4 is dedicated to the metallicity related results for galaxies in Virgo local cluster ( $z = 0.0038$ ). Discussion of the galaxy properties in relation to metallicity is performed across the two clusters in Section 6.5. Finally, we present our conclusions in Section 6.6.

## 6.2 Metallicity computation

There are different mechanisms for computing metallicity by determining different indices. The first method is by determining the N2 metallicity index (Denicoló et al., 2002) which is defined as  $N2 \equiv \log [NII]\lambda 6583/H\alpha$ . This ratio is highly sensitive to metallicity, with a tight linear correlation, through a combination of effects, on the one hand, as metallicity decreases (as measured by the (O/H) ratio), there is a tendency for the ionization to increase, hence decreasing the [NII]/[NIII] ratio (Pettini and Pagel, 2004). In addition, due to the secondary nature of nitrogen the (N/O) ratio itself decreases at high abundance end (e.g., Henry et al., 2000). The N2 abundance estimator and the oxygen abundance are related as:

$$12 + \log(O/H) = a + b \times N2, \quad (6.1)$$

where  $a$  and  $b$  are constants that can generally be determined with the least squares fits and their values depend on the data sample. Using the sample of 185 nearby emission line galaxies at redshift  $z \leq 0.075$  (Raimann et al., 2000b), mostly of HII and star burst, and some Syfert 2 local galaxies Raimann et al. (2000a) determined the values of the coefficients to be  $a = 8.89$  and  $b = 0.53$ . Denicoló et al. (2002) by compiling exhaustive sample of nearby extragalactic HII regions for metallicity calibrations, latter determined both coefficients to have larger ( $a = 9.12$ ,  $b = 0.73$ ) than the values from Raimann et al. (2000a). Pettini and Pagel (2004) further refined the sample from Denicoló et al. (2002), by extending to high redshifts and considering HII regions with well-derived values of O/H and N2 (either with electron temperature ( $T_e$ ) or photo-ionization modelling method), presented the most updated values of these coefficients **with formal statistical errors given by  $a = 8.90 \pm 0.04$  and  $b = 0.57 \pm 0.03$** , respectively.

A second method that can be implemented to determine metallicity is the O3N2 indicator (Alloin et al., 1979) defined mathematically in Equation 6.2 as:

$$O3N2 = \log\left(\frac{[OIII]\lambda 5007}{H\beta} \times \frac{H\alpha}{[NII]\lambda 6583}\right). \quad (6.2)$$

Similarly this metallicity index is related to the oxygen abundance as:

$$12 + \log(O/H) = c + d \times O3N2, \quad (6.3)$$

where c and d are also constants that can be determined with the least squares fits using the data available. Pettini and Pagel (2004), using a sample of 137 HII regions with well determined values of O/H and N2, determined the values of the coefficients to be  $c = 8.73$ , and  $d = -0.32$ ,  $-1 < O3N2 < 1.9$ . Kewley et al. (2013b) later determined the constant values for galaxies in star-forming sequence to be  $c = 8.97$  and  $d = -0.32$  for galaxies in the redshift ranges from  $z = 0.04$  to  $z = 0.1$ . They did this by implementing the stellar evolutionary synthesis and photo-ionisation models by determining chemical evolution with hydrodynamic simulations. Recently based on the equations from Kewley et al. (2013b), two metallicity calibrations, as in Equation 6.4 and 6.5, have been derived for galaxies in the SF sequence by Maier et al. (2016) as:

$$12 + \log(O/H) = 8.97 - 0.32 \times (\log([OIII]/H\beta) - 0.61 / (\log([OIII]/H\beta) - 1.1) + 0.08), \quad (6.4)$$

and

$$12 + \log(O/H) = 8.97 - 0.32 \times (1.1 + 0.61 / (\log(N2) + 0.08) - \log(N2)). \quad (6.5)$$

Another method for metallicity diagnosis using emission lines is the R23 index (Pagel et al., 1979). This indicator requires the  $[OII]\lambda 3727$ ,  $H\beta$  and the  $[OIII]$  lines to be measured. The R23 diagnostic index is defined using these measured values as in Equation 6.6.

$$R23 = \frac{[OIII] + [OII]}{H\beta} \quad (6.6)$$

The relations between the abundance of oxygen and R23 are generally double valued (degenerate), resulting with a high metallicity branch solution for  $12 + \log(O/H) > 8.5$  and a low metallicity branch solution corresponding to  $12 +$

$\log(O/H) < 8.5$ . Hence for breaking this degeneracy, we use the O32 ( $\equiv [OIII]/[OII]$ ) where  $O32 > 2$  giving the lower branch solution while  $O32 < 1$  yielding the upper branch metallicity solution. In addition to this, we also use the N2 diagnostic indicator for breaking the degeneracy to identify the right branch. Therefore the O32 and N2 are used for breaking the R23 degeneracy and to assess possible differences in N and O abundances versus metallicity. Considering the upper branch solution for the double-valued R23, the relationship between R23 and the oxygen abundance is analytically given by Tremonti et al. (2004) as:

$$12 + \log(O/H) = 9.185 - 0.313x - 0.264x^2 - 0.321x^3, \quad (6.7)$$

where  $x \equiv \log(R23)$ .

### 6.3 Gas metallicity of ZwCl0024+1652 cluster galaxies

In GLACE framework, a total of 174  $H\alpha$  emitters have already been presented by Sánchez-Portal et al. (2015). Not all but most of them (155 sources) have [NII] emission lines too. We derived the N2 ratio for galaxies drawn from our sample of  $H\alpha$  emitters. To start with a clean sub-sample of SF galaxies, we first removed those objects that are either broad-line AGNs (BLAGNs, 25 sources) or narrow-line AGNs (NLAGNs, 39 sources) according to the Kauffmann et al. (2003) criterion as described in Section 5.2.2.4. The masses of the objects were determined with Le Phare code (Ilbert et al., 2006) using the set of SED templates from Bruzual and Charlot (2003) as in Section 5.2.1.3. We found only 20 sources having [OIII] and  $H\beta$  lines out of the sample of  $H\alpha$  emitters (Section 5.2.2.4). The errors in the  $H\alpha$  and [NII] lines have been computed by propagation mechanism taking both the “on” bands and continuum noise into account as described by Sánchez-Portal et al. (2015). Then to finalize our sample, we eliminated objects for which the fractional error in the [NII]/ $H\alpha$  ratio was abnormally high. Since, there could be more sources both with [NII] and  $H\alpha$  emissions, N2 abundance estimator is preferred to be used for the metallicity computation. Furthermore, since stellar mass could be computed not for all sources, we only included galaxies for which a stellar mass was derived. Finally, we ended up with a sample of 53 objects having both lines [NII] and  $H\alpha$ , with stellar mass and SFR computed.

For studying the properties and evolution of galaxies in ZwCl0024+1652 cluster, we have derived the SFR, the sSFR, the stellar mass ( $M_*$ ) for the galaxies, the  $\Sigma_5$  local density have also been computed; details described in Chapter 5. We describe our sample by first presenting the distributions of these parameters in Figure 6.1, within the same plots showing the parameter distributions of the base sample. The normalized histograms in each case show that our final sample is within the space of the analysed parameter.

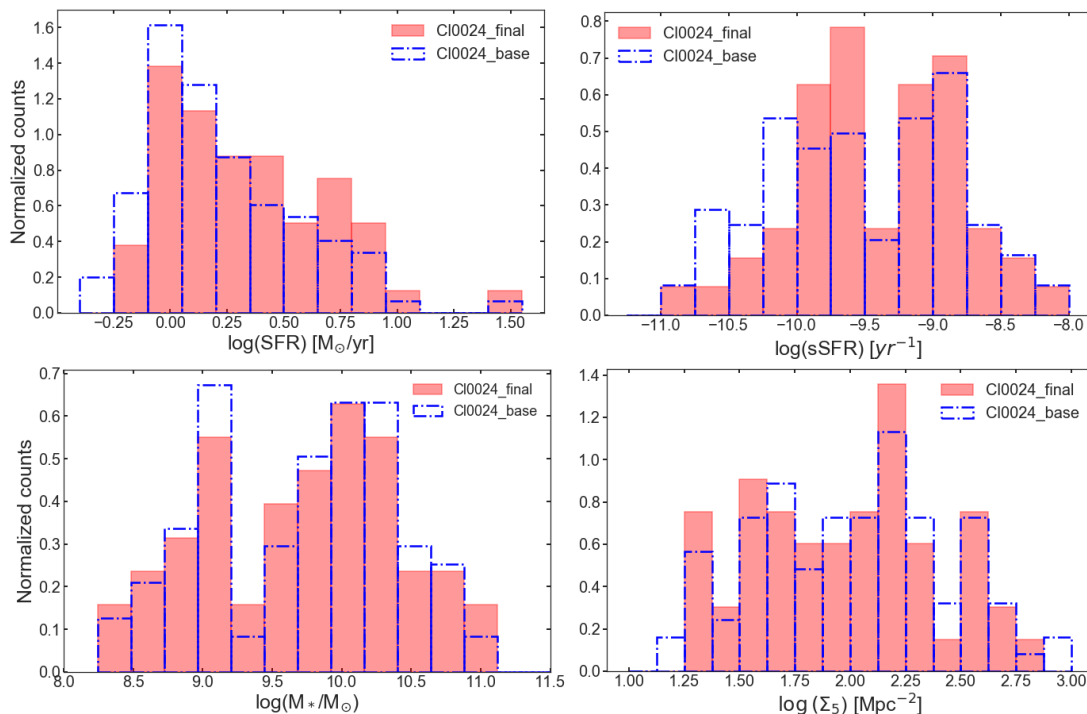


**Figure 6.1:** Normalized distributions of properties of galaxies in the ZwCl0024+1652: **top left:** representing the SFR; **top right:** showing the sSFR; **bottom left:** representing the distribution of  $M_*$ ; **bottom right:** describes the local density  $\Sigma_5$  distribution. Histograms are presented for parameter distributions of the base sample (blue dash dotted open histograms) and our final sample galaxies (red filled histograms), all for which  $Z$  is measured. The distributions show that our sample is reasonably within the space of SFR, sSFR,  $M_*$ , and  $\Sigma_5$  ranges, respectively.

To substantiate the consistency of our final sample, we applied different statistical tests. The first computation that we carried out is determining the median and the  $Q_1$ - $Q_3$  ranges for each parameter where 50% of the sample comes from in each case for the base and the final sample (where  $Q_1$  stands for first quartile whereas  $Q_3$  for third quartile). The results are given in Tables 6.1, 6.2, 6.3 and 6.4. The statistical results from these tables clearly reveal that our sample is consistent with the base

**Table 6.1:** Statistics of the SFR of galaxies in ZwCl0024+1652.

$\log(\text{SFR})$	Q1	Median	Q3
base sample	-0.02	0.17	0.43
final sample	0.04	0.29	0.54

**Table 6.2:** Statistics of the sSFR of galaxies in ZwCl0024+1652.

$\log(\text{sSFR})$	Q1	Median	Q3
base sample	-10.03	-9.52	-8.91
final sample	-9.80	-9.47	-8.89

**Table 6.3:** Statistics of the  $M_*$  of galaxies in ZwCl0024+1652.

$\log(M_*/M_\odot)$	Q1	Median	Q3
base sample	9.12	9.82	10.28
final sample	9.13	9.82	10.25

**Table 6.4:** Statistics of the  $\Sigma_5$  of galaxies in ZwCl0024+1652.

$\log(\Sigma_5)$	Q1	Median	Q3
base sample	1.67	2.04	2.29
final sample	1.64	2.01	2.21

**Table 6.5:** Summary of the KS2 statistical test results between the two samples of galaxies (the base sample versus final sample) ZwCl0024+1652 cluster.

KS2 index	$\log(\text{SFR})$	$\log(\text{sSFR})$	$\log(M_*/M_\odot)$	$\log(\Sigma_5)$
KS_statistic	0.17	0.15	0.054	0.08
P_value	0.27	0.38	1.0	0.98

sample. To further confirm this, we also have used the Kolmogorov Smirnov two-sample (KS2) test (Kolmogorov, 1933; Smirnov, 1948), that is one of the most useful and general nonparametric methods for comparing two samples. This test is sensitive to differences in both location and shape of the empirical cumulative distribution functions of the two samples resulting with two important indices namely, the KS\_statistic and the P\_value when applied. Applying the KS2 test to our data comparing each of the four parameters among the base and final sample we determined the KS\_statistic and the P\_value for each case, as summarized in Table 6.5. In each of the cases, the P\_value is greater than the critical value of this index denoted by “a” that is  $\simeq 0.05$  and the statistic value is less than its marginal index,  $\simeq 0.32$ . This leads us to the conclusion that both samples are drawn from the same distribution, hence our sample is consistent with the base sample.

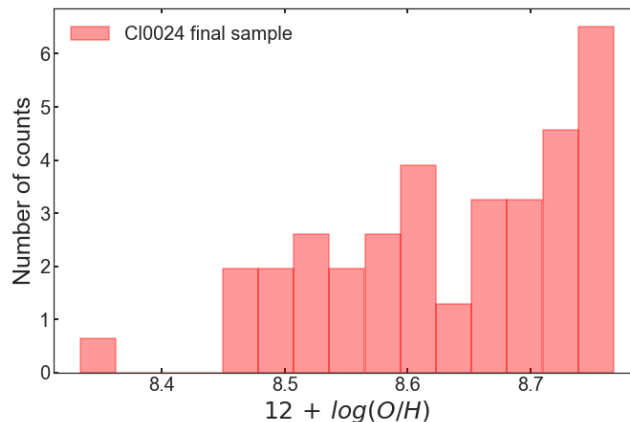
Using the N2 abundance estimator, we computed the metallicity  $Z$  following Equation 6.1 preferably including the prescription of Pettini and Pagel (2004), rewritten as in Equation 6.8.

$$12 + \log(O/H) = 8.90 + 0.57N2 \quad (6.8)$$

Our computation resulted in a metallicity distribution in which 50% of the sample galaxies have an abundance in the range  $8.56 \leq Z \leq 8.73$ . The distribution is described statistically in Table 6.6, and shown in the histogram plot of Figure 6.2.

**Table 6.6:** Statistical description of the metallicity of galaxies in ZwCl0024+1652 galaxy cluster computed with N2 index.

Name	Q1	Median	Q3
Z	8.56	8.65	8.73

**Figure 6.2:** The histogram distribution of N2 metallicity of galaxies in ZwCl0024+1652 galaxy cluster.

After measuring the sample metallicity, we produced a series of plots to explore the relationship of metallicity with other parameters. Here the four plots, describing metallicity as a function of stellar mass, radial distance from the cluster center, as a function of SFR and sSFR as well are presented in Figure 6.3. Out of 53 sources in our final sample, 42 sources are within the main cluster structure (“A”) while the remaining 11 sources in the infalling structure (“B”). Our results here show no clear correlation of metallicity to SFR, sSFR,  $M_*$  and  $\Sigma_5$  since the plots are randomly scattered without established pattern.

Finally, for galaxies in ZwCl0024+1652 cluster, we also have presented a plot of oxygen abundance metallicity ( $12 + \log(O/H)$ ) versus stellar mass in Figure 6.4, against the local galaxy density  $\Sigma_5$  represented with a colour bar as a third parameter. The large scatter of the plots precludes from deriving a clear relationship between the quantities. This high dispersion could be due to the relatively large errors in the  $H\alpha$  and specially in the  $[NII]$  fluxes, resulting in large errors in the N2 parameter. Moreover, the environmental effects also play a role in spreading or smearing the MZR. The dispersion of the relation may further be because the MZR could be biased towards higher  $[NII]$  fluxes resulting with the relation biased to higher metallicity. Even though the high scatter found in the relation prevents

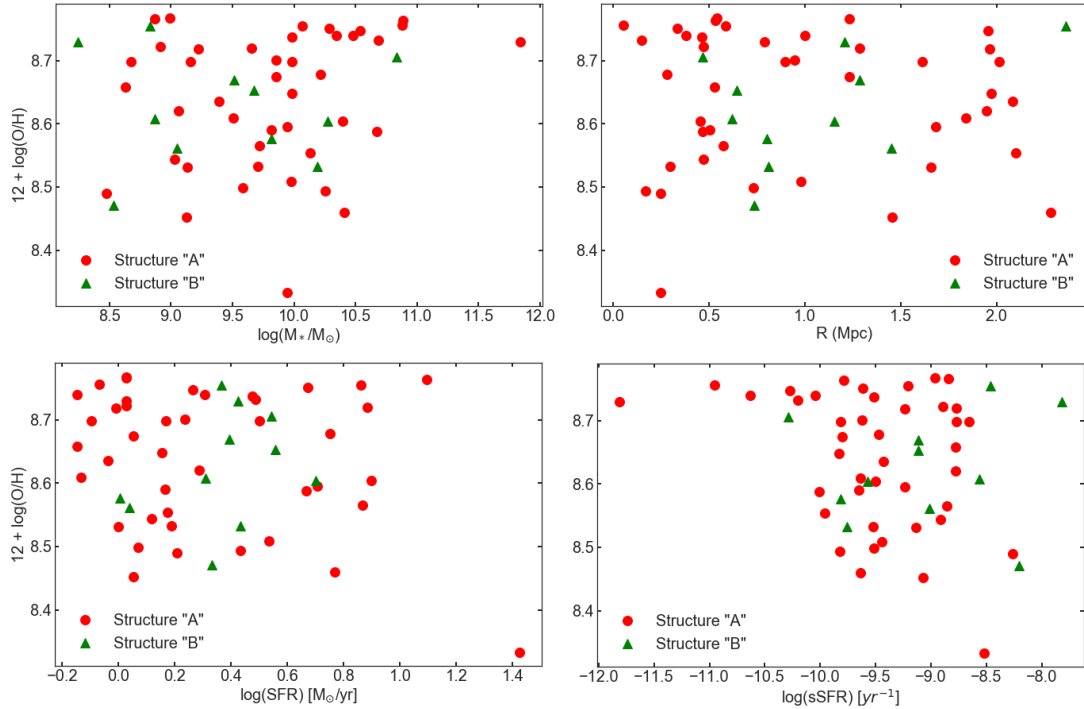


**Figure 6.3:** The plots describe the variation of galaxy gas metallicity in ZwCl0024+1652 as a function of  $M_*$  (**top left**), clustercentric distance (**top right**), SFR (**bottom left**) and sSFR (**bottom right**). Red dots and green triangles stand for sources in the main cluster structure (“A”) and in the infalling structure (“B”), respectively.

from drawing any clear conclusion, the plot could suggest that (a) more massive galaxies tend to be found in the highest density regions, and (b) highest metallicity galaxies also tend to be observed in the highest density regions.

## 6.4 Gas metallicity of galaxies in the Virgo cluster

Virgo is the local galaxy cluster chosen in our work for comparison with results in higher redshift clusters (see Section 6.5). Confirmed members of Virgo cluster were published in two exhaustive catalogues: the Virgo Cluster Catalogue (VCC; Binggeli et al., 1985) and the Extended Virgo Cluster Catalogue (EVCC; Kim et al., 2014). We used these public catalogues for detection of members and photometric comparisons (see Section 2.4). In addition to these, from results by Grossi



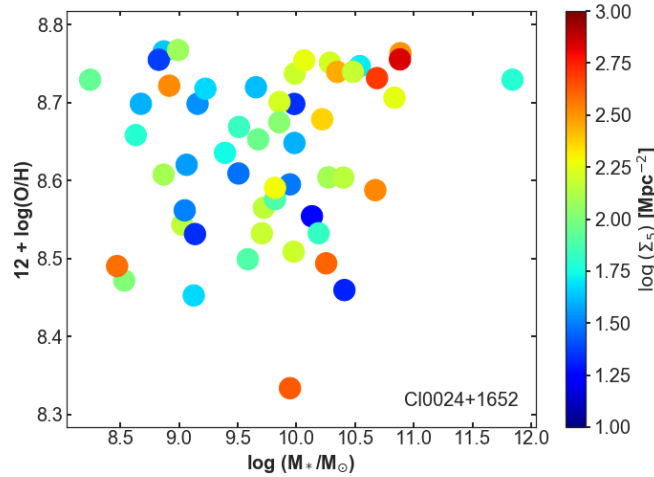


**Figure 6.4:** Plot for galaxies in ZwCl0024+1652 cluster describing the variation of  $Z$  of galaxies as a function of stellar mass representing the local density with colour bar.

et al. (2015) carrying out studies for star-forming dwarf galaxies (r-band magnitude brighter than 18) based on observations of Herschel Virgo Cluster Survey (HeViCS) and results from Peng et al. (2008) using the ACS Virgo cluster survey, we got the SFR and the stellar mass data. Moreover, since we need emission line fluxes for the Virgo member ELGs, we adapted emission lines data from spectrophotometric results of Virgo cluster galaxies (Gavazzi et al., 2004). Combining all these, we finally had a total sample of 44 Virgo member galaxies with all required parameters namely SFR, stellar mass, and the four emission line fluxes ( $H\alpha$ ,  $H\beta$ ,  $[OIII]$ ,  $[NII]$ ). Moreover, we computed the sSFR (i.e.,  $SFR/M_*$ ) and the clustercentric distance for the Virgo member galaxies.

The distributions of the galaxy parameters (SFR, sSFR,  $M_*$  and  $\Sigma_5$ ) derived for our sample galaxies from the Virgo cluster together with the parameter distributions of the total base sample are presented in Figure 6.5. In all plots, the normalized histogram in each case shows that our final sample is within the space of the analysed parameter.

To check for the consistency of our Virgo final sample, we first performed the computation of the median and the  $Q_1 - Q_3$  ranges for each parameter where 50% of the sample comes from in each case, for the base and the final sample as described for ZwCl0024+1652 in Section 6.3. The statistical results in this case are given in Tables 6.7, 6.8, 6.9 and 6.10. The statistics here shows that our final Virgo

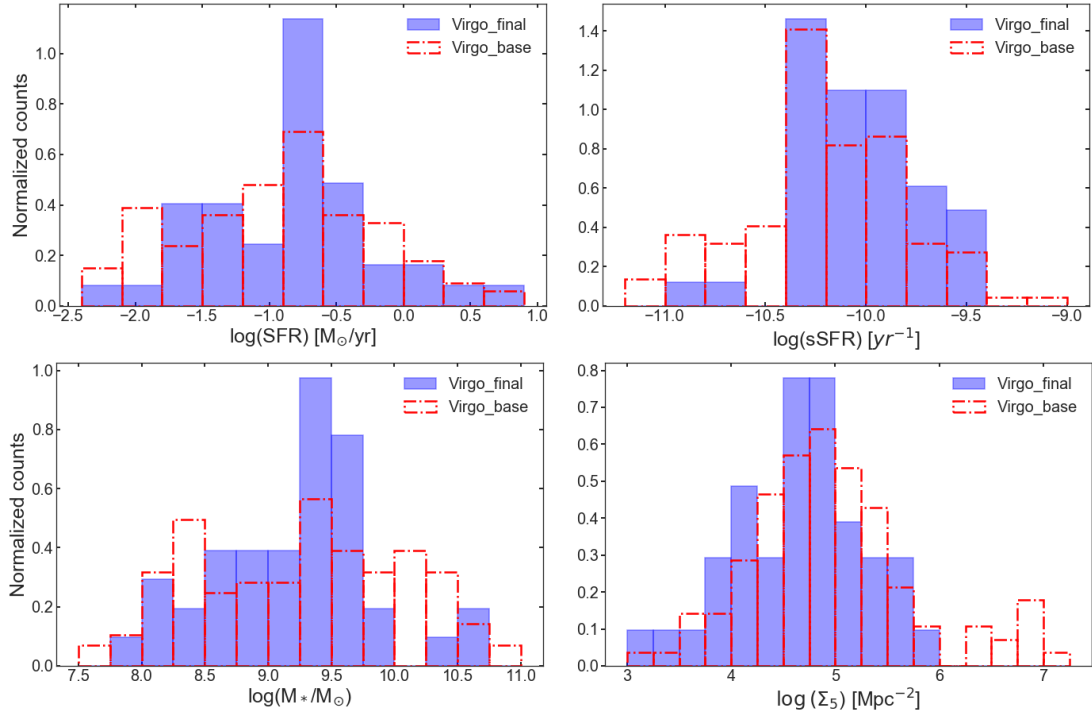


**Figure 6.5:** Normalized distributions of properties of galaxies in Virgo cluster with **top left** representing SFR distribution, the **top right** showing the sSFR distribution, the **bottom left** representing the distribution of  $M_*$ , and the **bottom right** describing the local density  $\Sigma_5$  distribution. Histograms are presented for parameter distributions of the base sample (red dash dotted open histograms) and our final sample galaxies (blue filled histograms) for which  $Z$  is measured. Both distributions for Virgo galaxies also show that our sample is reasonably within the space of the computed parameters: SFR, sSFR,  $M_*$  and  $\Sigma_5$ .

$\log(\text{SFR})$	Q1	Median	Q3
base sample	-1.46	-0.9	-0.47
final sample	-1.26	-0.8	-0.47

**Table 6.7:** Statistics of the SFR of galaxies in Virgo cluster.

$\log(\text{sSFR})$	Q1	Median	Q3
base sample	-10.41	-10.23	-9.96
final sample	-10.27	-10.06	-9.82

**Table 6.8:** Statistics of the sSFR of galaxies in Virgo cluster.

sample is also consistent with the base sample. We further applied the KS2 test (see Section 6.3) to our Virgo data comparing each of the four parameters among the base and final sample determining the KS\_statistic and the P\_value for each case, as summarized in Table 6.11. The P\_value is greater than the critical value of this index and the statistic value is less than its marginal index as in the case of ZwCl0024+1652, confirming that our final sample is consistent with the base sample in case of the Virgo cluster too.

$\log(M_*/M_\odot)$	Q1	Median	Q3
base sample	8.52	9.29	9.96
final sample	8.78	9.26	9.57

**Table 6.9:** Statistics of the  $M_*$  of galaxies in Virgo cluster.

$\log(\Sigma_5)$	Q1	Median	Q3
base sample	4.48	4.92	5.31
final sample	4.24	4.70	5.15

**Table 6.10:** Statistics of the  $\Sigma_5$  of galaxies in Virgo cluster.

**Table 6.11:** Summary of the KS2 statistical test results between the two samples of galaxies (the base sample versus final sample) Virgo galaxy cluster.

KS2 index	$\log(\text{SFR})$	$\log(\text{sSFR})$	$\log(M_*/M_\odot)$	$\log(\Sigma_5)$
KS_statistic	0.15	0.23	0.21	0.17
P_value	0.51	0.08	0.12	0.35

**Table 6.12:** Statistical description of the metallicity of galaxies in Virgo cluster derived using the N2 abundance estimator.

Name	Q1	Median	Q3
Z	8.39	8.54	8.61

Since we have both the  $H\alpha$  and  $[OIII]$  line fluxes, to keep consistency we derived the metallicity of the galaxies using N2 diagnostics as in Equation 6.8. The statistical distribution of the metallicity of Virgo cluster galaxies is given as in Table 6.12.

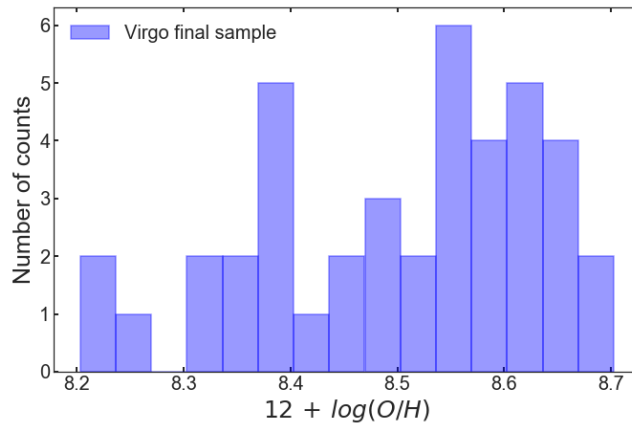


**Figure 6.6:** The histogram distribution of the N2-determined metallicity of galaxies in Virgo galaxy cluster.

As in the previous ones, we implemented diagnostic plots to investigate relationships of galaxy metallicity to other parameters for members of Virgo cluster. The plots are presented in Figure 6.7, where metallicity versus clustercentric distance and  $M_*$  relations in the top panel while the metallicity versus SFR and sSFR dependences in the bottom panel. The top left plot gives a positive correlation of

metallicity to the logarithmic stellar mass of galaxies in the Virgo cluster. The relation has a correlation coefficient of 0.73, with slope and intercepts of 0.153 and 7.09, respectively. On the other hand, the bottom right plot of the figure shows a negative correlation (anti-correlation) of metallicity to specific SFR. This relation has a correlation coefficient of -0.57, having a slope and intercept of -0.25 and 5.99, respectively. However, the scatter of the Z-R (top-right panel) and Z-SFR (bottom-left) plots is so large that we couldn't produce a reasonable linear fit to establish a clear relationship. Moreover, for galaxies in the Virgo cluster we have

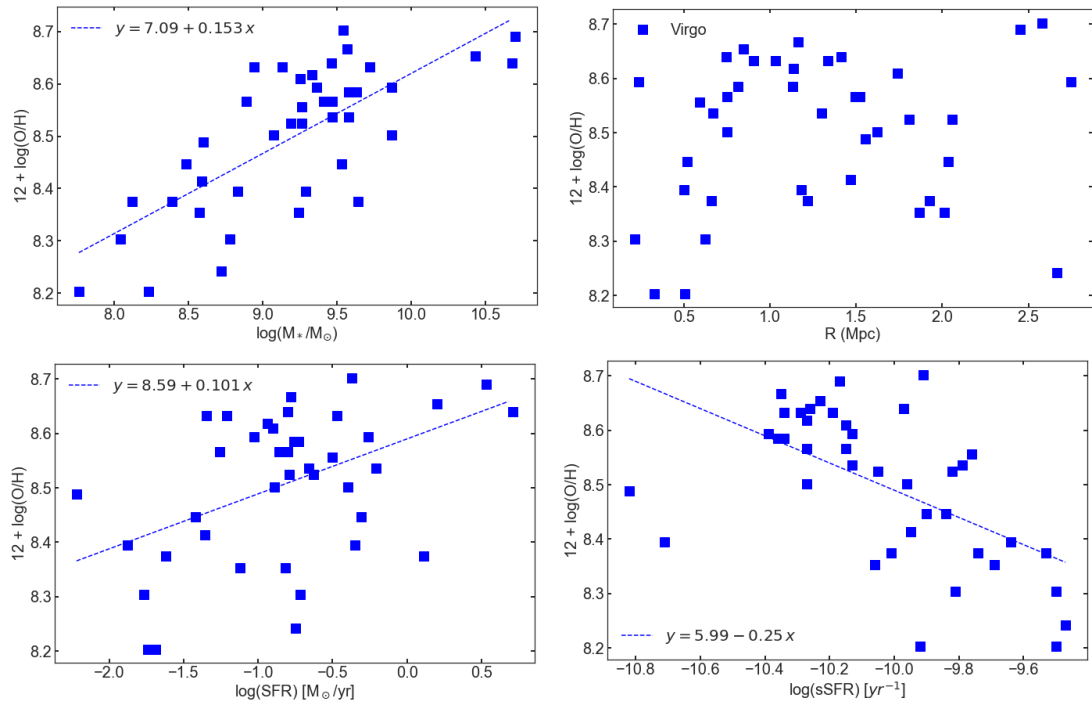


**Figure 6.7:** 2D plots describing the variation of Z of galaxies in Virgo cluster as a function of  $M_*$  (**top left**), as clustercentric distance R (**top right**), as a function of SFR (**bottom left**) and as sSFR (**bottom right**).

presented a plot of oxygen abundance metallicity ( $12 + \log(\text{O}/\text{H})$ ) versus stellar mass in Figure 6.8, against the local galaxy density  $\Sigma_5$  represented with colour bar as a third parameter as in case of ZwCl0024+1652 cluster. The MZR linear relation is clearly observed from this plot and we can also deduce that the galaxies in the most locally dense region have  $\log(M_*/M_\odot) \simeq 9.5$  and the metallicity  $12 + \log(\text{O}/\text{H}) \simeq 8.6$ .

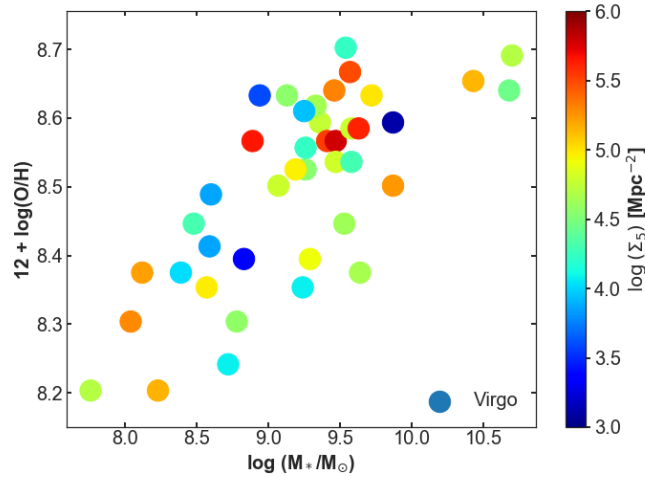


**Figure 6.8:** Plot for Virgo galaxy cluster describing the variation of  $Z$  of galaxies in the cluster as a function of stellar mass with local density represented with colour bar.

## 6.5 Discussion

We begin this section by comparing the properties of galaxies among the two clusters at different redshifts, that can be discussed based on Figure 6.9. We compare the galaxies in the two clusters in terms of stellar mass, star formation rate and specific star formation rate. All the three plots show that the Virgo member galaxies in our sample are characterized in general by lower values of  $M_*$ , SFR and sSFR than the corresponding ZwCl0024+1652 member galaxies. This can be illustrated by statistics of the parameters as given in Table 6.13 (for  $\log(M_*/M_\odot)$  represented by  $M_{stat}$ ), 6.14 (for  $\log(\text{SFR})$  denoted by  $\text{SFR}_{stat}$ ) and 6.15 (for  $\log(\text{sSFR})$  denoted by  $\text{sSFR}_{stat}$ ) in which the  $Q_1 - Q_3$  where 50% of the sources have the values and the median are presented for each parameter. We first compared our final sample galaxies taking the median values of the stellar mass. The  $M_{med} = 9.82$  for galaxies in ZwCl0024+1652 that is greater than the  $M_{med} (= 9.26)$  for our sample galaxies in Virgo cluster. Likewise, the galaxies in ZwCl0024+1652 are also characterized by larger  $\text{SFR}_{med} (= 0.29)$  than the Virgo cluster galaxies, with  $\text{SFR}_{med} = -0.80$  for Virgo members. Virgo cluster galaxies also are observed to have lower specific SFR in average with  $\text{sSFR}_{med} = -10.06$ , than the ZwCl0024+1652 member galaxies having  $\text{sSFR}_{med} = -9.47$ . The SFR was observed previously to increase with redshift for field galaxies at least at  $z \sim 0-2$  (e.g., Brinchmann et al., 2004; Elbaz et al., 2007; Pannella et al., 2009). Similarly

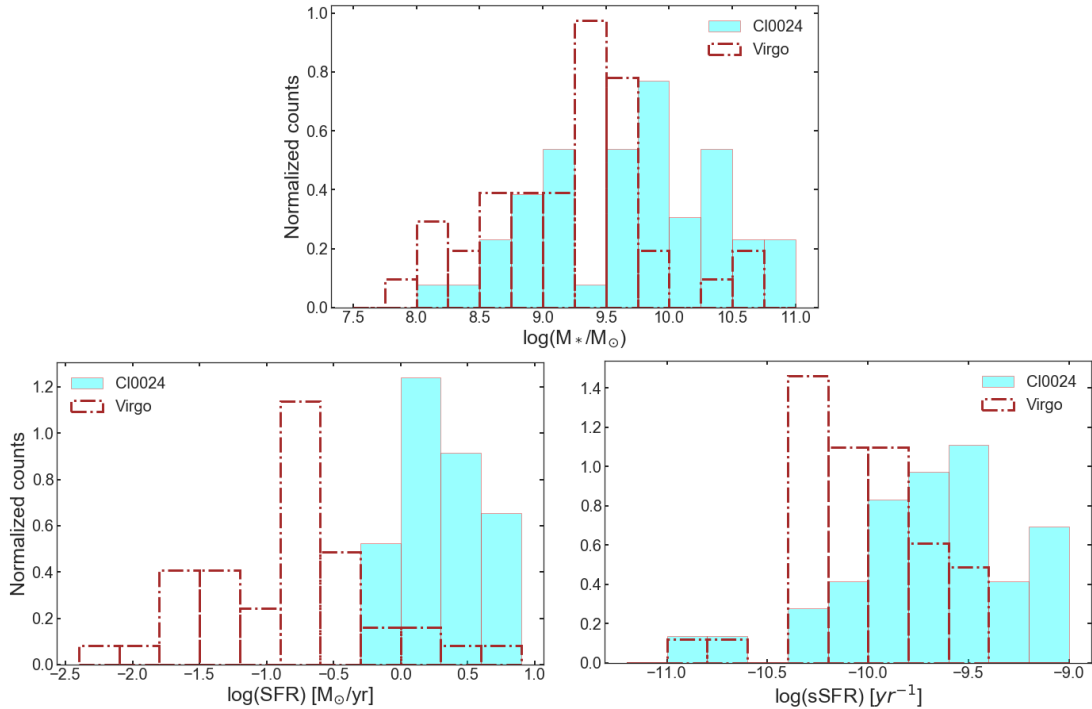


**Figure 6.9:** Histograms comparing the stellar mass (**top panel**), and star-forming properties: SFR (**bottom left**) and sSFR (**bottom right**). Cyan filled blocks represent ZwCl0024+1652 member galaxies while the dash dotted brown blocks describe the Virgo cluster galaxies.

**Table 6.13:** Statistical comparison of  $\log(M_*)$  of galaxies among both clusters. The stellar masses are measured in  $[M_\odot]$ .

Cluster	Q1	median	Q3
ZwCl0024+1652 ( $z \sim 0.4$ )	9.13	9.82	10.25
Virgo ( $z \sim 0.0038$ )	8.78	9.26	9.57

for cluster galaxies SFR was also reported to increase with redshift and cluster member galaxy population of higher SFR with more masses is observed at higher redshifts than the local Universe (Cowie et al., 1996; Postman et al., 1998, 2001). Analyzing cluster members in redshift ranges from  $z=0.4$  to  $0.8$ , Vulcani et al. (2010) investigated that higher values of SFRs and sSFRs occur at higher redshifts for both cluster members and field galaxies. In our work, the galaxies that we are comparing are of different star forming properties (SFR and sSFR) and stellar masses (higher for ZwCl0024+1652 member galaxies than Virgo members). Our results are in line with the common agreement that SF cluster galaxies at higher redshift are characterized by higher values of the properties we analyzed ( $M_*$ , SFR and sSFR) than those galaxies in lower redshift clusters.

**Table 6.14:** Statistical comparison of  $\log(\text{SFR})$  of galaxies among both clusters. SFR values are measured in  $[\text{M}_\odot] \text{yr}^{-1}$ .

Cluster	Q1	median	Q3
ZwCl0024+1652 ( $z \sim 0.4$ )	0.04	0.29	0.54
Virgo ( $z \sim 0.0038$ )	-1.26	-0.80	-0.47

**Table 6.15:** Statistical comparison of  $\log(\text{sSFR})$  of galaxies among both clusters. Specific SFR values are measured in  $[\text{yr}^{-1}]$ .

Cluster	Q <sub>1</sub>	median	Q <sub>3</sub>
ZwCl0024+1652 ( $z \sim 0.4$ )	-9.80	-9.47	-8.89
Virgo ( $z \sim 0.0038$ )	-10.27	-10.06	-9.82

**Table 6.16:** Statistical comparison of  $Z$  ( $\equiv 12 + \log(\text{O}/\text{H})$ ) of galaxies among both clusters.

Cluster	Q <sub>1</sub>	median	Q <sub>3</sub>
Virgo ( $z \sim 0.0038$ )	8.39	8.54	8.61
ZwCl0024+1652 ( $z \sim 0.4$ )	8.56	8.65	8.73

Next, we compared the metallicity and its dependence on different galaxy parameters in the two clusters. First, we explore the abundance indicator ( $12 + \log(\text{O}/\text{H})$ ). Metallicities of galaxies in each cluster were derived with the same approach (N2 indicator) and statistically described separately in the above sections. From Table 6.6, we deduce that the metallicity for ZwCl0024+1652 galaxy cluster ( $z \sim 0.4$ ) ranges from 8.33 to 8.77, with mean and median values of 8.63 and 8.65, respectively. In the same manner, the derived metallicity for galaxies in Virgo ( $z \sim 0.038$ ) was described in Table 6.12; where the values range from 8.20 to 8.89 with mean and median values given by 8.52 and 8.56, respectively. From our results we can see that the median metallicity for ZwCl0024+1652 cluster galaxies is larger than that of the Virgo cluster (as described in Table 6.16). The range of 50% metallicity in the middle for ZwCl0024+1652 galaxies (8.56-8.73) is greater than that for Virgo cluster galaxies (8.39-8.61). The histogram in Figure 6.10 shows the evolution of metallicity of galaxies with redshift of the host clusters. From this plot we deduce that metallicity in average is larger for higher redshift cluster galaxies as compared to the lower redshift counterparts. In short, metallicity of galaxies in galaxy clusters vary directly with redshift. This confirms a well established relation that massive galaxies, in higher redshift in our case, being characterized by higher metallicities than lower massive galaxies (e.g., Tremonti et al., 2004; Maiolino et al., 2008). This may be due to enhanced SFRs as a result

of higher masses (e.g., [Brinchmann et al., 2004](#)) and more of star-forming population in higher redshift cluster galaxies than the lower redshift ones. We can

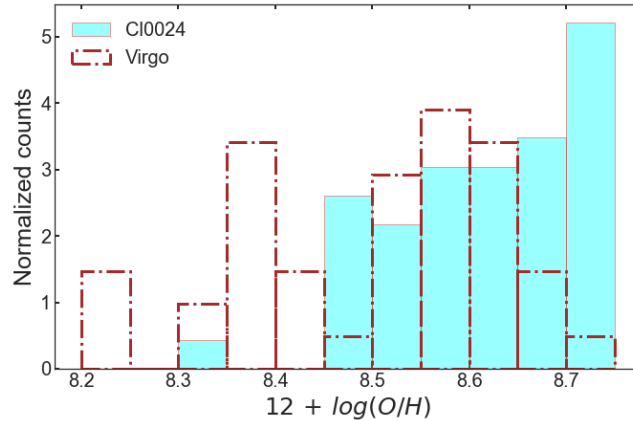


**Figure 6.10:** Histogram plot comparing the metallicity, with Cyan filled blocks representing ZwCl0024+1652 member galaxies while the dash dotted brown blocks describing the Virgo cluster galaxies.

understand from the plot that the metallicities are radially distributed almost in a constant manner out to  $R \sim 3$  Mpc for both galaxy clusters irrespective of redshift of the cluster, but slightly increasing with clustercentric distance for both cases [with slopes being,  $m=0.0026$  for ZwCl0024+1652, and  $0.036$  for Virgo]. In addition, the correlation coefficients were computed to be equal to  $0.0161$  and  $0.17$ , for ZwCl0024+1652 and Virgo, respectively]. Our work shows that the slope of the linear fit decreases with redshift, but the correlations are very weak inline with some previous works (e.g., [Sreedhar et al., 2012](#)), but the slope of the linear fit decreases with redshift. Our results do not agree with previous works that reported a negative correlation of metallicity to clustercentric distance (e.g., [Maier et al., 2016](#); [Gupta et al., 2016](#)).

This can be substantiated by previous works that higher redshift clusters may not have completed their process of formation hence field properties could affect more; that minimal effect of location of galaxy in the SF properties as well as metallicity would be observed (e.g., [Pintos-Castro et al., 2016](#)). In lower redshifts, the cluster could have relatively completed its formation that the galaxy location with respect to the cluster centre could strongly affect the member galaxy properties. That could be the reason for the slope becoming flat as we go up with redshift because at lower redshifts the cores of galaxy clusters are dominated by red, massive and passive ET galaxies while at higher redshifts a significant increase of LT galaxies is



observed at cluster cores; hence resulting with comparable amount of metallicity at the cluster outskirts (but very slowly increasing metallicity with clustercentric distance in our case for the higher redshift cluster).

We have explored and compared the variation of metallicity with stellar mass for galaxies in both clusters. To check the relationships for similar masses since we are dealing with extremely different galaxies, we grouped the masses into two bins; with low mass bin to be the range  $\log(M_*) [M_\odot] \equiv 8.5\text{--}9.25$ , while high mass bin ranges between  $\log(M_*) [M_\odot] \equiv 9.25\text{--}10.0$  values. We tested the relationships of metallicity ( $12 + \log(\text{O}/\text{H})$ ) versus  $\log(M_*) [M_\odot]$  together with the best linear fits both in low mass and high mass bins for galaxies in each cluster. For ZwCl0024+1652 cluster galaxies, we determined that the slopes are -0.01370 and -0.03403 respectively for comparisons in low mass and high mass bins respectively. This implies that a very weak anti-correlation is observed between metallicity and stellar mass, but differing for low and high mass bins. We observed that a fast decreasing trend of  $Z$  versus stellar mass is observed in high mass region than in low mass region for ZwCl0024+1652 cluster galaxies ( $z \sim 0.4$ ). For Virgo cluster galaxies we derived the slopes to be 0.2543 and 0.03430 respectively, for low mass and high mass bins. Hence for galaxies in Virgo cluster, a fast growing is observed in low mass while a slow positive correlation is observed for high mass bin in  $Z$  versus stellar mass plots. Apart from generally opposite correlation trend in both clusters, larger slope is observed in case of lower mass while smaller slopes are observed for high mass region for galaxies in both clusters. We verified that the mass-metallicity relation (MZR) evolves with redshift. Comparing the slopes in both mass bins for each cluster galaxies we deduce that the evolution of MZR with redshift is faster in low mass region than in the case of high stellar mass region. We are presenting our observations but couldn't arrive at well established results because of different biases. Therefore, the results should be taken with precautions since we are mapping different sample of galaxies in terms of their stellar mass, SFR, sSFR, and methods used to measure the parameters. In addition, our results could have been subject to biases resulting from small fraction of galaxies used in each case.

We further explored the variation of SFR with metallicity for the cluster galaxies. The  $Z$  versus SFR scatter plot is depicted in Figure 6.11. We clearly see from the plots that the metallicity is directly proportional to SFR for galaxies in each cluster. However, the scatter of  $Z$  versus SFR is in left bottom corner for Virgo cluster

with scatter points for ZwCl0024+1652 at the top right corner. That is the lower metallicity average for Virgo cluster galaxies results from lower average in SFR while the higher mean metallicity for ZwCl0024+1652 is a result of higher SFR (enhanced star formation). Therefore our results show that the positive correlation holds between the metallicity and SFR in galaxy clusters. Moreover, we can deduce that the Z - SFR relationship evolves with redshift in such a way that the slope becomes more flat while going up in redshift. The sample of galaxies in the Virgo cluster shows a very modest SFR, and low metallicity, while those sampled in the Cl0024+1652 cluster have a higher SFR and generally higher metallicity. However, as observed in Figure 6.11, both samples follow a consistent trend, that could suggest either a very mild, or no evolution of the relation from  $z = 0.4$  to  $z = 0.0038$ . Of course, the small samples and large scatter shown in the plot precludes from drawing a solid conclusion. As mentioned above, it should be accounted that our results are subject to different biases such as: different properties in the two clusters (stellar mass, SFR, sSFR, etc), different methods in measuring the properties, and small fraction of galaxies may not represent the whole sample.

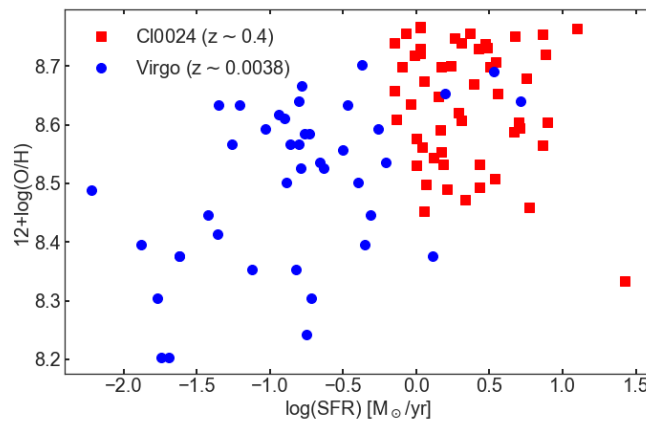


**Figure 6.11:** The Z versus SFR scatter plots, fits not indicated because the scatter points are clearly isolated and observed for each cluster.

Finally, we studied the relation between sSFR with metallicity for the cluster galaxies. We found for galaxies in both clusters that, larger sSFR results with smaller metallicity and vice versa. More precisely, we determined lower value sets in both parameters for Virgo ( $z \sim 0.038$ ) while higher value sets in the corresponding parameters for ZwCl0024+1652 cluster galaxies. We generally verify the anti-correlation (inverse relationship) between sSFR and Z for all the galaxies in

each cluster. To illustrate the way of evolution of sSFR -  $Z$  relation with redshift, if we consider two galaxy clusters  $GC_1$  with redshift  $z_1$  and  $GC_2$  with redshift  $z_2$  where  $z_1 < z_2$ , any value of sSFR results with metallicity  $Z_1$  in case of  $GC_1$  and  $Z_2$  for  $GC_2$  in such a way that  $Z_2 > Z_1$ . Once again we are aware that our findings here shall be tested again using larger and more consistent samples.

## 6.6 Conclusions

In this chapter we performed the metallicity studies of galaxy clusters at different redshifts towards the contribution to the studies of galaxy evolution in clusters to  $z \sim 1$ . We reduced a raw data from GLACE for ZwCl0024+1652 galaxy cluster ( $z \sim 0.4$ ) to derive different parameters including metallicity and used a published data from [Sánchez-Portal et al. \(2015\)](#) in the same framework. For Virgo local cluster at ( $z \sim 0.0038$ ), we used a public data from previous works by different authors ([Binggeli et al., 1985](#); [Gavazzi et al., 2004](#); [Peng et al., 2008](#); [Kim et al., 2014](#)). We then carried out the parameter computations for galaxies in both clusters and analysed the results. While, our results should be taken with care since the results are subject to different biases like: differences in galaxy properties (e.g., stellar mass, SFR, and sSFR) in the two clusters, methods in measuring the parameters, and a very small fraction of sample galaxies used. Subject to these biases, our brief summarized results and conclusions are given below.

- Metallicity is computed using the N2 abundance indicator and other related parameters are measured for 53 galaxies in ZwCl0024+1652 cluster, and 44 Virgo cluster member galaxies.
- The statistical analysis and the KS2 test applied on our samples verified that our sample selection is consistent with respect to the base sample of the two clusters.
- The metallicities on average are higher for ZwCl0024+1652 cluster galaxies in ( $\bar{Z} = 8.63$ ,  $Z_{med} = 8.65$ ) but lower metallicity values are observed for Virgo cluster galaxies ( $\bar{Z} = 8.52$ ,  $Z_{med} = 8.56$ ).
- Metallicities slightly correlate with clustercentric distance for both clusters while the correlation is relatively highest for Virgo than in case of galaxies in ZwCl0024+1652 cluster.

- The variation of metallicity with clustercentric distance evolves with redshift to  $z \sim 0.4$  in such a way that the correlation decreases becoming nearly zero at the higher redshift.
- We report anti-correlation between metallicity and logarithmic stellar mass both in low mass as well as high mass bins (with different slopes) for galaxies in ZwCl0024+1652 cluster at  $z \sim 0.4$ . While for galaxies in Virgo cluster the metallicity is directly proportional to the logarithmic stellar mass (the proportionality constant being different for both bins).
- In general, our plots in Figures 6.1 and 6.5 indicate that metallicity correlates positively with stellar mass. However, this relation is not clearly observed for the higher redshift cluster, ZwCl0024+1652.
- Our results show that MZR evolves with redshift in such a way that at lower redshift the mass strongly affects the metallicity than in case of higher redshifts.
- As in the case of metallicity, the SFR of galaxies in Virgo cluster is smaller on average while galaxies in ZwCl0024+1652 cluster are characterized by relatively higher SFR. This shows that the SFR together with metallicity both increase with redshift for galaxies in clusters.
- Moreover, the relation between SFR and metallicity becomes more tight at higher redshifts.
- Our results show that metallicity also varies with sSFR in an inversely proportional pattern (higher Z for lower sSFRs). That is Z anti-correlates with sSFR for all the cluster galaxies at redshifts in our range. The anti-correlation is clearly observed for Virgo cluster galaxies but significant dispersion is observed for ZwCl0024+1652 member galaxies.
- We determined that parameters associated to the star-forming properties (SFR and sSFR) are observed to be higher for ZwCl0024+1652 galaxies than that of Virgo cluster. Larger values of  $M_*$  and Z on average are also observed for members of the higher redshift cluster than those of Virgo cluster members. While we observed a higher average density characterizing regions within Virgo cluster as compared to that of ZwCl0024+1652 cluster.

# Chapter 7

## Summary and conclusions

In this thesis, we mainly aimed at the comprehensive studies of the properties of galaxies in clusters to a redshift  $z \sim 1$ . The summary of our works with the conclusions derived and future works are presented in this chapter.

### 7.1 General summary

The thesis focuses specifically on achieving three major goals: to perform a detailed morphological studies of cluster member galaxies at different redshifts, to analyse the SF/AGN properties in clusters of galaxies, and carrying out studies of metallicity in galaxy clusters. The fourth goal is to get clues about the transformation and evolution of galaxies in clusters and since the three major goals are studied based on galaxy clusters at different redshifts to  $z \sim 1$ , hence this is ultimately attained. For attaining the objectives, we used a GLACE TF data resulting from  $H\alpha$ /[NII] imaging consisting of a total of 174 ZwCl0024+1652 member  $H\alpha$  line emitters (Sánchez-Portal et al., 2015). For this cluster, we also used the HST/ACS imaging data and the WFP2 master catalogue data. For the RXJ1257+4738 cluster, we used a GLACE public data from Pintos-Castro (2014); Pintos-Castro et al. (2016) and  $H\beta$  raw imaging data and numerous public data have been used for the Virgo cluster: mainly VCC (Binggeli et al., 1985) and EVCC (Kim et al., 2014). The data we used is described in detail in Chapter 2.

The first objective was attained by performing a morphological classification of galaxies in a galaxy cluster ZwCl0024+1652 at  $z \sim 0.4$  and related analysis among

our sample of all the three clusters (including RXJ1257+4738 at  $z \sim 0.87$  and Virgo at  $z \sim 0.0038$ ). For ZwCl0024+1652 cluster members, we used the HST/ACS data for source extraction with SExtractor. Then applying a non parametric method called galSVM on the sources catalogue to measure the morphological parameters. The results have been presented in detail in Chapter 4, and partly published in [Beyoro-Amado et al. \(2019\)](#). Some of the main results are:

- The seven morphological parameters used in non-parametric methods: ELLIP, ASYM, CABR, GINI, SMOOTH, M20 and CCON were measured for ZwCl0024+1652 cluster members with I magnitudes up to  $\sim 26$  and up to the clustercentric distance of 1 Mpc..
- Computing the probabilities of being ET for 231 member galaxies with galSVM code implementing non-parametric technique, we classified a total of 180 galaxies into 97 ET (42%) and 83 LT (36%), with the remaining 51 (22%) being unclassified.
- The colour-colour and colour-magnitude diagrams plotted gave that higher fraction of ETs are in general located in redder and brighter regions, as expected.
- Comparing with a work of [Sánchez-Portal et al. \(2015\)](#), we found 39 ELGs with morphologies determined by our method where 28 and 11 galaxies are LT and ET, respectively.
- For this cluster at  $z \sim 0.4$ , larger fraction of ET resulted over the LT fraction throughout the clustercentric distance of 1 Mpc. Moreover, for magnitude (F775W) up to  $\sim 22$ , the ET fraction dominates.
- Comparing to [Parekh et al. \(2015\)](#), we determined that CCON and CABR could be equally important parameters as GINI and M20 for morphological classification of galaxies in clusters.
- Since we used results from [Pintos-Castro et al. \(2016\)](#) for RXJ1257+4738, we identified 10 ETs, 21 bETs and 4 LTs within the 1 Mpc clustercentric distance.
- ET fraction dominates over the LT to the r-band magnitude of  $\sim 23.75$  while reversed beyond that.

- Dominant ET fraction is observed over the LT fraction throughout the clustercentric distance for this cluster at  $\sim 0.87$ .
- For Virgo cluster members, we measured the clustercentric distance of the galaxies and identified 273 ( $\sim 68\%$ ) ET (majority being dEs), and 131 ( $\sim 32\%$ ) LT galaxies within 1 Mpc distance.
- For this cluster, the ET fraction dominates while significantly decreasing outwards over the LT fraction that is observed to increase in contrast.
- In all the three clusters, we have generally observed more proportion of ETs than LTs in the central parts up to 1 Mpc.

For achieving the second objective, we performed the analysis of the star forming and AGN properties of galaxies in clusters. For ZwCl0024+1652 cluster ( $z \sim 0.4$ ), we performed an extensive work by carrying out the reduction of GLACE TF data of [OIII] and  $H\beta$  imaging applying TFred. Part of our results has been published in [Beyoro-Amado et al. \(2021\)](#). Moreover, we used the [OII] fluxes as part of GLACE results measured by [Pintos-Castro \(2014\)](#) for further computation of the SF properties of the galaxies in RXJ1257+4738 cluster ( $z \sim 0.87$ ). However, for Virgo cluster, we used a public data of emission line fluxes and related parameters from [Grossi et al. \(2015\)](#) and [Gavazzi et al. \(2004\)](#), in addition to other ancillary data. We presented the work in detail in Chapter 5 and the main results include:

- We determined that out of the  $H\alpha$  emitters from [Sánchez-Portal et al. \(2015\)](#) in ZwCl0024+1652 cluster,  $\sim 20\%$  and  $\sim 34\%$  galaxies show [OIII] and  $H\beta$  emission lines, respectively, out to the  $H\alpha$  flux of  $2.43 \times 10^{-15} \text{ erg s}^{-1} \text{ cm}^{-2}$ .
- The BPT-NII diagnostic diagram produced for ZwCl0024+1652 member ELGs classified our galaxies as  $\sim 40\%$  SF,  $\sim 55\%$  composites and  $\sim 5\%$  LINER.
- We found that the cores of regular clusters are generally poor with SF, as well as AGN activity.
- Considering ZwCl0024+1652 cluster, it is determined that the fraction of SF galaxies and AGNs remain roughly constant across the low- and medium-density environments, dropping sharply towards high-density environments.

- We found that galaxies in RXJ1257+4738 are characterized on average by the highest star formation rate, while Virgo cluster galaxies with lowest SFRs in our sample.
- Our work indicate that SFR in general anti-correlates with local density for galaxies in clusters and galaxies in higher redshift cluster are characterized by lower local density.
- A positive correlation is observed on SFR versus  $M_*$ , but with slope varying with redshift.
- We have noted that our results are suffering from different biases. The samples that we used in the three clusters are different in properties, the SFRs were computed with different methods, the local densities were computed with different number of galaxies, and the fractions of the galaxies used in each case were small that couldn't lead us to precise results.

Finally, the last objective apart from the one to be achieved by analysing results from all the objectives is attained by computing and analysing metallicities of galaxies in two of the clusters (ZwCl0024+1652 and Virgo) at different redshifts. We couldn't include the metallicity analysis of galaxies in RXJ1257+4738 cluster because of shortage of data at this point. Metallicities are analysed in relation to different galaxy properties as presented with details in Chapter 6 and we pointed out some of the main results below.

- Metallicities were computed for galaxies in ZwCl0024+1652 cluster (53 members) and Virgo cluster (44 galaxies) using the N2 abundance estimator with prescription from [Pettini and Pagel \(2004\)](#).
- Slightly higher metallicities were determined for galaxies in ZwCl0024+1652 cluster ( $\bar{Z} = 8.63 \pm 0.014$ ) but lower for Virgo cluster galaxies ( $\bar{Z} = 8.52 \pm 0.021$ ).
- Metallicity is observed to correlate positively with clustercentric distance for all the members of the two clusters in our sample.
- Positive correlation is observed between metallicity and stellar mass for galaxies in Virgo cluster ( $z \sim 0.0038$ ), both in low and high mass bins. However, anti-correlation is observed between these parameters for galaxies in ZwCl0024+1652 cluster ( $z \sim 0.4$ ); in both mass bins.



- For galaxies in both clusters ( $z \sim 0-0.4$ ), we observed that metallicity correlates with SFR while anti-correlation is exhibited between sSFR and  $Z$ .

## 7.2 Conclusions

This work can be taken as a comprehensive one in studying the properties and evolution of galaxies in galaxy clusters to a redshift  $z \sim 1$ . We combined the GLACE TF noble raw data and other ancillary; published as well as unpublished data for ZwCl0024+1652 and RXJ1257+4738 clusters, but we used public data for Virgo cluster. Working towards achieving our objectives we have drawn conclusions at the end of each chapter, while the main conclusions derived from this work are given as follows.

From the results of morphologies for galaxies in ZwCl0024+1652 cluster, we conclude that greater ET proportion exists over the LT population for intermediate redshift clusters to a clustercentric distance of 1 Mpc. Similar evolution trend also works for Virgo cluster galaxies, with even more ET proportion in this case. However, because of poor statistics and limited previous works, we couldn't draw a conclusion for RXJ1257+4738 cluster. Generally, evolution of morphology takes place with redshift in such a way that LT population in clusters increases with redshift while the ET population decreases. We deduced that galaxies evolve morphologically from LT to ET as they pass through ICM within clusters in our sample. This could be due to the ram pressure stripping that makes the gas-rich LT galaxies to be stripped of their gases and transformed into gas-poor ET galaxies. We also conclude that for morphological classification, galSVM is a reliable tool to be used in non-parametric methods even for larger sample. Comparing our works to previous works ([Sánchez-Portal et al., 2015](#)), we verified that majority of ELGs are LT in morphology than being ET. One can see that galaxy morphology evolves with clustercentric distance in such a way that fraction of LT increases while the ET fraction decreases in going outwards from the cluster centre. We also infer that redshifts computed from the position of  $H\beta$  and [OIII] lines using the pseudo-spectra have been compared with previous results of [Sánchez-Portal et al. \(2015\)](#), finding a good correlation between all measurements and our TF redshifts would be of spectroscopic standard. Our results suggest that cores of clusters are less populated with ELGs with ET morphology (dominated by ELGs with LT morphology). From our works we deduce that SF galaxies and AGN

follow the local density-clustercentric distance anti-correlation for the two lower redshift clusters, and we confirmed this using GLACE TF observations, but for RXJ1257+4738 cluster the relationship is not monotonic that the cluster is not a regular.

It can also be concluded that SFR evolves with redshift in such a way that it increases with redshift (the local cluster galaxies have smallest SFRs). Galaxies in higher redshift cluster are characterized by lower local density. Significantly highest local density resulted for the Virgo cluster galaxies because their densities are computed with large number of member galaxies. Regarding the redshift evolution for RXJ1257+4738 cluster (highest redshift) the slope is steepest or tighter anti-correlation while nearly flat for Virgo (lowest redshift). Moreover, an established correlation is observed on SFR versus  $M_*$  for cluster galaxies of our sample, with the evolution that the variation is stronger for lower redshift cluster but weak for higher redshift cluster galaxies.

Metallicity analysis led us to a conclusion that metallicity of cluster galaxies evolve with redshift in such a way that lower redshift cluster galaxies are characterised by lower metallicity values and vice versa. Galaxy metallicity correlates with clustercentric distance, where the correlation is larger for galaxies of higher redshift cluster. The MZR evolves with redshift in such a way that at lower redshift, metallicity is strongly affected by mass than in case of higher redshift. That is, MZR is more evident in lower redshift measurements. The SFR- $Z$  correlation becomes more and more tight as redshift increases. We finally conclude that anti-correlation results between  $Z$  and sSFR of the cluster galaxies in such a way that the anti-correlation becomes more and more tight as redshift increases. Since our results are subject to different biases, our conclusions must be taken with great care. The biases may come from differences in properties (SFRs, sSFRs, masses, and local densities) of the samples of the three clusters, the different methods of computing the SFRs and sSFRs, and small fractions of the sample galaxies used that may not be able represent the galaxy cluster.

### **7.3 Future work**

The study of properties and evolution of galaxies in clusters is a very important experiment that can give a significant clue about the large scale studies of the

properties and evolution of the Universe. In this thesis we presented a comprehensive study of the properties and evolution of galaxies in three different clusters within a redshift range to  $z \sim 1$ . However, in future we are planing to carry out some of additional analysis that could help in getting more solid results regarding the comparison of the three clusters.

First, since there is only a visual morphological classification available for Virgo member galaxies, we have a plan to work on the morphological classifications of galaxies in this cluster using galSVM code.

Secondly, for ZwCl0024+1652 cluster galaxies, the reduction and flux measurements for [OII] emission lines have to be performed since we have a GLACE TF data observed with [OII] narrow band mapping. This is useful to further compute and test metallicity with different diagnostic diagrams other than only N2.

Finally, we have a plan to proceed with the GLACE TF data finallizing the reduction of [OIII] and  $H\beta$  imaging and measuring the emission line fluxes for galaxies in the RXJ1257+4738 cluster at about the highest redshift of our concern. With measured fluxes, we are planing to further compute and analyse different properties like SFR and metallicity in relation to other galaxy parameters. Adding these future works to our current results, we can have a more clear picture about galaxy properties and evolution within clusters up to a redshift of  $z \sim 1$ .

# Bibliography

- Abadi, M. G., Moore, B., and Bower, R. G. (1999). Ram pressure stripping of spiral galaxies in clusters. *MNRAS*, 308(4):947–954.
- Abazajian, K. N. et al. (2009). The Seventh Data Release of the Sloan Digital Sky Survey. *ApJS*, 182:543–558.
- Abell, G. O. (1958). The Distribution of Rich Clusters of Galaxies. *ApJS*, 3:211.
- Abraham, R. G. et al. (1994). The morphologies of distant galaxies. 1: an automated classification system. *AJ*, 432:75–90.
- Abraham, R. G. et al. (1996). The Morphologies of Distant Galaxies. II. Classifications from the Hubble Space Telescope Medium Deep Survey. *ApJSS*, 107:1–17.
- Abraham, R. G., van den Bergh, S., and Nair, P. (2003). A New Approach to Galaxy Morphology. I. Analysis of the Sloan Digital Sky Survey Early Data Release. *ApJ*, 588:218–229.
- Alberts, S. et al. (2014). The evolution of dust-obscured star formation activity in galaxy clusters relative to the field over the last 9 billion years. *MNRAS*, 437(1):437–457.
- Alberts, S. et al. (2016). Star Formation and AGN Activity in Galaxy Clusters from  $z=1-2$ : a Multi-Wavelength Analysis Featuring Herschel/PACS. *ApJ*, 825(1):72.
- Allen, R. J. et al. (2016). Differences in the Structural Properties and Star-formation Rates of Field and Cluster Galaxies at  $z \sim 1$ . *ApJ*, 826(1):60.
- Alloin, D. et al. (1979). Nitrogen and oxygen abundances in galaxies. *A&A*, 78:200–216.
- Alonso, M. S. et al. (2007). Active galactic nuclei and galaxy interactions. *MNRAS*, 375(3):1017–1024.
- Alonso, S. et al. (2012). Galaxy interactions. II. High density environments. *A&A*, 539:A46.
- Altieri, B. et al. (2010). Herschel deep far-infrared counts through Abell 2218 cluster-lens. *A&A*, 518:L17.
- Andrews, B. H. and Martini, P. (2013). The Mass-Metallicity Relation with the Direct Method on Stacked Spectra of SDSS Galaxies. *ApJ*, 765(2):140.
- Aniyan, A. K. and Thorat, K. (2017). Classifying Radio Galaxies with the Convolutional Neural Network. *ApJSS*, 230:20–34.
- Argudo-Fernández, M., Lacerna, I., and Duarte Puertas, S. (2018). The dependence of mass and environment on the secular processes of AGNs in terms of morphology, colour, and specific star-formation rate. *A&A*, 620:A113.
- Baldry, I. K. et al. (2006). Galaxy bimodality versus stellar mass and environment. *MNRAS*, 373(2):469–483.

- Baldwin, J. A., Phillips, M. M., and Terlevich, R. (1981). Classification parameters for the emission-line spectra of extragalactic objects. *PASP*, 93:5–19.
- Balogh, M. L. et al. (1997). Star Formation in Cluster Galaxies at  $0.2 < z < 0.55$ . *APJL*, 488:L75–L78.
- Balogh, M. L. et al. (1999). Differential Galaxy Evolution in Cluster and Field Galaxies at  $z \sim 0.3$ . *AJ*, 527:54–79.
- Balogh, M. L., Navarro, J. F., and Morris, S. L. (2000). The Origin of Star Formation Gradients in Rich Galaxy Clusters. *ApJ*, 540:113–121.
- Banerji, M. et al. (2010). Galaxy Zoo: reproducing galaxy morphologies via machine learning. *MNRAS*, 406:342–353.
- Barrena, R. et al. (2012). Environmental effects on the bright end of the galaxy luminosity function in galaxy clusters. *A&A*, 540:A90.
- Bekki, K. and Couch, W. J. (2003). Starbursts from the Strong Compression of Galactic Molecular Clouds due to the High Pressure of the Intracluster Medium. *ApJL*, 596(1):L13–L16.
- Bell, E. F. et al. (2003). The Optical and Near-Infrared Properties of Galaxies. I. Luminosity and Stellar Mass Functions. *ApJSS*, 149:289–312.
- Bell, E. F. et al. (2004). Nearly 5000 Distant Early-Type Galaxies in COMBO-17: A Red Sequence and Its Evolution since  $z \sim 1$ . *ApJ*, 608:752–767.
- Bershady, M. A., Jangren, A., and Conselice, C. J. (2000). Structural and Photometric Classification of Galaxies. I. Calibration Based on a Nearby Galaxy Sample. *AJ*, 119:2645–2663.
- Bertin, E. and Arnouts, S. (1996). SExtractor: Software for source extraction. *A&A SS*, 117:393–404.
- Beyoro-Amado, Z. et al. (2019). A morphological study of galaxies in ZwCl0024+1652, a galaxy cluster at redshift  $z \sim 0.4$ . *MNRAS*, 485:1528–1545.
- Beyoro-Amado, Z. et al. (2021). GLACE survey: galaxy activity in ZwCl0024+1652 cluster from strong optical emission lines. *MNRAS*, 501(2):2430–2450.
- Bilton, L. E., Pimblet, K. A., and Gordon, Y. A. (2020). The impact of disturbed galaxy clusters on the kinematics of active galactic nuclei. *MNRAS*, 499(3):3792–3805.
- Binggeli, B., Sandage, A., and Tammann, G. A. (1985). Studies of the Virgo Cluster. II - A catalog of 2096 galaxies in the Virgo Cluster area. *AJ*, 90:1681–1759.
- Binggeli, B., Tammann, G. A., and Sandage, A. (1987). Studies of the Virgo cluster. VI - Morphological and kinematical structure of the Virgo cluster. *AJ*, 94:251–277.
- Birzan, L. et al. (2019). A massive cluster at  $z = 0.288$  caught in the process of formation: The case of Abell 959. *MNRAS*, 487(4):4775–4789.
- Biviano, A. and Katgert, P. (2004). The ESO Nearby Abell Cluster Survey. XIII. The orbits of the different types of galaxies in rich clusters. *A&A*, 424:779–791.
- Blanton, M. R. and Roweis, S. (2007). K-Corrections and Filter Transformations in the Ultraviolet, Optical, and Near-Infrared. *AJ*, 133(2):734–754.
- Bonafede, A. et al. (2020). The Coma cluster at LOFAR frequencies I: insights into particle acceleration mechanisms in the radio bridge. *arXiv e-prints*, page arXiv:2011.08856.
- Bongiovanni, A. et al. (2005). The CIDA-UCM-Yale shallow survey for emission-line galaxies. *MNRAS*, 359(3):930–940.

- Bongiovanni, Á. et al. (2019). The OTELO survey. I. Description, data reduction, and multi-wavelength catalogue. *A&A*, 631:A9.
- Bongiovanni, Á. et al. (2020). The OTELO survey. A case study of [O III]  $\lambda$ 4959,5007 emitters at  $z = 0.83$ . *A&A*, 635:A35.
- Bornancini, C. and García Lambas, D. (2020). Host galaxy properties and environment of obscured and unobscured x-ray selected active galactic nuclei in the cosmos survey. *MNRAS*, 494(1):1189–1202.
- Bower, R. G., Kodama, T., and Terlevich, A. (1998). The colour-magnitude relation as a constraint on the formation of rich cluster galaxies. *MNRAS*, 299:1193–1208.
- Bower, R. G., Lucey, J. R., and Ellis, R. S. (1992). Precision photometry of early-type galaxies in the Coma and Virgo clusters: A test of the universality of the colour-magnitude relation. I - The data. II. Analysis. *MNRAS*, 254:589–613.
- Brinchmann, J. et al. (2004). The physical properties of star-forming galaxies in the low-redshift Universe. *MNRAS*, 351(4):1151–1179.
- Broadhurst, T. et al. (2000). A Spectroscopic Redshift for the Cl 0024+16 Multiple Arc System: Implications for the Central Mass Distribution. *ApJL*, 534:L15–L18.
- Brodwin, M. et al. (2010). SPT-CL J0546-5345: A Massive  $z_{\text{cl}}^1$  Galaxy Cluster Selected Via the Sunyaev-Zel'dovich Effect with the South Pole Telescope. *ApJ*, 721(1):90–97.
- Brodwin, M. et al. (2013). The Era of Star Formation in Galaxy Clusters. *ApJ*, 779(2):138.
- Brodwin, M. et al. (2015). The Massive and Distant Clusters of WISE Survey. III. Sunyaev-Zel'dovich Masses of Galaxy Clusters at  $z \sim 1$ . *ApJ*, 806(1):26.
- Bruzual, G. and Charlot, S. (2003). Stellar population synthesis at the resolution of 2003. *MNRAS*, 344:1000–1028.
- Bufanda, E. et al. (2017). The evolution of active galactic nuclei in clusters of galaxies from the Dark Energy Survey. *MNRAS*.
- Buitrago, F. et al. (2013). Early-type galaxies have been the predominant morphological class for massive galaxies since only  $z \sim 1$ . *MNRAS*, 428:1460–1478.
- Bustamante, S. et al. (2020). Galaxy pairs in the Sloan Digital Sky Survey - XIV. Galaxy mergers do not lie on the fundamental metallicity relation. *MNRAS*, 494(3):3469–3480.
- Butcher, H. and Oemler, A., J. (1978). The evolution of galaxies in clusters. I - ISIT photometry of C10024 + 1654 and 3C295. *ApJ*, 219:18–30.
- Butcher, H. and Oemler, A., J. (1984). The evolution of galaxies in clusters. V - A study of populations since  $z$  approximately equal to 0.5. *ApJ*, 285:426–438.
- Caglar, T. and Hudaverdi, M. (2017). XMM-Newton view of X-ray overdensities from nearby galaxy clusters: the environmental dependencies. *MNRAS*, 471(4):4990–5007.
- Campusano, L. E. et al. (2018). A 3D Voronoi+Gapper Galaxy Cluster Finder in Redshift Space to  $z \sim 0.2$ . II. An Abundant Cluster Population Dominated by Late-type Galaxies Unveiled. *ApJ*, 869(2):145.
- Cantale, N. et al. (2016). Disc colours in field and cluster spiral galaxies at  $0.5 \lesssim z \lesssim 0.8$ . *A&A*, 589:A82.
- Cassata, P. et al. (2007). The Cosmic Evolution Survey (COSMOS): The Morphological Content and Environmental Dependence of the Galaxy Color-Magnitude Relation at  $z \sim 0.7$ . *ApJSS*, 172:270–283.
- Cepa, J. (1998). OSIRIS Imaging and Spectroscopy for the GTC. *ApSS*, 263:369–372.

- Cepa, J. et al. (2005). The OTELO Project. volume 24 of *Revista Mexicana de Astronomia y Astrofisica Conference Series*, pages 82–87.
- Chabrier, G. (2003). Galactic Stellar and Substellar Initial Mass Function. *PASP*, 115:763–795.
- Chang, C.-C. and Lin, C.-J. (2011). LIBSVM: A Library for Support Vector Machines. *ACM Trans. Intell. Syst. Technol.*, 2:1–27.
- Chilingarian, I. V. and Zolotukhin, I. Y. (2012). A universal ultraviolet-optical colour-colour-magnitude relation of galaxies. *MNRAS*, 419(2):1727–1739.
- Christlein, D. and Zabludoff, A. I. (2005). Disentangling Morphology, Star Formation, Stellar Mass, and Environment in Galaxy Evolution. *ApJ*, 621(1):201–214.
- Chung, S. M. et al. (2011). A WISE View of Star Formation in Local Galaxy Clusters. *ApJ*, 743(1):34.
- Cid Fernandes, R., Stasińska, G., Mateus, A., and Vale Asari, N. (2011). A comprehensive classification of galaxies in the Sloan Digital Sky Survey: how to tell true from fake AGN? *MNRAS*, 413(3):1687–1699.
- Ciocan, B. I. et al. (2020). CLASH-VLT: Enhancement of (O/H) in  $z = 0.35$  RX J2248-4431 cluster galaxies. *A&A*, 633:A139.
- Cocato, L. et al. (2020). Formation of S0s in extreme environments I: clues from kinematics and stellar populations. *MNRAS*, 492(2):2955–2972.
- Coia, D. et al. (2005). An ISOCAM survey through gravitationally lensing galaxy clusters. IV. Luminous infrared galaxies in Cl0024 + 1654 and the dynamical status of clusters. *A&A*, 431:433–449.
- Cole, S. et al. (2000). Hierarchical galaxy formation. *MNRAS*, 319(1):168–204.
- Conselice, C. J., Bershad, M. A., and Jangren, A. (2000). The Asymmetry of Galaxies: Physical Morphology for Nearby and High-Redshift Galaxies. *ApJ*, 529:886–910.
- Conselice, C. J. et al. (2003). A Direct Measurement of Major Galaxy Mergers at  $z \lesssim 3$ . *AJ*, 126:1183–1207.
- Cooper, M. C. et al. (2008). The role of environment in the mass-metallicity relation. *MNRAS*, 390:245–256.
- Cooper, M. C. et al. (2012). The DEEP3 Galaxy Redshift Survey: the impact of environment on the size evolution of massive early-type galaxies at intermediate redshift. *MNRAS*, 419:3018–3027.
- Cortijo-Ferrero, C. et al. (2017). Star formation histories in mergers: the spatially resolved properties of the early-stage merger luminous infrared galaxies IC 1623 and NGC 6090. *MNRAS*, 467(4):3898–3919.
- Couch, W. J. et al. (2001). A Low Global Star Formation Rate in the Rich Galaxy Cluster AC 114 at  $z=0.32$ . *ApJ*, 549:820–831.
- Cowie, L. L. et al. (1996). New Insight on Galaxy Formation and Evolution From Keck Spectroscopy of the Hawaii Deep Fields. *AJ*, 112:839.
- Cucciati, O. et al. (2010). The VIMOS-VLT deep survey: the group catalogue. *A&A*, 520:A42.
- Cucciati, O. et al. (2012). The star formation rate density and dust attenuation evolution over 12 Gyr with the VVDS surveys. *A&A*, 539:A31.
- Cucciati, O. et al. (2017). The VIMOS Public Extragalactic Redshift Survey (VIPERS). The decline of cosmic star formation: quenching, mass, and environment connections. *A&A*, 602:A15.
- Czoske, O. et al. (2001). A wide-field spectroscopic survey of the cluster of galaxies Cl0024 + 1654. I. The catalogue. *A&A*, 372:391–405.

- Czoske, O. et al. (2002). A wide-field spectroscopic survey of the cluster of galaxies Cl0024+1654. II. A high-speed collision? *A&A*, 386:31–41.
- Dark Energy Survey Collaboration et al. (2016). The Dark Energy Survey: more than dark energy - an overview. *MNRAS*, 460:1270–1299.
- Darvish, B. et al. (2016). The Effects of the Local Environment and Stellar Mass on Galaxy Quenching to  $z \sim 3$ . *ApJ*, 825(2):113.
- Darvish, B. et al. (2017). Cosmic Web of Galaxies in the COSMOS Field: Public Catalog and Different Quenching for Centrals and Satellites. *ApJ*, 837(1):16.
- Davidge, T. J. (2020). Intermediate-mass Early-type Disk Galaxies in the Virgo Cluster. II. Near-Infrared Spectra and Evidence for Differences in Evolution. *AJ*, 159(5):186.
- Davies, R. I. et al. (2017). The role of host galaxy for the environmental dependence of active nuclei in local galaxies. *MNRAS*, 466(4):4917–4927.
- De Grandi, S. and Molendi, S. (2001). Metallicity Gradients in X-Ray Clusters of Galaxies. *ApJ*, 551(1):153–159.
- De Lucia, G. et al. (2007). The build-up of the colour-magnitude relation in galaxy clusters since  $z \sim 0.8$ . *MNRAS*, 374:809–822.
- Delaye, L. et al. (2014). Larger sizes of massive quiescent early-type galaxies in clusters than in the field at  $0.8 < z < 1.5$ . *MNRAS*, (1):203–223.
- Delgado-Serrano, R. et al. (2010). How was the Hubble sequence 6 Gyr ago? *A&A*, 509:A78.
- Demarco, R., Gobat, R., et al. (2010). Star Formation Histories in a Cluster Environment at  $z \sim 0.84$ . *ApJ*, 725:1252–1276.
- Denicoló, G., R. Terlevich, R., and E. Terlevich, E. (2002). New light on the search for low-metallicity galaxies - I. The N2 calibrator. *MNRAS*, 330:69–74.
- Deshev, B. et al. (2017). Galaxy evolution in merging clusters: The passive core of the “Train Wreck” cluster of galaxies, A520. *A&A*, 607:A131.
- Diaferio, A., Geller, M. J., and Rines, K. J. (2005). Caustic and Weak-Lensing Estimators of Galaxy Cluster Masses. *ApJL*, 628:L97–L100.
- Dieleman, S., Willett, K. W., and Dambre, J. (2015). Rotation-invariant convolutional neural networks for galaxy morphology prediction. *MNRAS*, 450:1441–1459.
- Digby-North, J. A. et al. (2010). Excess AGN activity in the  $z = 2.30$  Protocluster in HS 1700 + 64. *MNRAS*, 407:846–853.
- Domínguez Sánchez, H. et al. (2018). Improving galaxy morphologies for SDSS with Deep Learning. *MNRAS*, 476:3661–3676.
- Dressler, A. (1980). Galaxy morphology in rich clusters - Implications for the formation and evolution of galaxies. *ApJ*, 236:351–365.
- Dressler, A. et al. (1997). Evolution since  $z = 0.5$  of the Morphology-Density Relation for Clusters of Galaxies. *ApJ*, 490:577–591.
- Dressler, A. et al. (2013). The IMACS Cluster Building Survey. II. Spectral Evolution of Galaxies in the Epoch of Cluster Assembly. *ApJ*, 770(1):62.
- Dressler, A., Gunn, J. E., and Schneider, D. (1985). Spectroscopy of galaxies in distant clusters. III - The population of CL 0024 + 1654. *ApJ*, 294:70–80.



- Dressler, A., Thompson, I. B., and Shectman, S. A. (1985). Statistics of emission-line galaxies in rich clusters. *ApJ*, 288:481–486.
- Džudžar, R. et al. (2019). Group pre-processing versus cluster ram-pressure stripping: the case of ESO156-G029. *MNRAS*, 490(1):L6–L11.
- Eastman, J. et al. (2007). First Measurement of a Rapid Increase in the AGN Fraction in High-Redshift Clusters of Galaxies. *APJL*, 664:L9–L12.
- Ehlert, S. et al. (2014). X-ray bright active galactic nuclei in massive galaxy clusters - II. The fraction of galaxies hosting active nuclei. *MNRAS*, 437(2):1942–1949.
- Eisenhardt, P. R. M. et al. (2008). Clusters of Galaxies in the First Half of the Universe from the IRAC Shallow Survey. *ApJ*, 684:905–932.
- Elbaz, D. et al. (2007). The reversal of the star formation-density relation in the distant universe. *A&A*, 468(1):33–48.
- Elbaz, D. et al. (2018). Starbursts in and out of the star-formation main sequence. *A&A*, 616:A110.
- Ellison, S. L. et al. (2008). Galaxy Pairs in the Sloan Digital Sky Survey. I. Star Formation, Active Galactic Nucleus Fraction, and the Mass-Metallicity Relation. *AJ*, 135:1877–1899.
- Ellison, S. L. et al. (2009). The mass-metallicity relation in galaxy clusters: the relative importance of cluster membership versus local environment. *MNRAS*, 396:1257–1272.
- Erb, D. K. et al. (2006). The Mass-Metallicity Relation at  $z \gtrsim 2$ . *ApJ*, 644:813–828.
- Fairley, B. W. et al. (2002). Galaxy colours in high-redshift, X-ray-selected clusters - I. Blue galaxy fractions in eight clusters. *MNRAS*, 330:755–767.
- Falco, M. et al. (2014). A new method to measure the mass of galaxy clusters. *MNRAS*, 442(2):1887–1896.
- Fasano, G. et al. (2000). The Evolution of the Galactic Morphological Types in Clusters. *ApJ*, 542:673–683.
- Fasano, G. et al. (2012). Morphology of galaxies in the WINGS clusters. *MNRAS*, 420:926–948.
- Fasano, G. et al. (2015). Morphological fractions of galaxies in WINGS clusters: revisiting the morphology-density paradigm. *MNRAS*, 449(4):3927–3944.
- Filippenko, A. and Greenstein, J. L. (1984). Faint spectrophotometric standard stars for large optical telescopes. I. *PASP*, 96:530–536.
- Finlator, K. and Davé, R. (2008). The origin of the galaxy mass-metallicity relation and implications for galactic outflows. *MNRAS*, 385:2181–2204.
- Finn, R. A. et al. (2005).  $H\alpha$ -derived Star Formation Rates for Three  $z \simeq 0.75$  EDisCS Galaxy Clusters. *ApJ*, 630:206–227.
- Florez, J. et al. (2020). Exploring AGN and star formation activity of massive galaxies at cosmic noon. *MNRAS*, 497(3):3273–3296.
- Fouqué, P. et al. (2001). Structure, mass and distance of the Virgo cluster from a Tolman-Bondi model. *A&A*, 375:770–780.
- Gavazzi, G. et al. (2004). Spectrophotometry of galaxies in the Virgo cluster. II. The data. *A&A*, 417:499–514.
- Gavazzi, G. et al. (2018a).  $H\alpha$  imaging observations of early-type galaxies from the ATLAS<sup>3D</sup> survey. *A&A*, 611:A28.

- Gavazzi, G. et al. (2018b). Nuclear versus integrated spectroscopy of galaxies in the Herschel Reference Survey. *A&A*, 615:A104.
- Gavazzi, G., Savorgnan, G., and Fumagalli, M. (2011). The complete census of optically selected AGNs in the Coma supercluster: the dependence of AGN activity on the local environment. *A&A*, 534:A31.
- Geach, J. E. et al. (2006). A Panoramic Mid-Infrared Survey of Two Distant Clusters. *APJ*, 649:661–672.
- Geach, J. E. et al. (2009). The Nature of Dusty Starburst Galaxies in a Rich Cluster at  $z = 0.4$ : The Progenitors of Lenticulars? *ApJ*, 691:783–793.
- George, M. R. et al. (2013). Galaxies in X-Ray Groups. III. Satellite Color and Morphology Transformations. *ApJ*, 770(2):113.
- Gómez, P. L. et al. (2003). Galaxy Star Formation as a Function of Environment in the Early Data Release of the Sloan Digital Sky Survey. *ApJ*, 584(1):210–227.
- González, J. J. et al. (2014). General formulation for the calibration and characterization of narrow-gap etalons: the OSIRIS/GTC tunable filters case. *MNRAS*, 443:3289–3301.
- Goto, T. et al. (2003). The morphology-density relation in the Sloan Digital Sky Survey. *MNRAS*, 346(2):601–614.
- Graham, A. W., Soria, R., and Davis, B. L. (2019). Expected intermediate-mass black holes in the Virgo cluster - II. Late-type galaxies. *MNRAS*, 484(1):814–831.
- Gregg, M. and West, M. (2017). Ram Pressure Stripping and Morphological Transformation in the Coma Cluster. In *American Astronomical Society Meeting Abstracts #229*, volume 229, page 427.07.
- Grossi, M. et al. (2015). The Herschel Virgo Cluster Survey. XVIII. Star-forming dwarf galaxies in a cluster environment. *A&A*, 574:A126.
- Grossi, M. et al. (2020). Inverted metallicity gradients in two Virgo cluster star-forming dwarf galaxies: evidence of recent merging? *MNRAS*, 498(2):1939–1950.
- Guglielmo, V. et al. (2019). The XXL Survey. XXXVII. The role of the environment in shaping the stellar population properties of galaxies at  $0.1 \leq z \leq 0.5$ . *A&A*, 625:A112.
- Gunn, J. E. and Gott, J. Richard, I. (1972). On the Infall of Matter Into Clusters of Galaxies and Some Effects on Their Evolution. *ApJ*, 176:1.
- Guo, H. et al. (2019). Evolution of Star-forming Galaxies from  $z = 0.7$  to 1.2 with eBOSS Emission-line Galaxies. *ApJ*, 871(2):147.
- Gupta, A. et al. (2016). Radial Distribution of ISM Gas-phase Metallicity in CLASH Clusters at  $z \sim 0.35$ : A New Outlook on Environmental Impact on Galaxy Evolution. *ApJ*, 831(1):104.
- Haggard, D. et al. (2010). The Field X-ray AGN Fraction to  $z = 0.7$  from the Chandra Multiwavelength Project and the Sloan Digital Sky Survey. *ApJ*, 723:1447–1468.
- Haines, C. P. et al. (2009). LOCUSS: The Mid-Infrared Butcher-Oemler Effect. *ApJ*, 704:126–136.
- Haines, C. P. et al. (2013). LoCuSS: The Steady Decline and Slow Quenching of Star Formation in Cluster Galaxies over the Last Four Billion Years. *ApJ*, 775:126.
- Haines, C. P. et al. (2015). LoCuSS: The Slow Quenching of Star Formation in Cluster Galaxies and the Need for Pre-processing. *ApJ*, 806(1):101.
- Hansen, S. M. et al. (2009). The Galaxy Content of SDSS Clusters and Groups. *ApJ*, 699(2):1333–1353.

- Hayashi, M. et al. (2017). Evolutionary Phases of Gas-rich Galaxies in a Galaxy Cluster at  $z = 1.46$ . *ApJL*, 841(2):L21.
- Henry, R. B. C., Edmunds, M. G., and Köppen, J. (2000). On the Cosmic Origins of Carbon and Nitrogen. *ApJ*, 541(2):660–674.
- High, F. W. et al. (2010). Optical Redshift and Richness Estimates for Galaxy Clusters Selected with the Sunyaev-Zel'dovich Effect from 2008 South Pole Telescope Observations. *ApJ*, 723(2):1736–1747.
- Hirashita, H., Buat, V., and Inoue, A. K. (2003). Star formation rate in galaxies from UV, IR, and  $H\alpha$  estimators. *A&A*, 410:83–100.
- Holden, B. P. et al. (2007). Mass Selection and the Evolution of the Morphology-Density Relation from  $z = 0.8$  to 0. *ApJ*, 670:190–205.
- Hopkins, A. M. et al. (2013). Galaxy And Mass Assembly (GAMA): spectroscopic analysis. *MNRAS*, 430:2047–2066.
- Houghton, R. C. W. (2015). Revisiting the original morphology-density relation. *MNRAS*, 451(4):3427–3436.
- Hoyle, B. et al. (2012). The fraction of early-type galaxies in low-redshift groups and clusters of galaxies. *MNRAS*, 423:3478–3485.
- Hubble, E. and Humason, M. L. (1931). The Velocity-Distance Relation among Extra-Galactic Nebulae. *ApJ*, 74:43.
- Hubble, E. P. (1925). Cepheids in Spiral Nebulae. *Popular Astronomy*, 33:252–255.
- Huertas-Company, M. et al. (2007). Morphological evolution of  $z \sim 1$  galaxies from deep K-band AO imaging in the COSMOS deep field. *A&A*, 468:937–950.
- Huertas-Company, M. et al. (2008). A robust morphological classification of high-redshift galaxies using support vector machines on seeing limited images. I. Method description. *A&A*, 478:971–980.
- Huertas-Company, M. et al. (2009). A robust morphological classification of high-redshift galaxies using support vector machines on seeing limited images. II. Quantifying morphological k-correction in the COSMOS field at  $1 < z < 2$ : Ks band vs. I band. *A&A*, 497:743–753.
- Huertas-Company, M. et al. (2010). Evolution of blue E/S0 galaxies from  $z \sim 1$ : merger remnants or disk-rebuilding galaxies? *A&A*, 515:A3.
- Huertas-Company, M. et al. (2011). Revisiting the Hubble sequence in the SDSS DR7 spectroscopic sample: a publicly available Bayesian automated classification. *A&A*, 525:A157.
- Huertas-Company, M. et al. (2015). A Catalog of Visual-like Morphologies in the 5 CANDELS Fields Using Deep Learning. *ApJSS*, 221:8–30.
- Hughes, T. M. et al. (2013). The role of cold gas and environment on the stellar mass-metallicity relation of nearby galaxies. *A&A*, 550:A115.
- Humason, M. L. and Sandage, A. (1957). *Carnegie Yearbook 1956*, page P61.
- Hwang, H. S. et al. (2012). Activity in galactic nuclei of cluster and field galaxies in the local universe. *A&A*, 538:A15.
- Hwang, H. S., Shin, J., and Song, H. (2019). Evolution of star formation rate-density relation over cosmic time in a simulated universe: the observed reversal reproduced. *MNRAS*, 489(1):339–348.
- Ilbert, O. et al. (2006). Accurate photometric redshifts for the CFHT legacy survey calibrated using the VIMOS VLT deep survey. *A&A*, 457:841–856.

- Jáchym, P. et al. (2007). Gas stripping in galaxy clusters: a new SPH simulation approach. *A&A*, 472(1):5–20.
- Jaffé, Y. L. et al. (2015). BUDHIES II: a phase-space view of H I gas stripping and star formation quenching in cluster galaxies. *MNRAS*, 448:1715–1728.
- Jee, M. J. et al. (2005). Weak-Lensing Analysis of the  $z \simeq 0.8$  Cluster CL 0152-1357 with the Advanced Camera for Surveys. *ApJ*, 618:46–67.
- Jee, M. J. et al. (2007). Discovery of a Ringlike Dark Matter Structure in the Core of the Galaxy Cluster CL 0024+17. *ApJ*, 661(2):728–749.
- Jones, D. H., Shopbell, P. L., and Bland-Hawthorn, J. (2002). Detection and measurement from narrow-band tunable filter scans. *MNRAS*, 329:759–774.
- Kacprzak, G. G. et al. (2015). The absence of an environmental dependence in the mass metallicity relation at  $z = 2$ . *ApJ*, 802(2):L26.
- Karachentsev, I. D. and Nasonova Kashibadze, O. G. (2010). Blueshifted galaxies in the virgo cluster. *Astrophysics*, 53:32–41.
- Kartaltepe, J. S. et al. (2012). GOODS-Herschel and CANDELS: The Morphologies of Ultraluminous Infrared Galaxies at  $z \sim 2$ . *ApJ*, 757:23–38.
- Kartaltepe, J. S. et al. (2015). CANDELS Visual Classifications: Scheme, Data Release, and First Results. *ApJS*, 221:11–27.
- Kauffmann, G. et al. (2003). The host galaxies of active galactic nuclei. *MNRAS*, 346(4):1055–1077.
- Kauffmann, G. et al. (2004). The environmental dependence of the relations between stellar mass, structure, star formation and nuclear activity in galaxies. *MNRAS*, 353:713–731.
- Kelkar, K. et al. (2019). The time delay between star formation quenching and morphological transformation of galaxies in clusters: a phase-space view of EDisCS. *MNRAS*, 486(1):868–884.
- Kennicutt, Robert C., J. (1992). The Integrated Spectra of Nearby Galaxies: General Properties and Emission-Line Spectra. *ApJ*, 388:310.
- Kennicutt, Robert C., J. (1998). Star Formation in Galaxies Along the Hubble Sequence. *ARA&A*, 36:189–232.
- Kewley, L. J. and Ellison, S. L. (2008). Metallicity Calibrations and the Mass-Metallicity Relation for Star-forming Galaxies. *ApJ*, 681(2):1183–1204.
- Kewley, L. J. et al. (2001). Theoretical Modeling of Starburst Galaxies. *ApJ*, 556(1):121–140.
- Kewley, L. J. et al. (2006a). The host galaxies and classification of active galactic nuclei. *MNRAS*, 372:961–976.
- Kewley, L. J. et al. (2013a). The Cosmic BPT Diagram: Confronting Theory with Observations. *ApJL*, 774(1):L10.
- Kewley, L. J. et al. (2013b). Theoretical Evolution of Optical Strong Lines across Cosmic Time. *ApJ*, 774(2):100.
- Kewley, L. J., Geller, M. J., and Barton, E. J. (2006b). Metallicity and Nuclear Star Formation in Nearby Galaxy Pairs: Evidence for Tidally Induced Gas Flows. *AJ*, 131:2004–2017.
- Kim, S. et al. (2014). The Extended Virgo Cluster Catalog. *ApJSS*, 215:22–50.
- Klesman, A. J. and Sarajedini, V. L. (2014). A multi-wavelength survey of AGN in massive clusters: AGN distribution and host galaxy properties. *MNRAS*, 442(1):314–326.

- Kneib, J.-P. et al. (2003). A Wide-Field Hubble Space Telescope Study of the Cluster Cl 0024+1654 at  $z=0.4$ . II. The Cluster Mass Distribution. *ApJ*, 598:804–817.
- Kocevski, D. D. et al. (2012). CANDELS: Constraining the AGN-Merger Connection with Host Morphologies at  $z \sim 2$ . *ApJ*, 744:148–156.
- Kodama, T. and Arimoto, N. (1997). Origin of the colour-magnitude relation of elliptical galaxies. *A&A*, 320:41–53.
- Kodama, T. and Bower, R. G. (2001). Reconstructing the history of star formation in rich cluster cores. *MNRAS*, 321:18–36.
- Kodama, T. et al. (2004). A panoramic  $H\alpha$  imaging survey of the  $z=0.4$  cluster Cl0024.0+1652 with Subaru. *MNRAS*, 354:1103–1119.
- Kodama, T. and Smail, I. (2001). Testing the hypothesis of the morphological transformation from field spiral to cluster S0. *MNRAS*, 326:637–642.
- Kolmogorov, A. (1933). Sulla determinazione empirica di una legge di distribuzione. *G. Ist. Ital. Attuari.*, 4:83–91.
- Koopmann, R. A. and Kenney, J. D. P. (1998). The Trouble with Hubble Types in the Virgo Cluster. *APJL*, 497:L75–L79.
- Koulouridis, E. and Bartalucci, I. (2019). High density of active galactic nuclei in the outskirts of distant galaxy clusters. *A&A*, 623:L10.
- Koulouridis, E. et al. (2014). X-ray AGN in the XMM-LSS galaxy clusters: no evidence of AGN suppression. *A&A*, 567:A83.
- Kovač, K. et al. (2014). zCOSMOS 20k: Satellite galaxies are the main drivers of environmental effects in the galaxy population at least to  $z \sim 0.7$ . *MNRAS*, 438(1):717–738.
- Koyama, Y. et al. (2008). Mapping dusty star formation in and around a cluster at  $z = 0.81$  by wide-field imaging with AKARI. *MNRAS*, 391:1758–1770.
- Koyama, Y. et al. (2010). Panoramic  $H\alpha$  and mid-infrared mapping of star formation in a  $z = 0.8$  cluster. *MNRAS*, 403:1611–1624.
- Koyama, Y. et al. (2011). Red Star-forming Galaxies and Their Environment at  $z = 0.4$  Revealed by Panoramic  $H\alpha$  Imaging. *APJ*, 734:66.
- Koyama, Y. et al. (2013). On the evolution and environmental dependence of the star formation rate versus stellar mass relation since  $z \sim 2$ . *MNRAS*, 434(1):423–436.
- Krishnan, C. et al. (2017). Enhancement of AGN in a protocluster at  $z = 1.6$ . *MNRAS*, 470(2):2170–2178.
- Kroupa, P. (2001). On the variation of the initial mass function. *MNRAS*, 322(2):231–246.
- Kulas, K. R. et al. (2013). The Mass-Metallicity Relation of a  $z \sim 2$  Protocluster with MOSFIRE. *ApJ*, 774(2):130.
- Kuminski, E. et al. (2014). Combining Human and Machine Learning for Morphological Analysis of Galaxy Images. *PASP*, 126:959–967.
- Kuminski, E. and Shamir, L. (2016). A Computer-generated Visual Morphology Catalog of  $\sim 3,000,000$  SDSS Galaxies. *ApJSS*, 223:20–29.
- Laganá, T. F. and Ulmer, M. P. (2018). Star-formation rates of cluster galaxies: nature versus nurture. *MNRAS*, 475(1):523–531.

- Lamareille, F. et al. (2009). Physical properties of galaxies and their evolution in the VIMOS VLT Deep Survey. I. The evolution of the mass-metallicity relation up to  $z \sim 0.9$ . *A&A*, 495(1):53–72.
- Lang, K. R. (2013). *Essential Astrophysics*. Springer.
- Lara-López, M. A. et al. (2010a). OTELO Survey: Optimal Emission-Line Flux Determination with OSIRIS/GTC. *PASP*, 122:1495–1509.
- Lara-López, M. A. et al. (2010b). Study of star-forming galaxies in SDSS up to redshift 0.4. II. Evolution from the fundamental parameters: mass, metallicity and star formation rate. *A&A*, 519:A31.
- Larson, R. B., Tinsley, B. M., and Caldwell, C. N. (1980). The evolution of disk galaxies and the origin of S0 galaxies. *ApJ*, 237:692–707.
- Le Fèvre, O. et al. (2013). The VIMOS VLT Deep Survey final data release: a spectroscopic sample of 35 016 galaxies and AGN out to  $z \sim 6.7$  selected with  $17.5 \leq i_{AB} \leq 24.75$ . *A&A*, 559:A14.
- Lee, H.-R. et al. (2016). Measuring the Dust Stripping of Galaxies by the Hot Intracluster Gas in the Virgo Cluster. In *American Astronomical Society Meeting Abstracts #228*, volume 228, page 118.06.
- Lee, Y., Kim, S., Rey, S.-C., and Chung, J. (2020). Properties of Galaxies in Cosmic Filaments around the Virgo Cluster. *arXiv e-prints*, page arXiv:2011.11169.
- Leethochawalit, N. et al. (2018). Evolution of the Stellar Mass-Metallicity Relation. I. Galaxies in the  $z \sim 0.4$  Cluster Cl0024. *ApJ*, 856(1):15.
- Lehmer, B. D. et al. (2009). The Chandra Deep Protocluster Survey: Evidence for an Enhancement of AGN Activity in the SSA22 Protocluster at  $z = 3.09$ . *ApJ*, 691:687–695.
- Lequeux, J. et al. (1979). Reprint of 1979A&A....80..155L. Chemical composition and evolution of irregular and blue compact galaxies. *A&A*, 500:145–156.
- Li, F. et al. (2017). Fraction of the X-ray selected AGNs with optical emission lines in galaxy groups. *Ap&SS*, 362(4):88.
- Li, F. et al. (2019). Effect of richness on AGN and star formation activities in SDSS galaxy groups. *MNRAS*, 484(3):3806–3817.
- Lian, J. et al. (2018). The mass-metallicity relations for gas and stars in star-forming galaxies: strong outflow versus variable IMF. *MNRAS*, 474(1):1143–1164.
- Lidman, C. et al. (2008). HAWK-I imaging of the X-ray luminous galaxy cluster XMMU J2235.3-2557. The red sequence at  $z = 1.39$ . *A&A*, 489:981–988.
- Lintott, C. et al. (2011). Galaxy Zoo 1: data release of morphological classifications for nearly 900000 galaxies. *MNRAS*, 410:166–178.
- Lintott, C. J. et al. (2008). Galaxy Zoo: morphologies derived from visual inspection of galaxies from the Sloan Digital Sky Survey. *MNRAS*, 389:1179–1189.
- Liu, A. et al. (2020). The chemical evolution of galaxy clusters: Dissecting the iron mass budget of the intracluster medium. *A&A*, 637:A58.
- Longobardi, A. et al. (2020). A Virgo Environmental Survey Tracing Ionised Gas Emission (VESTIGE). VII. Bridging the cluster-ICM-galaxy evolution at small scales. *A&A*, 644:A161.
- Lotz, J. M., Primack, J., and Madau, P. (2004). A New Nonparametric Approach to Galaxy Morphological Classification. *AJ*, 128:163–182.

- Lukic, V. et al. (2018). Radio Galaxy Zoo: compact and extended radio source classification with deep learning. *MNRAS*, 476:246–260.
- Madau, P., Pozzetti, L., and Dickinson, M. (1998). The Star Formation History of Field Galaxies. *ApJ*, 498:106–116.
- Mahajan, S. et al. (2019). The Star Formation Reference Survey - III. A multiwavelength view of star formation in nearby galaxies. *MNRAS*, 482(1):560–577.
- Mahdavi, A. and Geller, M. J. (2001). The  $L_X$ - $\sigma$  Relation for Galaxies and Clusters of Galaxies. *ApJL*, 554:L129–L132.
- Mahoro, A. et al. (2019). Star formation in far-IR AGN and non-AGN galaxies in the green valley - II. Morphological analysis. *MNRAS*, 485(1):452–463.
- Maier, C. et al. (2015). Mass-metallicity relation of zCOSMOS galaxies at  $z \approx 0.7$ , its dependence on star formation rate, and the existence of massive low-metallicity galaxies. *A&A*, 577:A14.
- Maier, C. et al. (2016). CLASH-VLT: Strangulation of cluster galaxies in MACS J0416.1-2403 as seen from their chemical enrichment. *A&A*, 590:A108.
- Maier, C. et al. (2019a). Cluster induced quenching of galaxies in the massive cluster XMMXCS J2215.9-1738 at  $z \sim 1.5$  traced by enhanced metallicities inside half  $R_{200}$ . *A&A*, 626:A14.
- Maier, C. et al. (2019b). Slow-then-rapid quenching as traced by tentative evidence for enhanced metallicities of cluster galaxies at  $z \sim 0.2$  in the slow quenching phase. *A&A*, 621:A131.
- Maiolino, R. et al. (2008). AMAZE. I. The evolution of the mass-metallicity relation at  $z > 3$ . *A&A*, 488:463–479.
- Mannucci, F. et al. (2010). A fundamental relation between mass, star formation rate and metallicity in local and high-redshift galaxies. *MNRAS*, 408(4):2115–2127.
- Mantz, A. B. et al. (2017). The metallicity of the intracluster medium over cosmic time: further evidence for early enrichment. *MNRAS*, 472(3):2877–2888.
- Marshall, M. A. et al. (2018). Triggering active galactic nuclei in galaxy clusters. *MNRAS*, 474(3):3615–3628.
- Martínez, H. J., Coenda, V., and Muriel, H. (2008). On the relationship between environment and galaxy properties in clusters of galaxies. *MNRAS*, 391(2):585–590.
- Martini, P. et al. (2002). An Unexpectedly High Fraction of Active Galactic Nuclei in Red Cluster Galaxies. *APJL*, 576:L109–L112.
- Martini, P. et al. (2013). The Cluster and Field Galaxy Active Galactic Nucleus Fraction at  $z = 1$ –1.5: Evidence for a Reversal of the Local Anticorrelation between Environment and AGN Fraction. *ApJ*, 768:1.
- Martini, P., Sivakoff, G. R., and Mulchaey, J. S. (2009). The Evolution of Active Galactic Nuclei in Clusters of Galaxies to Redshift 1.3. *ApJ*, 701:66–85.
- Martis, N. S. et al. (2019). Stellar and Dust Properties of a Complete Sample of Massive Dusty Galaxies at  $1 \leq z \leq 4$  from MAGPHYS Modeling of UltraVISTA DR3 and Herschel Photometry. *ApJ*, 882(1):65.
- Marziani, P. et al. (2017). Emission line galaxies and active galactic nuclei in WINGS clusters. *A&A*, 599:A83.
- Mas-Hesse, J. M. and Kunth, D. (1991). Evolutionary population synthesis in starburst regions. *A&AS*, 88:399.
- Massey, P. and Gronwall, C. (1990). The Kitt Peak spectrophotometric standards - Extension to 1 micron. *ApJ*, 358:344–349.

- Matharu, J. et al. (2020). HST/WFC3 grism observations of  $z \sim 1$  clusters: evidence for evolution in the mass-size relation of quiescent galaxies from post-starburst galaxies. *MNRAS*, 493(4):6011–6032.
- Mayes, R. J. et al. (2020). Contribution of stripped nuclei to the ultracompact dwarf galaxy population in the Virgo Cluster. *MNRAS*.
- McAlpine, K. et al. (2015). The SKA view of the Interplay between SF and AGN Activity and its role in Galaxy Evolution. In *Advancing Astrophysics with the Square Kilometre Array (AASKA14)*, page 83.
- McDonald, M. et al. (2016). The Evolution of the Intracluster Medium Metallicity in Sunyaev Zeldovich-selected Galaxy Clusters at  $0 < z < 1.5$ . *ApJ*, 826(2):124.
- Mei, S. et al. (2007). The ACS Virgo Cluster Survey. XIII. SBF Distance Catalog and the Three-dimensional Structure of the Virgo Cluster. *ApJ*, 655:144–162.
- Mei, S. et al. (2012). Early-type Galaxies at  $z = 1.3$ . I. The Lynx Supercluster: Cluster and Groups at  $z = 1.3$ . Morphology and Color-Magnitude Relation. *ApJ*, 754:141.
- Melbourne, J. et al. (2007). Radius-dependent Luminosity Evolution of Blue Galaxies in GOODS-N. *ApJ*, 660:81–96.
- Menci, N. et al. (2008). The Red Sequence of High-Redshift Clusters: A Comparison with Cosmological Galaxy Formation Models. *ApJ*, 685:863–874.
- Mernier, F. et al. (2017). Radial metal abundance profiles in the intra-cluster medium of cool-core galaxy clusters, groups, and ellipticals. *A&A*, 603:A80.
- Metcalfe, L., Fadda, D., and Biviano, A. (2005). ISO's Contribution to the Study of Clusters of Galaxies. *The Space Science Review*, 119.
- Mihos, C. (2003). Interactions and Mergers of Cluster Galaxies. *ArXiv Astrophysics e-prints*, pages 425–446.
- Miller, C. J. et al. (2003). The Environment of Active Galactic Nuclei in the Sloan Digital Sky Survey. *ApJ*, 597:142–156.
- Milone, A. P. et al. (2017). Multiple stellar populations in Magellanic Cloud clusters - V. The split main sequence of the young cluster NGC 1866. *MNRAS*, 465(4):4363–4374.
- Mishra, H. D. and Dai, X. (2020). Lower AGN Abundance in Galaxy Clusters at  $z < 0.5$ . *AJ*, 159(2):69.
- Mo, W. et al. (2018). The Massive and Distant Clusters of WISE Survey. IV. The Distribution of Active Galactic Nuclei in Galaxy Clusters at  $z \sim 1$ . *ApJ*, 869(2):131.
- Mohamad Nizam, K. B. et al. (2019). Keck DEIMOS Spectroscopy of Compact Stellar Systems in the Next Generation Virgo Cluster Survey. In *American Astronomical Society Meeting Abstracts #233*, volume 233, page 173.06.
- Molendi, S. et al. (2016). A critical assessment of the metal content of the intracluster medium. *A&A*, 586:A32.
- Moles, M. et al. (2008). The Alhambra Survey: a Large Area Multimediuim-Band Optical and Near-Infrared Photometric Survey. *AJ*, 136:1325–1339.
- Moore, B. et al. (1996). Galaxy harassment and the evolution of clusters of galaxies. *Nature*, 379(6566):613–616.
- Moran, S. M. et al. (2005). A Wide-Field Hubble Space Telescope Survey of the Cluster Cl 0024+16 at  $z = 0.4$ . III. Spectroscopic Signatures of Environmental Evolution in Early-Type Galaxies. *ApJ*, 634:977–1001.
- Moran, S. M. et al. (2007). A Wide-Field Survey of Two  $z \sim 0.5$  Galaxy Clusters: Identifying the Physical Processes Responsible for the Observed Transformation of Spirals into S0s. *ApJ*, 671:1503–1522.



- Morrison, G. et al. (1997). The Evolution of the Radio Galaxy Population in Very-Rich Clusters. In *American Astronomical Society Meeting Abstracts*, volume 29, page 1399.
- Mouhcine, M., Baldry, I. K., and Bamford, S. P. (2007). The environmental dependence of the chemical properties of star-forming galaxies. *MNRAS*, 382(2):801–808.
- Mouhcine, M. et al. (2006). Star formation rates and chemical abundances of emission-line galaxies in intermediate-redshift clusters. *MNRAS*, 368:1871–1879.
- Muzzin, A. et al. (2012). The Gemini Cluster Astrophysics Spectroscopic Survey (GCLASS): The Role of Environment and Self-regulation in Galaxy Evolution at  $z \sim 1$ . *ApJ*, 746(2):188.
- Nadolny, J. et al. (2020). The OTELO survey. Nature and mass-metallicity relation for H $\alpha$  emitters at  $z \sim 0.4$ . *A&A*, 636:A84.
- Nair, P. and Abraham, R. G. (2010). A Catalog of Detailed Visual Morphological Classifications for 14,034 Galaxies in the Sloan Digital Sky Survey. *ApJSS*, 186:427–456.
- Nantais, J. B. et al. (2013). Morphology with light profile fitting of confirmed cluster galaxies at  $z = 0.84$ . *A&A*, 555:A5.
- Nantais, J. B. et al. (2017). Evidence for strong evolution in galaxy environmental quenching efficiency between  $z = 1.6$  and  $z = 0.9$ . *MNRAS*, 465(1):L104–L108.
- Natarajan, P. et al. (2009). The Survival of Dark Matter Halos in the Cluster Cl 0024+16. *ApJ*, 693:970–983.
- Nilo Castellón, J. L. et al. (2014). Low X-ray luminosity galaxy clusters - II. Optical properties and morphological content at  $0.18 < z < 0.70$ . *MNRAS*, 437:2607–2620.
- Nipoti, C. (2009). Cool gas accretion, thermal evaporation, and quenching of star formation in elliptical galaxies. *AN*, 330:910–911.
- Nipoti, C. and Binney, J. (2007). The role of thermal evaporation in galaxy formation. *MNRAS*, 382(4):1481–1493.
- Nishizawa, A. J. et al. (2018). First results on the cluster galaxy population from the Subaru Hyper Suprime-Cam survey. II. Faint end color-magnitude diagrams and radial profiles of red and blue galaxies at  $0.1 < z < 1.1$ . *PASJ*, 70:S24.
- Noeske, K. G. et al. (2007). Star Formation in AEGIS Field Galaxies since  $z=1.1$ : The Dominance of Gradually Declining Star Formation, and the Main Sequence of Star-forming Galaxies. *ApJL*, 660(1):L43–L46.
- Oemler, Jr., A. (1974). The Systematic Properties of Clusters of Galaxies. Photometry of 15 Clusters. *ApJ*, 194:1–20.
- Oemler, Augustus, J. et al. (2013). The IMACS Cluster Building Survey. III. The Star Formation Histories of Field Galaxies. *ApJ*, 770(1):63.
- Oh, S. et al. (2018). KYDISC: Galaxy Morphology, Quenching, and Mergers in the Cluster Environment. *ApJS*, 237(1):14.
- Okabe, N. et al. (2019). Halo concentration, galaxy red fraction, and gas properties of optically defined merging clusters. *PASJ*, 71(4).
- Oke, J. B. (1974). Absolute Spectral Energy Distributions for White Dwarfs. *ApJ Supplement*, 27:21–35.
- Oke, J. B. (1990). Faint spectrophotometric standard stars. *AJ*, 99:1621–1631.
- Oke, J. B. and Gunn, J. E. (1983). Secondary standard stars for absolute spectrophotometry. *ApJ*, 266:713–717.

- Old, L. J. et al. (2020). The GOGREEN survey: the environmental dependence of the star-forming galaxy main sequence at  $1.0 < z < 1.5$ . *MNRAS*, 493(4):5987–6000.
- Osterbrock, D. E. and Ferland, G. J. (2006). *Astrophysics of gaseous nebulae and active galactic nuclei*, volume 35. Mercury.
- Owers, M. S. et al. (2019). The SAMI Galaxy Survey: Quenching of Star Formation in Clusters I. Transition Galaxies. *ApJ*, 873(1):52.
- Pagel, B. E. J. et al. (1979). On the composition of HII regions in southern galaxies. I - NGC 300 and 1365. *MNRAS*, 189:95–113.
- Pannella, M. et al. (2009). Star Formation and Dust Obscuration at  $z \approx 2$ : Galaxies at the Dawn of Downsizing. *ApJL*, 698(2):L116–L120.
- Parekh, V. et al. (2015). Morphology parameters: substructure identification in X-ray galaxy clusters. *A&A*, 575:A127.
- Park, C., Gott, III, J. R., and Choi, Y.-Y. (2008). Transformation of Morphology and Luminosity Classes of the SDSS Galaxies. *ApJ*, 674:784–796.
- Park, C. and Hwang, H. S. (2009). Interactions of galaxies in the galaxy cluster environment. *ApJ*, 699(2):1595–1609.
- Patel, S. G. et al. (2011). The Star-formation-rate-Density Relation at  $0.6 < z < 0.9$  and the Role of Star-forming Galaxies. *ApJ*, 735(1):53.
- Paulino-Afonso, A. et al. (2018). VIS<sup>3</sup>COS. I. Survey overview and the role of environment and stellar mass on star formation. *A&A*, 620:A186.
- Peng, C. Y. et al. (2002). Detailed Structural Decomposition of Galaxy Images. *AJ*, 124:266–293.
- Peng, C. Y. et al. (2010a). Detailed Decomposition of Galaxy Images. II. Beyond Axisymmetric Models. *AJ*, 139:2097–2129.
- Peng, E. W. et al. (2008). The ACS Virgo Cluster Survey. XV. The Formation Efficiencies of Globular Clusters in Early-Type Galaxies: The Effects of Mass and Environment. *ApJ*, 681:197–224.
- Peng, Y.-j. et al. (2010b). Mass and Environment as Drivers of Galaxy Evolution in SDSS and zCOSMOS and the Origin of the Schechter Function. *ApJ*, 721(1):193–221.
- Peng, Y.-j. et al. (2012). Mass and Environment as Drivers of Galaxy Evolution. II. The Quenching of Satellite Galaxies as the Origin of Environmental Effects. *ApJ*, 757(1):4.
- Perez, J. et al. (2009). Global environmental effects versus galaxy interactions. *MNRAS*, 399(3):1157–1166.
- Pérez-Martínez, J. M. et al. (2020). Galaxy kinematics across different environments in the RXJ1347-1145 cluster complex. *A&A*, 637:A30.
- Pérez-Montero, E. et al. (2013). The cosmic evolution of oxygen and nitrogen abundances in star-forming galaxies over the past 10 Gyr. *A&A*, 549:A25.
- Pettini, M. and Pagel, B. E. J. (2004). [OIII]/[NII] as an abundance indicator at high redshift. *MNRAS*, 348(3):L59–L63.
- Pimblet, K. A. et al. (2001). The Las Campanas/AAT rich cluster survey - I. Precision and reliability of the photometric catalogue. *MNRAS*, 327:588–600.
- Pimblet, K. A. et al. (2002). The Las Campanas/AAT Rich Cluster Survey - II. The environmental dependence of galaxy colours in clusters at  $z \sim 0.1$ . *MNRAS*, 331(2):333–350.

- Pimblet, K. A. et al. (2013). The drivers of AGN activity in galaxy clusters: AGN fraction as a function of mass and environment. *MNRAS*, 429:1827–1839.
- Pintos-Castro, I. (2014). *Multiwavelength study of the population of galaxies in intermediatedredshift clusters: the case of RXJ1257.2+4738 at  $z \sim 0.9$* . Phd thesis, Universidad de La Laguna.
- Pintos-Castro, I. et al. (2013). Multi-wavelength landscape of the young galaxy cluster RXJ1257.2 + 4738 at  $z = 0.866$ . I. The infrared view. *A&A*, 558:A100.
- Pintos-Castro, I. et al. (2016). Multi-wavelength landscape of the young galaxy cluster RXJ 1257.2 + 4738 at  $z = 0.866$ . II. Morphological properties. *A&A*, 592:A108.
- Pintos-Castro, I. et al. (2019). The Evolution of the Quenching of Star Formation in Cluster Galaxies since  $z \sim 1$ . *ApJ*, 876(1):40.
- Poggianti, B. M. (2003). Color, spectral and morphological transformations of galaxies in clusters. *Ap&SS*, 285(1):121–131.
- Poggianti, B. M. et al. (1999). The Star Formation Histories of Galaxies in Distant Clusters. *ApJ*, 518:576–593.
- Poggianti, B. M. et al. (2008). The Relation between Star Formation, Morphology, and Local Density in High-Redshift Clusters and Groups. *ApJ*, 684(2):888–904.
- Poggianti, B. M. et al. (2017). GASP. I. Gas Stripping Phenomena in Galaxies with MUSE. *ApJ*, 844(1):48.
- Popesso, P. et al. (2007). RASS-SDSS galaxy cluster survey. VI. The dependence of the cluster SFR on the cluster global properties. *A&A*, 461:411–421.
- Porqueres, N. et al. (2018). Imprints of the large-scale structure on AGN formation and evolution. *A&A*, 612:A31.
- Postman, M. et al. (2005). The Morphology-Density Relation in  $z \sim 1$  Clusters. *ApJ*, 623:721–741.
- Postman, M. and Geller, M. J. (1984). The morphology-density relation - The group connection. *ApJ*, 281:95–99.
- Postman, M., Lubin, L. M., and Oke, J. B. (1998). A Study of Nine High-Redshift Clusters of Galaxies. II. Photometry, Spectra, and Ages of Clusters 0023+0423 and 1604+4304. *AJ*, 116(2):560–583.
- Postman, M., Lubin, L. M., and Oke, J. B. (2001). A Study of Nine High-Redshift Clusters of Galaxies. IV. Photometry and Spectra of Clusters 1324+3011 and 1604+4321. *AJ*, 122(3):1125–1150.
- Pović, M. et al. (2009). OTELO Survey: Deep BVRI Broadband Photometry of the Groth Strip. II. Optical Properties of X-Ray Emitters. *ApJ*, 706:810–823.
- Pović, M. et al. (2012). AGN-host galaxy connection: morphology and colours of X-ray selected AGN at  $z \leq 2$ . *A&A*, 541:A118.
- Pović, M. et al. (2013). The ALHAMBRA survey: reliable morphological catalogue of 22051 early- and late-type galaxies. *MNRAS*, 435:3444–3461.
- Pović, M. et al. (2015). The impact from survey depth and resolution on the morphological classification of galaxies. *MNRAS*, 453:1644–1668.
- Press, W. H. and Schechter, P. (1974). Formation of galaxies and clusters of galaxies by self-similar gravitational condensation. *ApJ*, 187:425–438.
- Puddu, E. et al. (2021). AMICO galaxy clusters in KiDS-DR3: Evolution of the luminosity function between  $z = 0.1$  and  $z = 0.8$ . *A&A*, 645:A9.
- Quadri, R. F. et al. (2012). Tracing the Star-formation-Density Relation to  $z \sim 2$ . *ApJ*, 744:88.

- Raimann, D. et al. (2000a). Gas properties of HII and starburst galaxies: relation with the stellar population. *MNRAS*, 316:559–568.
- Raimann, D. et al. (2000b). Population synthesis of HII galaxies. *MNRAS*, 314(2):295–306.
- Ramón-Pérez, M. et al. (2019a). The OTELO survey. II. The faint-end of the H $\alpha$  luminosity function at  $z \sim 0.40$ . *A&A*, 631:A10.
- Ramón-Pérez, M. et al. (2019b). The OTELO survey. III. Demography, morphology, IR luminosity and environment of AGN hosts. *A&A*, 631:A11.
- Rasheed, M. A. and Mohammad, K. K. (2019). Morphological Distribution of Galaxies in Some Nearby Clusters. *Open Astronomy*, 28(1):98–109.
- Reynolds, J. H. (1920). Photometric measures of the nuclei of some typical spiral nebulae. *MNRAS*, 80:746.
- Roediger, E. (2009). Ram pressure stripping of disk galaxies in galaxy clusters. *Astronomische Nachrichten*, 330:888.
- Rosa-González, D., Terlevich, E., and Terlevich, R. (2002). An empirical calibration of star formation rate estimators. *MNRAS*, 332:283–295.
- Rousselot, P. et al. (2000). Night-sky spectral atlas of OH emission lines in the near-infrared. *A&A*, 354:1134–1150.
- Rowlands, K. et al. (2018). SDSS-IV MaNGA: spatially resolved star formation histories and the connection to galaxy physical properties. *MNRAS*, 480(2):2544–2561.
- Ruderman, J. T. and Ebeling, H. (2005). The Origin of the Spatial Distribution of X-Ray-luminous Active Galactic Nuclei in Massive Galaxy Clusters. *ApJL*, 623:L81–L84.
- Rudnick, G., Jablonka, P., Moustakas, J., Aragón-Salamanca, A., Zaritsky, D., Jaffé, Y. L., De Lucia, G., Desai, V., Halliday, C., Just, D., Milvang-Jensen, B., and Poggianti, B. (2017). Determining the halo mass scale where galaxies lose their gas. *ApJ*, 850(2):181.
- Salim, S. et al. (2014). A Critical Look at the Mass-Metallicity-Star Formation Rate Relation in the Local Universe. I. An Improved Analysis Framework and Confounding Systematics. *ApJ*, 797(2):126.
- Sánchez Almeida, J. et al. (2018). Local anticorrelation between star formation rate and gas-phase metallicity in disc galaxies. *MNRAS*, 476(4):4765–4781.
- Sánchez-Portal, M. et al. (2015). GLACE survey: OSIRIS/GTC tuneable filter H $\alpha$  imaging of the rich galaxy cluster ZwCl0024.0 + 1652 at  $z = 0.395$ . I. Survey presentation, TF data reduction techniques, and catalogue. *A&A*, 578:A30.
- Saracco, P. et al. (2017). Cluster and field elliptical galaxies at  $z \sim 1.3$ . The marginal role of the environment and the relevance of the galaxy central regions. *A&A*, 597:A122.
- Saracco, P. et al. (2019). Age, metallicity, and star formation history of spheroidal galaxies in cluster at  $z \sim 1.2$ . *MNRAS*, 484(2):2281–2295.
- Sazonova, E. et al. (2020). The Morphology-Density Relationship in  $1 < z < 2$  Clusters. *ApJ*, 899(1):85.
- Scarlata, C. et al. (2007). COSMOS Morphological Classification with the Zurich Estimator of Structural Types (ZEST) and the Evolution Since  $z = 1$  of the Luminosity Function of Early, Disk, and Irregular Galaxies. *ApJSS*, 172:406–433.
- Schawinski, K. et al. (2007). Observational evidence for AGN feedback in early-type galaxies. *MNRAS*, 382(4):1415–1431.

- Schawinski, K. et al. (2014). The green valley is a red herring: Galaxy Zoo reveals two evolutionary pathways towards quenching of star formation in early- and late-type galaxies. *MNRAS*, 440:889–907.
- Seaton, M. J. (1979). Interstellar extinction in the UV. *MNRAS*, 187:73.
- Serna, A. and Gerbal, D. (1996). Dynamical search for substructures in galaxy clusters. A hierarchical clustering method. *A&A*, 309:65–74.
- Sérsic, J. L. (1963). Influence of the atmospheric and instrumental dispersion on the brightness distribution in a galaxy. *Boletín de la Asociación Argentina de Astronomía La Plata Argentina*, 6:41–43.
- Simard, L. et al. (2002). The DEEP Groth Strip Survey. II. Hubble Space Telescope Structural Parameters of Galaxies in the Groth Strip. *ApJSS*, 142:1–33.
- Simard, L. et al. (2009). Evolution of the early-type galaxy fraction in clusters since  $z = 0.8$ . *A&A*, 508:1141–1159.
- Simard, L. et al. (2011). A Catalog of Bulge+disk Decompositions and Updated Photometry for 1.12 Million Galaxies in the Sloan Digital Sky Survey. *ApJSS*, 196:11–30.
- Simmons, B. D. et al. (2017). Galaxy Zoo: quantitative visual morphological classifications for 48 000 galaxies from CANDELS. *MNRAS*, 464:4420–4447.
- Sivakoff, G. R. et al. (2008). Wide-Field Chandra X-Ray Observations of Active Galactic Nuclei in Abell 85 and Abell 754. *APJ*, 682:803–820.
- Skillman, E. D. et al. (1996). Chemical Abundances in Virgo Spiral Galaxies. II. Effects of Cluster Environment. *ApJ*, 462:147.
- Smirnov, N. (1948). Table for estimating the goodness of fit of empirical distributions. *Ann. Math. Statist.*, 19:279–281.
- Smith, G. P. et al. (2005). Evolution since  $z = 1$  of the Morphology-Density Relation for Galaxies. *ApJ*, 620:78–87.
- Sobral, D. et al. (2015). MC<sup>2</sup>: boosted AGN and star formation activity in CIZA J2242.8+5301, a massive post-merger cluster at  $z = 0.19$ . *MNRAS*, 450(1):630–645.
- Sobral, D. et al. (2016). The nature of H $\alpha$  star-forming galaxies at  $z \sim 0.4$  in and around Cl 0939+4713: the environment matters. *MNRAS*, 458(4):3443–3454.
- Speagle, J. S. et al. (2014). A Highly Consistent Framework for the Evolution of the Star-Forming “Main Sequence” from  $z \sim 0$ –6. *ApJS*, 214(2):15.
- Sreedhar, Y. H. et al. (2012). Ages and Metallicities of Cluster Galaxies in A779 Using Modified Strömgren Photometry. *ApJ*, 747(1):68.
- Stanford, S. A., Eisenhardt, P. R., and Dickinson, M. (1998). The Evolution of Early-Type Galaxies in Distant Clusters. *ApJ*, 492:461–479.
- Stasińska, G. et al. (2015). Retired galaxies: not to be forgotten in the quest of the star formation - AGN connection. *MNRAS*, 449(1):559–573.
- Steyrleithner, P. et al. (2020). The effect of ram-pressure stripping on dwarf galaxies. *MNRAS*, 494(1):1114–1127.
- Strazzullo, V. et al. (2013). Galaxy Evolution in Overdense Environments at High Redshift: Passive Early-type Galaxies in a Cluster at  $z \sim 2$ . *ApJ*, 772:118.
- Stroe, A. et al. (2015). The rise and fall of star formation in  $z \sim 0.2$  merging galaxy clusters. *MNRAS*, 450(1):646–665.

- Stuardi, C. et al. (2019). Particle re-acceleration and Faraday-complex structures in the RXC J1314.4-2515 galaxy cluster. *MNRAS*, 489(3):3905–3926.
- Su, Y. et al. (2019). Extended X-Ray Study of M49: The Frontier of the Virgo Cluster. *AJ*, 158(1):6.
- Tarsitano, F. et al. (2018). A catalogue of structural and morphological measurements for DES Y1. *MNRAS*, 481:2018–2040.
- Tasca, L. A. M. et al. (2009). The zCOSMOS redshift survey: the role of environment and stellar mass in shaping the rise of the morphology-density relation from  $z \sim 1$ . *A&A*, 503:379–398.
- Thorp, M. D. et al. (2018). Spatially resolved star formation and metallicity profiles in post-merger galaxies from MaNGA. *MNRAS*, 482(1):L55–L59.
- Tiley, A. L. et al. (2020). K-CLASH: spatially-resolving star-forming galaxies in field and cluster environments at  $z \sim 0.2$ – $0.6$ . *MNRAS*, 496(1):649–675.
- Tiwari, J., Mahajan, S., and Singh, K. P. (2020). Age and metallicity of galaxies in different environments of the Coma supercluster. *NA*, 81:101417.
- To, C.-H. et al. (2020). RedMaPPer: Evolution and Mass Dependence of the Conditional Luminosity Functions of Red Galaxies in Galaxy Clusters. *ApJ*, 897(1):15.
- Tody, D. (1986). The IRAF Data Reduction and Analysis System. In Crawford, D. L., editor, *Instrumentation in astronomy VI*, volume 627 of *Society of Photo-Optical Instrumentation Engineers (SPIE) Conference Series*, page 733.
- Tody, D. (1993). IRAF in the Nineties. In Hanisch, R. J., Brissenden, R. J. V., and Barnes, J., editors, *Astronomical Data Analysis Software and Systems II*, volume 52 of *Astronomical Society of the Pacific Conference Series*, page 173.
- Tomczak, A. R. et al. (2019). Conditional quenching: a detailed look at the SFR-density relation at  $z \sim 0.9$  from ORELSE. *MNRAS*, 484(4):4695–4710.
- Trager, S. C. et al. (1998). Old Stellar Populations. VI. Absorption-Line Spectra of Galaxy Nuclei and Globular Clusters. *ApJS*, 116:1–28.
- Tran, K.-V. H. et al. (2010). Reversal of Fortune: Confirmation of an Increasing Star Formation-Density Relation in a Cluster at  $z = 1.62$ . *ApJL*, 719:L126–L129.
- Tremonti, C. A. et al. (2004). The Origin of the Mass-Metallicity Relation: Insights from 53,000 Star-forming Galaxies in the Sloan Digital Sky Survey. *ApJ*, 613:898–913.
- Trenti, M. et al. (2012). Overdensities of Y-dropout galaxies from the brightest-of-reionizing galaxies survey: A candidate protocluster at redshift  $z \approx 8$ . *ApJ*, 746:55–66.
- Treu, T. et al. (2003). A Wide-Field Hubble Space Telescope Study of the Cluster Cl 0024+16 at  $z = 0.4$ . I. Morphological Distributions to 5 Mpc Radius. *ApJ*, 591:53–78.
- Tully, R. B., Mould, J. R., and Aaronson, M. (1982). A color-magnitude relation for spiral galaxies. *ApJ*, 257:527–537.
- Ulmer, M. P. et al. (2009). Cluster and cluster galaxy evolution history from IR to X-ray observations of the young cluster RXJ1257.2 + 4738 at  $z = 0.866$ . *A&A*, 503:399–408.
- Umehata, H. et al. (2015). Alma deep field in ssa22: A concentration of dusty starbursts in a  $z = 3.09$  protocluster core. *ApJ*, 815(1):L8.
- Valentino, F. et al. (2015). Metal Deficiency in Cluster Star-Forming Galaxies At  $z = 2$ . *ApJ*, 801(2):132.

- Van Brummelen, G. (2012). *Heavenly mathematics: The forgotten art of spherical trigonometry*. Princeton University Press.
- van den Bosch, F. C. et al. (2008). The importance of satellite quenching for the build-up of the red sequence of present-day galaxies. *MNRAS*, (1):79–91.
- Vollmer, B. et al. (2012). The influence of the cluster environment on the star formation efficiency of 12 Virgo spiral galaxies. *A&A*, 543:A33.
- von der Linden, A. et al. (2010). Star formation and AGN activity in SDSS cluster galaxies. *MNRAS*, 404(3):1231–1246.
- Vulcani, B. et al. (2010). Comparing the Relation Between Star Formation and Galaxy Mass in Different Environments. *ApJL*, 710(1):L1–L6.
- Vulcani, B. et al. (2015). From Blue Star-forming to Red Passive: Galaxies in Transition in Different Environments. *ApJ*, 798(1):52.
- Vulcani, B. et al. (2018). Enhanced Star Formation in Both Disks and Ram-pressure-stripped Tails of GASP Jellyfish Galaxies. *ApJ*, 866(2):L25.
- Weinmann, S. M. et al. (2006). Properties of galaxy groups in the Sloan Digital Sky Survey - I. The dependence of colour, star formation and morphology on halo mass. *MNRAS*, 366(1):2–28.
- Wen, X.-Q. et al. (2013). The stellar masses of galaxies from the 3.4  $\mu\text{m}$  band of the WISE All-Sky Survey. *MNRAS*, 433(4):2946–2957.
- Wen, X.-Q. et al. (2014). Star formation rates of star-forming galaxies from the WISE All-Sky Survey. *MNRAS*, 438(1):97–115.
- Wetzel, A. R., Tinker, J. L., and Conroy, C. (2012). Galaxy evolution in groups and clusters: star formation rates, red sequence fractions and the persistent bimodality. *MNRAS*, 424:232–243.
- Whitaker, K. E. et al. (2012). The Star Formation Mass Sequence Out to  $z = 2.5$ . *ApJL*, 754(2):L29.
- Whitmore, B. C. (1994). The effect of the cluster environment on galaxies. (I). In Durret, F., Mazure, A., and Tran Thanh Van, J., editors, *Clusters of Galaxies*, volume 14, page 69.
- Whitmore, B. C., Gilmore, D. M., and Jones, C. (1993). What determines the morphological fractions in clusters of galaxies? *ApJ*, 407:489–509.
- Willett, K. W. et al. (2013). Galaxy Zoo 2: detailed morphological classifications for 304122 galaxies from the Sloan Digital Sky Survey. *MNRAS*, 435:2835–2860.
- Willett, K. W. et al. (2017). Galaxy Zoo: morphological classifications for 120,000 galaxies in HST legacy imaging. *MNRAS*, 464:4176–4203.
- Woo, J. et al. (2013). Dependence of galaxy quenching on halo mass and distance from its centre. *MNRAS*, 428:3306–3326.
- Worthey, G. (1994). Comprehensive Stellar Population Models and the Disentanglement of Age and Metallicity Effects. *ApJS*, 95:107.
- Wright, E. L. et al. (2010). The Wide-field Infrared Survey Explorer (WISE): Mission Description and Initial On-orbit Performance. *AJ*, 140(6):1868–1881.
- Wu, X.-P., Fang, L.-Z., and Xu, W. (1998). Updating the  $\sigma$ - $T$  relationship for galaxy clusters. *A&A*, 338:813–818.

- Yates, R. M., Kauffmann, G., and Guo, Q. (2012). The relation between metallicity, stellar mass and star formation in galaxies: an analysis of observational and model data. *MNRAS*, 422(1):215–231.
- Zandivarez, A. and Martínez, H. J. (2011). Luminosity function of galaxies in groups in the Sloan Digital Sky Survey Data Release 7: the dependence on mass, environment and galaxy type. *MNRAS*, 415(3):2553–2565.
- Zhang, C. et al. (2020). High-redshift galaxy groups as seen by ATHENA/WFI. *A&A*, 642:A17.
- Zhang, Y.-Y. et al. (2005). XMM-Newton study of the lensing cluster of galaxies CL0024 + 17. *A&A*, 429:85–99.
- Ziparo, F. et al. (2014). Reversal or no reversal: the evolution of the star formation rate-density relation up to  $z \sim 1.6$ . *MNRAS*, 437:458–474.
- Zu, Y. (2020). H I gas content of SDSS galaxies revealed by ALFALFA: implications for the mass-metallicity relation and the environmental dependence of H I in the local Universe. *MNRAS*, 496(1):111–124.
- Zwicky, F. (1942). On the Clustering of Nebulae. *ApJ*, 95:555–564.
- Zwicky, F. et al. (1961). *Catalogue of galaxies and of clusters of galaxies, Vol. I*. California Institute of Technology.
- Zwicky, F., Herzog, E., and Wild, P. (1963). *Catalogue of galaxies and of clusters of galaxies, Vol. 2*. California Institute of Technology.
- Zwicky, F., Herzog, E., and Wild, P. (1966). *Catalogue of galaxies and of clusters of galaxies, Vol. 3*. California Institute of Technology.



# Appendix A

## Morphological catalogue of galaxies in ZwCl0024+1652 galaxy cluster

### Brief description of the columns of Table A.1

- # Column 1 ... Source index (galaxy number);
- # Column 2 ... Right Ascension in decimal degrees (J2000);
- # Column 3 ... Declination in decimal degrees (J2000)
- # Column 4 ... MAG AUTO (F775W) (measured by SExtractor for each source);
- # Column 5 ... Redshift values for each galaxy from the public data of ZwCl0024+1652 master catalogue generated by a team working on a A Wide Field Survey of Two  $z = 0.5$  Galaxy Clusters (see Treu et al. 2003 and Moran et al. 2005);
- # Column 6 ... Distance of the galaxy from the centre of the cluster (clustercentric distance) measured in Mpc;
- # Column 7 ... The final probability computed taking the uncertainty (error) into account (used for morphologically classifying the galaxies in current work);
- # Column 8 ... The final morphological class [Early Type (ET), Late Type (LT) or Undecided (UD)] based on the final probability value;

**Table A.1:** A complete morphological catalogue of ZwCl0024+1652 cluster (Beyoro-Amado et al., 2019).

Num	RA(Deg)	DEC(Deg)	F775W_Mag	z	R(Mpc)	$P_{FINAL}$	Morpho.
1	6.62029	17.13273	23.448	0.381	0.9763	0.3049	LT
2	6.65543	17.13758	20.7002	0.394	0.6997	0.1017	LT

*Continued on next page*

Table A.1 – Continued from previous page

Num	RA(Deg)	DEC(Deg)	F775W_Mag	z	R(Mpc)	P <sub>FINAL</sub>	Morpho.
3	6.63273	17.13629	23.1702	0.366	0.7356	0.76	ET
4	6.64078	17.13619	24.5245	0.378	0.6845	0.5944	UD
5	6.66708	17.13923	21.4544	0.3999	0.8261	0.7411	ET
6	6.65664	17.13732	24.035	0.447	0.7183	0.5125	UD
7	6.64736	17.1385	22.5379	0.384	0.6226	0.6945	ET
8	6.65052	17.1408	20.4002	0.4032	0.579	0.8953	ET
9	6.65826	17.13911	23.4508	0.363	0.6958	0.5632	UD
10	6.65599	17.14167	19.5078	0.394	0.6094	0.8861	ET
11	6.6469	17.14069	21.3739	0.4	0.5644	0.6863	ET
12	6.62441	17.14087	21.0016	0.4002	0.7467	0.8753	ET
13	6.6474	17.14215	20.5597	0.3957	0.5281	0.1107	LT
14	6.64605	17.14047	23.1934	0.36	0.5683	0.8615	ET
15	6.6425	17.14154	22.7241	0.426	0.5405	0.1154	LT
16	6.67315	17.14125	22.8809	0.384	0.9045	0.8183	ET
17	6.62605	17.14116	24.6259	0.363	0.714	0.4777	UD
18	6.62269	17.14166	21.4808	0.4172	0.7613	0.5744	UD
19	6.64196	17.14299	22.565	0.4447	0.504	0.0798	LT
20	6.64751	17.14333	22.0297	0.396	0.4979	0.8329	ET
21	6.66867	17.14424	20.9217	0.3932	0.7678	0.8845	ET
22	6.64884	17.14444	21.3359	0.3989	0.4762	0.2491	LT
23	6.66162	17.14372	23.42	0.363	0.6473	0.1697	LT
24	6.61418	17.14458	21.9037	0.3942	0.883	0.2971	LT
25	6.65014	17.14468	23.3977	0.399	0.4789	0.3293	LT
26	6.66494	17.14537	21.9198	0.39	0.6767	0.8482	ET
27	6.64494	17.14608	20.7211	0.36	0.4199	0.907	ET
28	6.63475	17.14475	25.8019	0.3898	0.5139	0.4822	UD
29	6.6435	17.14577	21.323	0.36	0.4282	0.4232	UD
30	6.61911	17.14577	23.0451	0.426	0.7622	0.0914	LT
31	6.62184	17.14616	22.6058	0.3987	0.7006	0.0989	LT
32	6.65953	17.14744	20.7678	0.3956	0.5404	0.8903	ET
33	6.65121	17.14582	25.8606	0.414	0.4599	0.1187	LT
34	6.65263	17.1471	21.7675	0.3954	0.4445	0.7648	ET
35	6.65458	17.14709	24.0218	0.402	0.4693	0.1756	LT
36	6.6489	17.14971	19.9283	0.3951	0.3441	0.8471	ET
37	6.65121	17.14797	22.1035	0.3951	0.4083	0.648	ET
38	6.64091	17.14888	20.9124	0.447	0.3569	0.1405	LT
39	6.63635	17.14934	21.4125	0.3964	0.3894	0.6616	ET
40	6.67298	17.14845	23.5263	0.405	0.801	0.4745	UD
41	6.65566	17.14886	23.6672	0.381	0.4479	0.5723	UD
42	6.6633	17.14956	22.0716	0.357	0.5772	0.5554	UD
43	6.64817	17.14979	22.2302	0.36	0.3365	0.545	UD
44	6.61715	17.15194	20.1213	0.3925	0.7302	0.8468	ET
45	6.64752	17.15046	22.752	0.396	0.3153	0.1358	LT
46	6.6283	17.15064	21.986	0.3931	0.501	0.733	ET
47	6.63037	17.15086	23.5137	0.363	0.4568	0.1104	LT
48	6.63168	17.15031	25.038	0.405	0.4422	0.7858	ET
49	6.64513	17.15516	18.8744	0.36	0.1831	0.4889	UD
50	6.65621	17.15237	20.3236	0.3907	0.3916	0.9024	ET
51	6.65824	17.15106	22.3989	0.363	0.4525	0.084	LT
52	6.65145	17.15099	23.8336	0.387	0.3413	0.436	UD
53	6.64463	17.15209	21.9848	0.363	0.2623	0.3156	LT
54	6.66678	17.15131	24.6219	0.417	0.6287	0.454	UD

Continued on next page

Table A.1 – *Continued from previous page*

Num	RA(Deg)	DEC(Deg)	F775W_Mag	z	R(Mpc)	P <sub>FINAL</sub>	Morpho.
55	6.65972	17.15265	21.284	0.36	0.4578	0.9001	ET
56	6.65381	17.15337	21.2959	0.394	0.3296	0.7446	ET
57	6.65758	17.15183	24.6804	0.45	0.427	0.5667	UD
58	6.65938	17.1535	21.6181	0.391	0.4387	0.9027	ET
59	6.66313	17.15344	21.0142	0.3857	0.5222	0.8292	ET
60	6.63911	17.15301	23.2838	0.381	0.2717	0.8615	ET
61	6.63186	17.15443	20.1085	0.3996	0.3711	0.2863	LT
62	6.67148	17.155	21.3835	0.399	0.7043	0.1843	LT
63	6.64865	17.15377	21.1794	0.3968	0.2436	0.8916	ET
64	6.66093	17.15397	21.279	0.3967	0.4668	0.9056	ET
65	6.65776	17.15599	19.1729	0.401	0.3722	0.8685	ET
66	6.61728	17.15431	21.5251	0.4003	0.7068	0.1168	LT
67	6.64838	17.15517	21.1793	0.429	0.208	0.2945	LT
68	6.62902	17.15389	22.1341	0.4	0.4393	0.7113	ET
69	6.63428	17.15375	23.6427	0.363	0.3333	0.1342	LT
70	6.65292	17.15468	21.3563	0.42	0.2898	0.8487	ET
71	6.65186	17.15414	22.0784	0.432	0.281	0.4804	UD
72	6.66795	17.1542	22.5816	0.423	0.6261	0.6722	ET
73	6.65822	17.15454	21.7862	0.399	0.4	0.8864	ET
74	6.64588	17.16072	18.7662	0.3968	0.0531	0.4805	UD
75	6.63045	17.15615	21.2998	0.3867	0.3807	0.1182	LT
76	6.63987	17.15554	20.4931	0.3976	0.2049	0.8455	ET
77	6.63636	17.15507	23.3481	0.42	0.2715	0.8659	ET
78	6.61882	17.15563	21.495	0.39	0.6603	0.1071	LT
79	6.65203	17.15726	20.4487	0.3889	0.2306	0.1995	LT
80	6.63291	17.15549	22.7461	0.426	0.3341	0.1155	LT
81	6.63961	17.15658	19.9954	0.3916	0.1868	0.177	LT
82	6.66696	17.15652	20.9747	0.3989	0.5847	0.2927	LT
83	6.67075	17.15665	21.7649	0.429	0.6761	0.2803	LT
84	6.64952	17.15754	20.472	0.3908	0.1766	0.1622	LT
85	6.66044	17.15706	20.7111	0.36	0.4242	0.8989	ET
86	6.6401	17.15854	20.2574	0.3922	0.1413	0.6864	ET
87	6.64527	17.15836	20.0527	0.4052	0.1008	0.9003	ET
88	6.63466	17.15668	21.6178	0.391	0.2805	0.2344	LT
89	6.65307	17.15792	20.6466	0.384	0.2447	0.438	UD
90	6.66568	17.15714	21.3815	0.45	0.5497	0.8623	ET
91	6.64736	17.15716	22.7978	0.414	0.1502	0.5071	UD
92	6.65535	17.15794	21.5778	0.366	0.2964	0.9002	ET
93	6.65677	17.15772	20.4298	0.3927	0.3317	0.8603	ET
94	6.64809	17.15888	20.1277	0.3914	0.1266	0.9118	ET
95	6.67151	17.1591	20.7244	0.3946	0.6844	0.7259	ET
96	6.65453	17.15708	24.638	0.45	0.2873	0.2706	LT
97	6.61849	17.15719	24.8985	0.432	0.6591	0.1464	LT
98	6.66146	17.1588	20.8637	0.36	0.4371	0.8621	ET
99	6.67289	17.15794	24.2284	0.444	0.7228	0.7631	ET
100	6.65778	17.16042	20.0753	0.3909	0.3394	0.4207	UD
101	6.65196	17.15813	24.3683	0.384	0.2175	0.1235	LT
102	6.64749	17.16272	19.1354	0.3973	0.0807	0.8737	ET
103	6.64589	17.15836	25.638	0.414	0.1056	0.6225	UD
104	6.64792	17.1598	22.1865	0.372	0.1082	0.2974	LT
105	6.64983	17.16019	21.1095	0.3969	0.1466	0.8426	ET
106	6.65947	17.16018	22.5865	0.36	0.382	0.1701	LT

*Continued on next page*

Table A.1 – *Continued from previous page*

Num	RA(Deg)	DEC(Deg)	F775W_Mag	z	R(Mpc)	P <sub>FINAL</sub>	Morpho.
107	6.66653	17.16157	21.2897	0.3952	0.5555	0.1292	LT
108	6.64477	17.16119	21.2874	0.372	0.0265	0.4163	UD
109	6.6333	17.16136	19.958	0.3879	0.2766	0.1015	LT
110	6.65208	17.16165	20.2817	0.3884	0.1942	0.8907	ET
111	6.64498	17.1619	21.0447	0.42	0.0173	0.4174	UD
112	6.63458	17.16128	21.5814	0.3932	0.2448	0.1466	LT
113	6.67041	17.1633	19.4952	0.396	0.653	0.8675	ET
114	6.65618	17.16267	20.8276	0.3913	0.2968	0.8816	ET
115	6.65836	17.16128	25.023	0.39	0.3517	0.1184	LT
116	6.64668	17.1635	20.3955	0.3897	0.0692	0.8464	ET
117	6.666	17.16246	22.9023	0.3978	0.542	0.7295	ET
118	6.64315	17.16233	24.8953	0.384	0.03	0.1309	LT
119	6.61387	17.16243	24.5134	0.398	0.7621	0.2776	LT
120	6.62957	17.1628	22.9569	0.36	0.3697	0.3091	LT
121	6.64378	17.16349	21.33	0.39	0.0386	0.8955	ET
122	6.66702	17.16246	25.2037	0.429	0.5676	0.5513	UD
123	6.63476	17.16291	23.9308	0.384	0.2403	0.7706	ET
124	6.63249	17.16318	23.7558	0.417	0.2974	0.8238	ET
125	6.67233	17.16408	22.1028	0.444	0.7024	0.1011	LT
126	6.64801	17.16515	20.5658	0.396	0.1218	0.8768	ET
127	6.66753	17.16404	23.6593	0.45	0.5825	0.4212	UD
128	6.64232	17.1647	21.6811	0.393	0.0845	0.831	ET
129	6.66254	17.16715	20.5398	0.3949	0.4743	0.1008	LT
130	6.66091	17.16405	23.3063	0.391	0.4178	0.0798	LT
131	6.62033	17.16573	21.5479	0.395	0.6078	0.1268	LT
132	6.65096	17.16672	19.4725	0.3891	0.2052	0.8884	ET
133	6.62484	17.1646	22.6097	0.441	0.492	0.8128	ET
134	6.67138	17.16723	19.2375	0.3966	0.6898	0.8863	ET
135	6.66666	17.16447	24.4633	0.45	0.5621	0.2917	LT
136	6.64355	17.1645	25.629	0.363	0.0654	0.0911	LT
137	6.66343	17.16487	23.2312	0.384	0.4833	0.8103	ET
138	6.65057	17.16527	22.1599	0.414	0.1766	0.1776	LT
139	6.65516	17.16668	20.6449	0.3936	0.2961	0.5316	UD
140	6.65351	17.1666	20.7834	0.3916	0.2579	0.0968	LT
141	6.65991	17.16624	20.8716	0.3976	0.4044	0.898	ET
142	6.66158	17.16647	20.0063	0.3927	0.4463	0.0997	LT
143	6.66799	17.16528	24.5179	0.429	0.5975	0.2812	LT
144	6.67155	17.1663	21.7234	0.3968	0.6896	0.9081	ET
145	6.63169	17.16625	22.7025	0.414	0.3343	0.4696	UD
146	6.63338	17.16737	20.5882	0.3993	0.3067	0.4528	UD
147	6.63758	17.16602	24.384	0.426	0.1974	0.561	UD
148	6.65391	17.16758	21.5423	0.432	0.2792	0.2628	LT
149	6.6188	17.17009	21.4536	0.388	0.6718	0.1433	LT
150	6.63878	17.16763	23.2423	0.417	0.2003	0.5022	UD
151	6.65302	17.16813	21.5552	0.39	0.2684	0.2634	LT
152	6.64251	17.16921	19.9636	0.3897	0.1915	0.8129	ET
153	6.63998	17.16744	22.2701	0.3899	0.177	0.2083	LT
154	6.63525	17.1674	23.7723	0.417	0.266	0.727	ET
155	6.62453	17.16848	21.1077	0.3959	0.5226	0.7559	ET
156	6.61927	17.16786	23.8576	0.36	0.6447	0.4739	UD
157	6.64404	17.17113	20.1546	0.3899	0.2363	0.902	ET
158	6.66608	17.16898	22.1692	0.366	0.5729	0.361	LT

*Continued on next page*

Table A.1 – *Continued from previous page*

Num	RA(Deg)	DEC(Deg)	F775W_Mag	z	R(Mpc)	P <sub>FINAL</sub>	Morpho.
159	6.63384	17.16949	21.5399	0.426	0.3258	0.8486	ET
160	6.66141	17.17045	20.275	0.3922	0.4799	0.7933	ET
161	6.62949	17.17117	19.6956	0.4007	0.4405	0.7762	ET
162	6.64513	17.16935	22.6762	0.366	0.1907	0.858	ET
163	6.65401	17.16999	21.2714	0.3965	0.3181	0.8308	ET
164	6.62559	17.16977	22.0972	0.3938	0.5098	0.1242	LT
165	6.6431	17.1728	19.3792	0.3862	0.2816	0.8953	ET
166	6.66207	17.17266	19.5732	0.395	0.5226	0.5607	UD
167	6.63711	17.17323	20.8549	0.3862	0.3425	0.0832	LT
168	6.6278	17.17047	23.6703	0.396	0.468	0.1865	LT
169	6.63752	17.17036	23.8004	0.405	0.2751	0.4564	UD
170	6.67254	17.17081	22.1516	0.447	0.7415	0.5684	UD
171	6.65932	17.17085	24.0548	0.42	0.4392	0.5643	UD
172	6.64564	17.17251	20.2261	0.3884	0.2742	0.8979	ET
173	6.63837	17.1717	22.8561	0.366	0.292	0.1214	LT
174	6.62307	17.17144	23.0003	0.351	0.5852	0.1559	LT
175	6.62116	17.17345	19.9167	0.396	0.6511	0.8671	ET
176	6.63529	17.17383	19.7378	0.397	0.3812	0.8758	ET
177	6.66364	17.17202	22.6856	0.3959	0.5483	0.2934	LT
178	6.65143	17.17221	22.7781	0.417	0.3186	0.8222	ET
179	6.63839	17.17401	20.1499	0.394	0.3451	0.8768	ET
180	6.6218	17.17224	25.0163	0.441	0.6228	0.7642	ET
181	6.62974	17.17316	23.8589	0.399	0.4658	0.0866	LT
182	6.63877	17.17587	20.8412	0.3983	0.3863	0.1254	LT
183	6.6465	17.17358	23.0043	0.426	0.3051	0.5104	UD
184	6.63643	17.17356	21.9286	0.3965	0.3589	0.1833	LT
185	6.62843	17.17473	21.6285	0.417	0.5171	0.4465	UD
186	6.63073	17.17414	21.5563	0.395	0.4637	0.8723	ET
187	6.64496	17.17349	25.6477	0.372	0.2983	0.799	ET
188	6.66371	17.17416	24.6774	0.45	0.5783	0.7951	ET
189	6.66558	17.17536	21.5254	0.429	0.6348	0.4533	UD
190	6.62282	17.17563	20.6108	0.399	0.6441	0.7649	ET
191	6.64139	17.17413	25.6852	0.3957	0.3232	0.1202	LT
192	6.63014	17.17505	21.9064	0.393	0.4906	0.3506	LT
193	6.65818	17.17517	21.6632	0.3965	0.4869	0.2735	LT
194	6.65549	17.17683	21.8247	0.3965	0.4758	0.1841	LT
195	6.64273	17.17554	21.955	0.441	0.3539	0.1205	LT
196	6.62921	17.17487	23.8919	0.3954	0.5046	0.4308	UD
197	6.64393	17.17501	23.9261	0.36	0.338	0.122	LT
198	6.64529	17.17557	22.3548	0.396	0.3532	0.8058	ET
199	6.64974	17.17519	23.8982	0.363	0.3683	0.7997	ET
200	6.66715	17.17565	24.233	0.363	0.6719	0.4346	UD
201	6.64566	17.17661	21.8527	0.386	0.381	0.5529	UD
202	6.66909	17.17666	24.3635	0.417	0.727	0.3088	LT
203	6.6671	17.17676	24.4551	0.45	0.6867	0.5694	UD
204	6.64065	17.17756	21.4845	0.426	0.4148	0.5948	UD
205	6.62277	17.17799	22.7426	0.357	0.6809	0.7428	ET
206	6.63075	17.18205	18.7608	0.3961	0.6229	0.5722	UD
207	6.6524	17.17936	20.8358	0.3964	0.4947	0.8557	ET
208	6.64012	17.17929	22.8399	0.39	0.4619	0.8851	ET
209	6.62845	17.17898	24.5281	0.444	0.5941	0.1963	LT
210	6.61831	17.18115	19.8381	0.3948	0.8198	0.879	ET

*Continued on next page*

Table A.1 – *Continued from previous page*

Num	RA(Deg)	DEC(Deg)	F775W_Mag	z	R(Mpc)	P <sub>FINAL</sub>	Morpho.
211	6.65615	17.18435	21.3451	0.399	0.653	0.8646	ET
212	6.67289	17.18376	19.788	0.3916	0.9118	0.918	ET
213	6.65544	17.18406	20.9472	0.396	0.6383	0.1286	LT
214	6.64645	17.18565	20.2203	0.394	0.6185	0.1988	LT
215	6.64438	17.18039	23.1954	0.36	0.4786	0.4857	UD
216	6.65612	17.18201	22.954	0.42	0.5988	0.5642	UD
217	6.65681	17.18058	24.8601	0.429	0.5755	0.5192	UD
218	6.62057	17.17976	23.9093	0.408	0.7528	0.825	ET
219	6.64689	17.17983	23.4919	0.39	0.4684	0.214	LT
220	6.62921	17.18585	20.8603	0.3931	0.7276	0.8785	ET
221	6.64994	17.18755	21.3985	0.36	0.6806	0.8869	ET
222	6.61486	17.18511	24.8841	0.432	0.9518	0.7522	ET
223	6.64427	17.18201	20.1612	0.3934	0.5209	0.8522	ET
224	6.61494	17.18648	25.9495	0.36	0.9733	0.5468	UD
225	6.65585	17.18599	23.6625	0.36	0.6885	0.4122	UD
226	6.62011	17.18055	23.3693	0.3911	0.7747	0.2654	LT
227	6.6524	17.18544	19.6788	0.3807	0.6431	0.172	LT
228	6.62905	17.18709	22.0732	0.444	0.7575	0.548	UD
229	6.62331	17.18748	21.7678	0.3955	0.8471	0.1501	LT
230	6.65309	17.18695	24.232	0.408	0.6861	0.4208	UD
231	6.63452	17.18605	24.4649	0.447	0.6731	0.2911	LT

# Appendix B

## Catalogue of [OIII] and H $\beta$ emitters in ZwCl0024+1652 galaxy cluster

### Brief description of the columns of Table B.1

#Column 1 ... H $\alpha$  line ID number with subscript O for offset and C for centre position;

#Column 2 ... HST ID number; = -99. if not available;

#Column 3 ... Right Ascension in decimal degrees (J2000);

#Column 4 ... Declination in decimal degrees (J2000);

#Column 5 ... Clustercentric distance in Mpc;

#Column 6 ... TF redshift measured with [OIII] line; = 99.0 if not available;

#Column 7 ... TF redshift measured with H $\beta$  line; = 99.0 if not available;

#Column 8 ... List of emission lines detected;

#Column 9 ... BPT-NII classification (our work); = -99.9 if not available;

**Table B.1:** The [OIII] and H $\beta$  catalogue of ZwCl0024+1652 cluster ([Beyoro-Amado et al., 2021](#)).

id_H $\alpha$	id_HST	RA(Deg)	DEC(Deg)	R(Mpc)	z_[OIII]	z_H $\beta$	EL_detected	Spec_Class
1015_O	-99	6.6232	17.2470	2.8131	99.0	0.3955	H $\beta$ ,H $\alpha$ ,[NII]	99.9
1039_O	136	6.5373	17.2530	4.5367	99.0	0.3958	H $\beta$ ,H $\alpha$ ,[NII]	99.9
1057_O	-99	6.5649	17.2295	1.8003	0.3922	99.0	[OIII],H $\alpha$ ,[NII]	99.9
1097_O	-99	6.5642	17.2282	3.6278	0.3957	0.3954	H $\beta$ ,[OIII],H $\alpha$ ,[NII]	Composite
1157_O	109	6.5377	17.2212	4.1462	0.4057	0.4039	H $\beta$ ,[OIII],H $\alpha$ ,[NII]	SF
1173_O	-99	6.6182	17.2600	3.1621	0.3876	0.3917	H $\beta$ ,[OIII],H $\alpha$ ,[NII]	SF
1204_O	-99	6.5762	17.2169	1.4760	0.3970	99.0	[OIII],H $\alpha$ ,[NII]	99.9

*Continued on next page*

Table B.1 – Continued from previous page

id_H $\alpha$	id_HST	RA(Deg)	DEC(Deg)	R(Mpc)	z_[OIII]	z_H $\beta$	EL_detected	Spec_Class
1219_O	-99	6.6373	17.2581	2.8682	99.0	0.3808	H $\beta$ ,H $\alpha$ ,[NII]	99.9
1220_O	-99	6.6007	17.2576	3.3879	99.0	0.4005	H $\beta$ ,H $\alpha$ ,[NII]	99.9
12_C	151	6.6790	17.1034	1.5490	99.0	0.3911	H $\beta$ ,H $\alpha$	99.9
138_C	-99	6.6427	17.1284	0.8800	0.3771	99.0	[OIII],H $\alpha$ ,[NII]	99.9
139_O	10	6.6304	17.1563	1.5274	99.0	0.3889	H $\beta$ ,H $\alpha$ ,[NII]	99.9
146_O	60	6.6347	17.1569	1.4203	99.0	0.3916	H $\beta$ ,H $\alpha$ ,[NII]	99.9
193_C	9	6.6672	17.1393	0.8364	99.0	0.4041	H $\beta$ ,H $\alpha$ ,[NII]	99.9
200_C	47	6.6788	17.1399	0.6450	99.0	0.3954	H $\beta$ ,H $\alpha$ ,[NII]	99.9
219_C	-99	6.5686	17.1445	3.1001	99.0	0.4020	H $\beta$ ,H $\alpha$ ,[NII]	99.9
247_O	-99	6.6333	17.1675	1.4574	0.3990	0.3988	H $\beta$ ,[OIII],H $\alpha$ ,[NII]	SF
253_C	6	6.6154	17.1476	1.9319	0.3796	0.3823	H $\beta$ ,[OIII],H $\alpha$ ,[NII]	Composite
255_C	-99	6.5991	17.1471	2.3346	99.0	0.4001	H $\beta$ ,H $\alpha$ ,[NII]	99.9
263_C	134	6.6410	17.1489	0.3649	0.3996	99.0	[OIII],H $\alpha$ ,[NII]	99.9
265_C	131	6.5777	17.1491	0.4872	0.4074	99.0	[OIII],H $\alpha$ ,[NII]	99.9
277_O	-99	6.5705	17.1674	3.0240	99.0	0.3913	H $\beta$ ,H $\alpha$ ,[NII]	99.9
278_O	31	6.6295	17.1713	1.5648	0.3965	0.4005	H $\beta$ ,[OIII],H $\alpha$ ,[NII]	Composite
282_O	-99	6.6021	17.1685	2.2377	99.0	0.3798	H $\beta$ ,H $\alpha$ ,[NII]	99.9
285_C	28	6.6283	17.1508	1.5998	0.3918	0.3938	H $\beta$ ,[OIII],H $\alpha$ ,[NII]	SF
291_O	156	6.6188	17.1702	1.8273	99.0	0.3879	H $\beta$ ,H $\alpha$ ,[NII]	99.9
308_C	94	6.6715	17.1551	0.1770	0.3991	99.0	[OIII],H $\alpha$ ,[NII]	99.9
320_C	12	6.6291	17.1539	1.5663	0.3967	0.3993	H $\beta$ ,[OIII],H $\alpha$	0.0
332_C	92	6.5760	17.1549	2.8874	0.3776	0.3833	H $\beta$ ,[OIII],H $\alpha$ ,[NII]	SF
337_C	-99	6.5636	17.1550	0.4354	0.4013	99.0	[OIII],H $\alpha$ ,[NII]	99.9
338_C	63	6.6396	17.1568	1.2975	99.0	0.3880	H $\beta$ ,H $\alpha$ ,[NII]	99.9
339_C	122	6.6188	17.1558	1.8180	0.3894	0.3917	H $\beta$ ,[OIII],H $\alpha$ ,[NII]	SF
358_C	43	6.6420	17.1571	0.1903	0.4044	99.0	[OIII],H $\alpha$	99.9
405_C	163	6.6746	17.1647	0.4244	99.0	0.3919	H $\beta$ ,H $\alpha$ ,[NII]	99.9
408_C	-99	6.5756	17.1635	2.8926	99.0	0.3915	H $\beta$ ,H $\alpha$ ,[NII]	99.9
422_C	159	6.6777	17.1641	0.3473	0.3931	0.3917	H $\beta$ ,[OIII],H $\alpha$ ,[NII]	Composite
433_C	120	6.6724	17.1641	0.0902	0.3977	99.0	[OIII],H $\alpha$ ,[NII]	99.9
456_C	2	6.5918	17.1682	2.4927	99.0	0.3950	H $\beta$ ,H $\alpha$ ,[NII]	99.9
501_O	-99	6.6061	17.1910	0.8045	0.3773	99.0	[OIII],H $\alpha$ ,[NII]	99.9
559_C	139	6.6718	17.2345	1.9133	0.3916	99.0	[OIII],H $\alpha$ ,[NII]	99.9
560_C	15	6.5983	17.2327	2.9817	0.3965	0.4000	H $\beta$ ,[OIII],H $\alpha$ ,[NII]	Composite
574_C	130	6.6214	17.2341	2.5835	99.0	0.3940	H $\beta$ ,H $\alpha$ ,[NII]	99.9
575_C	150	6.6078	17.1741	2.1148	99.0	0.3984	H $\beta$ ,H $\alpha$ ,[NII]	99.9
582_C	-99	6.6413	17.1744	1.2957	99.0	0.3945	H $\beta$ ,H $\alpha$ ,[NII]	99.9
620_C	144	6.6083	17.1749	2.1053	0.4065	0.4037	H $\beta$ ,[OIII],H $\alpha$ ,[NII]	SF
625_C	51	6.6284	17.1749	1.6103	99.0	0.3967	H $\beta$ ,H $\alpha$ ,[NII]	99.9
658_C	-99	6.6408	17.2275	2.1408	99.0	0.3965	H $\beta$ ,H $\alpha$ ,[NII]	99.9
675_C	-99	6.6465	17.1857	1.2868	99.0	0.3953	H $\beta$ ,H $\alpha$ ,[NII]	99.9
677_C	-99	6.6730	17.1838	0.7439	99.0	0.3883	H $\beta$ ,H $\alpha$ ,[NII]	99.9
728_C	177	6.6028	17.2114	2.5705	0.3952	0.3962	H $\beta$ ,[OIII],H $\alpha$ ,[NII]	Composite
72_C	93	6.5809	17.1174	1.2192	0.3965	99.0	[OIII],H $\alpha$ ,[NII]	99.9
72_O	-99	6.5467	17.1507	3.6261	99.0	0.3922	H $\beta$ ,H $\alpha$ ,[NII]	99.9
748_C	19	6.6176	17.2188	2.3761	0.3801	0.3820	H $\beta$ ,[OIII],H $\alpha$ ,[NII]	Composite
758_C	37	6.6147	17.2163	2.3935	0.3988	0.3964	H $\beta$ ,[OIII],H $\alpha$ ,[NII]	Composite
762_C	34	6.6124	17.2176	2.4610	99.0	0.3945	H $\beta$ ,H $\alpha$ ,[NII]	99.9
772_C	114	6.6567	17.2150	1.6476	99.0	0.3999	H $\beta$ ,H $\alpha$ ,[NII]	99.9
773_C	107	6.6070	17.2147	2.5275	99.0	0.3988	H $\beta$ ,H $\alpha$ ,[NII]	99.9
777_C	52	6.6142	17.2141	2.3695	99.0	0.3825	H $\beta$ ,H $\alpha$ ,[NII]	99.9
783_C	-99	6.6182	17.2129	2.2711	0.4035	0.4056	H $\beta$ ,[OIII],H $\alpha$ ,[NII]	Composite

Continued on next page



Table B.1 – *Continued from previous page*

id_H $\alpha$	id_HST	RA(Deg)	DEC(Deg)	R(Mpc)	z_[OIII]	z_H $\beta$	EL_detected	Spec_Class
814_C	165	6.6135	17.2080	1.2346	0.3755	99.0	[OIII],H $\alpha$ ,[NII]	99.9
826_C	77	6.6402	17.2055	1.7212	99.0	0.3973	H $\beta$ ,H $\alpha$ ,[NII]	99.9
847_O	69	6.5356	17.2496	4.5269	99.0	0.3973	H $\beta$ ,H $\alpha$	99.9
850_C	167	6.6072	17.2015	2.3521	0.3936	0.3943	H $\beta$ ,[OIII],H $\alpha$ ,[NII]	Composite
875_C	-99	6.6021	17.1917	2.3658	99.0	0.3916	H $\beta$ ,H $\alpha$ ,[NII]	99.9
882_C	48	6.6165	17.1938	2.0541	99.0	0.4052	H $\beta$ ,H $\alpha$ ,[NII]	99.9
886_C	-99	6.6412	17.1951	1.5311	0.3919	0.3961	H $\beta$ ,[OIII],H $\alpha$ ,[NII]	LINER
888_C	-99	6.6400	17.1948	1.5515	0.3855	0.3889	H $\beta$ ,[OIII],H $\alpha$ ,[NII]	Composite
927_C	1	6.5951	17.1869	2.4948	99.0	0.3975	H $\beta$ ,H $\alpha$ ,[NII]	99.9
929_C	-99	6.6525	17.1855	0.6390	0.3798	99.0	[OIII],H $\alpha$ ,[NII]	99.9
935_C	141	6.6113	17.1841	2.0846	99.0	0.3941	H $\beta$ ,H $\alpha$ ,[NII]	99.9
948_C	79	6.6200	17.1806	1.8529	0.3906	0.3915	H $\beta$ ,[OIII],H $\alpha$ ,[NII]	SF
97_C	125	6.6455	17.1208	1.5632	99.0	0.4086	H $\beta$ ,H $\alpha$ ,[NII]	99.9
998_O	170	6.6106	17.2693	3.4715	99.0	0.3933	H $\beta$ ,H $\alpha$ ,[NII]	99.9